



Using Semi-Empirical Models For Predicting The Luminescence –Structure Relationships in Near-UV Excited Phosphors Activated with Divalent Europium or Mercury-like Cations

Mariam Amer

► To cite this version:

Mariam Amer. Using Semi-Empirical Models For Predicting The Luminescence –Structure Relationships in Near-UV Excited Phosphors Activated with Divalent Europium or Mercury-like Cations. Material chemistry. Université Clermont Auvergne [2017-2020], 2017. English. NNT : 2017CLFAC069 . tel-01791280

HAL Id: tel-01791280

<https://theses.hal.science/tel-01791280>

Submitted on 14 May 2018

HAL is a multi-disciplinary open access archive for the deposit and dissemination of scientific research documents, whether they are published or not. The documents may come from teaching and research institutions in France or abroad, or from public or private research centers.

L'archive ouverte pluridisciplinaire **HAL**, est destinée au dépôt et à la diffusion de documents scientifiques de niveau recherche, publiés ou non, émanant des établissements d'enseignement et de recherche français ou étrangers, des laboratoires publics ou privés.

UNIVERSITÉ CLERMONT-AUVERGNE

U.F.R. Sciences et Technologies

ÉCOLE DOCTORALE DES SCIENCES FONDAMENTALES

N°932

THÈSE

Présentée pour obtenir le grade de

DOCTEUR D'UNIVERSITÉ

Spécialité : Chimie, Sciences des Matériaux

Par **Mariam AMER**

Diplômé Master Nanostructures et nanophotoniques de l'Institut Pascal-Clermont Ferrand

Using Semi-Empirical Models For Predicting The Luminescence – Structure Relationships in Near-UV Excited Phosphors Activated with Divalent Europium or Mercury-like Cations.

Soutenue publiquement le 13 Décembre 2017 devant la commission d'examen :

Rapporteurs

M. Alain BRAUD

Maître de conférences, Université de Caen, ENSICAEN

M. Bruno VIANA

Directeur de Recherche CNRS, Chimie ParisTech, LCMCP

Examineurs

M.^{me} Geneviève CHADEYRON

Professeur des Universités, SIGMA Clermont, UCA, ICCF

M.^{me} Véronique JUBERA

Maître de conférences, Université de Bordeaux, ICMCB

M.^{me} Audrey POTDEVIN

Maître de conférences, SIGMA Clermont, UCA, ICCF

Directeur de thèse

M. Philippe BOUTINAUD

Professeur des Universités, SIGMA Clermont, UCA, ICCF

Résumé

La stratégie la plus utilisée aujourd'hui pour la conception de nouveaux matériaux luminescents est basée sur des méthodes d'essais-erreurs. Cependant, ces méthodes peuvent souvent entraîner une consommation d'argent et de temps. En ce sens, un modèle théorique agissant comme un outil prédictif peut servir comme une stratégie alternative. De tels modèles sont également étudiés et utilisés par des scientifiques du monde entier, mais ils sont pour la plupart difficiles à utiliser. Dans ce travail, deux modèles semi-empiriques conviviaux et faciles à utiliser ont été proposés pour la conception de luminophores intégrés dans le développement de technologies importantes, en particulier dans les éclairages à base de LED et les cellules solaires. Ces modèles sont: 1) le modèle de facteur environnemental (EF) basé sur la théorie diélectrique de la liaison chimique proposée par Philips et 2) le modèle de transfert de charge métal-métal (MMCT) utilisées pour trouver des relations entre les propriétés structurales d'un matériau et sa luminescence. Le modèle EF a été appliqué à la famille des composés $A^I B^{II} PO_4$ (A^I = cation monovalent, B^{II} = cation divalent) dopés à Eu^{2+} . Il était capable d'estimer l'énergie du bord d'excitation et d'identifier les sites de dopage à $\pm 1000\text{ cm}^{-1}$. Il peut donc être utilisé pour la conception de nouveaux luminophores appartenant à cette famille. Dans la deuxième partie, les deux modèles ont été utilisés pour identifier la nature de la luminescence dans les oxydes dopés à Bi^{3+} . A cet effet, une méthode combinant les modèles motionnés avec les valeurs de Stokes shift a été trouvée fiable. En outre, la a été jugée utile pour expliquer la modification des propriétés luminescentes de $YVO_4:Bi^{3+}$ sous haute pression. Dans la troisième partie, les deux modèles ont été utilisés pour explorer la luminescence des oxydes dopés à Sb^{3+} par analogie avec Bi^{3+} . Cependant, les résultats n'étaient pas assez bons pour identifier la nature de la luminescence dans ces matériaux. La raison pourrait être liée à la position décentrée du dopant (Sb^{3+}).

Mots Clés : modèles semi-empiriques, propriétés optiques, propriétés structurales, Eu^{2+} , Bi^{3+} , Sb^{3+} , LEDs.

Abstract

The most used strategy for the design of new luminescent materials today is based on trial-error methods. However, these methods may often result in consummation of money and time. In this sense, a theoretical model acting as a predictive tool can serve as an alternative strategy. Such models are also studied and used by scientists around the world but they are mostly difficult to use. In this work, two friendly and easy to use semi-empirical theoretical models were proposed as a criterion for designing phosphors integrated in the development of important technologies especially in LED-based lightings and solar cells. These models are: 1) the environmental factor model (EF) based on the dielectric theory of chemical bonding proposed by Philips and 2) the metal to metal charge transfer (MMCT) model by Boutinaud that were both used for the purpose of finding relationships between the structural properties of a material and its luminescence. The EF model was applied on the family of $A^I B^{II} PO_4$ (A^I = monovalent cation, B^{II} = divalent cation) compounds doped with Eu^{2+} . It was able to estimate the excitation edge energy and to identify the doping sites within uncertainty of $\pm 1000\text{ cm}^{-1}$. It can therefore, be used for the design of new phosphors belonging to this family. In a second part, both models were used to identify the nature of luminescence in Bi^{3+} -doped oxides. For this purpose, a method combining the mentioned models along with the values of the Stokes shift was found reliable. In addition, the method was found useful to explain the change in luminescent properties of $YVO_4:Bi^{3+}$ under high pressure. In the third part, the two models were used to explore the luminescence of Sb^{3+} -doped oxides by analogy with Bi^{3+} . However, the results were not good enough to identify the nature of luminescence in these materials. The reason could be related to the off-centered position of the dopant (Sb^{3+}).

Key words: Semi-empirical models, optical properties, structural properties, Eu^{2+} , Bi^{3+} , Sb^{3+} , LEDs.

Acknowledgements

I would like to thank all people who contributed to this work.

First, I would like to thank my supervisor, the director of this thesis, Philippe BOUTINAUD for all the support he gave me during the last three years and especially at the end when I was writing this manuscript and was under pressure to finish before the deadline. Thank you for believing in my work in the first place and giving me the opportunity to be a member of the ML group at the ICCF Clermont-Ferrand. I extremely appreciate the efforts you did to make this work successful. I cannot forget all the hours you spent with me explaining, correcting or solving problems. Thanks for your care to always make me comfortable without putting any pressures on me. It was really an honor to work with you, I learned a lot from you.

I want to thank the head of the ML group, Genevieve CHADEYRON for her support, her smile and sympathy. Such a lovely person with all the positivity.

I would also like to thank all the members of the ML group and the ICCF especially the PhD students Sihem SEBAI, Mourad Seraiche, Paul Legentil, and the post-doctorants Rachod BOONSNIN, Mohamad KHAYWAH, Yasser Ahmad and Jeff NYALOSASO with whom I shared good moments. It was nice to meet you all.

Special thanks to all the persons who helped me with the experimental part: Rachid MAHIOU, Daniel ZAMBON, Anthony BARROS, Jeremy PEYROUX, Nathalie CAPERAA and Rodolphe THIROUARD.

I would like to thank all my Lebanese friends in Clermont.

I thank my parents and my family for their support and especially my father who was the first to encourage me towards a PhD degree and who supported me financially and emotionally. Thank you for being such a great father!

Finally, maybe it was not meant to be without you. Your presence in my life made the last three years much easier. Thanks for all your support that I will never ever forget. In the hard times you were there to give me power and confidence. Thank you for every moment we shared together my partner, my friend and my guardian: Hussein...

Table of Contents

General Introduction.....	11
Chapter 1: State of the art	15
1.1. Introduction to luminescence and its applications.....	15
1.2. Basic principles of luminescence	15
1.3. Effect of crystal structure on luminescence	24
1.4. Spectroscopy of important luminescent activators.....	26
1.4.1. <i>4f elements</i>	26
1.4.2. <i>Transition metal ions</i>	31
1.4.3. <i>Mercury like ions (s^2)</i>	31
1.5. LED- based lighting materials.....	36
1.6. Semi-empirical models.....	39
1.6.1. <i>Importance of semi-empirical models</i>	39
1.6.2. <i>Overview of some theoretical models</i>	39
1.6.3. <i>The Environmental factor (EF) model</i>	40
1.6.4. <i>MMCT model</i>	50
Bibliography	53
Chapter 2 The doping sites in $A^I B^II PO_4:Eu^{2+}$ and their consequence on the photoluminescence excitation spectra	59
2.1. Introduction	59
2.2. Synthesis and structural/microstructural characterizations of $NaZnPO_4:Eu^{2+}$	61
2.3. Luminescence properties of $NaZnPO_4:Eu^{2+}$	65
2.4. Calculation of the environmental factors in $A^I B^II PO_4$ lattices	67
2.5. Doping sites in $A^I B^II PO_4:Eu^{2+}$	72
2.6. Designing $A^I B^II PO_4-Eu^{2+}$ phosphors for solid state LED-based lighting.....	75
2.7. Conclusion.....	79
Bibliography	80
Chapter 3: The origin of luminescence in Bi^{3+} - doped closed transition metal oxides.....	85
3.1. Introduction	85
3.2. Synthesis and photoluminescence of closed transition metal oxides doped with Bi^{3+}	86

3.3. Calculations of MMCT and E_A energies in Bi^{3+} -doped transition metal oxides	88
3.4. Assigning the origin of luminescence in closed shell metallic oxides doped with Bi^{3+} with the help of Stokes shift values	91
3.5. Criterion for the assignment of the luminescence signals in Bi^{3+} -doped transition metal oxides ..	94
3.6. Energy Level Structure of Bi^{3+} in YVO_4 under high hydrostatic pressure	97
3.6.1. Luminescence of $\text{Z-YVO}_4\text{:Bi}^{3+}$ under pressure ($P < 8\text{GPa}$)	100
3.6.2. Luminescence of $\text{S-YVO}_4\text{:Bi}^{3+}$ under pressure ($P \geq 9\text{GPa}$)	105
3.7. Conclusion	109
Bibliography	111
Chapter 4: Luminescence of Sb^{3+} in closed-shell transition metal oxides	117
4.1. Introduction	117
4.2. Synthesis of closed shell transition metal oxides doped with Sb^{3+}	119
4.3. Luminescence of transition metal oxides doped with Sb^{3+}	119
4.3.1. Luminescence of Sb^{3+} -doped Zirconates.....	119
4.3.2. Luminescence of Sb^{3+} -doped niobates and tantalates	120
4.3.3. Luminescence of Sb^{3+} -doped molybdates.....	122
4.4. Application of the EF and MMCT models to Sb^{3+} -doped compounds	123
4.4.1. Calculation of environmental factors $h\nu(X(i))$	123
4.4.2. Establishing an empirical equation for A band transitions	126
4.4.3. Establishing an empirical equation for MMCT (or D-like) transitions	130
4.5. Origin of the photoluminescence excitation in Sb^{3+} -doped closed shell transition metal oxides .	130
4.6. Conclusion	133
Bibliography	134
General Conclusion	139
Appendix A: Electronegativities of different cations	141
Appendix B Coordination Matrices	144
Appendix C: XRD patterns of Sb^{3+} -doped compounds	178

General Introduction

Nowadays, luminescent materials, or phosphors, are integrated in a various range of important technologies starting from television screens, computers, mobile phones, lasers, red indicators to X-ray photography, cathode ray tubes and solid state lightings...Despite the huge production of phosphors, a lot of them still present considerable drawbacks especially under the effect of temperature. It is straightforward to improve the quality of these materials by creating new compositions of luminescent materials. This becomes inevitable basically for LED based lighting uses to help obtaining the warm white light. For this purpose broad band emitting phosphors in the visible region and excited in the UV region are of particular interest. However, the spectral range of emission and excitation of such materials is generally strongly dependent on the nature of the dopant and on that of the host lattice. For this reason, they are usually difficult to design. Most of the time, this difficulty is overcome by preparing as much new materials as possible and study their optical properties. This approach, typically based on combinational chemistry, is time and sometimes matter consuming, with uncertain results. The second approach is to develop methods that allow predicting the properties and then save money and time. A number of theoretical methods and semi-empirical models have been established in order to explain the properties of luminescent materials and especially to relate these properties to the crystal structure. However, these approaches were either too complicated or lack the ability to be applied in a wide range of compounds.

The purpose of this work is to introduce friendly and easy to use methods helping for the design of band-like emitting compounds in which the dopant is either Eu^{2+} or the mercury like ions Bi^{3+} and Sb^{3+} . The choice of these dopants is justified as follows: (1) Eu^{2+} has a strategic interest for LED-based lighting in many different host lattices, including silicates and phosphates. Its choice, in this context, is obvious. (2) Bi^{3+} is not a rare earth, which is, in the context of LED-based lighting, of economical interest. The luminescence of this ion could be very bright in complex transition metal oxides like for instance YVO_4 . Here, the broad yellow emission that is obtained, which has a charge transfer character, could eventually replace the Ce^{3+} emission in YAG, thus eliminating the need of Ce^{3+} . Bi^{3+} is also a well-known sensitizer of trivalent lanthanide luminescence, subject that there is a maximum of overlap between the emission of Bi^{3+} and the absorption of the trivalent lanthanide. In this connection, the prediction of the spectral distribution of the Bi^{3+} features is of great importance. (3) Sb^{3+} is a mercury-like cation with s^2

electron configuration, like Bi^{3+} , but its luminescence behavior in transition metal oxides is almost unknown. There is an opportunity here to start re-investigating the optical properties of this forgotten activator at the light of our newly developed models.

This manuscript is divided into four chapters:

The first chapter is an introduction that explains luminescence of different phosphors and introduces two semi-empirical models, the environmental factor model (EF) and the metal to metal charge transfer (MMCT) model, to be investigated for being a good compromise between efficiency and ease of use.

The second chapter presents the application of the environmental factor model on the case of Eu^{2+} ions incorporated in monophosphate lattices of the type ABPO_4 ($\text{A} = \text{Li}^+, \text{Na}^+, \text{K}^+$; $\text{B} = \text{Mg}^{2+}, \text{Ca}^{2+}, \text{Sr}^{2+}, \text{Ba}^{2+}$). Our motivation here is to evaluate the relevancy of the model, try to identify the nature of doping sites in the materials and propose a criterion for the design of $\text{ABPO}_4:\text{Eu}^{2+}$ phosphors. In the context of the work, the phosphate $\text{NaZnPO}_4:\text{Eu}^{2+}$ is prepared and its photoluminescence is firstly described.

The third chapter is an investigation of the nature of the luminescence of Bi^{3+} in transition metallic oxides containing metal cations that have closed-shell d^0 electron configuration (i.e. titanates, vanadates, niobates, molybdates, etc...). This is achieved on the basis of EF and MMCT models. In the specific case of $\text{YVO}_4:\text{Bi}^{3+}$, which has a strategic importance, it appeared that energy levels of different origin are degenerated, which makes their identification impossible by the mean of standard photoluminescence spectroscopy. In this case, high hydrostatic pressure was applied in the range 0-20 GPa in order to check whether this degeneracy could be lifted. In this purpose, our models are refined to take into account the action of external pressure.

The fourth and last chapter presents the preparation and spectral measurements of new Sb^{3+} -doped closed-shell transition metal oxides. Again, the EF and MMCT models are used to get better insight in the complex luminescence of these compounds.

Chapter 1: State of the art

1.1. Introduction to luminescence and its applications

Luminescence is the emission of light (electromagnetic radiation) as a result of electronic transitions in a material. It is also known as “cold body radiation” and is in contrast with the phenomenon of black or hot body radiation caused by heating the material at high temperatures for a certain time until it glows (incandescence)^{(1),(2)}. Luminescent materials, also called phosphors, are widely present in our daily lives almost everywhere we go. They can be used in television screens, computers, mobile phones, organic LEDs, inorganic LEDs, lasers, X-ray photography, red indicators, etc....

Luminescence takes place, in principle, when the material absorbs external energy then converts it into photons⁽¹⁾. According to the source of energy, luminescence can be classified into several types such as cathodoluminescence, electroluminescence, fluorescence, photoluminescence... Luminescent materials vary in the color of radiation they emit and in its intensity. It can be any color of the visible spectrum and even an infrared or ultraviolet radiation.

Luminescence was first found in nature and was thought of as a kind of magical phenomenon. An example is the famous Barite BaSO_4 stone of Bologna discovered in the 1600 which glows under exposure to sunlight and emits light for hours in the darkness. It was considered mysterious for 400 years. Throughout the years, scientific explanations for this phenomenon had been made especially after the great evolution of material science. People now not only can understand how luminescence works, they can also create nicely color emitting phosphors.

1.2. Basic principles of luminescence

A luminescent material is usually created by doping a micron-sized or nano-sized grain of solid, called the host lattice, within some amount of cations (usually a few percent or less), called activators or center ions. The host can be an insulator, a conductor, a glass or a semi-conductor depending on the target of application. The activators used are usually rare earth ions in their divalent or trivalent oxidation states (Eu^{2+} , Eu^{3+} , Yb^{2+} , Dy^{3+} , Ce^{3+} ...), transition metal cations (Mn^{2+} , Mn^{4+} , Cr^{3+} ...) and mercury like cations/ s^2 ions (Bi^{3+} , Sb^{3+} , Sn^{2+} , Pb^{2+} ..). When a luminescent ion is exposed to a source of energy, it will be excited (Figure 1). In most of the cases, the activator absorbs the energy and one of its electrons moves

from the ground state to a higher excited level of energy (absorption of energy). Because this excitation level is unstable, the electron returns back to the ground state by losing its energy in the form of photons (emission)^{(1),(3)}. The energy levels of the ion can be derived from Hund's rule and are usually indicated by the general spectroscopic term $^{2S+1}L_J$, where S is the total spin, L the total orbital angular momentum and J the total angular momentum of the orbital electrons^{(4),(5)}. L is written as S, P, D, F, G, H, I, for L=0, 1, 2, 3, 4, 5, 6 respectively.

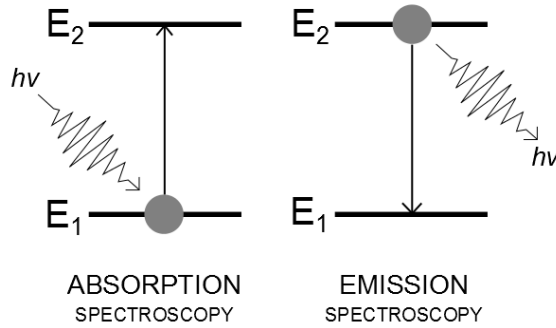


Figure 1. Absorption and emission of energy. E_1 is the ground state and E_2 is the excited state. $h\nu$ is the energy absorbed or emitted.

The configurational coordinate diagram is a good way to illustrate schematically the details of emission and absorption mechanisms of a luminescent center (Figure 2). It can be defined as a plot of the interatomic distance (R), which is the distance between the center and the neighboring ligand (surrounding anions), versus potential energy (E). It is generally assumed that the ligands are always vibrating back and forth towards the central ion in a symmetrical stretching mode of motion. This vibration, being harmonic, is treated as a quantum harmonic oscillator and thus, the relation between the potential energy E and R (the distance of the ligand from the ion) has a parabolic shape^{(1),(5)}:

$$E = \frac{1}{2}kR^2, \text{ } k \text{ is the oscillator constant.} \quad (1)$$

The solution of the Schrödinger Equation in that case that yields the sub levels of energy is:

$$E_v = \left(v + \frac{1}{2}\right)h \quad (2)$$

Where ν is the frequency of the oscillator and h is Plank's constant.⁽¹⁾

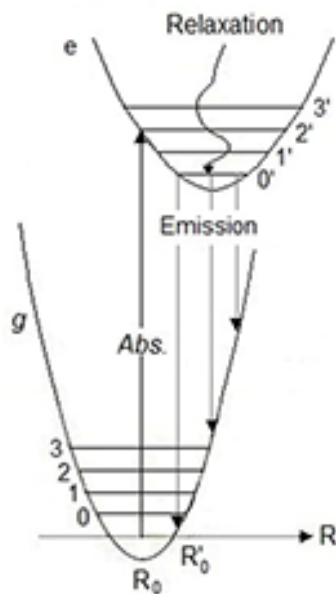


Figure 2. Example of a one-coordinate configurational diagram of a luminescent center. The lower (g) and upper (e) parabolas represent the ground and excited states respectively. R_0 and R'_0 are the equilibrium distances between the center and the ligands in the ground and excited states respectively⁽⁴⁾.

The lower parabola (g) in Figure 2 represents the ground state and the upper one (e) is the first (or lowest-lying) excited state. The horizontal lines in each parabola are the vibrational sub levels. R_0 is the equilibrium position of the distance between the ion and the ligands in the ground state. In the excited state, the luminescent center usually undergoes a change in the chemical bonding with the neighboring anions which results in a new equilibrium interatomic distance R'_0 ⁽¹⁾.

A transition between the vibrational sub levels of the ground state or those of the excited state does not lead to the emission of light. It is called relaxation, where energy is dissipated as heat to the surroundings⁽¹⁾. In most cases, excitation is followed by relaxation to lower vibrational levels of the excited state. Emission occurs only after the return of the electron to the ground state. Hence, the excitation and emission energies are not equal as shown in the figure. The difference between the two energies is known as the Stokes shift.

Vertical transitions are electronic or vibronic in nature and are responsible for the intensity of the signal. Horizontal movements, however, are nuclear because they are related to the interatomic distance. Both types of movements are combined to define the type of signal that will be displayed after excitation or emission. The probability of having an optical transition is proportional to:

$$\langle e|r|g\rangle\langle\chi_n|\chi\rangle \quad (3)$$

Where r is the electronic dipole operator and χ_n and χ are the vibrational wave functions of the excited state and the ground state, respectively. The first term of Equation (3) represents the electronic element and the second one is called the vibrational overlap.

In the first vibrational level, the wavefunction is maximum at R_0 , whereas in higher vibrational levels the wavefunction is maximum at the edges of the parabola (Figure 3).

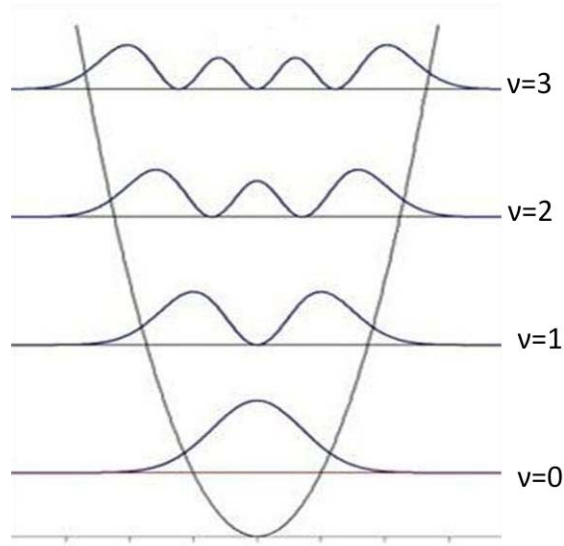


Figure 3. Wavefunctions in the vibrational levels of the ground state. It is maximum at the equilibrium position in the first vibrational levels, whereas in higher levels it is maximum at the edges of the parabola.

This means that the transition starting from R_0 has the maximum intensity of the signal. When the two parabolas lie exactly above each other, that is when $R = R_0$, the energy of this transition dominates the spectrum and appears as a sharp line. It is called the zero-phonon transition. In the other case where R is different from R_0 , other energies could be possible and the signal appears as a broad band (Figure 4).

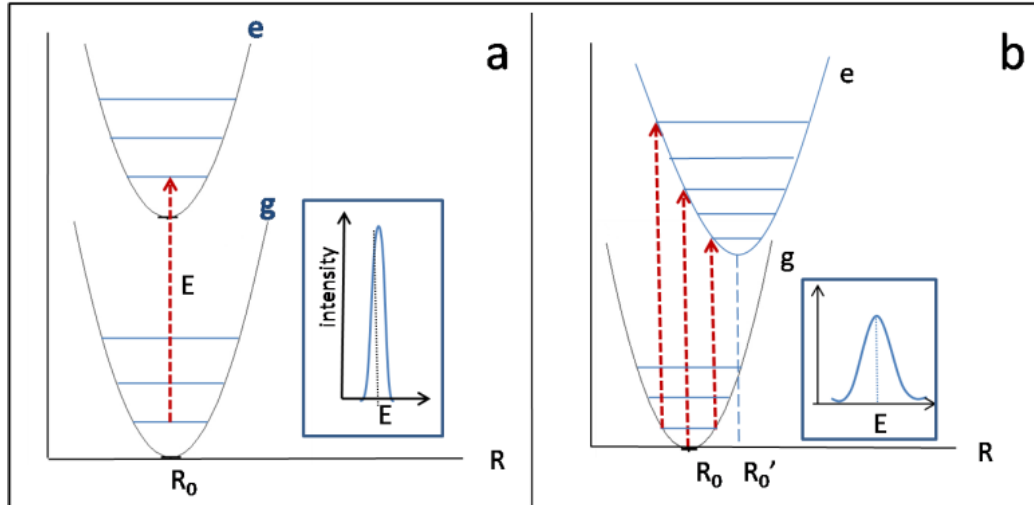


Figure 4. Effect of interactions on the spectral shape, in a) $\Delta R=0$ results in a sharp line, while in b) a broad band appears because $\Delta R>0$.

The vibrational overlap is then responsible for the shape of the band. A broad band is always accompanied by a large Stokes shift. That can be confirmed by this Equation:

$$\Delta E = S\hbar\omega \quad (4)$$

Where ΔE is the Stokes shift, S is the Huang-Rhys parameter that measures the dopant-lattice (electron-phonon) interactions and $\hbar\omega$ is the energy difference between the vibrational levels. S is proportional to:

$$k \frac{R' - R}{\hbar\omega} \quad (5)$$

The difference between R_0 and R_0' (ΔR) is a very important parameter that reflects the interactions and couplings of the ion with its ligands and informs us about the type of signal expected to be seen. The above information can give three types of couplings:

- Weak coupling ($\Delta R=0$) → small Stokes shift and very narrow band (sharp line).
- Intermediate coupling ($\Delta R>0$) → large Stokes shift and broad band.
- Strong coupling ($\Delta R \gg 0$) → very large Stokes shift and very broad band.

Materials that show sharp lines will be out of the context of this work because they present atomic-like luminescence that does not change much according to the crystal structure. Instead, the

interest will be focused on broad band absorbing and emitting materials whose spectral features are more difficult to predict.

Non-radiative transitions from the excited to the ground state are also possible. In that case, the absorbed energy is partially or completely transformed into heat through the crystal. This is quenching⁽⁶⁾. It usually happens when the material is exposed to high temperatures. It may also occur after energy transfer to a luminescent quencher (for example a defect) in case of high concentration of the activator.

From the configurational diagram viewpoint, non-radiative return to the ground state takes place when the electron reaches the intersection of the two parabolas. In that case, the electron moves to a vibrational level of the ground state that is nearly resonant with that occupied by the electron in the excited state (intersystem crossing) (Figure 5).

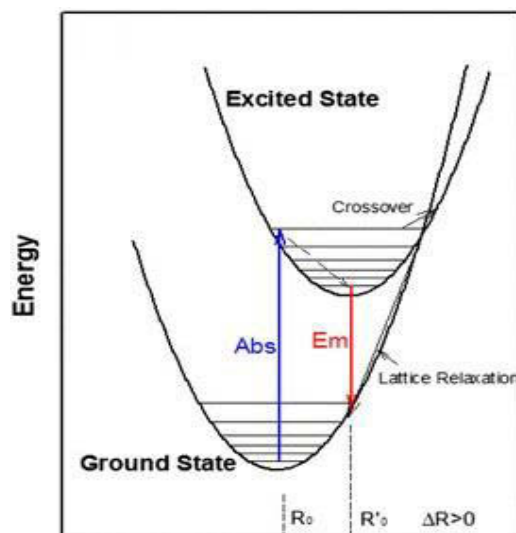


Figure 5. Configuration coordinate diagram showing the difference between radiative and non-radiative returns to the ground state. The radiative transition is represented by the red arrow (Em). The non-radiative process is described by the black arrows (intersystem crossing).

This process is almost impossible to occur when the the excited state (e) and the ground state (g) are parallel ($\Delta R=0$) (Figure 6). However, another form of non-radiative process exists in that case, in particular when the excitation ends at a higher excited state (e') which is not parallel to the ground state⁽⁷⁾. The system then relaxes to the first excited state, from where the emission takes place. This is called internal relaxation. The ratio of non-radiative to radiative transitions determines the efficiency of

a luminescent material. Therefore, it constitutes one of the most important challenges for the design of phosphors.

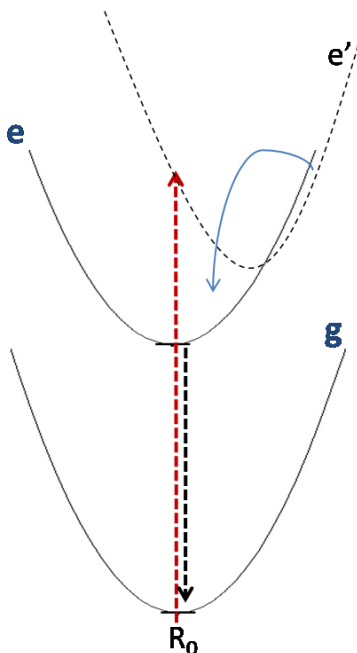


Figure 6 .Illustration of internal relaxation. The red and black arrows indicate the absorption and emission respectively. The blue arrow shows the crossing from the higher excited state e' to the lowest excited state e .

In optical transitions, there are some restrictions that define allowed and forbidden transitions. They are called selection rules that limit the transitions to levels having the same spin and different parity (Laporte rule). For example, $d-d$ and $f-f$ transitions are parity forbidden⁽⁸⁾. However, sometimes these rules can be broken with the help of physical interactions like spin-orbit coupling and electron-vibration coupling. Here it is said that the selection rules are “relaxed”. This affects strongly the intensity of the signal.

The activator is in most cases responsible for absorption and emission. In the configurational coordinate diagram, the activator and its neighboring sites are viewed as an isolated molecule, while in reality they are not deprived from the whole crystal. In other words, transitions to and from the energy levels of the host are possible and can have important role in the luminescence process. In fact, there are hosts that do not even need an activator to generate luminescence. Those are called intrinsic or self-activated materials like for instance CaWO_4 that was used in X-rays for years and is considered one of the most efficient phosphors^{(1),(9)}. Here, the WO_4^{2-} group acts as the activator. This is in general the case of all materials with closed shell transition metal complexes such as the titanates (TiO_4^{4-} , TiO_6^{8-} , TiO_5^{6-}),

molybdates (MoO_4^{2-} , MoO_6^{6-}), niobates (NbO_4^{3-} , NbO_6^{7-}), zirconates (ZrO_6^{8-}), tungstates (WO_4^{2-} , WO_6^{6-}) and tantalates (TaO_6^{7-} , TaO_8^{11-})⁽¹⁰⁾. These materials are characterized by broad band emissions usually in the visible region that are, most of the time, intense only at low temperature. Emission resulting from such a mechanism is called charge transfer CT luminescence. In this case, an electron from the oxygen atoms is transferred to the metal (i. e. ligand to metal charge transfer) in the complex unit to form a self trapped exciton which is responsible for luminescence upon electron-hole recombination. In doped lattices, a transition is called metal to metal charge transfer (MMCT) when the electron is transferred from the activator to the metal (or cation) in the host lattice. This was reported in a number of transition metal oxides doped with Bi^{3+} , which will be an important subject of this thesis. The occurrence of MMCT depends on the tendency of the dopant to be oxidized and the lattice metal to be reduced.

The states of energy of a host are defined as bands. Since the host (a solid) is made up of a number of atoms, the energy levels of atoms can be grouped into two bands: the valence band (VB) where the majority of electrons are located and the conduction band (CB) where most of the holes are found (Figure 7). The difference between the two bands is called the band gap or the forbidden zone where no charge carriers should be found. This is true if we consider the crystal to be perfect, but in reality defects are always found in the structures of crystals. When the host is excited, an electron from the valence band moves to the conduction band leaving a hole in the valence band. Emission occurs as a result of electron-hole recombination. This happens when an electron from the CB drops to combine with the hole of the VB. However, this is not always the case because the recombination may place take inside the band gap at energy levels induced by defects. Energy states related to activators, defects and impurities can exist inside the band gap and sometimes higher in the conduction band. They are known as traps because they can trap (capture) electrons or holes and cause quenching of the host's luminescence⁽¹¹⁾. Levels located close to the conduction band or the valence band are known as shallow traps. Deep traps also exist and are more likely to cause quenching because they need higher energies to move an electron or a hole from the trap to the conduction or valence band. Knowing the location of the states of the activator or impurity with respect to the band gap energy is essential for the analysis of optical spectra.

Following this scheme, an electron may be excited from the ground state of an activator into the conduction band where it is moved to the host lattice during relaxation. This is known as photoionization.

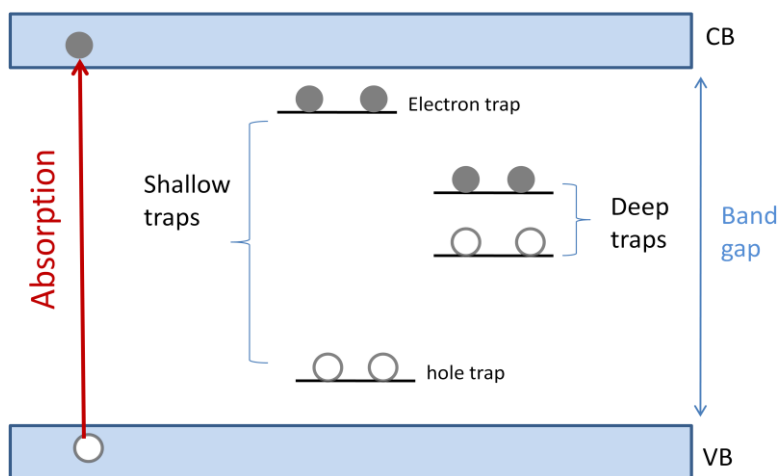


Figure 7. Scheme showing the locations of shallow and deep traps of impurities in the band gap. CB is the conduction and VB is the valence band. Black filled circles represent the electrons and white circles represent holes. Shallow traps are located near the CB or VB. Deep traps are located deep inside the band gap.

In that case, the electron may either delocalize in the conduction band or remain in Coulomb interaction with the center to form a trapped exciton, i.e. an electron-hole combination which can emit when the electron recombines with the hole. This changes the charge distribution on the center and affects the chemical bonding so the excited charge transfer state has a different equilibrium position and hence, broad bands are to be expected. In case of delocalization, the electron moves in the conduction band and be trapped at some distance by a defect. In that case, there is no emission but an afterglow may be observed (a delayed radiative recombination of the electron and hole), also called long lasting luminescence. Here, the recombination takes places once the electron is de-trapped by the effect of thermal or photonic stimulation.

In some hosts, the activator cannot be easily excited. An additional ion (called sensitizer) is then introduced into the host to assist to the excitation of the activator. The sensitizer S absorbs the energy then transfers it to the activator A following the scheme:



Two conditions are necessary for this energy transfer to be possible:

- The ground states and excited states of S and A should be equal. An overlap between the emission band of S and the absorption band of A (Figure 8).

- The interactions between the centers depend on the distance between the two ions.

This can be seen in the Equation proposed by Dexter of the transfer rate P_{SA} :

$$P_{SA} = \frac{\pi}{\hbar} |\langle S^* A^* | H_{SA} | S^* A \rangle|^2 \int g_S(E) g_A(E) dE \quad (6)$$

The integral represents the spectral overlap between the two centers and the Hamiltonian H_{SA} is the interaction. For instance, in the halophosphate $\text{Ca}_{10}(\text{PO}_4)_6(\text{F}, \text{Cl})\text{:Sb}^{3+}, \text{Mn}^{2+}$ that has been used in lamps for decades ⁽¹²⁾, Mn^{2+} acts as a yellow activator and Sb^{3+} acts both as a blue activator and as a sensitizer for the Mn^{2+} luminescence.

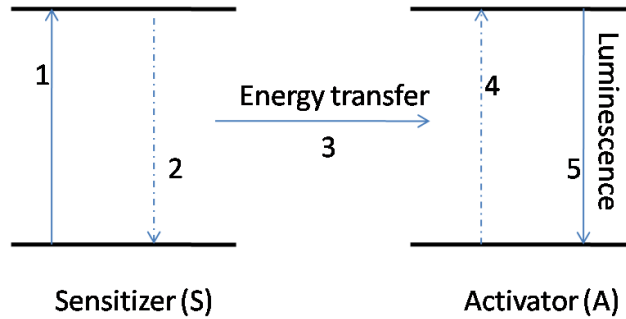


Figure 8. Energy transfer from the sensitizer to the activator leading to luminescence.

Energy transfer is also possible when $S=A$ (energy transfer between identical centers). In this case, energy can migrate within the host lattice depending on the concentration of the dopant. This could lead to concentration quenching if the excitation energy is transferred to a sink. Energy migration is also observed in the previously mentioned transition metal oxides when doped with rare earth or s^2 ions, where the host acts as a sensitizer. As an example, in $\text{YVO}_4\text{:Eu}^{3+}$, electrons of the tetrahedral $(\text{VO}_4)^{3-}$ units are first excited, migration occurs at some distance and then energy is transferred to the Eu^{3+} ion which is responsible for the emission.

1.3. Effect of crystal structure on luminescence

As stated already, many cations of the periodic table can be used for the creation of luminescent materials. A number of famous series of phosphors including rare earth ions, transition metal and mercury-like cations have been used through the years. Emission energies ranging between infra red to ultra violet can be seen under excitation of luminescent materials. The cause of this diversity from one

material to another is the choice of the central ion on one hand, and the crystal structure of the host lattice on another hand. It is quite obvious that doping different ions in the same host will result in different optical characteristics because they have different energy level configurations. Moreover, combining the same ion in different hosts will not necessarily give similar optical results. When incorporated in the host, the center undergoes some perturbations and splitting of its energy levels. Some of them are caused by the crystal field which is defined as the electric field on a cation site created due to the presence of neighboring anions, so it strongly depends on the oxidation state of the cation and the type of coordination (number and nature of ligands).

The crystal field mainly acts on the external orbitals. The d orbital is, for instance, five-fold degenerated. In the free ion, the five sub levels have the same energy. When subjected to the crystal field, these levels are perturbed and take different values of energy. The magnitude of the crystal field is different from one crystal to another depending on the type and symmetry of the ligands. Figure 9 shows how the d orbitals split under the effect of crystal field (Δ) in different symmetries. In octahedral or octahedrally-related point symmetry, orbitals of the d levels that point toward the ligands are two-fold (e_g) while those that project between the ligands are three fold (t_{2g}). In octahedral coordination, the crystal field is considered very strong. The shift of the e_g orbitals is 60% upward of the magnitude of the crystal field and 40% downward for t_{2g} . The crystal field strength is also known as $10 Dq$, where D and q are parameters depending on the charge of the ligands and the interatomic distance. The strength of the crystal field increases according to the following sequence:

Tetrahedral (4 fold) < dodecahedral (12 fold) < cubic (8 fold) < octahedral (6 fold).

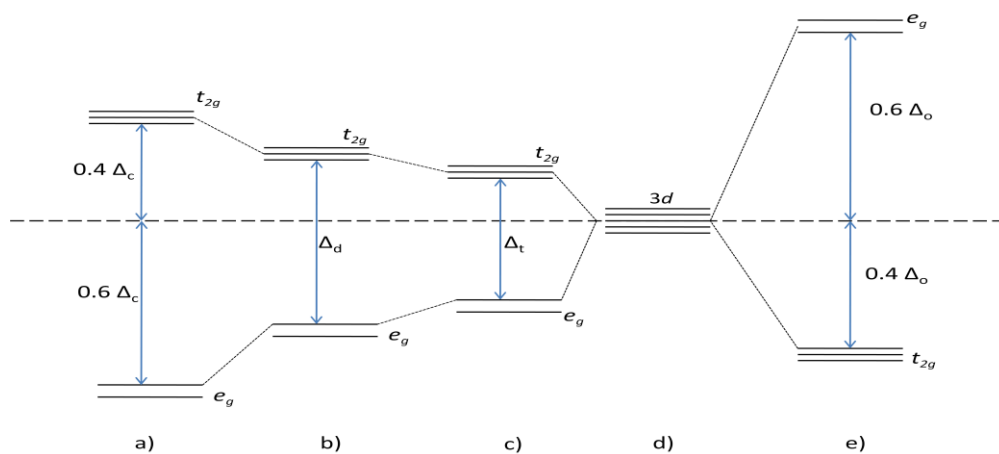


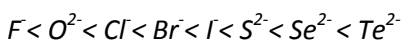
Figure 9. Crystal field splitting of d levels in a) 8-fold b) 12-fold c) 4-fold d) spherical and e) 6-fold symmetries. ⁽¹³⁾

The magnitude of the crystal field is affected by several factors. The interatomic distance is very important, a small decrease in the interatomic distance leads to a large increase in the crystal field. The valence of the cation also plays a role, for example, trivalent cations encounter a stronger crystal field than divalent. Other factors like temperature and pressure can also affect this magnitude.

The splitting of d levels caused by the crystal field always takes place without changing the position of their barycenter of energy (E_c). However, another phenomenon intervenes in the perturbation of the d levels altering the position of the E_c to lower energies caused by covalency. This is known as the nephelauxetic effect. The interactions between electrons are reduced when the covalency is strong because they are spread out over wider orbitals and this causes the shift of the levels to lower energies⁽¹⁾. As shown by Jorgensen, the nephelauxetic parameter β depends mainly on the electronegativity of the anion:

$$\beta = B(\text{complex})/B(\text{ligand}) \quad (7)$$

Where B is the Racah parameter. This means that the most electronegative ion has the lowest nephelauxetic effect. This effect increases in the following order:



Another important aspect is the Jahn-Teller effect. It is the case especially where the radius of the dopant is very small compared to that of the cation it is replacing. This will lead to a distortion of the site and to removing the degeneracy of energy levels. It is said that the ion goes “off center”. This is familiar in s^2 ions as will be seen later.

1.4. Spectroscopy of important luminescent activators

1.4.1. 4f elements

Rare earth ions are widely used in the production of luminescent materials especially lanthanides. These elements have an incompletely filled 4f shell (4f elements). The intra-4fⁿ transitions are forbidden by the selection rules but can be relaxed by several couplings like quadrupole interactions, electric dipole interactions and magnetic dipole interaction. Trivalent lanthanides Ln^{3+} ($Ln = Eu, Dy, Yb, Sm, \dots$) usually show sharp lines, but also intense, in their spectral behavior attributed to f-f transitions⁽¹⁴⁾. The reason is that their 4f shell is shielded from the environment by the filled 5s² and 5p⁶ levels, and therefore, the effect of the host lattice is very weak on these ions and their spectra are similar to those

of the free ion⁽¹⁵⁾. This can be seen in the Dieke diagram that shows the energy levels of trivalent lanthanides in LaF₃. The horizontal lines represent the magnitude of the crystal field splitting⁽¹⁶⁾.

The property of sharp lines of $4f^n$ in rare earth ions is very important for obtaining bright red, blue or green colors. This advantage has played a big role for the design of luminescent materials in different fields of application such as the red emitting YVO₄:Eu³⁺⁽¹⁷⁾ or Y₂O₂S:Eu³⁺ in televisions and lamps, in addition to the blue colored Sr₃(PO₄)₅Cl:Eu²⁺ and green colored GdMgB₅O₁₀:Ce³⁺, Tb³⁺ also used in lamps⁽¹⁾. However, as stated before, our interest is in ions that show broad band spectra. This is the case of the lanthanides that show $4f^n$ to $4f^{n-1} 5d^1$ transitions. These are mostly divalent Ln²⁺ (Ln = Eu, Yb, Sm....) in addition to some trivalent Ln³⁺ like Ce³⁺ that tend to be oxidized⁽¹⁸⁾. Ce³⁺ has the simplest excitation spectrum (one electron in its outer shell). It has especially been used to understand the perturbations of the lanthanide energy levels in a crystal and to study the relation of $4f^n$ to $4f^{n-1} 5d$ transitions with the crystal structure⁽¹⁹⁾. Analogies are often made with the case of Eu²⁺^{(20),(21)}. Figure 10 shows that the excited state ($4f^{n-1} 5d$) is shifted with respect to the ground state ($4f^n$) which is the reason of broad band formation and presence of Stokes shift in these ions⁽²²⁾.

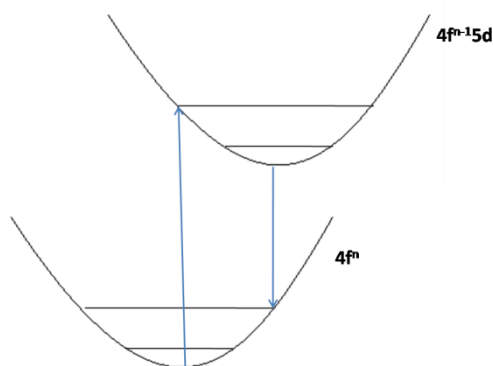


Figure 10. Ground state $4f^n$ and excited state $4f^{n-1} 5d$ of divalent lanthanides.

This is due to the fact that the 5d levels of a lanthanide are very sensitive to the crystal environment. Figure 11 shows the 5d energy levels of Eu²⁺/Ce³⁺ in a cubic crystal⁽²³⁾. In addition to the crystal field splitting, the barycenter position (Ec) of the 5d levels is lowered by the nephelauxetic effect. The Ec energies and the 10 Dq of Eu²⁺ in a series of different hosts having cubic structures are compiled in Table 1. Both parameters show significant variations from one host to another. In the series of sodium halides, the energy Ec is minimum in NaI (31950 cm⁻¹) and maximum in NaF (38010 cm⁻¹). Knowing that

the energy of E_c in free Eu^{2+} is 46340 cm^{-1} , the lowering in the E_c is less in NaF than NaI which obeys the nephelauxetic order. The difference in E_c and CFS values explains the diversity of colors that Eu^{2+} can generate.

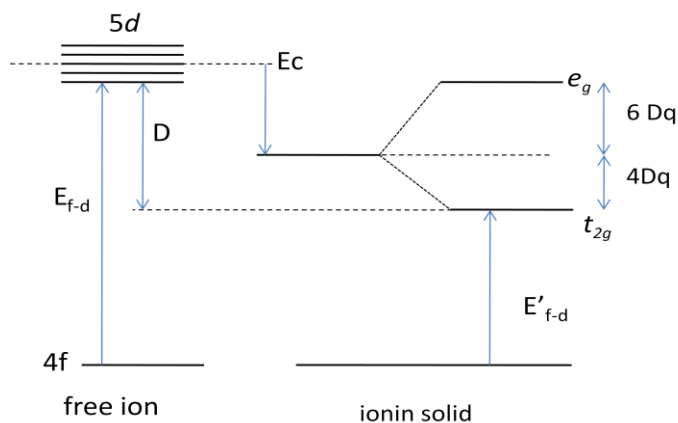


Figure 11. Energy splitting of 5d states and the lowering of their barycenter of energy E_c of a lanthanide in solid having cubic symmetry with respect to the free ion.

Table 1 Values of the barycenter energy E_c of 5d levels and the crystal field splitting $10Dq$ of Eu^{3+} in different cubic hosts. ⁽²⁴⁾

Host	$E_c (10^3 \text{ cm}^{-1})$	CFS $10Dq (10^3 \text{ cm}^{-1})$
NaF	38.01	18.35
NaCl	33.96	12.85
NaBr	33.11	11.75
NaI	31.95	10.63
RbI	32.44	9.06
CaF_2	37.79	15.5
SrF_2	37.34	13.5
SrCl_2	34.25	10.16
KMgF_3	41.00	7.5

The nephelauxetic effect and crystal field are known to act independently of each other ⁽²⁵⁾. However, both phenomena combine to create the so called red shift of a lanthanide in a solid. It is

indicated as D parameter in Figure 11. The red shift is defined as the difference between the f-d energy of a lanthanide of charge Q as a free ion and that of the same lanthanide in a crystal A ⁽²⁶⁾:

$$D(Q, A) = E_{fd}(n, Q, free) - E_{fd}(n, Q, A) \quad (8)$$

According to the work of Dorenbos, the red shift is the same for all divalent lanthanides in the same crystal on one condition that they substitute for the same cation site ⁽²⁷⁾. This means that if we know the transition energy of one divalent lanthanide, it is possible to know the energies of all the others because the f-d energies of the free ions are already known. The explanation of this model can be illustrated in Figure 12 that shows a representative scheme of the locations of 5d and 4f energy levels of divalent lanthanides with respect to the conduction and valence bands of the CaF₂ host ⁽²⁸⁾. The abscissa indicates the number of electrons in the 4f shell. The energies of 5d levels are considered constant for all divalent lanthanides. The 4f energies, in contrast, show a characteristic pattern. The same pattern was proved to exist for a huge number of hosts as well as in the gaseous state (free ion). With the help of this pattern, if we know the energy $E_{f-d}(n, Q, A)$ in Equation (8) for one lanthanide in a solid we can predict the energies f-d of all the lanthanides in this solid.

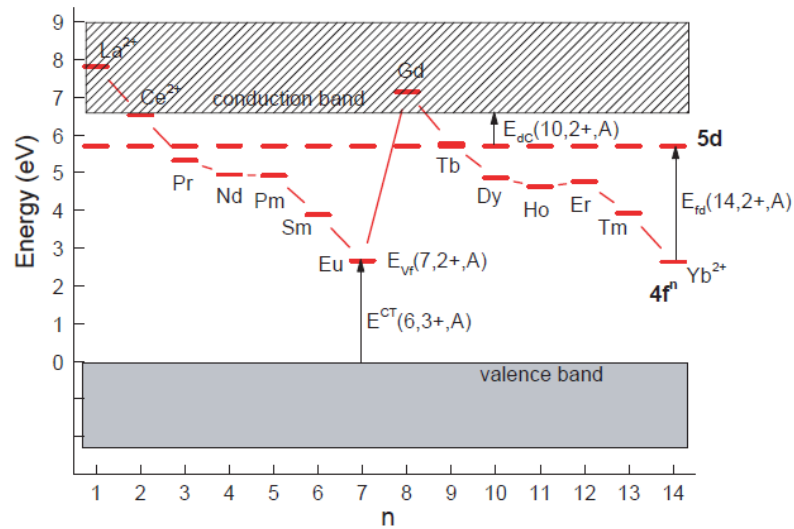


Figure 12. Location of 5d and 4fⁿ states of different divalent lanthanide ions in CaF₂. The abscissa n indicates the number of electrons in the 4f shell ⁽²⁸⁾.

For trivalent lanthanides, the red shift model is also true (Figure 13) ^{(29),(30)}. The red horizontal line represents the 5d state of Ln²⁺. As seen in the figure, the f-d energy is usually larger in trivalent lanthanides as compared to the divalent. In fact, the wavelength of the 4fⁿ to 4fⁿ⁻¹ 5d transition is

located far in the ultraviolet UV region in trivalent lanthanides. In divalent lanthanides, however, this transition shifts to lower energies and is located in the UV-visible region. The $4f^n$ energies are lowest for Ln^{2+} with half filled orbitals (Eu^{2+}) and completely filled $4f$ orbitals (Yb^{2+}), and highest for those with one electron (La^{2+}) and eight electrons (Gd^{2+}).

This work will deal precisely with Eu^{2+} that shows near UV absorption and visible emission. It is the most stable among divalent lanthanides and is widely studied⁽³¹⁾.

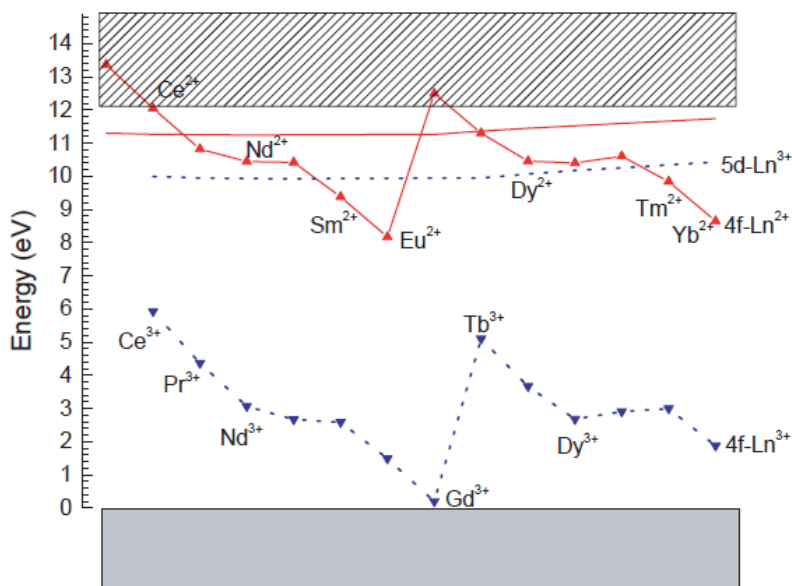


Figure 13. Locations of $5d$ and $4f^n$ energy levels of divalent and trivalent lanthanides in CaF_2 . The horizontal red line represents the $5d$ levels of the divalent Ln^{2+} ⁽²⁸⁾.

Luminescence as a result of the $4f^{n-1} 5d$ to $4f^n$ transition in lanthanides exhibits intense emission. Examples are the blue emitting $\text{Ca}_2\text{PO}_4\text{Cl}:\text{Eu}^{2+}$ and the green emitting $\text{Sr}(\text{SCN})_2:\text{Eu}^{2+}$. Ce^{3+} also shows visible emission as the case of the famous $\text{YAG}:\text{Ce}^{3+}$ that emits in the yellow region and is used in solid state lightings⁽³²⁾.

Rare earth ions were also reported to act as sensitizers to other rare earth activators or to transition metal ions as in $\text{BaMgAl}_{10}\text{O}_{17}:\text{Eu}^{2+}, \text{Mn}^{2+}$. Ln^{3+} show transitions with charge transfer character especially for these that tend to become divalent like Eu^{3+} and Yb^{3+} where an electron is transferred from the ligand to the center (LMCT)⁽³³⁾⁻⁽³⁵⁾. This was rarely noticed in the optical behavior of Ln^{2+} . On the other hand, energy transfer between Ln^{2+} identical ions is possible under the effect of concentration quenching.

1.4.2. Transition metal ions

Transition metals like Mn^{2+} and Cr^{3+} are known for their broad emissions in a number of hosts, for example, $\text{Zn}_2\text{SiO}_4:\text{Mn}^{2+}$ that emits a band of red to green colors and was used in lamps and cathode ray tubes. These ions have an incompletely filled d shell, having for example, d^1, d^3, d^5, \dots configurations. The origin of emission in materials doped with transition metal ions is either the $d-d$ transitions of the center, or possesses a charge transfer character in the case of closed shell transition metal oxides like CaWO_4 , YVO_4 , YNbO_4 , etc... The d^n energy levels of transition metal ions are found in the Tanabe-Sugano diagrams⁽³⁶⁾ for an octahedral or tetrahedral symmetry that show the effect of the crystal field on the perturbation of d^n configurations. This results from the fact that d^n levels are the outermost energy shells and are in direct contact with the ligands (surrounding anions), and this explains why transition metals doped materials usually have broad band absorption and emission spectra except Mn^{4+} and Cr^{3+} -doped materials in high crystal field, that are characterized by sharp spectral lines⁽³⁷⁾.

1.4.3. Mercury like ions (s^2)

Post-transition metal ions (Tl^+ , Sb^{3+} , Pb^{2+} , Bi^{3+} , Sn^{2+}) have also been used as luminescent centers for decades. The spectroscopy of these ions was investigated in the 60-70's, mostly to develop phosphors for lamps, and then almost forgotten. The last past years have evidenced a renewal of interest on s^2 mercury-like activators like Bi^{3+} for their efficient luminescence action in the UV or visible region and for their aptitude to serve as sensitizers for the trivalent lanthanide emission. The so-obtained phosphors show interesting properties for a possible use in LED-based lighting devices or for integration in solar cells, for instance $\text{YVO}_4:\text{Bi}^{3+}, \text{Eu}^{3+}$ ⁽³⁸⁾.

The s^2 configuration generates an intense parity allowed s^2 to sp absorption in the ultraviolet leading to a wide range of visible emission. Most s^2 ions are characterized by their broad band spectra and their considerably very large Stokes shifts especially in Sb^{3+} -doped materials. Their optical behavior is considered to be strongly affected by the type of crystal structure (case of strong coupling with the host). However, the influence of crystal field on these ions is not widely studied as for rare earth and transition metals.

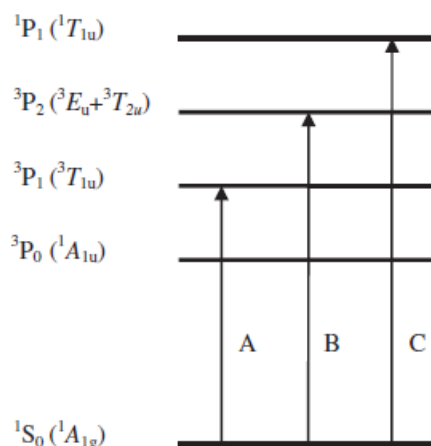


Figure 14. Energy levels of s^2 free ions. A, B and C represent the possible optical transitions.

Figure 14 shows the energy levels of s^2 free ions. The ground state is 1S_0 and the excited states resulting from spin orbit coupling are the triplets 3P_0 , 3P_1 , 3P_2 , and the singlet 1P_1 . These states generate 3 possible transitions:

- 1S_0 to 3P_1 called the A band
- 1S_0 to 3P_2 called the B band
- 1S_0 to 1P_1 called the C band

The transition to 3P_0 is strongly forbidden. The B band is however a forbidden transition but can be relaxed by coupling with unsymmetrical lattice vibrations. It has however a very low intensity. The C band is an allowed transition and A becomes allowed by the spin orbit coupling. 3P_1 and the underlying level 3P_0 are usually the emitting levels with an emission ratio largely depending on temperature. They lead to a wide range of radiations from UV to visible. Table 2 presents indicative Stokes shift values of Bi^{3+} in various crystals. The variation is of one order of magnitude which is considered large. The reason, although not always clear, is (at least for a part) related to the amount of the space available for Bi^{3+} in the lattice and the fact that s^2 lone pairs induce a stereochemical activity. When incorporated in a crystal, the s^2 ion is usually supposed to go off center in its ground state to obtain the preferred asymmetrical coordination. This is referred to as a pseudo Jahn-Teller effect. In the excited state, the ion relaxes to the center of the coordination polyhedron which results in a large Stokes shift. This phenomenon is observed in the spectra of most of s^2 -doped compounds except in those having six

coordination structures, where the s^2 ion is too large and cannot be relaxed to a different equilibrium distance because there is not enough space. Here a narrow Stokes shift is expected, which is the case of $\text{Cs}_2\text{NaYCl}_6:\text{Bi}^{3+}$. The large Stokes shift of Bi^{3+} -doped compounds was also found to be related to the trap depth, an aspect that is not well understood. The ^3P excited state is subject to both Jahn-Teller and spin orbit couplings. In structures where the spin orbit coupling is strong the Jahn-Teller effect is supposed to decrease.

Table 2 Stokes shift of Bi^{3+} in different hosts. ⁽¹⁾

Host	Stokes shift (cm^{-1})
$\text{Cs}_2\text{NaYCl}_6$	800
ScBO_3	1800
$\text{YAl}_3\text{B}_4\text{O}_{12}$	2700
CaLaAlO_4	7700
LaOCl	8500
La_2O_3	10800
$\text{Bi}_2\text{Al}_4\text{O}_9$	16000
$\text{Bi}_4\text{Ge}_3\text{O}_{12}$	17600
LaPO_4	19200
$\text{Bi}_2\text{Ge}_2\text{O}_9$	20000

In addition to the three bands shown in Figure 5, a D band also appears in the excitation and emission spectra of Bi^{3+} -doped compounds especially in oxides with d^0 or d^{10} metal cations. The energy of the D-like excitation band is usually close to that of the A band, while the emission, owing to a larger Stokes shift, is usually located at lower energy relative to the A-like emission, i.e. in the visible region of the spectrum. Different explanations on the origin of the D band have been made. It was previously ascribed to a ligand to metal charge transfer. Although recent studies suggest two other hypotheses:

- The D band is a result of the formation of Bi^{3+} pairs or clusters. After excitation, an electron is transferred from one Bi^{3+} to another nearby Bi^{3+} within an intervalence charge transfer (IVCT) process. This creates Bi^{2+} and Bi^{4+} ions ⁽³⁹⁾.

- The D band is a result of metal to metal charge transfer (MMCT) from Bi^{3+} to the metal M^{n+} in the host. The transition is expressed as $\text{Bi}^{3+}(6s^2)/\text{M}^{n+}(\text{d}^0) \rightarrow \text{Bi}^{4+}(6s^1)/\text{M}^{(n-1)+}(\text{d}^1)$ or $\text{Bi}^{3+}(6s^2)/\text{M}^{n+}(\text{d}^{10}) \rightarrow \text{Bi}^{4+}(6s^1)/\text{M}^{(n-1)+}(\text{s}^1)$. This is also viewed as an impurity trapped exciton (bound of electron hole pair) with the hole being localized on Bi^{3+} and the electron delocalized on the nearest cationic neighbors.

The first hypothesis was confirmed in a number of hosts by the work of Srivastava, for instance $(\text{Y,Gd})_3\text{Ga}_5\text{O}_{12}:\text{Bi}^{3+}$ and $\text{GdAlO}_3:\text{Bi}^{3+}$, where the luminescence was shown to be strongly dependent on the concentration of Bi^{3+} ions⁽³⁹⁾. After Dorenbos, for an electron to move from Bi^{3+} to Bi^{2+} , the ground state of Bi^{2+} should be located lower than the $^3\text{P}_1$ state of Bi^{3+} as shown in Figure 15 represented by the red line. This causes the quenching of the A band⁽⁴⁰⁾. This model, however, supposes that one Bi^{3+} acts as an electron donor while the other Bi^{3+} acts as an electron acceptor within the pair. This would lead to consider that both ions in the pair do not have the same electronegativity. The reason for that is at the moment somewhat unclear for us.

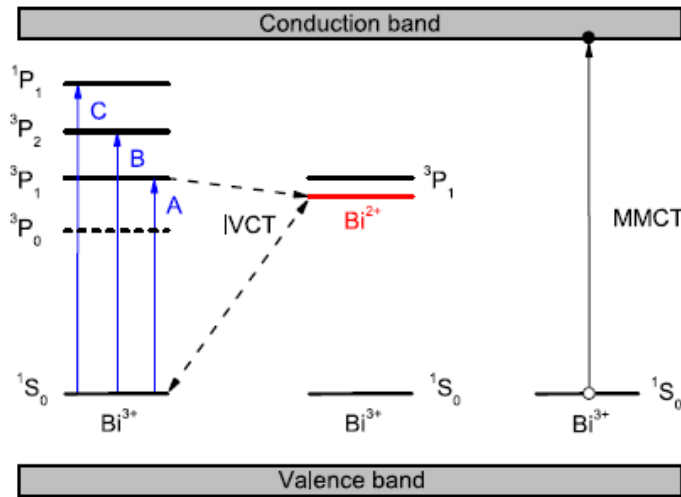


Figure 15. The 3 possible transition bands of Bi^{3+} indicated by blue arrows A, B and C. The MMCT charge transfer transition from Bi^{3+} to the conduction band of the host indicated by the vertical black arrow. The ground state of Bi^{2+} in red⁽⁴⁰⁾.

The MMCT, being the transition of photoionization of Bi^{3+} , seems to have higher energies than the transition from Bi^{3+} to Bi^{2+} . However, the MMCT model, proposed by Boutinaud suggested that this energy is also located lower than ^3P states in a number of oxides like in the case of $\text{YVO}_4:\text{Bi}^{3+}$, where the ^3P states are located in the conduction band⁽⁴¹⁾. Luminescence from the A band is quenched and the

emission spectrum shows a broad visible band related to the D state. As a matter of fact, three configurations can be found for Bi^{3+} states in oxides (Figure 16):

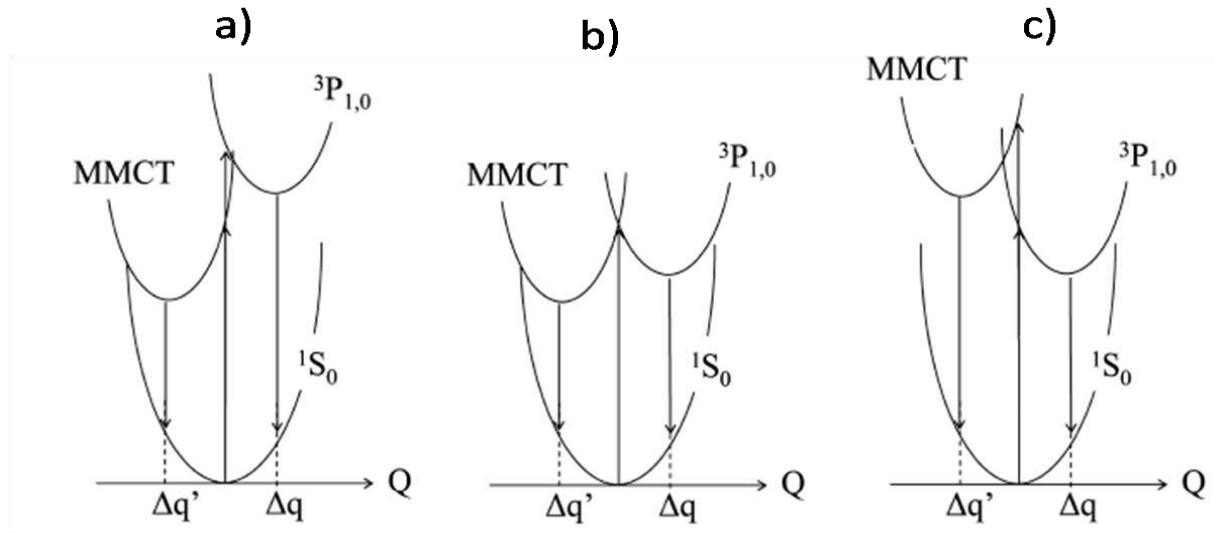


Figure 16. Three different configurations for the position of the MMCT state with respect to the $^3P_{1,0}$ states of Bi^{3+} in oxides: a) MMCT is lower than $^3P_{1,0}$ b) MMCT and $^3P_{1,0}$ are equal, it is the case where $^3P_{1,0}$ are located near the conduction band c) MMCT is higher than $^3P_{1,0}$.⁽⁴²⁾

- The MMCT state is located lower than the $^3P_{0,1}$ states. The MMCT state is directly excited and is emitting. Excitation in the $^3P_{0,1}$ states can be followed by the autoionization of Bi^{3+} , depending on the coupling strength between $^3P_{1,0}$ and the conduction band states. In the case of photoionization, the absorbed energy can be lost nonradiatively or transferred to the MMCT state, with subsequent emission from this latter state (Figure 16.a).
- $^3P_{0,1}$ and MMCT energies are equal. This means that the $^3P_{1,0}$ states are located close to the bottom of the conduction band. Here, both MMCT and $^3P_{1,0}$ emit with different intensity ratios depending on the temperature (Figure 16.b). This was supposed to be the case of $\text{YPO}_4:\text{Bi}^{3+}$ in ref. (41). At low temperatures, this compound emits a narrow band upon excitation at 246 nm as well as the broad band of the MMCT state extending from 280 to 450 nm. At higher temperatures the D band becomes more intense relative to the A band (Figure 17). However, in other studies, the second emission was ascribed to Bi^{3+} pairs⁽⁴³⁾. This question is therefore still open.

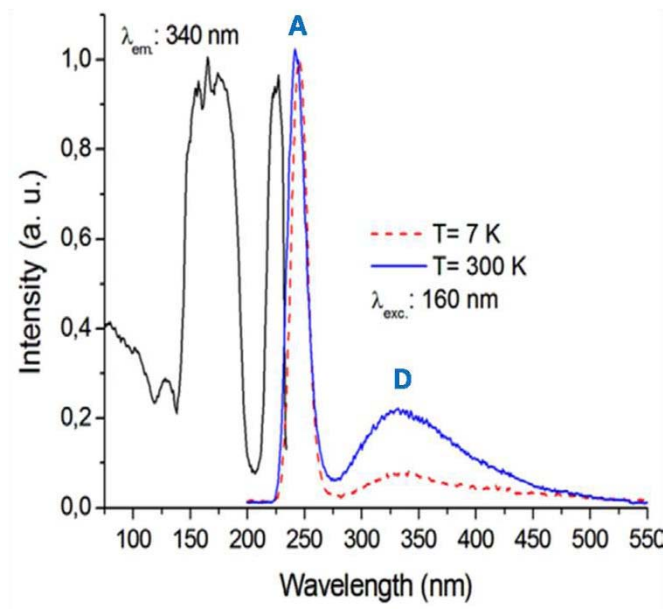


Figure 17. Luminescence spectra of $\text{YPO}_4:\text{Bi}^{3+}$ at various temperatures ⁽⁴¹⁾.

- MMCT is higher than $^3\text{P}_{0,1}$, like in the case of $\text{La}_2\text{Zr}_2\text{O}_7:\text{Bi}^{3+}$ ⁽⁴⁴⁾. Emission from the $^3\text{P}_{1,0}$ states follows a direct $^1\text{S}_0 \rightarrow ^3\text{P}_1$ transition. Excitation of the MMCT state is still possible and can be followed either by MMCT emission or by $^3\text{P}_{1,0} \rightarrow ^1\text{S}_0$ depending on temperature. (Figure 16.c).

Sb^{3+} also shows similar properties as those of Bi^{3+} . However, it is much less studied due to its relatively unusual large Stokes shift that causes stray quenching of the emission at room temperature. The halophosphate $\text{Ca}_{10}(\text{PO}_4)_6(\text{F},\text{Cl}):\text{Sb}^{3+}:\text{Mn}^{2+}$ ⁽⁴⁵⁾ that shows intense blue emission from Sb^{3+} at room temperature despite a Stokes shift as large as 19000 cm^{-1} possesses, in this connection, an exceptional behavior that is still not understood today. In Sb^{3+} -doped compounds the JT effect is more important than Bi^{3+} -doped compounds because Sb^{3+} has a smaller radius. For instance in $\text{YPO}_4:\text{Sb}^{3+}$, two emissions from the ^3P excited state are observed. This is typically due to the JT effect which induces two minima on the $^3\text{P}_1$ state. This behavior is not observed in $\text{YPO}_4:\text{Bi}^{3+}$ ⁽⁴⁶⁾.

1.5. LED- based lighting materials

Luminescent materials are integrated in solid state lighting packages especially in LEDs (light emitting diodes). Figure 18 shows the structure of a LED lamp. The LED chip is made up of two semiconductors, one of n-type (that has more electrons) and the other of p-type (that has more holes). When a voltage is

applied through the p-n junction, electrons from the n-type recombine with holes from the p-type resulting in light emission.

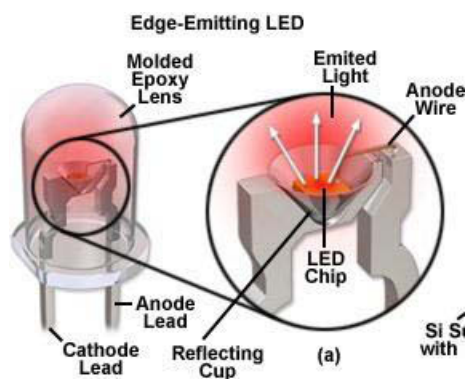


Figure 18. Structure of a LED chip.

In addition to indoor and outdoor lightings, LEDs are used as indicators in electronic devices, calculators, clocks, DVD players, traffic signs... Early LEDs were mainly red or infra-red emitting materials and were used in the 1960's as replacements for incandescent and neon lamps in electronic indicators. In the 1970's blue LEDs appeared made up of GaAs and GaN but they were not very bright until 1990's when the first InGaN was used. The evolution of LEDs continued to improve until white LED was produced.

The production of LED lightings is still widely open and there are many concerns, worldwide, for the development of these materials. These new lighting products are gradually entering our homes and offices forcing the incandescent lamps out of the lighting markets. It is expected that the number of consumers of LED lights will increase in the following years. This is due to LEDs being considered friends with the environment, having longer lifetimes up to 60,000 hours compared to incandescent lamps (1000 hours) and being able to save energy at least 75% less energy than other type of lightings. They also emit less infra red radiation so their surface is not hot. However, they can be affected by heat inside the semiconductor originating from the electric current, which can reduce the light output. Other disadvantages for the usage of LED lamps are their price that is still considerably higher than that of incandescent and halogen lamps. The brightness of these devices has been taken into consideration because they produce less lumens/W than incandescent lamps. That's why there is an urge now to develop this kind of technology. The aim is to find new compositions of luminescent materials in a faster

and cheaper manner than trial-error –based methods and that can lead to more efficient, brighter and lower price phosphors especially for the improvement of white LED lightings.

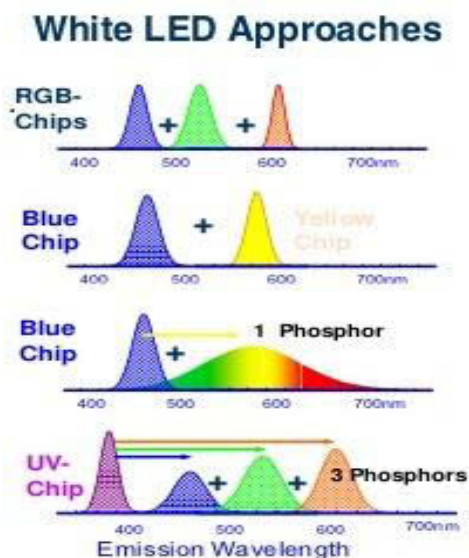


Figure 19. Different approaches for obtaining white LEDs⁽⁴⁷⁾

Depending on the purpose of application of the white light, four different strategies are available (Figure 19):

- Three RGB (red, green, blue) LED chips. The three colors emitted from the three different LEDs are mixed together to generate a combined spectrum that appears white to the eye.
- One blue chip with one yellow chip.
- One blue chip with one phosphor. The phosphor absorbs the energy emitted from a blue LED and emits a yellow light. Combined blue and yellow give white light. The color temperature can be turned from cold to warm white by adding a red component to the spectrum (i.e. a second phosphor).
- One UV chip with three phosphors. Each of the three phosphors can be excited by UV coming from the LED. One red, one green and one blue emitting phosphor should be used.

The third method is, for the moment, the most attractive one because blue based LEDs for white light have better luminous efficiency. The most used system is blue InGaN (460 nm) or GaN mixed with

$\text{Y}_3\text{Al}_5\text{O}_{12}:\text{Ce}^{3+}$ (YAG: Ce^{3+})⁽⁴⁸⁾. This has a high efficiency but a low color rendering index (CRI) and gives cool white light due to the lack of a red component. As a matter of fact, all phosphors used to combine with the blue LED to produce warm white light result either in low CRI or low efficacy. The color rendering index is defined as the ability of the system to produce light similar to the natural light (daylight). This cannot be easily reached with blue-based LEDs because of the high intensity of blue color. In this sense, considerations of the UV-based LEDs are now taken into account by using near UV InGaN based LEDs hoping to create warm white light with better efficiency and color rendering index⁽⁴⁹⁾. In this context, the development of white LEDs is centered on the improvement of phosphors absorbing in the near-UV region and emitting broad band visible light. It is assumed that this type of systems for white light will be dominant in the coming years.

1.6. Semi-empirical models

1.6.1. Importance of semi-empirical models

In reference to the studied behaviors of the different luminescent materials, not a lot of anticipation can be done when creating new phosphors. Only after synthesis and spectroscopy could we know the optical properties and the importance of the new produced compounds. An approach to favor the development of luminescent materials is to test as much as possible of new compositions. Looking through the periodic table, a plenty of compounds can be created. In this sense, some people use trial-error methods like for instance, combinatorial screening chemistry that allows the synthesis of thousands of compounds using a single process. However, another approach for the mission is to find and develop methods that could serve as predictive tools for the production of phosphors. In this way we can save a lot of time and work...

1.6.2. Overview of some theoretical models

A number of theoretical models were investigated to understand the structure-luminescence relationships. Some scientists used density functional theory (DFT) ab initio calculations and others used semi-empirical models ranging from very easy approaches to very complicated ones. For instance, only one structural parameter such as the radius (or size) of the ion or the distance between ion and ligands, may be used to establish relations between the optical properties and the structure of the material. On the other hand, models involving a series of structural parameters are also found in the literature like Judd-Ofelt theory^{(50),(51)} or Dorenbos polarizable ligand model⁽⁵²⁾. Although none of these models can be

considered perfectly applicable for the design of phosphors, some of them have shown interesting aspects that may form a good base for better explanations of luminescence-structure complexes. Dorenbos found a correlation between the energy shift of $5d$ configuration of Ce^{3+} with a parameter called the spectroscopic polarizability related to the polarization of the ligands in oxides, and a parameter called the average cation electronegativity in Fluorides. Judd and Ofelt succeeded in finding a relation between structural parameters and spectral intensities especially of rare earth ions in solids. The environmental factor (EF) model and the MMCT model, that we wish to introduce and test in the present manuscript, are two recent semi-empirical models that we found friendly and easy using.

1.6.3. The Environmental factor (EF) model

The environmental factor model, developed by Shi and Zhang ⁽²⁴⁾, is based on the dielectric theory of chemical bonding proposed by Pauling and developed by Philips, Van Vechten, and Levine ⁽⁵³⁾⁻⁽⁵⁶⁾. This theory has been successfully applied to a wide variety of physical problems before being extended to phosphors as a possible designing tool. The concept of the EF model is to decompose the crystal lattice into binary units, each representing one type of cation-anion bond, then treat each of them as one separate crystal. This enables us to know the physical properties of every single bond in the whole crystal, and thus, study the environmental factors of each cation site available for the dopant to occupy in the crystal.

Going through the calculations, let us take as an example the monophosphate of formula ABPO_4 , where A is a monovalent cation and B a divalent cation, to show how binary crystals can be obtained. Such compounds will be investigated in Chapter 2. To individuate the crystallographic sites ($i = 1, 2, \dots, n$) that may be occupied by the cations and anions in the crystal structure, the compound will be reformulated as $A(i)_{a_i}B(i)_{b_i}P(i)_{p_i}O(i)_{o_i}$, where $a_i = m_i(A)/Z$, $b_i = m_i(B)/Z$, $p_i = m_i(P)/Z$, $o_i = m_i(O)/Z$ and $\sum_{i=1}^n a_i = a$, $\sum_{i=1}^n b_i = b$, $\sum_{i=1}^n p_i = p$, $\sum_{i=1}^n o_i = o$. In the case of ABPO_4 , for instance, we would have $a=b=p=1$ and $o=4$. In these expressions, $m_i(A)$, $m_i(B)$, $m_i(P)$ and $m_i(O)$ are the multiplicity of the different Wyckoff sites (i) occupied by atoms A, B, P and O, respectively and Z is the number of formula units per unit cell. The compound will then be expressed as a sum of oxo-units:

$$A(i) a_i \frac{N_{O(i)-A(i)}}{N_{A(i)}} O(i) o_i \frac{N_{A(i)-O(i)}}{N_{O(i)}}, \quad B(i) b_i \frac{N_{O(i)-B(i)}}{N_{B(i)}} O(i) o_i \frac{N_{B(i)-O(i)}}{N_{O(i)}} \quad \text{and} \quad P(i) p_i \frac{N_{O(i)-P(i)}}{N_{P(i)}} O(i) o_i \frac{N_{P(i)-O(i)}}{N_{O(i)}},$$

where $N_{A(i)-O(i)}$, $N_{B(i)-O(i)}$ and $N_{P(i)-O(i)}$ indicate the number of oxygen atoms $O(i)$ surrounding $A(i)$, $B(i)$ and

P(i), respectively, while $N_{O(i)-A(i)}$, $N_{O(i)-B(i)}$ and $N_{O(i)-P(i)}$ indicate the number of cations A(i), B(i) and P(i) surrounding oxygen O(i), respectively. $N_{A(i)}$, $N_{B(i)}$ and $N_{O(i)}$ are the coordination numbers of the considered atoms in the lattice. This information requires perfect knowledge of the crystal structure of the compound. In practice, they are extracted from ICSD databases and treated using VESTA software⁽⁵⁷⁾.

For ease of use, matrices containing all the necessary information are settled. As an illustration, we show in Table 3 the matrix of an ABPO₄ lattice in which one crystallographic site is present for A, B and P (i.e. i=1) and two sites are present for the oxygen atoms (i.e. i=2):

Table 3 Example of coordination matrix of an ABPO₄ lattice with one cation site A(1), B(1), P(1) and two oxygen sites O(1), O(2).

	A(1)	B(1)	P(1)	O(1)	O(2)
O(1)	$N_{A(1)-O(1)}$	$N_{B(1)-O(1)}$	$N_{P(1)-O(1)}$		
O(2)	$N_{A(1)-O(2)}$	$N_{B(1)-O(2)}$	$N_{P(1)-O(2)}$		
A(1)				$N_{O(1)-A(1)}$	$N_{O(2)-A(1)}$
B(1)				$N_{O(1)-B(1)}$	$N_{O(2)-B(1)}$
P(1)				$N_{O(1)-P(1)}$	$N_{O(2)-P(1)}$
N_{Total}	$N_{A(1)-O(1)} +$ $N_{A(1)-O(2)}$	$N_{B(1)-O(1)} +$ $N_{B(1)-O(2)}$	$N_{P(1)-O(1)} +$ $N_{P(1)-O(2)}$	$N_{O(1)-A(1)} + N_{O(1)-B(1)}$ $+ N_{O(1)-P(1)}$	$N_{O(2)-A(1)} + N_{O(2)-B(1)}$ $+ N_{O(2)-P(1)}$

The matrices of all the investigated lattices in this work are given in Appendix B. Taking the example of KSrPO₄, that contains atoms K(1) in 4c Wyckoff site, Sr(1) in 4c Wyckoff site, O(1) in 4c Wyckoff site, O(2) atom in 8d Wyckoff site and O(3) in 4c Wyckoff site, and knowing that Z=4, we write KSrPO₄ as K(1)₁Sr(1)₁P(1)₁O(1)₁O(2)₂O(3)₁. The corresponding matrix provided by the crystal structure of this compound is given in Table 4. This matrix gives information on the coordination numbers of each atom. Reading the matrix gives the following: $N_{K(1)} = 10$, $N_{Sr(1)} = 9$, $N_{P(1)} = 4$, $N_{O(1)} = 4$, $N_{O(2)} = 5$, $N_{O(3)} = 4$, $N_{K(1)-O(1)} = 3$, $N_{K(1)-O(2)} = 6$, $N_{K(1)-O(3)} = 1$, $N_{Sr(1)-O(1)} = 2$, $N_{Sr(1)-O(2)} = 4$, $N_{Sr(1)-O(3)} = 3$, $N_{P(1)-O(1)} = 1$, $N_{P(1)-O(2)} = 2$, $N_{P(1)-O(3)} = 1$, $N_{O(1)-K(1)} = 1$, $N_{O(2)-K(1)} = 2$, $N_{O(3)-K(1)} = 1$, $N_{O(1)-Sr(1)} = 2$, $N_{O(2)-Sr(1)} = 2$, $N_{O(3)-Sr(1)} = 2$, $N_{O(1)-P(1)} = 1$, $N_{O(2)-P(1)} = 1$ and $N_{O(3)-P(1)} = 1$.

This allows the decomposition of K(1)Sr(1)P(1)O(1)O(2)O(3) in the following sum of binary units:

$$K(1) \frac{3}{10} O(1) \frac{1}{4} + K(1) \frac{6}{10} O(2) \frac{2x2}{5} + K(1) \frac{1}{10} O(3) \frac{1}{4} + Sr(1) \frac{2}{9} O(1) \frac{2}{4} + Sr(1) \frac{4}{9} O(2) \frac{2x2}{5} +$$

$$Sr(1) \frac{3}{9} O(3) \frac{3}{6} + P(1) \frac{1}{4} O(1) \frac{1}{4} + P(1) \frac{1}{2} O(2) \frac{1x2}{5} + P(1) \frac{1}{4} O(3) \frac{1}{4}$$

Table 4 Coordination matrix of KSrPO₄

	K(1)	Sr(1)	P(1)	O(1)	O(2)	O(3)
O(1)	3	2	1			
O(2)	6	4	2			
O(3)	1	3	1			
K(1)				1	2	1
Sr(1)				2	2	2
P(1)				1	1	1
Total	10	9	4	4	5	4

The environmental factors he and Fc are then calculated for each cation site in these binary units. For a given binary crystal $A(i)_\alpha O(i)_\beta$, the two factors $he(A(i))$ and $Fc(A(i))$ corresponding to the $A(i)$ site are calculated as:

$$he(A(i)) = \sqrt{\sum_1^{N_{A(i)}} fc_{(A(i)-O(i))} \alpha_{(A(i)-O(i))} Q_{O(i)}^2} \quad (9)$$

and

$$Fc(A(i)) = \frac{39.74 d_{(A(i)-O(i))}^{-2.48} Q_{O(i)} f_{i(A(i)-O(i))}}{N_{A(i)}} \quad (10)$$

In these expressions, $fc_{(A-O)}$ and $f_{i(A-O)}$ represent respectively the fractional covalency and ionicity of each $A(i)-O(i)$ bond in the unit, $\alpha_{(A(i)-O(i))}$ is the volume polarization of each $A(i)-O(i)$ bond, $d_{(A(i)-O(i))}$ is the $A(i)-O(i)$ distance in the unit and $Q_{O(i)}$ is the effective charge carried by the oxygen atoms in site (i) of the binary unit. For a given $A(i)_\alpha O(i)_\beta$ unit, $Q_{O(i)}$ is calculated as $Q_{O(i)} = \frac{\alpha}{\beta} Q_{A(i)}$, where $Q_{A(i)}$ is the effective charge of cation $A(i)$, taken as its bond valence sum. The bond valence sum is known from the bond valence model which is a development of Pauling's rules that estimates the oxidation state of the central atom only from bond lengths determined by X-ray or neutron diffraction⁽⁵⁷⁾. The bond valence sum V of a central atom can be determined from:

$$V = \sum_{i=1}^n \exp\left(\frac{l_i - l_0}{b}\right) \quad (11)$$

Where b is a constant equal to 0.37\AA , l_i is the bond length between the central atom and another neighboring atom and l_0 is a bond valence parameter of the central atom. In this work, the bond valence sum was determined directly from VESTA by inserting the bond valence parameter taken from the work of O'KEEFFE⁽⁵⁸⁾.

For instance in the $K(1)_{3/10}O(1)_{1/4}$ unit, we have $Q_{K(1)} = 1.368$ and $Q_{O(1)} = 1.64$. The quantity $d_{(A(i)-O(i))}^{-2.48}$ (in eV) represents the homopolar part of the energy gap $E_{h(A(i)-O(i))}$ separating the bonding and anti-bonding states in the $A(i)-O(i)$ bond. This energy comes from the interaction of dipole moments and other multiple moments and is the origin of bond covalency⁽⁵⁶⁾. Values of $fc_{(A(i)-O(i))}$ and $fi_{(A(i)-O(i))}$ are calculated as:

$$fc_{A(i)-O(i)} = E_{h(A(i)-O(i))}^2 / (E_{h(A(i)-O(i))}^2 + C_{(A(i)-O(i))}^2) \quad (12)$$

and

$$fi_{A(i)-O(i)} = C_{(A(i)-O(i))}^2 / (E_{h(A(i)-O(i))}^2 + C_{(A(i)-O(i))}^2) \quad (13)$$

where $C_{(A(i)-O(i))}$ is the heteropolar parts of the energy gap characterizing the $A(i)-O(i)$ bond. The volume polarization $\alpha_{(A(i)-O(i))}$ of each $A(i)-O(i)$ bond is obtained using:

$$\alpha_{(A(i)-O(i))} = v_{(A(i)-O(i))} \frac{3}{4\pi} \left(\frac{\epsilon_{(A(i)-O(i))} - 1}{\epsilon_{(A(i)-O(i))} + 2} \right) \quad (14)$$

where $v_{(A(i)-O(i))}$ is the volume (in cm^3) of the $A(i)-O(i)$ bond and $\epsilon_{(A(i)-O(i))}$ is the dielectric constant of this bond.

The heteropolar parts of the $A(i)-O(i)$ bond energy gap is calculated as:

$$\left. \begin{aligned} C_{A(i)-O(i)} &= \frac{14.4b'_{(A(i)-O(i))}}{r_{(A(i)-O(i))}} \exp\left(-k_{s(A(i)-O(i))} r_{(A(i)-O(i))}\right) \left| Z_{A(i)}^* - \frac{n}{m} Z_{O(i)}^* \right| \text{ (if } n \geq m) \\ C_{A(i)-O(i)} &= \frac{14.4b'_{(A(i)-O(i))}}{r_{(A(i)-O(i))}} \exp\left(-k_{s(A(i)-O(i))} r_{(A(i)-O(i))}\right) \left| \frac{m}{n} Z_{A(i)}^* - Z_{O(i)}^* \right| \text{ (if } n \leq m) \end{aligned} \right\} \quad (15)$$

With $r_{(A(i)-O(i))} = d_{(A(i)-O(i))}/2$ and $b'_{(A(i)-O(i))} = 0.089 < N_{(A(i)-O(i))} >^2$. The quantity $\langle N_{(A(i)-O(i))} \rangle$ is the average coordination number of the $A(i)-O(i)$ bond. It is defined as:

$$\langle N_{(A(i)-O(i))} \rangle = \frac{\alpha}{\alpha+\beta} N_{A(i)} + \frac{\beta}{\alpha+\beta} N_{O(i)} \quad (16)$$

The term $\exp\left(-k_{s_{(A(i)-O(i))}} r_{(A(i)-O(i))}\right)$ represents the Thomas-Fermi screening factor in which :

$$k_{s_{(A(i)-O(i))}} = (4k_{F_{(A(i)-O(i))}}/\pi a_{bohr})^2 \quad (17)$$

$$k_{F_{(A(i)-O(i))}} = (3\pi^2 N_{(A(i)-O(i))}^*)^{1/3} \quad (18)$$

In Equation (17), a_{bohr} is the Bohr's radius. The quantity $N_{(A(i)-O(i))}^*$ in Equation (18) is the number of effective valence electrons per cubic centimeter in the A(i)-O(i) bond, calculated as:

$$N_{A(i)-O(i)}^* = \left(\frac{Z_{A(i)}^*}{N_{A(i)}} + \frac{Z_{O(i)}^*}{N_{O(i)}}\right) / v_{(A(i)-O(i))} \quad (19)$$

where $Z_{A(i)}^*$ and $Z_{O(i)}^*$ are the number of effective valence electrons on the A(i) and O(i) atoms of the bond and $v_{(A(i)-O(i))}$ is the volume of the bond. $Z_{A(i)}^*$ and $Z_{O(i)}^*$ are calculated as: $Z^*=Z.q$, where Z is the number of valence electrons of the atom and q is the effective charge of the electron in the considered bond which can be obtained for each atom as $Q/(\text{formal valence state})$. For instance in $K(1)_{3/10}O(1)_{1/4}$ unit, we would have $q_K=1.368/1=1.368$, $q_O=1.64/2=0.82$, $Z_K^*=Z_K.q_K=1.368$ and $Z_O^*=Z_O.q_O=0.82 \times 6=4.92$. The bond volume $v_{A(i)-O(i)}$ is obtained from:

$$v_{(A(i)-O(i))} = d_{(A(i)-O(i))}^3 / \sum_i d_{(A(i)-O(i))}^3 N_{(A(i)-O(i))}^b \quad (20)$$

where $N_{(A(i)-O(i))}^b = ZN_{(A(i)-O(i))} / V$ is the number of chemical bonds of type A(i)-O(i) per cubic centimeter. Z is the number of formula per unit cell and V is the volume of the unit cell. Coming back to $KSrPO_4$, we have $Z=4$ and $V=394 \text{ (\AA}^3\text{)}$, then for $K(1)_{3/10}O(1)_{1/4}$, we have $N_{(K1-O1)}^b = 0.03 \text{ (\AA}^{-3}\text{)}$. The dielectric constant $\epsilon_{(A(i)-O(i))}$ of the A(i)-O(i) bond required in Equation (14) is obtained from:

$$\epsilon_{(A(i)-O(i))} = 1 + 4\pi\chi_{(A(i)-O(i))} \quad (21)$$

$\chi_{(A(i)-O(i))}$ is the susceptibility of the A(i)-O(i) bond, defined as:

$$\chi_{(A(i)-O(i))} = (\hbar\Omega_{(A(i)-O(i))})^2 / 4\pi E_{g(A(i)-O(i))}^2 \quad (22)$$

The quantity $\Omega_{(A(i)-O(i))}$ is the plasma frequency of the A(i)-O(i) bond, calculated as :

$$\hbar\Omega_{(A(i)-O(i))} = 37.16 \sqrt{N_{(A(i)-O(i))}^*} \quad (23)$$

The term $E_{g(A(i)-O(i))}$ represents the average value of the energy gap, calculated as

$$E_{g(A(i)-O(i))}^2 = E_{h(A(i)-O(i))}^2 + C_{(A(i)-O(i))}^2 \quad (24)$$

In this work, we have designed an excel program that helps to calculate the environmental factors in an easy and automatic way. After filling the data in the coordination matrix with the multiplicity of each atom and Z in KSrPO_4 (Tables 5 and 6), the formula allowing the decomposition into binary crystals is automatically obtained (Table 6). Table 7 compiles another set of input data obtained from VESTA. It includes the distances of all the bonds and the charge of the cation site in each bond in KSrPO_4 . The calculations of all parameters are then done automatically by the program and the two factors h_e and F_c are obtained for each cation site in the KSrPO_4 crystal (Table 8).

Table 5 Input data of the coordination of the different atoms with the corresponding multiplicity in KSrPO_4 .

	K	Sr	P	O1	O2	O3
O1	3	2	1	0	0	0
O2	6	4	2	0	0	0
O3	1	3	1	0	0	0
K	0	0	0	1	2	1
Sr	0	0	0	2	2	2
P	0	0	0	1	1	1
Total	10	9	4	4	5	4
multiplicity	4	4	4	4	8	4

Table 6 Formula of KSrPO_4 obtained automatically by the excel program.

Z	Formula											
4	K	1	Sr	1	O1	1	O2	2	O3	1	P	1

Table 7 Input distances, V_{cell} and Q_A for each bond in the KSrPO_4 crystal.

Parameters	KSrPO4	KSrPO4	KSrPO4	KSrPO4	KSrPO4	KSrPO4
	K-O1	K-O2	K-O3	Sr-O1	Sr-O2	Sr-O3
$d_{A-O1} (\text{\AA})$	2.858	2.9399	2.654	2.6305	2.6064	2.897
$d_{A-O2} (\text{\AA})$	2.9399	2.858	2.9399	2.9399	2.9399	2.9399
$d_{A-O3} (\text{\AA})$	2.654	2.654	2.858	2.654	2.654	2.654
$d_{B-O1} (\text{\AA})$	2.6305	2.6305	2.6305	2.858	2.6305	2.6305
$d_{B-O2} (\text{\AA})$	2.6064	2.6064	2.6064	2.6064	2.858	2.6064
$d_{B-O3} (\text{\AA})$	2.897	2.897	2.897	2.897	2.897	2.858
$d_{C-O1} (\text{\AA})$	1.561	1.561	1.561	1.561	1.561	1.561
$d_{C-O2} (\text{\AA})$	1.536	1.536	1.536	1.536	1.536	1.536
$d_{C-O3} (\text{\AA})$	1.529	1.529	1.529	1.529	1.529	1.529
$V_{\text{cell}} (\text{\AA}^3)$	394.208	394.208	394.208	394.208	394.208	394.208
Q_A	1.37	1.37	1.37	1.99	1.99	1.99

Table 8 Obtained set of parameters involved in the calculation of the environmental factors h_e and F_c of K Sr PO_4 by the excel program. Only Sr and K sites were considered here.

	C	D	E	F	G	H	I
		K-O1	K-O2	K-O3	Sr-O1	Sr-O2	Sr-O3
$K_F (\text{\AA}^{-1})$		1.97261	1.58168	1.56515	1.85259	1.86972	1.87056
$K_S (\text{\AA}^{-1})$		2.17895	1.95113	1.94091	2.11163	2.12137	2.12184
$E_h (\text{ev})$		2.93896	2.74008	3.53145	3.61021	3.69357	2.84181
$C (\text{ev})$		6.92055	6.9139	6.56689	7.39256	10.1808	5.85848
$E_g (\text{ev})$		7.51874	7.43708	7.45622	8.227	10.8301	6.51135
fc		0.15279	0.13574	0.22432	0.19257	0.11631	0.19048
$\hbar\omega_p$		18.9202	13.5845	13.372	17.2201	17.4595	17.4712
χ		0.50391	0.26551	0.25595	0.34864	0.20682	0.57292
ϵ		7.3323	4.33645	4.21631	5.38115	3.59896	8.19948
α		0.85481	0.72202	0.52196	0.58303	0.44353	0.92615
fi		0.847209	0.864256	0.775679	0.807433	0.883687	0.80952
h_{ei}		1.0559	0.61903	0.03506	0.1753	0.25171	0.92961
h_e		1.307667225			1.164737562		
F_c		0.272755808			0.345929417		

Based on the investigation of a series of cubic host lattices including fluorides, bromides, chlorides, iodides, oxides, sulfides and selenides consisting of one or more cation sites with different coordination symmetries, Zhang has established a correlation between h_e and the centroid energy E_c of the $4f^{n-1}5d^1$ electron configuration of ions like Ce^{3+} and $\text{Eu}^{2+ (24)}$ (Figure 20).

A fitting of the data then led to the following semi-empirical Equation that allows calculating E_c (in cm^{-1}) from the knowledge of h_e :

$$E_c = A + B e^{-k h_e} \quad (25)$$

For Eu^{2+} , $A = 27130$, $B = 16450$ and $k = 1.817$. For Ce^{3+} , $A = 12490$, $B = 37930$ and $k = 0.662$. In the case of Eu^{2+} , the accuracy of the model is estimated by us at $\pm 360 \text{ cm}^{-1}$. Equation (25) is basically valid for lattices having cubic-related symmetry.

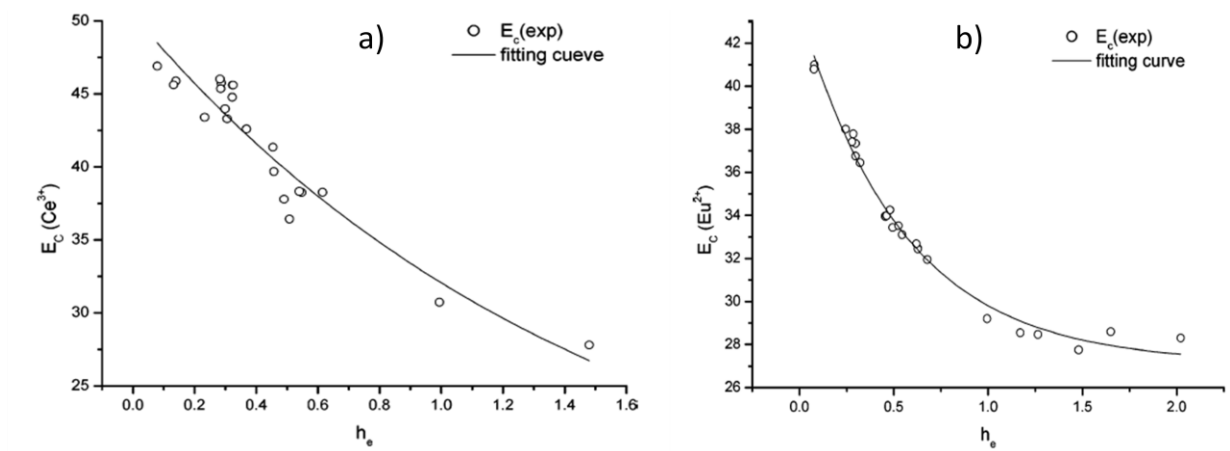


Figure 20. Correlation between the environmental factor h_e and the centroid energy of the 5d levels of a) Ce^{3+} and b) Eu^{2+} in various cubic lattices ⁽²⁴⁾

In another work, an empirical relationship has also been established between F_c and the crystal field strength E_{10Dq} (in cm^{-1}) for Eu^{2+} and Ce^{3+} in cubic halide lattices ⁽⁵⁹⁾ (Figure 21):

$$E_{10Dq} = A + B \cdot F_c \quad (26)$$

For Eu^{2+} , $A = 4990$ and $B = 18770$. For Ce^{3+} , $A = 3270$ and $B = 14340$. In the case of Eu^{2+} , the accuracy of the model is estimated by us at $\pm 470 \text{ cm}^{-1}$.

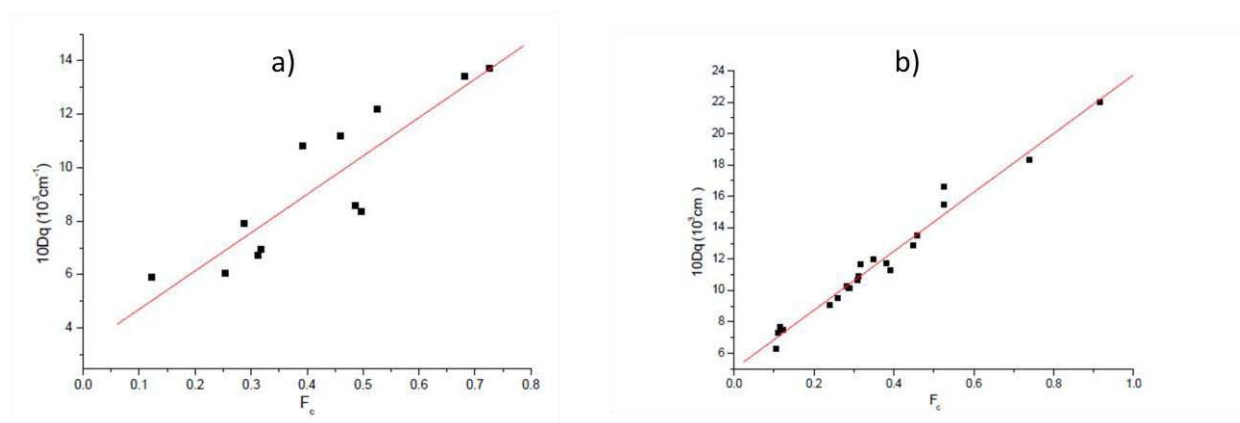


Figure 21. Correlation between the environmental factor F_c and the crystal field splitting $10 Dq$ of a) Ce^{3+} and b) Eu^{2+} in cubic halides ⁽⁵⁹⁾.

In the case of s^2 ions like Bi^{3+} and Pb^{2+} , semi-empirical Equations have also been established between h_e and the excitation energy of the A transition band in a number of host lattices having different crystal structures^{(60), (61)} (Figure 22).

For Bi^{3+} , two relationships have been introduced to estimate the energy of A and C transitions. For the A transition, we have⁽⁶⁰⁾:

$$E_A(\text{Bi}) = e^{-h_e/} \quad (27)$$

and for the C transition⁽⁶⁰⁾:

$$E_C(\text{Bi}) = e^{-h_e/} \quad (28)$$

In the case of Pb^{2+} the relation was found to be linear. The energy of the A transition is calculated as⁽⁶¹⁾:

$$E_A(\text{Pb}) = -h_e \quad (29)$$

All energies are given in cm^{-1} .

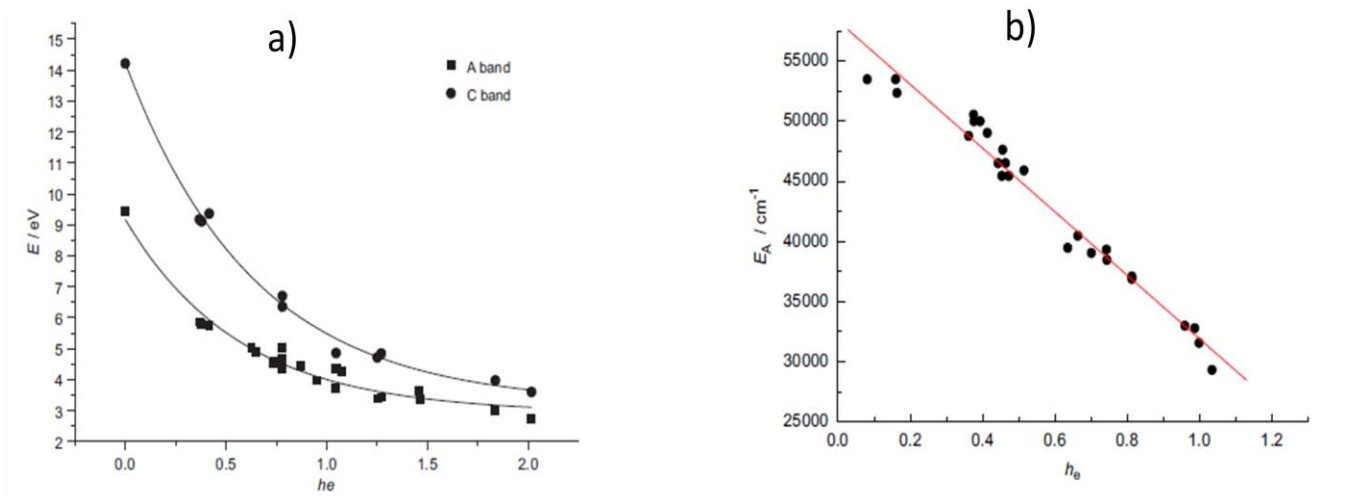


Figure 22. Correlation between the environmental factor h_e and the energy of the excitation bands (a) A and C of Bi^{3+} and of (b) Pb^{2+} (A band only) in different types of crystals.^{(60), (61)}

1.6.4. MMCT model

The metal to metal charge transfer model, proposed by Boutinaud ^{(42),(62)}, aims to calculate the MMCT energy of dopants in transition metal oxides from the knowledge of few structural and electronic parameters. The model was especially applied for ions with s^2 configuration like Bi^{3+} and Pb^{2+} in d^0/d^{10} transition metal oxides. An empirical Equation has then be introduced on the basis of the investigation of about 60 different transition metal oxides with various crystal structures:

$$MMCT (cm^{-1}) = k_{CN'} \left[\chi_{CN} (\text{Bi}^{3+}) - \alpha_{CN'}^{CN} \frac{\chi_{CN'} (M^{n+})}{d_{corr}} \right] \quad (30)$$

This Equation allows the calculation of the energy of the charge transfer between Bi^{3+} and the closest-lying transition metal M^{n+} in the host lattice (i. e. D-like transition). In Equation (30), CN and CN' are the coordination numbers of Bi^{3+} and M^{n+} in their respective crystallographic sites. Parameters $\chi_{CN}(\text{Bi}^{3+})$ and $\chi_{CN'}(M^{n+})$ are the electronegativities of Bi^{3+} and of the transition metal ion M^{n+} , respectively extracted from the work of Li and Xue ⁽⁶³⁾ (see Appendix A). The quantity d_{corr} represents the shortest Bi^{3+} - M^{n+} distance in the host lattice. This value is corrected for the doping effect (i. e. difference of ionic radius between Bi^{3+} and the substituted cation in coordination number (CN) following:

$$d_{corr} = d_{host} + \frac{1}{2} [r(\text{Bi}^{3+}) - r(M^{n+})] \quad (31)$$

where $r(\text{Bi})$ and $r(M^{n+})$ are the corresponding crystal radii, as deduced from the work of R. D. Shannon ⁽⁶⁴⁾ and d_{host} is the shortest distance between M^{n+} and the substituted cation site in the lattice. This data is obtained from ICSD data bases by using VESTA.

The value of $\chi_{CN}(\text{Bi}^{3+})$ can be calculated for any value of CN following the procedure given in Li and Xue ⁽⁶³⁾:

$$\chi_{CN} (\text{Bi}^{3+}) = \frac{0.105n^*}{r(\text{Bi}^{3+})} \sqrt{\frac{I_m}{13.6}} + 0.863 \quad (32)$$

Where n^* is the effective principle quantum number (4.36 for Bi^{3+}) and I_m is the ultimate ionization energy (25.56 eV for Bi^{3+}). $r(\text{Bi}^{3+})$ is the coordination-dependent ionic radius of Bi^{3+} . The two parameters $k_{CN'}$ and $\alpha_{CN'}^{CN}$ in Equation (30) are crystal-structure related quantities. Values are given in Tables 9 and 10.

Table 9 Useful structure-related parameters for Equation (30) ⁽⁴²⁾.

CN	$r(\text{Bi}^{3+})$ (Å)	$\chi_{\text{CN}}(\text{Bi}^{3+})$	k_4 (cm ⁻¹)	$k_{\text{CN}'>4}$ (cm ⁻¹)
5	1.10	1.43	48950	38461
6	1.17	1.40	50000	39285
7	1.24	1.37	51095	40145
8	1.31	1.34	52239	41044
9	1.35	1.33	52631	41353
10	1.41	1.305	53640	42145
12	1.50	1.28	54690	42970

Table 10 Useful structure-related parameters for Equation (30) ⁽⁴²⁾.

CN	$\alpha_{\text{CN}'}^{\text{CN}}$	
	CN' = 4	CN' = 6, 7, 8, 9
5	1.06	1.18
6	1.04	1.16
7	1.02	1.13
8	0.99	1.11
9	0.99	1.10
10	0.97	1.08
12	0.95	1.06

From the above Tables, it is clear that lattices in which the transition metal is tetra-coordinated (CN' = 4) will behave differently from lattices in which the transition metal is hexa or higher coordinated (CN' ≥ 6). This is clearly exemplified in Figure 23 where the experimental excitation energies of Bi³⁺ in transition metal oxides are plotted against $\frac{\chi_{\text{CN}'}(M^{n+})}{d_{\text{cor}}}$.

For ease of use and fast evaluation of MMCT energies, one may consider average values of $\chi_{\text{CN}}(\text{Bi}^{3+})$, $k_{\text{CN}'}$ and $\alpha_{\text{CN}'}^{\text{CN}}$ as follows: $\chi_{\text{CN}}(\text{Bi}^{3+}) = 1.31$ (corresponding to frequently encountered 8-fold coordinated sites), $k_4 = 52000$ cm⁻¹, $k_{\text{CN}'\geq 6} = 41000$ cm⁻¹ and $\alpha_{\text{CN}'}^{\text{CN}} = 1$. We see from Figure 23 that the accuracy of the method is about ± 1500 cm⁻¹.

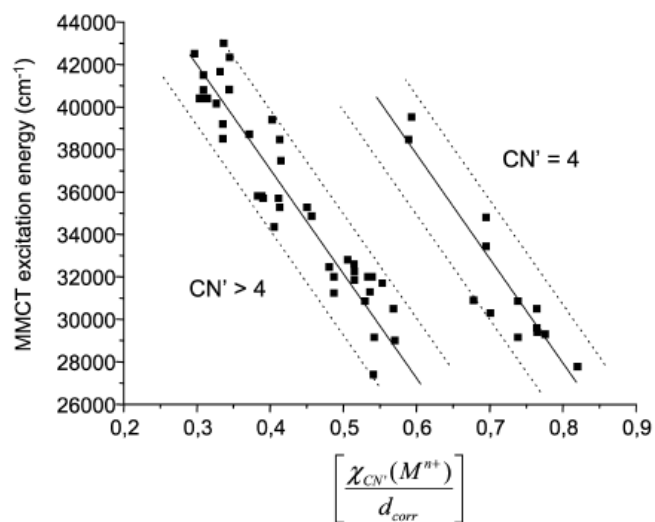


Figure 23. Variation of the $Bi^{3+} \rightarrow M^{n+}$ MMCT energy against the ratio $\frac{\chi_{CN'}(M^{n+})}{d_{corr}}$ in Bi^{3+} -doped transition metal oxides. Solid lines correspond to Equation (30) and appropriate parameters given by Tables 9 and 10.

Bibliography

1. **G. Blasse and B.C. Grabmaier.** *Luminescent Materials*: Springer-Verlag Berlin Heidelberg New York, 1994.
2. **R.G.D. Tilley.** *Colour and the optical properties of materials*: John Wiley & Sons Chichester, United Kingdom, 2011.
3. **K.V.R. Murthy and H.S. Virk.** *Luminescence Phenomena: An Introduction*. 2014, Defect and Diffusion Forum, Vol. 347, pp. 1-34.
4. **C.R. Cornejo.** *Luminescence - An Outlook on the Phenomena and their Applications*, edited by J.Thirumalai: INTECH, 2016.
5. **A. Kitai.** *Luminescent materials and applications*: John Wiley and sons Ontario Canada, 2008.
6. **J.A. DeLuca.** *An Introduction to Luminescence in inorganic solids*. 1980, Journal of Chemical Education, Vol. 57, pp. 541-545.
7. **G. Blasse.** *Luminescence of inorganic solids: from isolated centers to concentrated systems*. 1988, Progress in Solid State Chemistry, Vol. 18, pp. 79-171.
8. **Z. Luo, Y. Huang and X. Chen.** *Spectroscopy of solid state laser and luminescent materials*: Nova Science Publishers New York, 2007.
9. **D. Spassky, V. Mikhailin and M. Nazarov.** *Luminescence and energy transfer mechanisms in CaWO_4 single crystals*. 2012, Journal of luminescence, Vol. 132, pp. 2753–2762.
10. **G. Blasse.** *The Luminescence of Closed-Shell Transition-Metal Complexes. New Developments*: Springer-Verlag Heidelberg, Structure and Bonding 1980, Vol. 42, pp. 1-41.
11. **C.R. Ronda.** Emission and Excitation Mechanisms of Phosphors. *Luminescence from theory to applications*: Wiley-VCH Verlag GmbH & Co.KGAA. Germany, 2008.
12. **G. Blasse.** *Luminescence of Calcium Halophosphate- Sb^{3+} , Mn^{2+} at low temperatures*. 1983, Chemical Physics letters, Vol. 104, pp. 160-162.
13. **R. Burns.** Outline of Crystal field theory. *Mineralogical Applications of Crystal Field Theory* Cambridge University Press New York, 1970.
14. **E.A. Seregina, A.A. Seregin and G.V. Tikhonov.** *Spectral and luminescent characteristics of trivalent lanthanide ions in a POCl_3 - SnCl_4 inorganic solvent*. 2014, Condensed Matter Spectroscopy, Vol. 116, p.p. 469-485.
15. **I. Pelant and J. Valenta.** *Luminescence spectroscopy of semiconductors*: Oxford University Press New York, 2012.

16. **P.C. de Sousa Filho, J.F. Lima and O.A. Serra** *From Lighting to Photoprotection: Fundamentals and Applications of Rare Earth Materials*. 2015, Journal of the Brazilian Chemical Society, Vol. 26, pp. 2471-2495.
17. **I.E. Kolesnikov, D.V. Tolstikova, A.V. Kurochkin, S.A. Pulkin, A.A. Manshina and M.D. Mikhailov**. *Concentration effect on photoluminescence of Eu^{3+} -doped nanocrystalline YVO_4* . 2015, Journal of Luminescence, Vol. 158, pp. 469-474.
18. **S. Zhang, G. Jinxia, J. Guozhi and Z. Lui**. *Effect of annealing on the spectroscopy performance of $\text{YVO}_4:\text{Ce}^{3+}$ single crystals*. 2015, Optical materials, Vol. 39, pp. 178-181.
19. **P. Dorenbos**. *5d-level energies of Ce^{3+} and the crystalline environment.I.Fluoride Compounds*. 2000, Physical Reviews B, Vol. 62, p. 15640.
20. **A.B. Parmentier, P.F. Smet and D. Poelman**. *Broadband Luminescence in Rare Earth Doped Sr_2SiS_4 :Relating Energy Levels of Ce^{3+} and Eu^{2+}* . 2013, Materials, Vol. 6, pp. 3663-3675.
21. **P. Dorenbos**. *Relation between Eu^{2+} and Ce^{3+} f d-transition energies in inorganic compounds*. 2003, Journal of Physics Condensed Matter, Vol. 15, pp. 4797–4807.
22. **G. Blasse**. *On the nature of Eu^{2+} luminescence*. 1973, Physica Status Solidi B, Vol. 55, p. K131.
23. **P. Dorenbos**. *A Review on How Lanthanide Impurity Levels Change with Chemistry and Structure of Inorganic Compounds*. 2013, The Electrochemical Society, Vol. 2, pp. R3001-R3011.
24. **J.S. Shi and S.Y. Zhang**. *Barycenter of Energy of Lanthanide $4f^{n-1}5d$ Configuration in Inorganic Crystals*. 2004, Journal of Physical Chemistry B, Vol. 108, pp. 18845-18849.
25. **P. Dorenbos**. *5d-level energies of Ce^{3+} and the crystalline environment.IV.Aluminates and “simple” oxides*. 2002, Journal of Luminescence, Vol. 99, pp. 283-299.
26. **P. Dorenbos**. *Ce^{3+} 5d-centroid shift and vacuum referred 4f electron binding energies of all lanthanide impurities in 150 different compounds*. 2013, Journal of Luminescence, Vol. 135, pp. 93–104.
27. **P. Dorenbos**. *f→d transition energies of divalent lanthanides in inorganic compounds*. 2003, Journal of Physics Condensed Matter, Vol. 15, pp. 575-594.
28. **P. Dorenbos**. *Locating lanthanide impurity levels in the forbidden band of host crystals*. 2004, Journal of Luminescence, Vol. 108, pp. 301–305.
29. **P. Dorenbos**. *The 4f $4f^{n-1}5d$ transitions of the trivalent lanthanides in halogenides and chalcogenides*. 2000, Journal of Luminescence, Vol. 91, pp. 91-106.
30. **P. Dorenbos**. *The 5d level positions of the trivalent lanthanides in inorganic compounds*. 2000, Journal of Luminescence, Vol. 91, pp.155-176.

31. **D.B. Abdu.** *A Review of Lanthanides As Activators In Luminescence.* July 2016, Journal of applied chemistry, Vol. 9, pp. 2278-5736.
32. **Y. Zhu, N. Narendran and Y. Gu.** *Investigation of the optical properties of YAG:Ce phosphor.* Troy, NY : Society of Photo-optical instrumentation engineers, 2006.
33. **H. Rétot, A. Bessière, B. Viana, and A. Galtayries.** *Location of trivalent lanthanide dopant energy levels in $(\text{Lu}_{0.5}\text{Gd}_{0.5})_2\text{O}_3$.* June 2011, Journal of Applied Physics, Vol. 109, p. 123518.
34. **M.D. Birowosuto, P. Dorenbos, C.W.E. van Eijk, K.W. Kramer and H.U. Gudel.** *Scintillation properties and anomalous Ce^{3+} emission of $\text{Cs}_2\text{NaREBr}_6:\text{Ce}^{3+}$ ($\text{RE} = \text{La}, \text{Y}, \text{Lu}$).* 2006, Journal of Physics Condensed Matter, Vol. 18, pp. 6133–6148.
35. **G. Blasse.** *The influence of Charge-Transfer and Rydberg States on the Luminescence Properties of Lanthanides and Actinides.* Springer-Verlag Heidelberg 1976, Structure and Bonding, Vol. 26, pp.43-79.
36. **D.N. Sathyanarayana.** *Electronic Absorption Spectroscopy and Related Techniques:* Universities Press India, 2001.
37. **A. Patra, R.E. Tallman and B.A. Weistein.** *Effect of crystal structure and dopant concentration on the luminescence of Cr^{3+} in Al_2O_3 nanocrystals.* 2004, Optical Materials, Vol. 27, pp. 1396-1401.
38. **Z. Xia, D. Chen, M. Yang and T. Ying.** *Synthesis and luminescence properties of $\text{YVO}_4:\text{Eu}^{3+}, \text{Bi}^{3+}$ phosphor with enhanced photoluminescence by Bi^{3+} doping.* 2010, Journal of Physics and Chemistry of Solids, Vol. 71, pp. 175-180.
39. **A.A. Setlur and A.M. Srivastava.** *The nature of Bi^{3+} luminescence in garnet hosts.* 2006, Optical materials, Vol. 29, pp. 405-415.
40. **R.H.P. Awater, P. Dorenbos.** *The Bi^{3+} 6s and 6p electron binding energies in relation to the chemical environment in inorganic compounds.* 2017, Journal of Luminescence, Vol. 184, pp. 221-231.
41. **E. Cavalli, F. Angiuli, F. Mezzadri, M. Trevisani, M. Bettinelli, P. Boutinaud and M.G. Brik.** *Tunable luminescence of Bi^{3+} -doped $\text{YPr}_x\text{V}_{1-x}\text{O}_4$ ($0 \leq x \leq 1$).* 2014, Journal of Physics Condensed matter, Vol. 26, pp. 385503-385515.
42. **P. Boutinaud.** *Revisiting the Spectroscopy of the Bi^{3+} Ion in Oxide Compounds.* 2013, Inorganic Chemistry , Vol. 52, p. 6028–6038.
43. **A.M. Srivastava and S.J. Camardello.** *Concentration dependence of the Bi^{3+} luminescence in LnPO_4 ($\text{Ln}=\text{Y}^{3+}, \text{Lu}^{3+}$).* 2015, Optical Materials , Vol. 39, pp. 130-133.
44. **A.M. Srivastava and W.E. Beers.** *On the impurity trapped exciton luminescence in $\text{La}_2\text{Zr}_2\text{O}_7:\text{Bi}^{3+}$.* 1990, Journal of Luminescence, Vol. 81, pp. 293-300.
45. **E.W.J.L. Oomen, W.M.A. Smit and G. Blasse.** *Luminescence of the Sb^{3+} ion in Calcium Fluoroapatite and other phosphates.* 1998, Materials chemistry and Physics, Vol. 19, pp. 357-368.

46. **J. Grafmeyer, J.C. Bourcet and J. Janin.** *Luminescence properties of Sb^{3+} in Yttrium phosphates.* 1976, Journal of Luminescence, Vol. 11, pp. 369-380.
47. *LEDs Basics: LED Fundamentals, LED Light Site by OSRAM Opto Semiconductors.*
www.slideshare.net/OSRAMLEDLIGHT. December 6, 2012.
48. **C. Ronda.** *Challenges in Application of Luminescent Materials.* 2014, Progress In Electromagnetics Research, Vol. 147, pp. 81-93.
49. **C. Zhang, S. Huang, D. Yang, X. Kang, M.S hang, C. Peng and J. Lin.** *Tunable luminescence in Ce^{3+} , Mn^{2+} -codoped calcium fluorapatite through combining emissions and modulation of excitation: a novel strategy to white light emission.* 2010, Journal of Materials Chemistry, Vol. 20, pp. 6674–6680.
50. **B.R. Judd.** *Optical Absorption Intensities of Rare-Earth Ions.* 1962, Physical Reviews, Vol. 127, p. 750.
51. **G.S. Ofelt.** *Intensities of Crystal Spectra of Rare-Earth Ions.* 1962, J.Chem.Phys, Vol. 37, p. 511.
52. **P. Dorenbos.** *Relating the energy of the $[Xe]5d^1$ configuration of Ce^{3+} in inorganic compounds with anion polarizability and cation electronegativity.* 2002, Physical Reviews B, Vol. 65, p. 235110.
53. **J. A. Van. Vechten.** *Quantum Dielectric Theory of Electronegativity in Covalent Systems.I. Electronic Dielectric Constant.* 1969, Physical Review, Vol. 182, pp. 891-905.
54. **J.C. Philips.** *Dielectric Definition of electronegativity.* 1968, Physical review letters, Vol. 20, pp. 550-553.
55. **J. A. Van.Vechten.** *Quantum Dielectric Theory of Electronegativity in Covalent Systems.II. Ionization Potentials and Interband Transition Energies.* 1969, Physical review, Vol. 187, pp. 1007-1020.
56. **B.F. Levine.** *d-Electron Effects on Bond Susceptibilities and Ionicities.* 1973, Physical review B, Vol. 7, pp. 2591-2600.
57. **K. Momma and F.Izumi.** *VESTA: a Three-Dimensional Visualization System for Electronic and Structural Analysis.* 2008, Journal of Applied Crystallography, vol. 41, pp. 653-658.
58. **N.E. Brese and M.O'Keeffe.** *Bond valence parameters for solids.* 1990, Acta Crystallographica B, Vol. 47, pp. 192-197.
59. **J.S. Shi, Z.J. Wu, S.H. Zhou and S.Y. Zhang.** *Dependence of crystal field splitting of 5d levels on hosts in the halide crystals.* 2003, Chemical Physics Letters, Vol. 380, pp. 245–250.
60. **L. Wang, Q. Sun, Q. Liu and J. Shi.** *Investigation and application of quantitative relationship between sp energy levels of Bi^{3+} ion and host lattice.* 2012, Journal of Solid State Chemistry, Vol. 191, pp. 142-146.
61. **Q. Sun, J. Wang and J. Shi.** *Prediction and assignment of site occupation and energy levels for Pb^{2+} ions.* 2010, Journal of Solid State Chemistry, Vol. 183, pp. 1174–1179.

62. **P. Boutinaud and E. Cavalli.** *Predicting metal-to-metal charge transfer in closed-shell transition metal.* 2011, Chemical Physics letters, Vol. 503, pp. 239–243.
63. **K. Li and D. Xue.** *Estimation of Electronegativity Values of Elements in Different Valence States.* 2006, Journal of Physical Chemistry A, Vol. 110, pp. 11332–11337.
64. **R.D. Shannon.** *Revised effective ionic radii and systematic studies of interatomic distances in halides and chalcogenides.* 1976, Acta Crystallographica Section A, Vol. 32, pp. 751-767.

Chapter 2 The doping sites in $A^I B^{II} PO_4:Eu^{2+}$ and their consequence on the photoluminescence excitation spectra

2.1. Introduction

Among divalent lanthanides, Eu^{2+} and Yb^{2+} exhibit the lowest energy values for the 4f-5d transitions (Chapter 1). Being more stable, Eu^{2+} ion is widely used in designing phosphors for different applications especially for the LED lighting. To match the needs of the LED lighting market today, phosphors absorbing in the near UV or blue and emitting in the visible region are highly required. Browsing the literature, we can find that a number of Eu^{2+} doped compounds have been studied for this purpose⁽¹⁾⁻⁽⁶⁾. The family of $ABPO_4$ where A^I and B^{II} are monovalent and divalent cations respectively, also serve as relevant hosts for Eu^{2+} in extensive research studies owing to their attractive photoluminescent properties upon blue or near-UV excitation in addition to their excellent thermal stabilities⁽⁷⁾⁻⁽¹³⁾. Figure 1 shows the excitation spectra of a group of $ABPO_4:Eu^{2+}$ hosts showing broad band signals extending to the UV and blue regions.

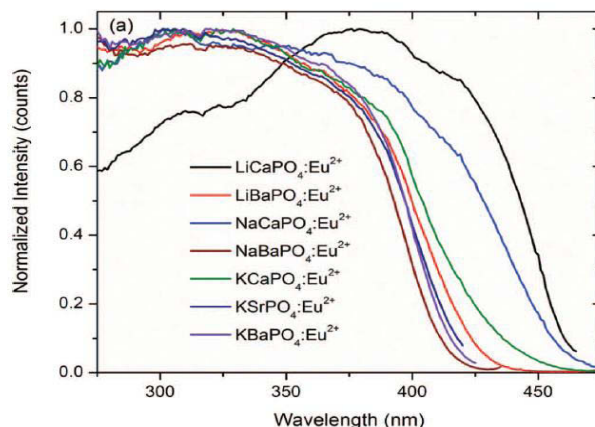


Figure 1. Excitation spectra of $ABPO_4:Eu^{2+}$ phosphors⁽¹⁴⁾.

The crystal field splitting of the 5d states of Eu^{2+} in a crystal and correspondingly the red shift depend mainly on the type of coordination of the cation site in which Eu^{2+} accommodates. In this connection, the $\text{A}^{\text{I}}\text{B}^{\text{II}}\text{PO}_4$ family which includes many members with many possible crystal structures and doping sites depending on the nature of A^{I} (typically Li^+ , Na^+ , K^+ , Cs^+ , Rb^+ , Ag^+ , NH_4^+) and B^{II} (typically Be^{2+} , Mg^{2+} , Ca^{2+} , Sr^{2+} , Ba^{2+} , Cd^{2+} , Zn^{2+} , Mn^{2+} , Fe^{2+} , Co^{2+} , Ni^{2+} , Cu^{2+}), gives a variety of luminescent outputs that can be explored. This can be seen from Figure 1 where the excitation edge attributed to Eu^{2+} in these compounds can vary by 100 nm. Note that the excitation edge in this chapter will be taken as the wavelength where the excitation has lost 50% of its lowest-lying maximum intensity. It marks the limit above which the excitation in the first spin and dipole allowed $4f^7 \rightarrow 4f^65d^1$ transition of Eu^{2+} becomes inefficient.

However, not all of these members have been studied in the literature. The series of studied compounds are ABPO_4 with $\text{A} = \text{Li}^+$, Na^+ , K^+ , Cs^+ , Rb^+ and $\text{B} = \text{Mg}^{2+}$, Ca^{2+} , Sr^{2+} , Ba^{2+} ⁽⁷⁾⁻⁽¹⁶⁾. For most of these compounds, the excitation edge can easily be picked up from the archival literature. This is what we have done in the present work. Doing so, we found important discrepancies in the edge position for a few lattices. In $\text{CsMgPO}_4\text{:Eu}^{2+}$, for instance, the excitation edge is reported either at 395 nm ⁽¹⁷⁾ or at 460 nm ⁽⁷⁾, which makes a mismatch of 65 nm. In $\text{NaMgPO}_4\text{:Eu}^{2+}$, the excitation edge is found at 377 nm for a corresponding blue emission ⁽¹⁸⁾ or close to 500 nm for a corresponding red emission ⁽¹¹⁾, depending on the preparation method. There are no clear explanations for these behaviors. One possible explanation could be related to the fact that Eu^{2+} may be inserted in either A^{I} or B^{II} sites, with concomitant difference in the luminescence signals. As a matter of fact, this lack of information on the nature of the doping sites for Eu^{2+} prevents the prospective design of materials and restricts the preparation of phosphors to trial-error procedures that are matter and time-consuming. Therefore, a better understanding of the relationship between the redshift and the crystal structure would in this connection, be of great help.

In this chapter, the determination of the accommodating sites in $\text{A}^{\text{I}}\text{B}^{\text{II}}\text{PO}_4\text{:Eu}^{2+}$ will be investigated with the help of the EF model. Calculations of the environmental factors $h_e(X(i))$ and $F_c(X(i))$ allow us to calculate the energy of the first spin and dipole allowed $4f^7 \rightarrow 4f^65d^1$ transition of Eu^{2+} for each possible cation site in 25 different ABPO_4 hosts. This energy will be assimilated to the photoluminescence excitation edge defined above. By comparing the calculated energy of this transition for each cation site with that of the experimental data on the excitation edge positions we can identify the doping sites in each host. At the end, this will allow us to conclude on the potential interest of the method for the predictive design of Eu^{2+} -doped $\text{A}^{\text{I}}\text{B}^{\text{II}}\text{PO}_4$ hosts usable for LED-based lighting. In addition to this phenomenological approach,

we have prepared the compound $\text{NaZnPO}_4\cdot\text{Eu}^{2+}$ and investigated its luminescence properties. The choice of this lattice is motivated by the fact that only one kind of site (Na(1)) is possible for Eu^{2+} . For this reason, as it will be detailed in the following, this compound will be considered as a model system.

2.2. Synthesis and structural/microstructural characterizations of $\text{NaZnPO}_4\cdot\text{Eu}^{2+}$

$\text{NaZnPO}_4\cdot\text{Eu}^{2+}$ was prepared by standard solid state method using Na_2CO_3 (ACROS, >99.6%) as the alkaline source, $\text{NH}_4\text{H}_2\text{PO}_4$ (Sigma-ALDRICH, >98.5%) as the phosphate source, $\text{Zn}(\text{NO}_3)_2\cdot 6\text{H}_2\text{O}$ (ACROS, 98%) as the zinc source and Eu_2O_3 (PURATREM, 99.99%) as the dopant source. The nominal doping rate was 1 mol%. The reagents were homogeneously mixed in stoichiometric proportions with the presence of ethanol. The mixtures were dried at 80°C and heated at 300 °C in air for 15h. An amount of the sample was used to obtain the high temperatures X-ray diffraction (HTK) patterns by using an X-pert Pro diffractometer (Panalytical) with Cu anode. The patterns collected in the temperature 650 °C to 1010 °C are reproduced in Figure 2. At 650°C to 710°C, the compound seems to consist of NaZnPO_4 monoclinic phase. At 860°C < T < 920 °C, the compound presents at least two phases (monoclinic and orthorhombic) with additional features that are not identified by any of the two phases marked by (*). At T ≥ 950 °C, the main features start to disappear until we have a destruction of the compound at T= 1010 °C. One main peak remains at ≈ 40° which is related to platinum originating from the heating strip where the powder was installed during the X-ray experiments. As we were looking for a well-crystallized monoclinic compound, the sample was treated at 850 °C for 6h. The flowing atmosphere was a mixture of argon and hydrogen (95/5) in order to reduce Eu^{3+} to Eu^{2+} .

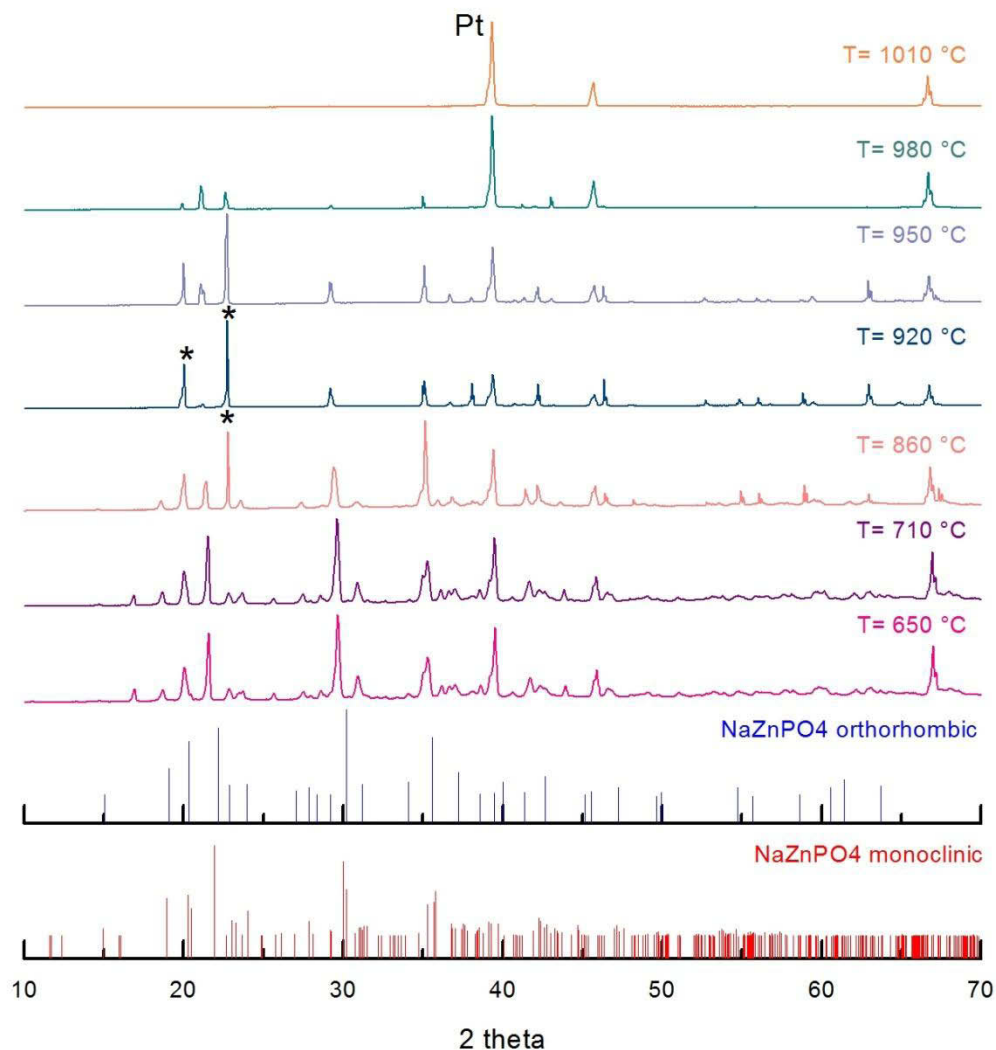


Figure 2. High temperature X-ray diffraction patterns of $\text{NaZnPO}_4:\text{Eu}^{2+}$. The heating rate was 1°C/min and the dwell time was 2 and half hours.

The corresponding X-ray diffraction pattern recorded at ambient temperature is shown in Figure 3. It is consistent with the monoclinic polymorph of NaZnPO_4 (JCPDS standard 01-079-0217), except a weak reflection (*) which belongs to NaZnP_3O_9 (JCPDS 96-703-5628). This very small amount of extra phase was not considered as significant enough to affect the luminescence properties.

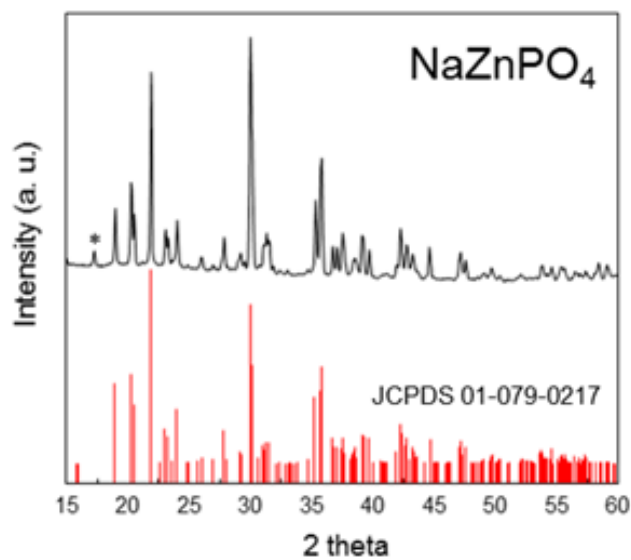


Figure 3. XRD pattern of $\text{NaZnPO}_4 \cdot \text{Eu}^{2+}$ collected at room temperature.

* marks a reflection that is not indexed using the JCPDS standard 01-079-0217 (see text).

The monoclinic crystal structure of NaZnPO_4 (ICSD 87557) is represented in Figure 4.

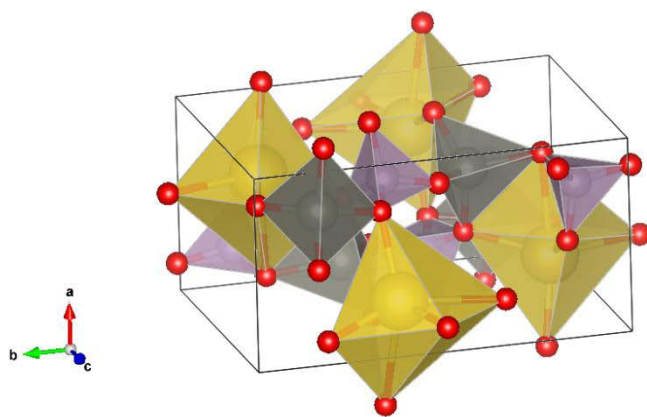


Figure 4. Crystal structure of monoclinic NaZnPO_4 ($P 2_1/n$)

It has the $P 2_1/n$ space group ($n^\circ 14$). It has one Na site with wyckoff position 4e, one Zn site with wyckoff position 4e and four oxygen sites O(1), O(2), O(3) and O(4) with wyckoff position 4e. The number of formula per unit cell is $Z=4$. The volume of the unit cell is 385 \AA^3 . The unit cell parameters $a=5.004 \text{ \AA}$, $b=5.004 \text{ \AA}$ and $c=24.632 \text{ \AA}$, $\alpha=\beta=90^\circ$ and $\gamma=120^\circ$. The Na atom is coordinated by one O(1), three

O(2), one O(3) and one O(4) oxygen atoms which give a total coordination of 6-fold forming a distorted octahedron having C_1 point symmetry with Na-O interatomic distances ranging from 2.301 to 2.998 Å and O-Na-O bond angles ranging from 54 to 107°. The distortion index D. I., of the corresponding (NaO_6) polyhedron is calculated as⁽¹⁹⁾:

$$D.I. = \frac{1}{N} \sum_{i=1}^N \frac{|l_i - l_{av}|}{l_{av}} \quad (1)$$

where l_i is the distance from the central atom to the i^{th} coordinating atom, l_{av} is the average bond length and N is the coordination number. This data gives information on the degree of irregularity of a given polyhedron. In the case of $NaZnPO_4$, the D.I. value of (NaO_6) octahedra amounts $\approx 10\%$. The very small Zn^{2+} sites being tetrahedrally coordinated in the lattice, are not expected to accommodate Eu^{2+} . There is therefore no doubt that the Eu^{2+} ion occupies the Na^+ sites in the compound.

The sample was also studied by electron scanning microscopy using a JSM-5910 LV microscope from Jeol operated at 15 kV. A representative image is shown in Figure 5. The microstructure of $NaZnPO_4:Eu^{2+}$ consists of a large granular distribution covering the range ≈ 10 -100 μm .

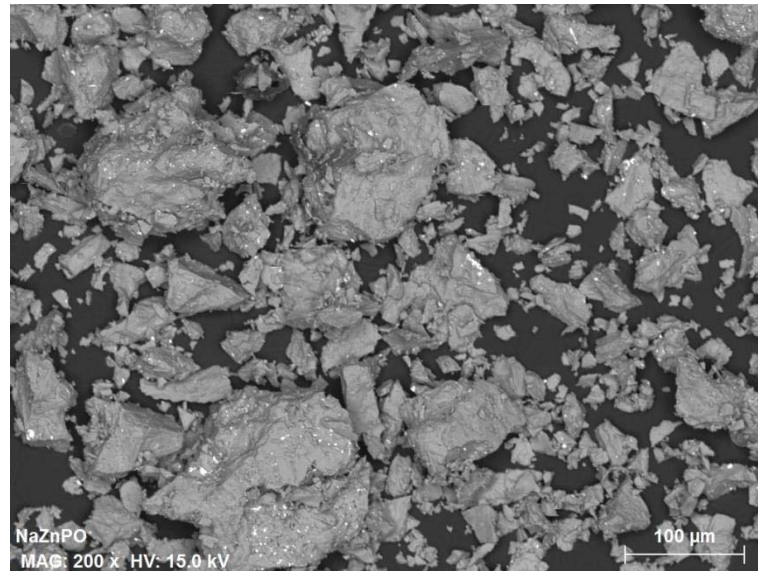


Figure 5. SEM image for $NaZnPO_4:Eu^{2+}$.

The corresponding microprobe images shown in Figure 6 illustrate the highlighted distribution of each atom showing the elemental concentrations in the powder. The green color is related to phosphorous, the blue to sodium, the brown to zinc and red to oxygen. These images confirm

homogenous distribution of the ions within the material. Eu^{2+} could not be observed due to the small doping rate.

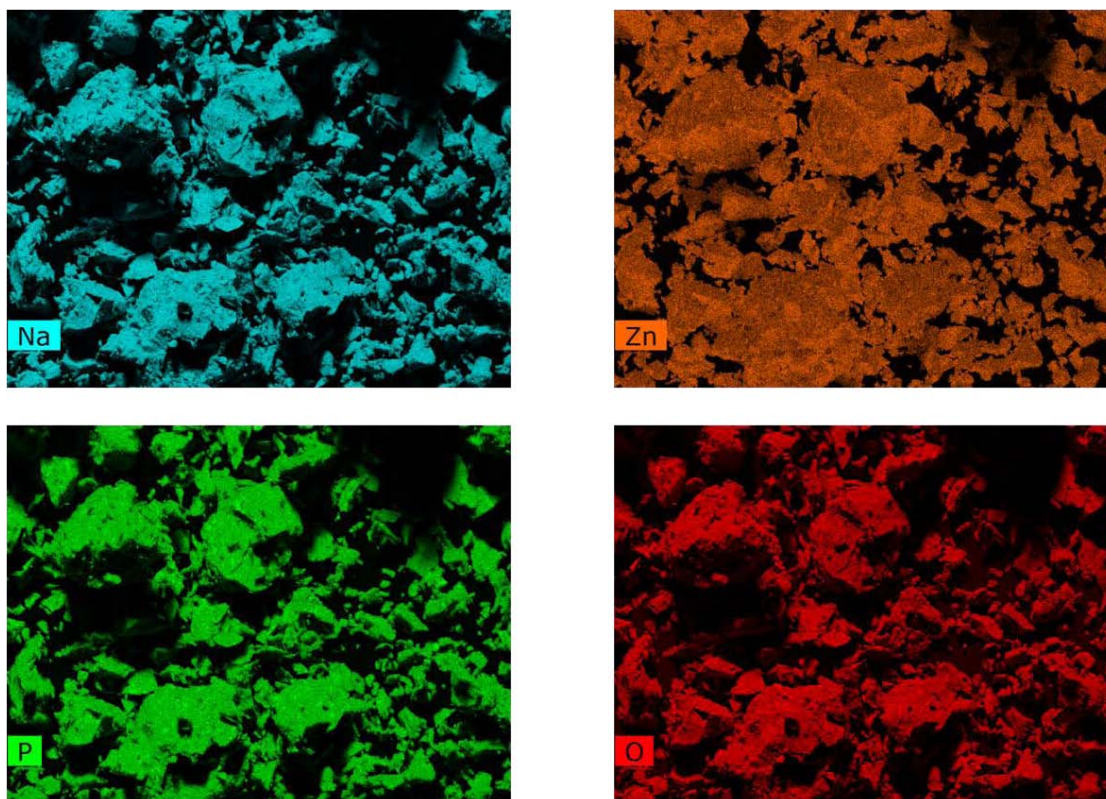


Figure 6. SEM image highlighting the distribution of each atom in the obtained powder of NaZnPO_4

2.3. Luminescence properties of $\text{NaZnPO}_4:\text{Eu}^{2+}$

The steady state excitation and emission spectra were collected using a setup of devices designed by Horiba Jobin Yvon company. A Xenon lamp of 400 W was used as the light source (Figure 7) and two Jobin-Yvon/Horiba TRIAX 180 and TRIAX 550 monochromators were used for the selection of excitation and emission wavelengths. The emission of the sample is focalised on a bundle of fiber optics connected to triax 550 and detected using a CCD SYMPHONY detector of 1024x256 pixels cooled by liquid nitrogen. The excitation spectra were detected by a hamamatsu R928 photomultiplier. The emission signal of $\text{NaZnPO}_4:\text{Eu}^{2+}$ being too weak to be accurately measured at room temperature, the powder was cooled down to 77 K after being conditioned in sealed ultrapure quartz tube and immersed in liquid nitrogen. The excitation spectra were spectrally corrected using sodium salicylate.



Figure 7. Experimental set-up for steady-state luminescence measurements.

At 77 K, the compound emits in the blue spectral range. The corresponding excitation shows a broad spectrum from 270 to 450 nm containing three bands ascribable to the splitting of the lowest-lying $4f^65d^1(t_{2g})$ manifold as a result of the C_1 distortion of the octahedral Eu^{2+} site (Figure 8). The Stokes shift is $\approx 2000 \text{ cm}^{-1}$ and the excitation edge is estimated at 437 nm. We did not observe any extra luminescence ascribable to Eu^{3+} impurities.

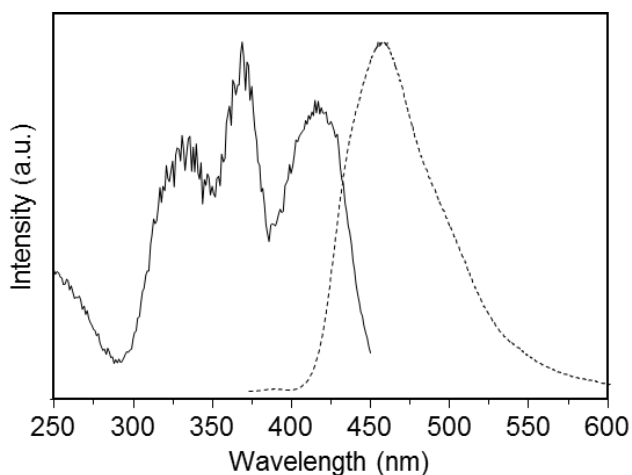


Figure 8. Photoluminescence excitation ($\lambda_{em} = 520 \text{ nm}$, solid line) and emission ($\lambda_{exc} = 370 \text{ nm}$, dotted line) spectra of $\text{NaZnPO}_4 \cdot \text{Eu}^{2+}$ at 77K

2.4. Calculation of the environmental factors in A^IB^{III}PO₄ lattices

As stated in Chapter 1, it is possible to connect $h\nu(X(i))$ and $F_c(X(i))$ respectively to the centroid energy $E_c(X(i))$ and the crystal field splitting $10Dq(X(i))$ for a given site $X(i)$ occupied by Eu^{2+} . We show in Figure 9 the energy levels of the Eu^{2+} as a free ion and when incorporated in a solid with cubic symmetry. If the position of centroid energy $E_c(X(i))$ and the magnitude of the crystal field splitting $10Dq(X(i))$ are known for the cation site $X(i)$, then the energy $E_{fd}(X(i))$ corresponding to the first allowed $4f^7 \rightarrow 4f^65d^1$ transition can be calculated using the following Equation:

$$E_{fd}(X(i)) = E_c(X(i)) + Dq(X(i)) \quad (2)$$

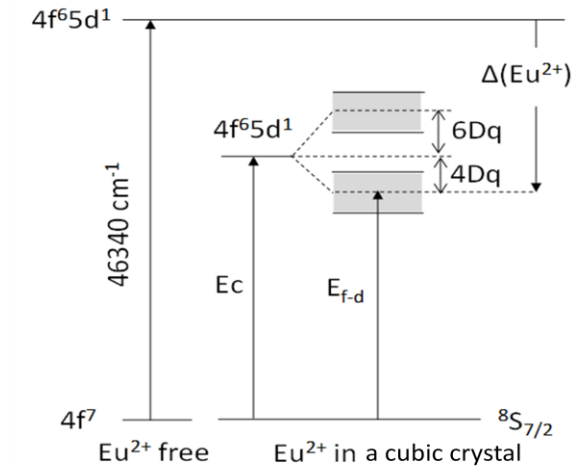


Figure 9. Energy levels of Eu^{2+} in a cubic crystal. E_c is the barycenter energy and E_{fd} represents the $4f^7 \rightarrow 4f^65d^1$ transition.

$E_c(X(i))$ and $Dq(X(i))$ can be obtained from the Equations (25) and (26) of Chapter one respectively, which can be written for the purpose of this work as:

$$E_c(X(i) \text{ cm}^{-1}) = e^{[-h\nu(X(i))]} \quad (3)$$

$$Dq(X(i) \text{ cm}^{-1}) = F_c(X(i)) \quad (4)$$

Knowing that Equations (3) and (4) have errors of $\pm 360 \text{ cm}^{-1}$ and $\pm 470 \text{ cm}^{-1}$ respectively, then we can estimate the error of Equation (2) at $\pm 550 \text{ cm}^{-1}$.

At this point, several concerns have to be taken into account:

- 1) First, Equation (3) was initially established for hosts with cubic symmetry⁽²⁰⁾. In the ABPO₄ family, most of the lattices do not have cubic symmetry, which raises a question of uncertainty of applying the Equation on these lattices.
- 2) Equation (4) was found for cubic halides⁽²¹⁾. This means that we should consider the influence of the type of anion. However, this influence was assumed to be very low if we compare for example, the crystal field splitting of Ce³⁺ in LiYF₄ and YPO₄⁽²²⁾ that are very close.
- 3) None of the ABPO₄ lattices are cubic, they present distortions in their polyhedra relative to the ideal octahedral, cubal, dodecahedral or cuboctahedral polyhedra. This will be figured out by using Equation (1). Further, the incorporation of Eu²⁺ induces even more distortions especially when substituted in smaller B^{II} sites^{(16),(23)}. This causes a stress for anions around the center resulting in changing the shape of the polyhedron. On the other hand, the substitution in the A^I sites demands charge compensation that may also affect the shape of the coordination polyhedron in an unknown manner.

The above arguments lead to conclude that the applicability of the model on ABPO₄:Eu²⁺ could result in large errors that basically need to be corrected by reformulating Equation (2). Unfortunately, this is in practice very difficult to maintain. We have therefore decided to apply the model on our compounds and tentatively estimate the importance of these errors. This is the reason why we have prepared NaZnPO₄:Eu²⁺ for which we are sure that Eu²⁺ is incorporated in the single Na⁺ Wyckoff position. Assuming that the octahedron is the geometry for which the CFS of Eu²⁺ is the strongest in the A^IB^{II}PO₄ lattices, we estimate that the difference between experimental and calculated excitation edges induced by the local site distortion in NaZnPO₄:Eu²⁺ should be representative of the largest committed error with respect to an equation in which we would have implemented a correction from non-cubic crystal fields.

The results of calculations of $he(X(i))$, $Fc(X(i))$ and $D.I.(X(i))$ are all compiled in Table 1. The calculations of $he(X(i))$ and $Fc(X(i))$ were carried out for each cation site X(i) that is considered as a possible doping site in a number of ABPO₄ lattices using Equations (9) and (10) of Chapter 1. Therefore, the four and five-coordinated sites were not included in the calculations because it is nearly impossible for these to act as accommodating sites for Eu²⁺ ions. Furthermore, such low-coordinated sites are not reproduced by Equation (2). In practice, this concerns the Mg²⁺ sites in CsMgPO₄ and α -KMgPO₄ (ICSD

72401), the Li^+ sites in LiCaPO_4 and LiSrPO_4 and all the Zn^{2+} , Be^{2+} and P^{5+} sites. The useful structural data were obtained from the ICSD database and treated using VESTA⁽²⁴⁾. For lattices that present more than one polymorph like for instance KZnPO_4 , the calculations were made for all the different structures found in the ICSD database. However, for the compounds reported in the literature and for which the crystal structure of the synthesized polymorph is known with certainty, the calculations were made only for the corresponding polymorph. For the lattices LiBaPO_4 , NaSrPO_4 and RbSrPO_4 that have been investigated from a luminescence viewpoint when doped with Eu^{2+} , the calculations could not be achieved because the structure is not available in the ICSD database. We also could not proceed for the calculations of KCaPO_4 (ICSD 27958) for which the available crystal data present errors and is not reliable (the PO_4 tetrahedron could not be observed with VESTA). In NaBaPO_4 (ICSD 15253), the structure has a cation site with wyckoff position 4i that has an occupancy of half Na^+ and half Ba^{2+} . Here, the charge of the cation ($\text{Na}^+, \text{Ba}^{2+}$) required for the calculations of the environmental factors, was taken as 1.5 ((charge of Na^+ + charge of Ba^{2+})/2). Lattices based on transition metals (Mn^{2+} , Fe^{2+} , Co^{2+} , Ni^{2+} and Cu^{2+}) were not considered in the present work.

Table 1 Structural characteristics and corresponding environmental factors for a selection of $\text{A}^{\text{I}}\text{B}^{\text{II}}\text{PO}_4$ lattices. N represents the coordination number of the considered cation site. D.I. is the distortion index of the cation polyhedron.

ABPO_4	ICSD	Space group	Cation site X(i)	N	Point group	D.I.% (X(i))	Fc(X(i))	he(X(i))
CsMgPO_4	260423	Pnma	Cs^+ (1)	11	Cs	4.8	0.18	1.28
LiMgPO_4	201138	Pnma	Li^+ (1)	6	Ci	1.4	0.36	0.74
			Mg^{2+} (1)	6	Cs	2.4	1.06	1.13
LiCaPO_4	66387	$\text{P3}_1\text{C}$	Ca^{2+} (1)	8	C1	6	0.60	1.28
LiSrPO_4	Ref. (25)	P6_5	Sr^{2+} (1)	8	C1	4.6	0.38	2.10
$\alpha\text{-NaMgPO}_4$	59249	$\text{P2}_1\text{2}_1\text{2}_1$	Na^+ (1)	8	C1	8.4	0.22	0.75
			Na^+ (2)	8	C1	9.2	0.21	0.58
			Na^+ (3)	8	C1	9	0.16	0.98
			Mg^{2+} (1)	6	C1	11.5	0.88	1.39
			Mg^{2+} (2)	6	C1	5.4	0.88	1.25
			Mg^{2+} (3)	6	C1	10.3	0.70	0.80
NaCaPO_4	35629	Pnma	Na^+ (1)	8	C1	7.4	0.21	0.84

			Na ⁺ (2)	7	C1	7.9	0.22	0.81
			Na ⁺ (3)	9	C1	6	0.15	0.71
			Ca ²⁺ (1)	8	C1	2.9	0.41	1.04
			Ca ²⁺ (2)	8	C1	3.9	0.61	1.06
			Ca ²⁺ (3)	8	C1	3.8	0.52	0.93
NaBaPO ₄	15253	C2/m	Na ⁺ (1)	6	C2h	0.6	0.18	0.98
			Ba ²⁺ (1)	12	C2h	7.6	0.10	0.74
			½Na ⁺ , ½Ba ²⁺	10	Cs	3.1	0.06	1.11
RbBaPO ₄	72001	Pnma	Rb ⁺ (1)	10	Cs	4.2	0.22	1.36
			Ba ²⁺ (1)	9	Cs	3.9	0.31	1.18
α-KMgPO ₄	50926	P2 ₁ /c	K ⁺ (1)	8	C1	5.1	0.11	0.82
			K ⁺ (2)	7	C1	7.8	0.13	0.80
KSrPO ₄	83598	Pnma	K ⁺ (1)	10	Cs	4.9	0.27	1.30
			Sr ²⁺ (1)	9	Cs	5.1	0.34	1.16
KBaPO ₄	202430	Pnma	K ⁺ (1)	10	Cs	4.9	0.17	1.17
			Ba ²⁺ (1)	9	Cs	3.6	0.36	1.34
LiCdPO ₄	71862	Pnma	Li ⁺ (1)	6	Cs	4.1	0.93	0.73
			Cd ²⁺ (1)	6	Ci	2.9	2.77	1.36
LiCdPO ₄	65050	Pna2 ₁	Li ⁺ (1)	6	C1 C1	4.2	0.32	0.77
			Cd ²⁺ (1)	6		3	0.87	1.39
NaCdPO ₄	6210	Pnma	Na ⁺ (1)	6	Ci	1.6	0.24	1.00
			Cd ²⁺ (1)	6	Cs	2.5	1.20	1.00
NaCdPO ₄	14048	Pna2 ₁	Na ⁺ (1)	6	C1	1.7	0.40	1.55
			Cd ²⁺ (1)	6	C1	2.5	0.73	1.40
NaBePO ₄	166581	P2 ₁ /n	Na ⁺ (1)	9	C1	3.6	0.11	0.46
			Na ⁺ (2)	6	C1	3.1	0.35	0.83
			Na ⁺ (3)	6	C1	5.2	0.34	0.86

KBePO ₄	202603	Pna2 ₁	K ⁺ (1)	11	C1	6	0.1	1.23
NH ₄ BePO ₄	92846	Pna2 ₁	NH ₄ ⁺ (1)	10	C1	5.6	1.96	0.93
AgBePO ₄	51083	P2 ₁ /n	Ag ⁺ (1)	9	C1	2.6	0.08	0.49
			Ag ⁺ (2)	6	C1	4.6	0.20	0.79
			Ag ⁺ (3)	6	C1	7.9	0.18	0.87
NaZnPO ₄	85557	P2 ₁ /n	Na ⁺ (1)	6	C1	9.6	0.27	3.11
β-KZnPO ₄	88955	Pna2 ₁	K ⁺ (1)	9	C1	8	0.06	0.67
γ-KZnPO ₄	88956	Pnma	K ⁺ (1)	7	Cs	7.2	0.20	2.77
α-KZnPO ₄	72401	P6 ₃	K ⁺ (1)	9	C1	8	0.11	0.73
			K ⁺ (2)	9	C1	11.4	0.12	0.66
			K ⁺ (3)	10	C1	9.8	0.11	0.57
			K ⁺ (4)	9	C3	6.1	0.15	1.28
			K ⁺ (5)	9	C3	6	0.10	0.67
			K ⁺ (6)	9	C3	1.9	0.08	0.64
NH ₄ ZnPO ₄	280954	P6 ₃	NH ₄ ⁺ (1)	8	C1	7.4	0.07	0.92
			NH ₄ ⁺ (2)	9	C3	5.9	0.05	0.75
NH ₄ ZnPO ₄	85444	P2 ₁	NH ₄ ⁺ (1)	7	C1	5.5	0.15	2.13
			NH ₄ ⁺ (2)	9	C1	4.5	0.09	0.96

We note that the D.I.(X(i)) values of all lattices barely exceed 10%. It comes that the 10% D.I. calculated for the Na⁺ sites of NaZnPO₄ is representative of the largest distortion among all the investigated ABPO₄ lattices.

2.5. Doping sites in $A^I B^{II} PO_4:Eu^{2+}$

We have compiled in Table 2 the experimental values of the energies E_{exp} corresponding to the photoluminescence excitation edge in the members $A^I B^{II} PO_4:Eu^{2+}$ whose optical properties have been already investigated in the literature or in the present work (i.e. $NaZnPO_4:Eu^{2+}$). For each cation site $X(i)$ that can potentially accommodate Eu^{2+} in the considered $A^I B^{II} PO_4$ lattice, we give the energy values $E_c(X(i))$, $Dq(X(i))$ and $E_{fd}(X(i))$ as calculated from Equations (2) - (4), using the environmental factors compiled in Table 1.

Table 2 Experimental and calculated spectroscopic properties of Eu^{2+} -doped $ABPO_4$ lattices.

Lattice (space group)	E_{exp} (cm^{-1})	$X(i)$	$E_c(X(i))$ (cm^{-1})	$Dq(X(i))$ (cm^{-1})	$E_{fd}(X(i))$ (cm^{-1})
$NaZnPO_4(P2_1/n)$	22880*	$Na^+(1)$	27190	1005	23170
$CsMgPO_4(Pnma)$	25315 ⁽¹⁷⁾ 21740 ⁽⁷⁾	$Cs^+(1)$	28737	611	26293
$LiMgPO_4(Pnma)$	25315 ⁽¹⁶⁾	$Li^+(1)$ $Mg^{2+}(1)$	31418 29241	1175 2489	26719 19286
$LiCaPO_4(P3_1c)$	22575 ⁽¹⁴⁾ 22440 ⁽¹²⁾	$Ca^{2+}(1)$	28737	1625	22237
$LiSrPO_4(P6_5)$	23750 ⁽¹³⁾ 23585 ⁽²⁵⁾	$Sr^{2+}(1)$	27492	1212	22643
$NaMgPO_4(P2_12_12_1)$	26525 ⁽¹⁸⁾	$Na^+(1)$ $Na^+(2)$ $Na^+(3)$ $Mg^{2+}(1)$ $Mg^{2+}(2)$ $Mg^{2+}(3)$	31340 32864 29902 28446 28827 30975	919 893 799 2151 2151 1829	27692 29292 26705 19843 20224 23723
β - $NaCaPO_4(Pnma)$	23310 ⁽¹⁴⁾	$Na^+(1)$	30705	895	27133

	24630 ⁽¹⁷⁾	Na ⁺ (2)	30905	919	27258
	23925 ⁽¹⁰⁾	Na ⁺ (3)	31657	788	28536
		Ca ²⁺ (1)	29616	1268	24362
		Ca ²⁺ (2)	29527	1644	22952
		Ca ²⁺ (3)	30166	1475	24266
NaBaPO ₄ (C2/m)	25445 ⁽¹⁴⁾	Na ⁺ (1)	29902	837	26555
	26670 ⁽²⁶⁾	Ba ²⁺ (1)	31417	687	28671
		½Na ⁺ , ½Ba ²⁺	29319	612	26873
RbBaPO ₄ (Pnma)	25905 ⁽¹⁷⁾	Rb ⁺ (1)	28520	1419	24872
		Ba ²⁺ (1)	29057	2526	24734
KMgPO ₄ (P2 ₁ /c)	27930 ⁽²³⁾	K ⁺ (1)	30837	705	28016
		K ⁺ (2)	30975	743	28003
KSrPO ₄ (Pnma)	26740 ⁽¹⁷⁾	K ⁺ (1)	28680	1006	24657
	25250 ⁽⁸⁾	Sr ²⁺ (1)	29129	1137	24580
	26315 ⁽²⁷⁾				
KBaPO ₄ (Pnma)	26740 ⁽¹⁷⁾	K ⁺ (1)	29093	818	25821
	25250 ⁽⁸⁾	Ba ²⁺ (1)	35082	3014	23626
	26110 ⁽²⁶⁾				
	25775 ⁽²⁷⁾				

* this work

The results show that for a number of sites, the experimental energy of the excitation edge matches that of the calculated E_{fd} with an error of $\pm 1000 \text{ cm}^{-1}$. However, in few cases the error is as large as $\pm 6682 \text{ cm}^{-1}$ like the case of $\text{Mg}^{2+}(1)$ in NaMgPO_4 . We also point out that for a given $\text{AB}^{\text{II}}\text{PO}_4\text{:Eu}^{2+}$ lattice, the experimental edge position is not defined with an accuracy better than $\pm 750 \text{ cm}^{-1}$ (e.g. KSrPO_4 and KBaPO_4), depending on the synthesis condition, Eu^{2+} concentration, temperature at which the spectra are collected, relevancy of the spectral corrections, etc...In $\beta\text{-NaCaPO}_4\text{:Eu}^{2+}$ or $\text{CsMgPO}_4\text{:Eu}^{2+}$, the accuracy is even worse ($>\pm 1000 \text{ cm}^{-1}$). As a matter of comparison, the energy difference between E_{exp} and $E_{fd}(\text{Na}(1))$ in $\text{NaZnPO}_4\text{:Eu}^{2+}$ is 290 cm^{-1} , which is much below the above uncertainties. In these

circumstances, we come to the conclusion that the refinement of Equation (2) to take into consideration a non-cubic CFS would, in fact, not lead to a significant improvement of the accuracy of our analysis.

We can see from Table 2 that the experimental energy may match only one value of E_{fd} corresponding to one cation site (e.g. in LiMgPO_4 , the E_{exp} being 25315 cm^{-1} , is in agreement with the calculated value 26719 cm^{-1} corresponding to site Li^+ but very far from that of site Mg^{2+} , 19286 cm^{-1}). In other lattices, the experimental data can match the calculated energy of more than one site like in KMgPO_4 for which both $\text{K}^+(1)$ and $\text{K}^+(2)$ sites (28016 and 28003 cm^{-1} respectively) are in agreement with E_{exp} (27930 cm^{-1}). This is interesting for the purpose of identifying the doping sites in each lattice. We will assume here that the sites for which the difference in absolute value between E_{fd} and E_{exp} is less than 1000 cm^{-1} can be identified as possible doping sites for Eu^{2+} .

To have a complete vision of the situation, we have plotted the scheme of Figure 10 showing the difference $E_{fd}(X(i)) - E_{exp}$ for each cation site in each lattice. For sake of clarity, only the average value of the different experimental excitation energies listed in Table 2 have been considered for each given $\text{A}^I\text{B}^II\text{PO}_4\text{-Eu}^{2+}$ lattice (when necessary), except for $\text{CsMgPO}_4\text{:Eu}^{2+}$. In this case, it is clear from Table 2 that the Cs^+ site cannot account for an excitation edge positioned as low as 21740 cm^{-1} . This suggests that the corresponding transition is not of f-d character but more probably of excitonic origin as argued in ref. (28) or is due to Eu^{2+} ions in close interaction with cation vacancies, as argued in ref. (7). Such kinds of interactions cannot reliably be reproduced with Equation (2). The two vertical dotted lines represent the error of $\pm 1000 \text{ cm}^{-1}$. This accuracy represents approximately the energy of one lattice phonon and is in first approximation acceptable. The cation sites contained inside these two lines are well reproduced by the model and therefore considered as possible doping sites for Eu^{2+} . This concerns the Ca^{2+} sites of NaCaPO_4 and LiCaPO_4 , the Na^+ sites of NaZnPO_4 , NaBaPO_4 and NaMgPO_4 (glaserite form), the K^+ sites of KMgPO_4 and KBaPO_4 , the Cs^+ site of CsMgPO_4 , both Li^+ and Sr^{2+} sites in LiSrPO_4 and both Rb^+ and Ba^{2+} sites of RbBaPO_4 . The Li^+ sites of LiMgPO_4 and the $\text{K}^+/\text{Sr}^{2+}$ sites of KSrPO_4 are also located very close to this interval. In KSrPO_4 , we note that the cation sites would be located within the $\pm 1000 \text{ cm}^{-1}$ interval by considering an experimental excitation edge of 25250 cm^{-1} for this lattice (see Table 2) instead of taking the average value of the available experimental data. The sites for which $E_{fd}(X(i)) > E_{exp}$ by more than 1000 cm^{-1} are related to higher lying excitation levels and are of lesser interest in the context of the present work. The sites for which $E_{fd}(X(i)) - E_{exp} < 1000 \text{ cm}^{-1}$ could not be considered as doping sites because they do not contribute to the experimental excitation band.

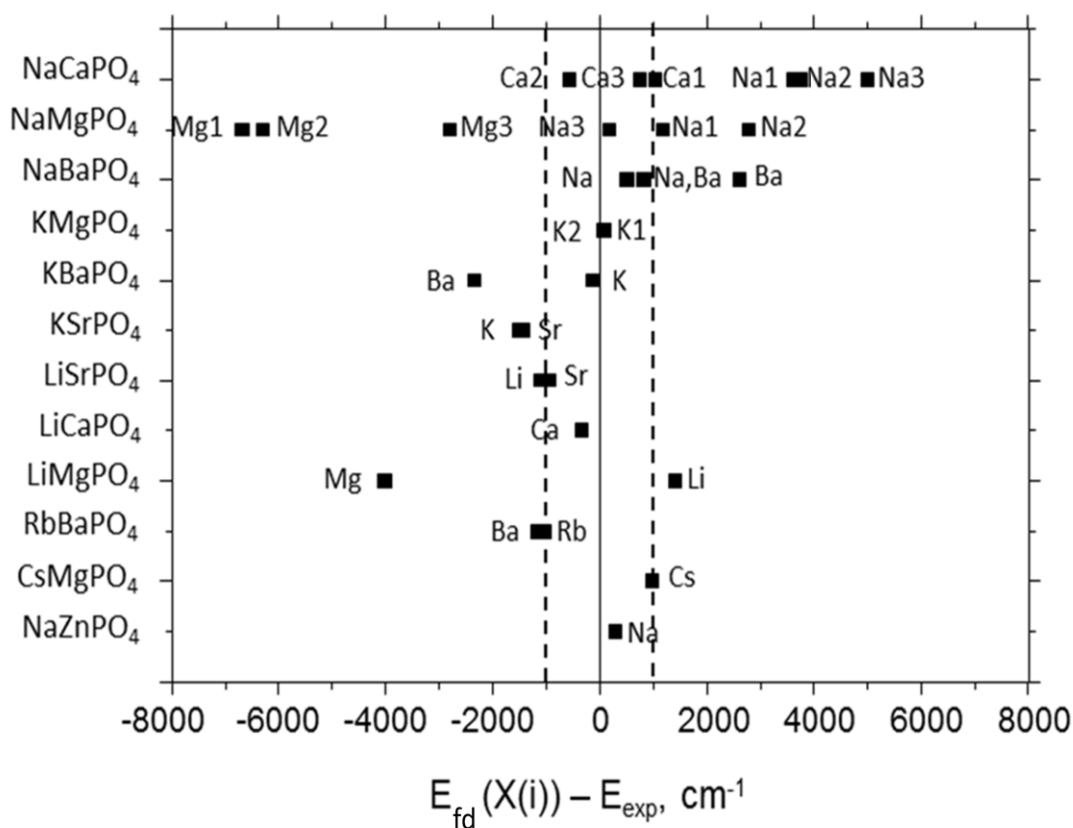


Figure 10 .Difference between calculated and experimental excitation edge energies for different cation sites $X(i)$ in $A^I B^{II} PO_4:Eu^{2+}$.

2.6. Designing $A^I B^{II} PO_4 - Eu^{2+}$ phosphors for solid state LED-based lighting

Using the EF model we have shown that it is possible to determine the nature of the doping sites in $A^I B^{II} PO_4$ lattices that contribute to the photoluminescence excitation edge of Eu^{2+} within an accuracy of $\pm 1000 \text{ cm}^{-1}$. The method will now tentatively be used to assist the design of $A^I B^{II} PO_4 - Eu^{2+}$ phosphors for an application in solid state LED-based lighting.

For this, we show in Figure 11 a plot of $he(X(i))$ versus $Fc(X(i))$. We can see that no correlation is found between the two factors. Knowing that $he(X(i))$ is related to centroid energy and that $Fc(X(i))$ is related to the crystal field splitting, then Figure 11 is in agreement with the well-admitted fact that the centroid energy and the crystal field splitting behave independently of each other⁽²⁹⁾. The three solid curves in this plot indicate the combinations of $(he(X(i)), Fc(X(i)))$ that give an excitation edge located at 400 nm (25000 cm^{-1}), 450 nm (22220 cm^{-1}) and 500 nm (20000 cm^{-1}) according to Equation (2). The dots

in this figure belong to the different cation sites $X(i)$ of the $ABPO_4$ lattices. Here, we have incorporated all the lattices listed in Table 1 including those that are not reported in the literature as doped with Eu^{2+} .

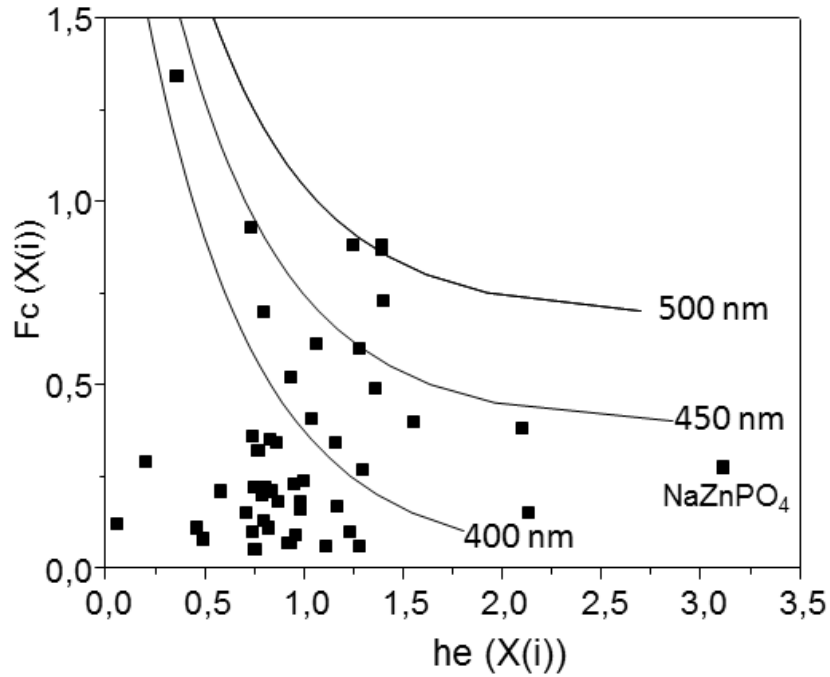


Figure 11. $F_c(X(i))$ vs $h_e(X(i))$ plot for the different cation sites in $A'B''PO_4$ lattices. The solid lines indicate the $(F_c(X(i)), h_e(X(i)))$ values corresponding to excitation edges located at 400, 450 and 500 nm in $A'B''PO_4:Eu^{2+}$.

We find that up to 14 cation sites potentially available for Eu^{2+} have a predicted excitation edge located in the 400 - 450 nm range. This means that the corresponding sites, if occupied by Eu^{2+} , have a chance to be excited using a LED source emitting in the 400 – 450 nm range. We note further that 3 cation sites are close to the 500 nm line. This is the case of the Cd^{2+} sites in $Pna2_1$ polymorphs of $LiCdPO_4$ and $NaCdPO_4$ and of the Mg^{2+} (2) sites in $NaMgPO_4$. In this connection, we point out that the excitation edge reported at 500 nm in ref. (11) for $NaMgPO_4:Eu^{2+}$ could be well explained by the incorporation of some amount of Eu^{2+} in the Mg^{2+} (2) sites.

In complement to Figure 11, we provide in Figure 12 an abacus allowing an easy estimation of the excitation edge wavelengths (λ_{edge}) that can be reached in $A'B''PO_4 - Eu^{2+}$ lattices for a selection of $(F_c(X(i)), h_e(X(i)))$ couples. The horizontal dotted lines in this graph mark the emission wavelength of three excitation sources emitting respectively at 375, 400 or 450 nm. This could, for instance, be LEDs. The intersection between the abacus and one given dotted line gives immediately the sets of $F_c(X(i))$ and

$he(X(i))$ values that characterizes the doping site $X(i)$ in $A^I B^II PO_4-Eu^{2+}$ for which the calculated excitation edge matches the emission of the considered LED and, therefore, is excited.

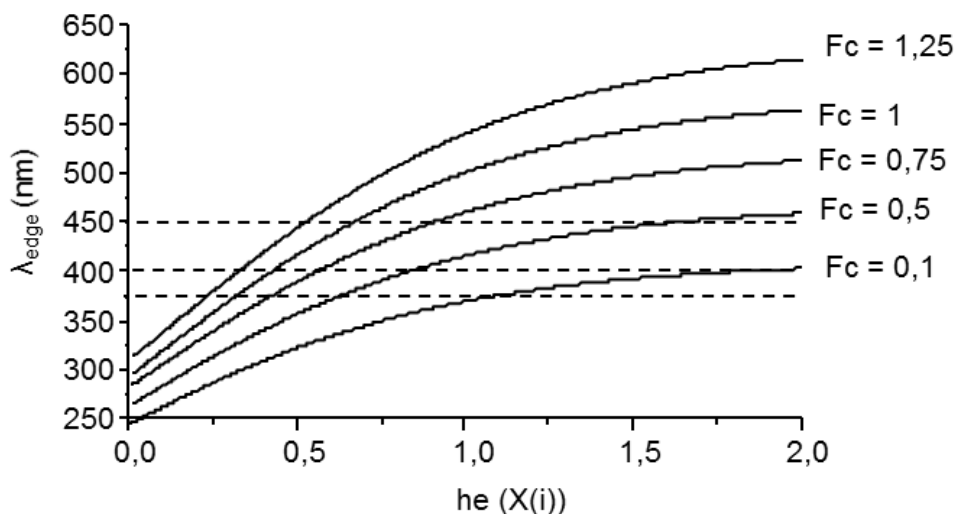


Figure 12. Calculated excitation edge wavelengths λ_{edge} for a selection of $(Fc(X(i)), he(X(i)))$ couples in $A^I B^II PO_4: Eu^{2+}$ lattices. The horizontal dotted lines mark the emission wavelength of a 375, 400 and 450 nm emitting LED. See text for further details.

At this stage we are able to predict the possible doping sites in any $ABPO_4:Eu^{2+}$ phosphate phosphor and study the possibility of these phosphates to be designed for LED lighting applications by predicting the location of the excitation edge.

We will now investigate the compounds of the $A^I B^II PO_4$ family that are not studied in the literature and for which the excitation edge is yet unknown. For discussion, we should take into account the overlap between the excitation edge of the $A^I B^II PO_4-Eu^{2+}$ phosphor and the emission spectral distribution of a given LED. Figure 13 shows the typical emission spectrum of a blue commercial LED (InGaN). The FWHM (full width at half maximum) indicates the range of energy in which the emission of the LED is efficient. The excitation edge of the phosphor should then overlap with the emission of the LED source inside this range to maintain the best luminescent outputs. This will be considered here in addition to the uncertainty of the prediction of the excitation edge by the EF model to propose the set of phosphors of the $ABPO_4$ family that are suitable for the design of LED lighting.

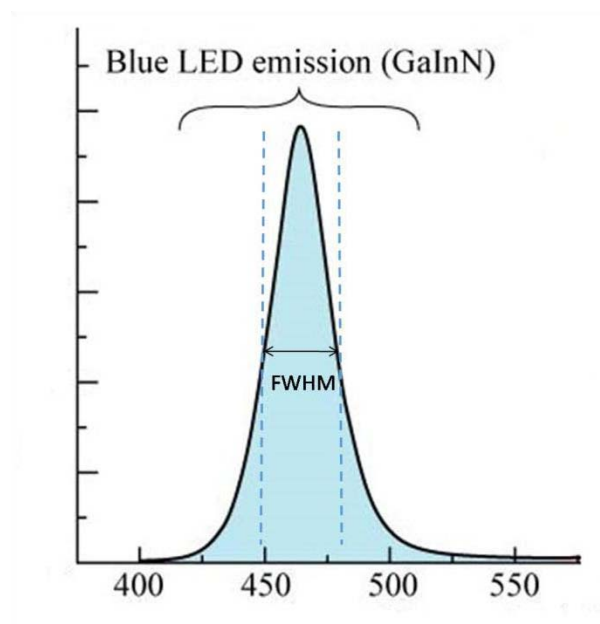


Figure 13. Emission spectrum of a blue LED.

Typically, the FWHM is about 10 nm for 375 nm (near UV) LED, 12 nm for 400 nm (violet) LED and 20 nm for 450 nm (blue) LED. These are average values that also depend on the current/power at which the LED is operated. The larger these values, the larger the FWHM. These three ranges are represented in Figure 14 by the grey columns for the 375 nm, 400 nm and 450 nm LED sources, in correspondence with the calculated excitation edges ($\pm 1000 \text{ cm}^{-1}$) represented in horizontal bars of all cation sites potentially available for Eu^{2+} in a selection 13 $\text{A}^{\text{I}}\text{B}^{\text{II}}\text{PO}_4$ lattices in which the luminescence properties have not yet been described in the literature. The overlaps between the grey zones in this graph indicate the nature of the Eu^{2+} doping sites in $\text{A}^{\text{I}}\text{B}^{\text{II}}\text{PO}_4$ that have the best chance to be excited using a blue, a violet or a Near-UV LED. Using a blue InGaN LED as excitation source, we find that only the $\text{Pna}2_1$ polymorph of $\text{NaCdPO}_4\text{-Eu}^{2+}$ and the Pnma polymorph of $\text{LiCdPO}_4\text{-Eu}^{2+}$ have realistic chance to be excited, while all the other compounds should be excitable using a 375 nm LED.

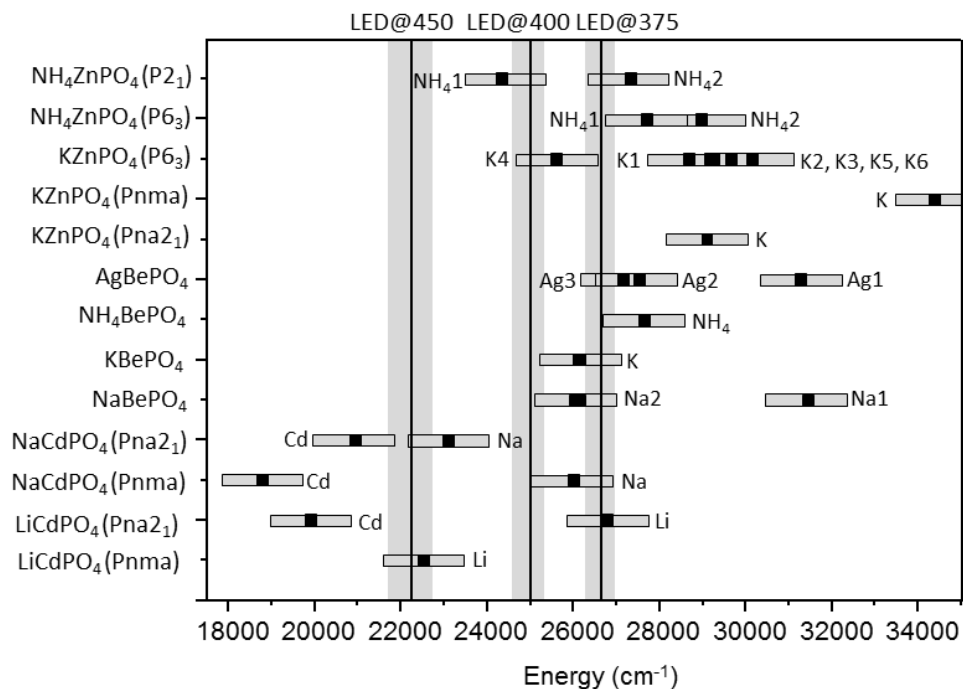


Figure 14. Calculated position of the excitation edge of different cation sites in $\text{A}^{\text{I}}\text{B}^{\text{II}}\text{PO}_4$ lattices. The horizontal bars mark the $\pm 1000 \text{ cm}^{-1}$ uncertainty on the values. The vertical bars mark the spectral output of blue, violet and near UV LEDs.

2.7. Conclusion

The nature of the doping sites $\text{X}(\text{i})$ that correspond to the photoluminescence excitation edge in Eu^{2+} -doped $\text{A}^{\text{I}}\text{B}^{\text{II}}\text{PO}_4$ lattices ($\text{A} = \text{Li}^+, \text{Na}^+, \text{K}^+, \text{Rb}^+, \text{Cs}^+, \text{Ag}^+, \text{NH}_4^+$; $\text{B} = \text{Be}^{2+}, \text{Mg}^{2+}, \text{Ca}^{2+}, \text{Sr}^{2+}, \text{Ba}^{2+}, \text{Cd}^{2+}, \text{Zn}^{2+}$) is determined from the knowledge of two-crystal structure-related environmental factors $\text{he}(\text{X}(\text{i}))$ and $\text{Fc}(\text{X}(\text{i}))$ and by the application of empirical equations allowing the calculation of excitation edge energies. With an accuracy of $\pm 1000 \text{ cm}^{-1}$, the method appears to be usable as a predictive tool for the design of $\text{A}^{\text{I}}\text{B}^{\text{II}}\text{PO}_4$ - Eu^{2+} phosphors. It has however to be mentioned that our method does not give information on the Stokes shift and related emitted color and quantum efficiency of the phosphors. These issues require further developments.

Bibliography

1. J. Chena, Y. Zhaob, Z. Mao, D. Wang and L. Bie. *CaAlSiN₃:Eu²⁺-based color-converting coating application for white LEDs: Reduction of blue-light harm and enhancement of CRI value*. 2017, Materials Research Bulletin, Vol. 90, pp. 212-217.
2. C. Guoa, Y. Xu, X. Ding, M. Li, J. Yu, Z. Ren and J. Bai. *Blue-emitting phosphor M₂B₅O₉Cl: Eu²⁺ (M Sr, Ca) for white LEDs*. 2011, Journal of Alloys and Compounds, Vol. 509, pp. 38-41.
3. J. Wan, Q. Liu, G. Liu, Z. Zhou, J. Ni and R.J. Xie. *A novel Eu²⁺ activated G-La₂Si₂O₇ phosphor for white LEDs: SiC-reduction synthesis, tunable luminescence and good thermal stability*. 2017, Journal of Materials Chemistry C, Vol. 5, pp. 1614-1623.
4. K.Y. Yeh, C.C. Yang, W.R. Liu and M.G. Brik. *Novel blue-emitting phosphors - BaBeSiO₄:Eu²⁺*. 2015, Optical Materials Express, Vol. 6, p. 418.
5. X. Song, R. Fu, S. Agathopoulos, H. He, X. Zhao and R. Li. *Luminescence and Energy-Transfer Mechanism in SrSi₂O₂N₂: Ce³⁺, Eu²⁺ Phosphors for White LEDs*. 2010, Journal of The Electrochemical Society, Vol. 157, pp. J34-J38.
6. J.S. Kim, K.T. Lim, Y.S. Jeong, I.C. Choi and H.L. Park. *Full-color Ba₃MgSi₂O₈:Eu²⁺, Mn²⁺ phosphors for white-light-emitting diodes*. 2005, Solid State Communications, Vol. 135, pp. 21-24.
7. B. Ma, Z. Huang, M. Fang, Y. Liu, X. Wu. *Structural and luminescence properties of red-emitting Cs_{1-x}MgPO₄:xEu²⁺ phosphors for near-UV-pumped light emitting diodes*. 2015, Royal Society of Chemistry Advances, Vol. 5, pp. 9933-9938.
8. C.C. Lin, Z.R. Xiao, G.Y. Guo, T.S. Chan and R.S. Liu. *Versatile Phosphate Phosphors ABPO₄ in White Light-Emitting Diodes: Collocated Characteristics Analysis and Theoretical Calculations*. 2010, Journal of American Chemical Society, Vol. 132, pp. 3020-3028.
9. Z. Yang, G. Yang, S. Wang, J.T. ian, X.L.Q. Guo and G. Fu. *A novel green-emitting phosphor NaCaPO₄:Eu²⁺ for white LEDs*. 2008, Materials Letters, Vol. 62, pp. 1884-1886.
10. C. Qin, Y. Huang, L. Shi, G. Chen, X. Qiao and H.J. Seo. *Thermal stability of luminescence of NaCaPO₄: Eu²⁺ phosphor for white-light-emitting diodes*. 2009, Journal of Physics D: Applied Physics, Vol. 42, p. 185105.
11. S.W. Kim, T. Hasegawa, T. Ishigaki, K. Uematsu, K. Toda. *Efficient Red Emission of Blue-Light Excitable New Structure Type NaMgPO₄:Eu²⁺ Phosphor*. 2013, ECS Solid State Letters, Vol. 2, pp. R49-R51.
12. X. Zhang, F. Mo, L. Zhou, M. Gong. *Properties–structure relationship research on LiCaPO₄:Eu²⁺ as blue phosphor for NUV LED application*. 2013, Journal of Alloys and Compounds, Vol. 575, p. 314.

13. **Z.C. Wu, J.X. Shi, J. Wang, M.L. Gong and Q. Su.** *A novel blue-emitting phosphor $\text{LiSrPO}_4\text{:Eu}^{2+}$ for white LEDs.* 2006, Journal of Solid State Chemistry, Vol. 179, pp. 2356–2360.
14. **J. Mc Kittrick, M.E. Hannah, A. Piquette, J.K. Han, J.I. Choi, M. Anc, M. Galvez, H. Lugauer, J. B. Talbot and K. C. Mishra.** *Phosphor Selection Considerations for Near-UV LED Solid State Lighting.* 2013, ECS Journal of Solid State Science and Technology, Vol. 2, pp. R3119-R3131.
15. **D.K. Yim, H.J. Song, In-Sun Cho, J.A. Kim and K.S. Hong.** *A novel blue-emitting phosphor for near UV based white light-emitting-diodes.* 2011, Materials Letters, Vol. 65, pp. 1666-1668.
16. **S. Zhang, Y. Huang, L. Shi and H.J. Seo.** *The Luminescence characterization and structure of Eu^{2+} doped LiMgPO_4 .* 2010, Journal of Physics Condensed Matter, Vol. 22, p. 235402.
17. **C. Zhao, Z. Xia and M. Li.** *Eu^{2+} -activated full color orthophosphate phosphors for warm white light-emitting diodes.* 2014, RSC Advances, Vol. 4, pp. 33114-33119.
18. **W. Tang, Y. Zheng.** *Synthesis and luminescence properties of a novel blue emitting phosphor $\text{NaMgPO}_4\text{:Eu}^{2+}$.* 2010, Luminescence, Vol. 25, pp. 364-366.
19. **W.H. Baur.** *The geometry of polyhedral distortions , Predictive relationships for the phosphate group.* 1973, Acta Crystallographica Section B, Structural Science, Crystal Engineering and Materials, Vol. 30, pp. 1195-1215.
20. **S.Y. Zhang and J.S. Shi.** *Barycenter of Energy of Lanthanide $4f^{N-1}5d$ Configuration in Inorganic Crystals.* 2004, Journal of Physica Chemistry B, Vol. 108, pp. 18845-18849.
21. **J.S. Shi, Z.J. Wu, S.H. Zhou, S.Y. Zhang.** *Dependence of crystal field splitting of 5d levels on hosts in the halide crystals.* 2003, Chemical Physics Letters, Vol. 380, pp. 245-250.
22. **P. Dorenbos.** *Energy of the first $4f^7, 4f^65d$ transition of Eu^{2+} in inorganic compounds.* 2003, Journal of Luminescence , Vol. 104, pp. 239-260.
23. **S. Zhang, Y. Huang and H.J. Seo.** *Luminescence properties and structure of Eu^{2+} doped KMgPO_4 phosphor.* 2010, Optical Materials, Vol. 32, pp. 1545-1548.
24. **K. Momma and F. Izumi.** *VESTA: a three-dimensional visualization system for electronic and structural analysis.* 2008, Journal of Applied Crystallography, Vol. 41, pp. 653-658.
25. **C.C. Lin, C.C. Shen and R.S. Liu.** *Spiral-Type Heteropolyhedral Coordination Network Based on Single-Crystal LiSrPO_4 : Implications for Luminescent Materials.* 2013, Chemistry A European Journal, Vol. 19, pp. 19358-15365.
26. **T. Wanjun and C. Donghua.** *Photoluminescent Properties of $\text{ABaPO}_4\text{:Eu}$ ($\text{A}=\text{Na}, \text{K}$) Phosphors Prepared by the Combustion-Assisted Synthesis Method.* 2009, Journal of the American Ceramic Society, Vol. 92, pp. 1059-1061.

27. **S.H.M. Poort, W. Janssen and G. Blasse.** *Optical properties of Eu^{2+} -activated orthosilicates and orthophosphates.* 1997, Journal of Alloys and Compounds, Vol. 260, pp. 93-97.
28. **Y. Huang and H.J. Seo.** *Luminescence of Eu^{2+} Ions in CsMgPO_4 Phosphor: Anomalous Emission and its Origin.* 2011, Journal of Electrochemical society, Vol. 158, pp. J260-J263.
29. **P. Dorenbos.** *5d-level energies of Ce^{3+} and the crystalline environment. IV. Aluminates and "simple" oxides.* 2002, Journal of Luminescence, Vol. 99, pp. 283-299.

Chapter 3: The origin of luminescence in Bi^{3+} -doped closed transition metal oxides

3.1. Introduction

The luminescence of Bi^{3+} has gained a great attention during the last years owing to its broad and intense band emission in the UV and visible region⁽¹⁾⁻⁽³⁾. Bi^{3+} is especially reported as a good sensitizer for trivalent lanthanides especially Eu^{3+} , enhancing its red emission in a number of compounds like for instance, $\text{CaMoO}_4:\text{Eu}^{3+}:\text{Bi}^{3+}$ ⁽⁴⁾ and $\text{Y}_4\text{MgSi}_3\text{O}_{13}:\text{Bi}^{3+}:\text{Eu}^{3+}$ ⁽⁵⁾. A number of transition metal oxides containing transition metal ions M^{n+} with d^0 electron configuration (e.g. CaTiO_3 ⁽³⁾, YNbO_4 ⁽⁶⁾, YVO_4 ⁽⁷⁾,...) doped with Bi^{3+} has recently been the subject of extensive work. As stated in Chapter 1, the self luminescence in these undoped materials gives rise to emission in the UV or visible region resulting from a ligand-to-metal charge transfer. The incorporation of Bi^{3+} in these complex oxides induces new emission and excitation features that are generally red-shifted with respect to the optical signals of the undoped host lattices. These new features are ascribed either to a metal-to-metal charge transfer from Bi^{3+} to a nearby M^{n+} (and then recognized as D band), are associated to the formation of Bi^{3+} clusters or are simply attributed to regular A transitions (i.e. internal $^1\text{S}_0 \rightarrow ^3\text{P}_{0,1}$ transitions of isolated Bi^{3+} ion). It appears therefore that the origin of the luminescence in these compounds is not yet totally fixed and is still subject of controversy.

In this chapter, a number of Bi^{3+} -doped transition metal oxides will be investigated. The EF model as well as the MMCT model will be used to discuss the origin of luminescence in these materials and help predicting the locations of the A and D states at the light of the three possible configurations introduced in Chapter 1 (Figure 16). Calculations of the A band transition excitation energy, E_A , will be carried out using the EF model. The MMCT model will be used to calculate MMCT energies ($\text{Bi}^{3+}-\text{M}^{n+}$). Analysis of the results will be made by comparing the calculated energies to the experimental data collected from the literature and from the present work. For this purpose, the following compounds doped with Bi^{3+} will be prepared: GdVO_4 , LaVO_4 , CaMoO_4 , LiNbO_3 , NaNbO_3 , ANbO_4 ($A=\text{Y, Gd, La}$), CaNb_2O_6 , $\text{M}'\text{YTao}_4$, $\text{LiNbO}_3-\text{Bi}^{3+}$ and $\text{NaNbO}_3-\text{Bi}^{3+}$. In addition, the Stokes shift will be used to introduce a criterion from which the origin of the luminescence signals in these materials can be ascribed.

The two models will also be used to study the yellow emission of $\text{YVO}_4\text{:Bi}^{3+}$ as a special case. This compound has only one accommodating site available for Bi^{3+} which makes it a good example to study the Bi^{3+} luminescent properties. It is known for long to glow brightly in the yellow region with an emission band peaking at 570 nm in correspondence with a Stokes shift of $\approx 11500 \text{ cm}^{-1}$. The corresponding internal quantum efficiency has recently been measured at 0.93 ⁽⁷⁾. This interesting optical behaviour makes this compound a possible rare-earth free candidate for replacing the Ce^{3+} in the YAG yellow phosphor in LED lighting. Despite this attractive luminescent action, not much is known on the exact nature of the emitting state (A or D) in this phosphor. In the present work, we will use the action of high pressure (up to 20 GPa) to get better insight in the nature of this emitting state expecting that pressure could lift in some way the degeneracy of the involved A and D levels. In other luminescent materials, the effect of pressure was found to be very important in altering the energy level locations and the degree of the different couplings which led to important change in the optical behaviour like in the case of $\text{CaWO}_4\text{:Pr}^{3+}$ and $\text{CaMoO}_4\text{:Pr}^{3+}$ ^{(8),(9)}. However, the effect of pressure on the luminescence of $\text{YVO}_4\text{:Bi}^{3+}$ has not been investigated so far. This part of the work will be carried out through collaboration with Dr Sebastian Mahlik from the Institute of Experimental Physics of the University of Gdańsk, Poland.

3.2. Synthesis and photoluminescence of closed transition metal oxides doped with Bi^{3+}

Several transition metal oxides doped with Bi^{3+} were prepared in the context of this work. The raw chemicals and experimental conditions (temperature/duration) used for the syntheses are given in Table 1. The nominal doping rate was 5 mol %. This content was chosen not too high to limit the formation of Bi-related dimers and not too low to insure incorporation of Bi^{3+} within the host lattices in spite of the evaporation of Bi_2O_3 at high temperature. The thermal treatments were carried out in air to limit the possible formation of Bi^{2+} centers, whose luminescence signatures could interfere with the emission and excitation spectra of Bi^{3+} , thus making the spectral analysis possibly difficult. All the compounds were checked by X-ray diffraction and were concluded to be single phased.

Table 1 Raw materials and experimental conditions used for the synthesis of several closed-shell transition metal oxides doped with Bi³⁺.

Host lattice	Raw chemicals (analytical grade)	Temperature (°C) / duration (h)	JCPDS standard
GdVO ₄	Gd ₂ O ₃ , V ₂ O ₅	650 / 6	17-0260
LaVO ₄	La(OH) ₃ , V ₂ O ₅	1100 / 24	23-0324
CaMoO ₄	CaCO ₃ , Mo ₂ O ₃	780 / 3	29-0351
LiNbO ₃	Li ₂ CO ₃ , Nb ₂ O ₅	1200 / 4	20-631
NaNbO ₃	Na ₂ CO ₃ , Nb ₂ O ₅	1200 / 4	33-1270
YNbO ₄	Y ₂ O ₃ , Nb ₂ O ₅	1200 / 4	23-1486
GdNbO ₄	Gd ₂ O ₃ , Nb ₂ O ₅	1200 / 4	22-1104
LaNbO ₄	La(OH) ₃ , Nb ₂ O ₅	1200 / 4	22-1125
CaNb ₂ O ₆	CaCO ₃ , Nb ₂ O ₅	1200 / 4	39-1392
M'-YTao ₄	Y ₂ O ₃ , Ta ₂ O ₅	1200 / 12	72-2018

The photoluminescence emission and excitation spectra were collected at 300 K using the same set-up as in Chapter 2. We show in Figure 1 the photoluminescence spectra of the Bi³⁺-doped lattices listed in Table 1. As anticipated, we find no trace of Bi²⁺ ions in the luminescence spectra. This specie, when present, should show narrow band-like emission from the reddish-orange to the NIR region ^{(10),(11)} in correspondence with excitation signals in the UV (²P_{1/2} → ²S_{1/2} transition) and in the visible (²P_{1/2} → ²P_{3/2} transition). Due to the action of the crystal field, the ³P_{3/2} level is splitted into two components, which gives rise, in fact, to two transitions, the highest-lying band being located usually in the violet-blue region and the lowest-lying one beyond 500 nm. These characteristic signals are absent from our spectral data. Further, as already demonstrated by Peng et. al ⁽¹²⁾, Bi²⁺ is preferably stabilized in Sr²⁺ or Ba²⁺ sites, which are not present in our selection of compounds. The Bi³⁺-doped vanadates, the molybdate CaMoO₄-Bi³⁺ and the two niobates LiNbO₃-Bi³⁺ and NaNbO₃-Bi³⁺ emit in the yellow region, like CaTiO₃-Bi³⁺ ⁽³⁾ or YVO₄-Bi³⁺ ⁽⁷⁾. In contrast, the other niobates and the tantalate glow in the blue region. The emission of M'-YTao₄-Bi³⁺ was ascribed to regular A-like transition on the basis of the data reported in 1970 by Blasse and Brill (excitation at 290 nm and emission at 430 nm) ⁽¹³⁾. This assignment will be revised at the light of the spectra displayed in Figure 1. All the materials show luminescence that differ from that of the undoped lattices. Dealing for instance with LiNbO₃-Bi³⁺ and NaNbO₃-Bi³⁺, we know that at low temperature, LiNbO₃ has an emission at 440 nm with a corresponding excitation peaking at 260 nm while NaNbO₃ shows two emission bands at 480 and 540 nm correlated with excitation maxima at 300 and 320 nm, respectively ⁽¹⁴⁾.

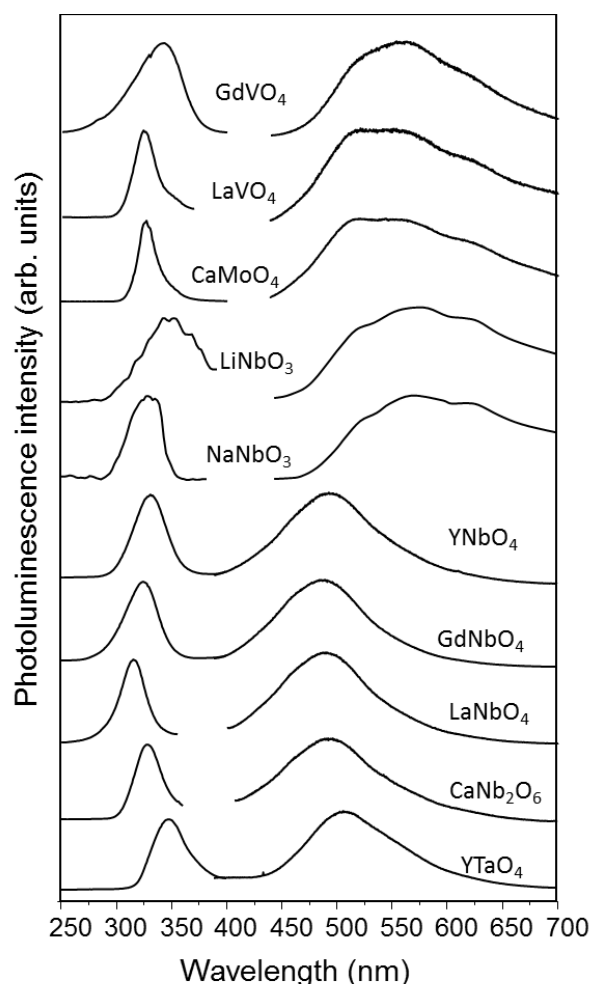


Figure 1. Photoluminescence excitation (left) and emission (right) spectra of some closed-shell transition metal oxides doped with Bi^{3+} .

3.3. Calculations of MMCT and E_A energies in Bi^{3+} -doped transition metal oxides

In this part, the obtained results of our calculations of the energies of the A and D bands using the empirical models EF and MMCT will be compared to the experimental data which helps assigning the origin of emission in the investigated compounds. The experimental data represent the energy of the maximum of the lowest-lying excitation band in the excitation spectrum. These features are supposed to be related to Bi^{3+} . They are collected from the literature and from the present work and denoted by E_{exp} .

The energies $E_A(X(i))$ are calculated from Equation (27) of Chapter 1 for each cation site $X(i)$ of the host lattice. The MMCT energies are calculated using Equation (30) of Chapter 1. The results of

calculations for 19 lattices are compiled in Table 2. The values of the calculated environmental factor $he(X(i))$ for each cation site $X(i)$ in each host lattice, the values of the electronegativity $\chi_{CN'}(M^{n+})$ and the shortest $Bi^{3+}-M^{n+}$ interatomic distances corrected for the doping effect d_{corr} are also given in this Table 2. The necessary values of $\chi_{CN}(Bi^{3+})$ can be found in Tables 9 and 10 of Chapter 1. Some lattices may contain different nature of M^{n+} cations, for instance $Ti^{4+}(3d^0)$ and $Y^{3+}(4d^0)$ in $Y_2Ti_2O_7$, raising therefore two possible charge transfer transitions: $Bi^{3+}-Y^{3+} \rightarrow Bi^{4+}-Y^{2+}$ and $Bi^{3+}-Ti^{4+} \rightarrow Bi^{4+}-Ti^{3+}$. In this situation, calculations are made for both $Bi^{3+} \rightarrow Ti^{4+}$ and $Bi^{3+} \rightarrow Y^{3+}$ charge transfer transitions and the considered metal cation is specified in the third column of the table. The factor $he(X(i))$ is calculated only for cation sites that can reasonably be considered as doping sites for Bi^{3+} . In practice, this excludes all the M^{n+} sites like Ti^{4+} , Sn^{4+} , Zr^{4+} , V^{5+} , Nb^{5+} , Ta^{5+} , Mo^{6+} and W^{6+} . Lattices presenting more than a single excitation signal are individuated by letters (a), (b), etc...in correspondence with the considered signal. In the case of $PbWO_4-Bi^{3+}$, only the lowest-lying emission at 563 nm identified recently as an excitonic (or MMCT)-like transition⁽¹⁵⁾, has been compiled in Table 2.

Table 2 Results of the calculations of E_A and MMCT energies. X is the doping site for Bi^{3+} in coordination CN. * this work

Host lattice (ICSD)	X (CN)	M^{n+} (CN')	d_{corr} (Å)	$he(X(i))$	$\chi_{CN'}(M^{n+})$	$E_{exp}(Bi^{3+}, cm^{-1})$	Stokes shift (cm^{-1})	$E_A(X(i), cm^{-1})$	MMCT (Bi^{3+}, cm^{-1})
$CaTiO_3$ (96258)	Ca^{2+} (8+4)	Ti^{4+} (6)	3.19	1.31	1.73	27000 ⁽¹⁶⁾	9140 ⁽¹⁶⁾	28620	30320
$Y_2Ti_2O_7$ (83593)	Y^{3+} (8)	Ti^{4+} (6) Y^{3+} (8)	3.64 3.64	1.00	1.73 1.29	31130 ⁽¹⁷⁾	12660 ⁽¹⁷⁾	32120	33375 38875
$CaSnO_3$ (193658)	Ca^{2+} (8+4)	Sn^{4+} (6)	3.23	1.20	1.71	32825 ⁽¹⁸⁾	10725 ⁽¹⁸⁾	29590	30970
$Y_2Sn_2O_7$ (a) $Y_2Sn_2O_7$ (b) (160115)	Y^{3+} (8)	Sn^{4+} (6) Y^{3+} (8)	3.73 3.73	0.99	1.71 1.29	35730 (a) ⁽¹⁹⁾ 34860 (b) ⁽¹⁹⁾	5600 (a) ⁽¹⁹⁾ 14000 (b) ⁽¹⁹⁾	32270	34140 39265
$CaZrO_3$ (37264)	Ca^{2+} (8+4)	Zr^{4+} (6)	3.30	1.19	1.61	32245 ⁽¹⁸⁾	6690 ⁽¹⁸⁾	29730	32800
$La_2Zr_2O_7$ (a) $La_2Zr_2O_7$ (b) (22229)	La^{3+} (8)	Zr^{4+} (6) La^{3+} (8)	4.68 4.68	1.12	1.61 1.28	34840 (a) ⁽²⁰⁾ 40800 (b) ⁽²⁰⁾	8900 ⁽²⁰⁾ 21370 ⁽²⁰⁾	30525	39350 42555
$LiNbO_3$ (84578)	Li^+ (6)	Nb^{5+} (6)	3.21	0.75	1.86	28985*	11285*	36800	28635
$NaNbO_3$ (262895)	$Na1^+$ (6) $Na2^+$ (6)	Nb^{5+} (6)	3.38 3.28	0.59 0.69	1.86	30490*	12950*	38280 41125	29200
$CaNb_2O_6$ (15208)	Ca^{2+} (8)	Nb^{5+} (6)	3.47	1.08	1.86	30770*	10360*	30980	30610
$YNbO_4$ (a) $YNbO_4$ (b) $YNbO_4$ (c)	Y^{3+} (8)	Nb^{5+} (6)	3.61	1.04	1.86 1.29	32300 (a) ⁽²¹⁾ 31850 (b) ⁽²²⁾ 30800 (c)*	10800 (a) ⁽²¹⁾ 9330 (b) ⁽²²⁾	31530	31555

(100176)		Y ³⁺ (8)	3.83				9920(c) [*]		39675
GdNbO ₄ (20421)	Y ³⁺ (8)	Nb ⁵⁺ (6)	3.62	1.10	1.86	31000 [*]	9700 [*]	30780	31620
LaNbO ₄ (73390)	La ³⁺ (8)	Nb ⁵⁺ (6) La ³⁺ (8)	3.61 3.93	1.19	1.86 1.28	31700 [*]	11255 [*]	29660	32000 40180
YTaO ₄ (a) (38420)	Y ³⁺ (8)	Ta ⁵⁺ (6) Y ³⁺ (8)	3.55 4.02	1.06	1.92 1.29	29150 [*]	9730 [*]	31290	30390 40400
ScVO ₄ (78073)	Sc ³⁺ (8)	V ⁵⁺ (4) Sc ³⁺ (8)	3.00 3.87	0.95	2.46 1.35	27780 ⁽²³⁾	12030 ⁽²³⁾	32800	27360 39130
YVO ₄ (78074)	Y ³⁺ (8)	V ⁵⁺ (4) Y ³⁺ (8)	3.21 3.96	1.13	2.46 1.29	29000 ⁽⁷⁾	11450 ⁽⁷⁾	30395	30149 40180
GdVO ₄ (81703)	Gd ³⁺ (8)	V ⁵⁺ (4)	3.22	1.15	2.46	30500 [*]	11600 [*]	30198	30273
LaVO ₄ (8294)	La ³⁺ (9)	V ⁵⁺ (4) La ³⁺ (9)	3.33 4.19	1.64	2.46 1.26	30860 [*]	12340 [*]	27950	31585 41100
CaMoO ₄ (62219)	Ca ²⁺ (8)	Mo ⁶⁺ (4)	3.69	0.92	2.50	30900 [*]	12280 [*]	33365	34960
Y ₂ WO ₆ (20955)	Y ³⁺ (8)	W ⁶⁺ (4) Y ³⁺ (8)	3.34 3.70	1.29	2.59 1.29	29000 ⁽²¹⁾	10000 ⁽²¹⁾	28735	29675 39135
PbWO ₄ (56110)	Pb ²⁺ (8)	W ⁶⁺ (4)	3.79	0.96	2.59	32260 ⁽¹⁵⁾	14515 ⁽¹⁵⁾	32735	34465

The results indicate that both models account for the experimental data within an accuracy of $\approx \pm 4000 \text{ cm}^{-1}$, except for $\text{LiNbO}_3\text{-Bi}^{3+}$, $\text{NaNbO}_3\text{-Bi}^{3+}$ and $\text{La}_2\text{Zr}_2\text{O}_7\text{-Bi}^{3+}$ (b), which are much better reproduced by the MMCT model. It is worth noting that part of the inaccuracy of the methods is due to fluctuating values of experimental positions of the excitation bands as exemplified in Table 2 for $\text{YNbO}_4\text{-Bi}^{3+}$. In this particular case, the 3 input values (a-c) were kept to evaluate the impact of this fluctuation on the spectral assignment. Concerning $\text{YTaO}_4\text{-Bi}^{3+}$, we note that the calculated data match better the $E_{\text{exp}}(\text{Bi}^{3+}, \text{cm}^{-1})$ value given in Table 2 than the value (34500 cm^{-1}) reported by Blasse⁽²¹⁾. In this case, the error is so large ($> 5000 \text{ cm}^{-1}$) that the determination of the optical character of the involved transition cannot be achieved. It comes from this analysis that it is difficult to determine with certainty the origin of the luminescence in such compounds. To overcome this difficulty, we have investigated the Stokes shifts associated with the emissions. In the archival literature, the Stokes shift is sometimes used as a criterion to assign the origin of the emission in Bi^{3+} -activated systems, the larger values being generally ascribed to D-related signals or Bi-related clusters⁽²¹⁾. Note that the question of Bi^{3+} clusters is not considered in the present chapter.

3.4. Assigning the origin of luminescence in closed shell metallic oxides doped with Bi^{3+} with the help of Stokes shift values

Figure 2 shows the difference, in absolute scale, between experimental and calculated energies of E_A and MMCT given as $|E_{\text{exp}}(\text{Bi}^{3+}) - E_A(X)|$ and $|E_{\text{exp}}(\text{Bi}^{3+}) - \text{MMCT}(\text{Bi}^{3+})|$ for each investigated compound. The compounds in this figure are ordered along with increasing values of the Stokes shifts of their emission.

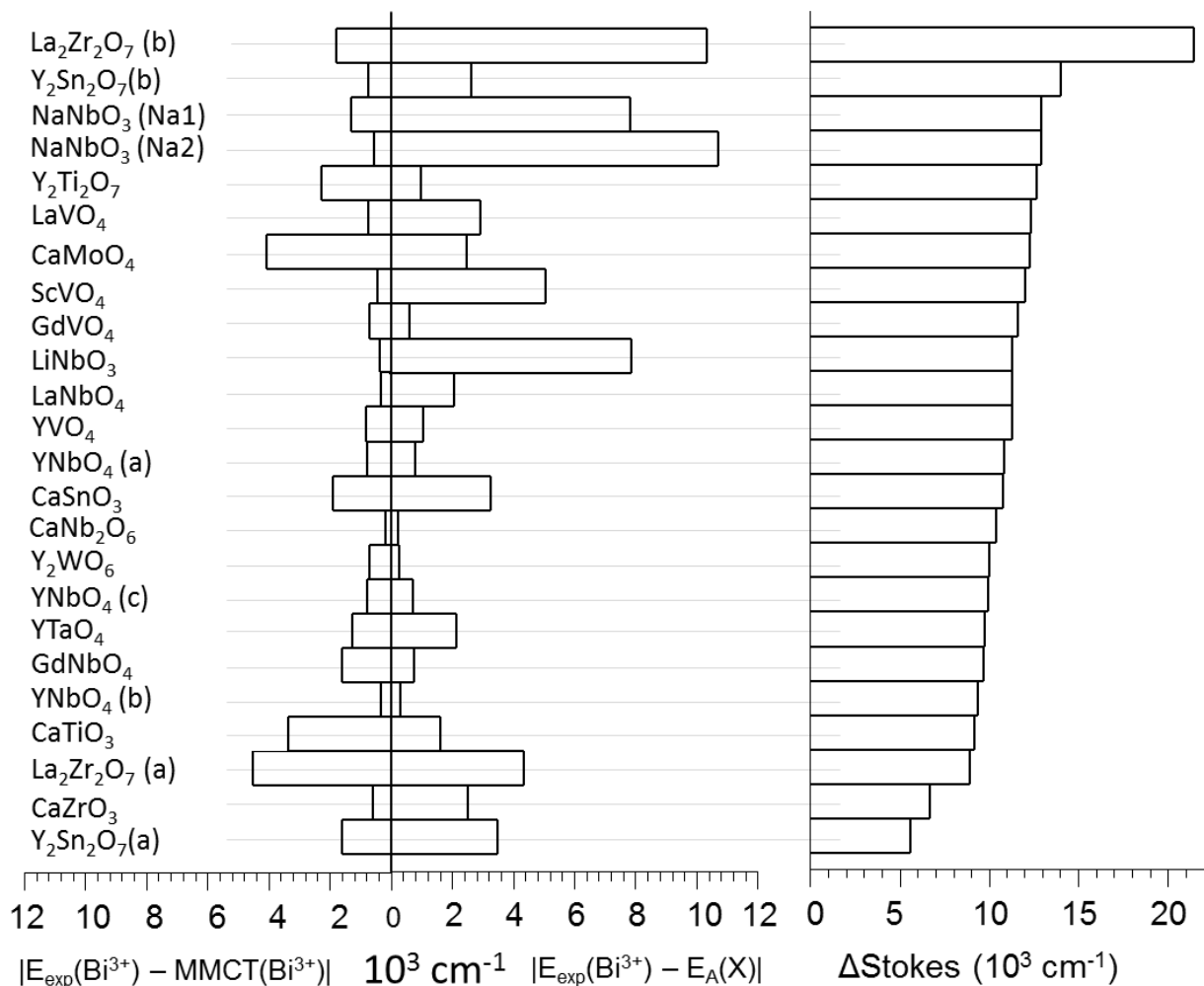


Figure 2. Left hand: difference, in absolute values, between experimental ($E_{\text{exp}}(\text{Bi}^{3+})$) and calculated (MMCT(Bi^{3+}) or $E_A(X)$) energies in some closed-shell transition metal oxides doped with Bi^{3+} . Right hand: corresponding Stokes shift values.

For some lattices (e.g. YNbO_4), several results are given in correspondence with each input value of the experimental energy. We point out that the MMCT energies calculated for Sc^{3+} , Y^{3+} and La^{3+} give rise

to high-lying excitation levels that are out of the scale displayed in Figure 2. These energies fall essentially in the region of C transitions as calculated using Equation (28) in Chapter 1.

Owing to Figure 2, the large Stokes shift found for $\text{La}_2\text{Zr}_2\text{O}_7\text{-Bi}^{3+}$ (b), $\text{NaNbO}_3\text{-Bi}^{3+}$, $\text{LaVO}_4\text{-Bi}^{3+}$, $\text{ScVO}_4\text{-Bi}^{3+}$, and $\text{LiNbO}_3\text{-Bi}^{3+}$ is in good agreement with an emission of MMCT origin and this is confirmed by a calculated MMCT energy very close to $E_{\text{exp}}(\text{Bi}^{3+}, \text{cm}^{-1})$ compared to $E_A(\text{X(i)}, \text{cm}^{-1})$. This means that these compounds should be classified without ambiguity as D-emitting phosphors. For $\text{La}_2\text{Zr}_2\text{O}_7\text{-Bi}^{3+}$ (b), $\text{LaVO}_4\text{-Bi}^{3+}$ and $\text{ScVO}_4\text{-Bi}^{3+}$, this conclusion is in line with previous reports^{(6),(20)}. The situation is more ambiguous for the other compounds, since the calculated $\text{MMCT}(\text{Bi}^{3+}, \text{cm}^{-1})$ and $E_A(\text{X(i)}, \text{cm}^{-1})$ energies are rather close. For instance, we find compounds with moderate Stokes shifts like $\text{CaZrO}_3\text{-Bi}^{3+}$ (recognized as a regular A-emitting phosphor)⁽¹⁸⁾ and $\text{CaTiO}_3\text{-Bi}^{3+}$ (recognized as a D-like phosphor)⁽³⁾ for which our calculations would lead to an opposite conclusion since the $\text{MMCT}(\text{Bi}^{3+}, \text{cm}^{-1})$ energy is very close to $E_{\text{exp}}(\text{Bi}^{3+}, \text{cm}^{-1})$ in the zirconate and $E_A(\text{X}, \text{cm}^{-1})$ very close to $E_{\text{exp}}(\text{Bi}^{3+}, \text{cm}^{-1})$ in the titanate.

The same ambiguity occurs for $\text{Y}_2\text{Ti}_2\text{O}_7\text{-Bi}^{3+}$, which is recognized as a D-like phosphor⁽¹⁷⁾ and for $\text{Y}_2\text{Sn}_2\text{O}_7\text{-Bi}^{3+}$ (a), which is recognized as regular A-emitter⁽¹⁹⁾. In $\text{La}_2\text{Zr}_2\text{O}_7\text{-Bi}^{3+}$, the lower-lying excitation state is of A character⁽²⁰⁾, as denoted by us as $\text{La}_2\text{Zr}_2\text{O}_7\text{-Bi}^{3+}$ (a) in the present work. This assignment was based on the relatively small Stokes shift compared to $\text{La}_2\text{Zr}_2\text{O}_7\text{-Bi}^{3+}$ (b) and is convincing. In this specific case, however, the error committed by both calculations exceeds $\pm 4000 \text{ cm}^{-1}$ with respect to $E_{\text{exp}}(\text{Bi}^{3+}, \text{cm}^{-1})$ (see Figure 2), which prevents confirming this assignment without ambiguity.

To help rationalizing the situation we have calculated the energy difference $\text{MMCT}(\text{Bi}^{3+})\text{-}E_A(\text{X})$ separating the calculated MMCT and A states on an energy level diagram. This raises 3 predictable situations that are depicted on Figure 3 and that were previously introduced in Chapter 1: we individuate lattices for which the D (or MMCT) state is located below the A state (scheme 3(a)), lattices for which the D state is located above the A state (scheme 3(c)) and lattices for which A and D state are almost degenerated (scheme 3(b)). This is for instance the case of $\text{YVO}_4\text{-Bi}^{3+}$ that will be investigated later in more details.

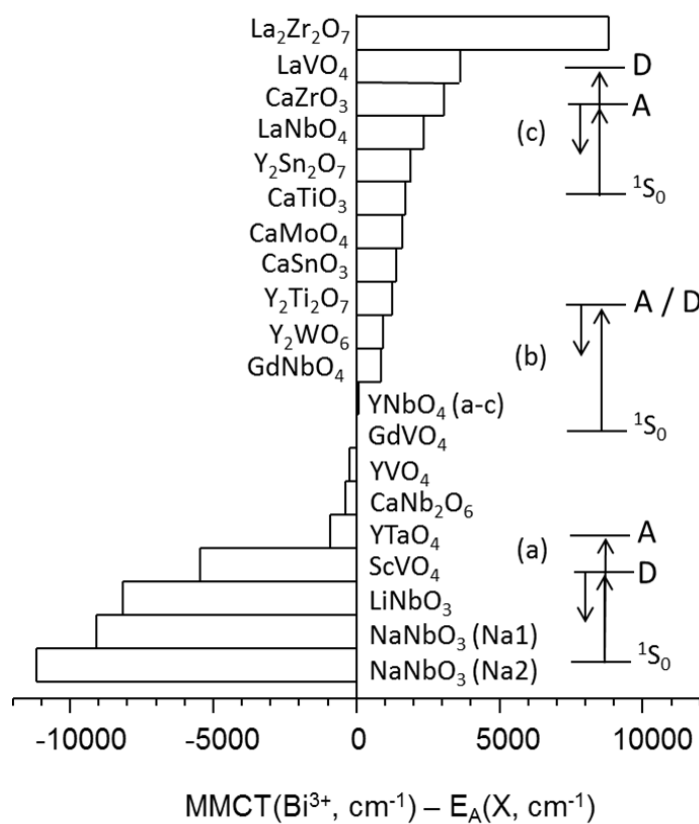


Figure 3. Difference between calculated ($MMCT(Bi^{3+})$) and $E_A(X)$ energies in some closed-shell transition metal oxides doped with Bi^{3+} .

Following the arguments in Chapter 1, these configurations can help knowing which states are responsible for the emission and the possible transitions we expect to see in the three situations. Correspondingly, we show in Figure 4 a plot of the $(\chi(X), \chi_{CN'}(M^{n+})/d_{corr})$ values for which the corresponding Bi^{3+} -doped lattice is described with scheme 3(b). Here we have made a distinction between lattices in which the transition metal is tetra-coordinated (i. e. $CN' = 4$) and lattices in which the transition metal has larger coordination ($CN' > 4$) (see Table 2). Lattices positioned above the curves belong to scheme 3(a) while lattices positioned below belong to scheme 3(c). Lattices like $NaNbO_3-Bi^{3+}$, $LiNbO_3-Bi^{3+}$ and $ScVO_4-Bi^{3+}$ have their MMCT state much lower in energy than their A state (scheme 3(a)) and should behave as D-like emitters with large Stokes shifts. This is in good agreement with Figure 2. The other lattices have their MMCT state either higher than the A state (scheme 3(c)) or at similar energies (scheme 3(b)) within $\pm 4000 \text{ cm}^{-1}$. For these, it remains difficult to assign the origin of the signals. The only remarkable exception is $La_2Zr_2O_7-Bi^{3+}$ (a) which has an unambiguous A-like character.

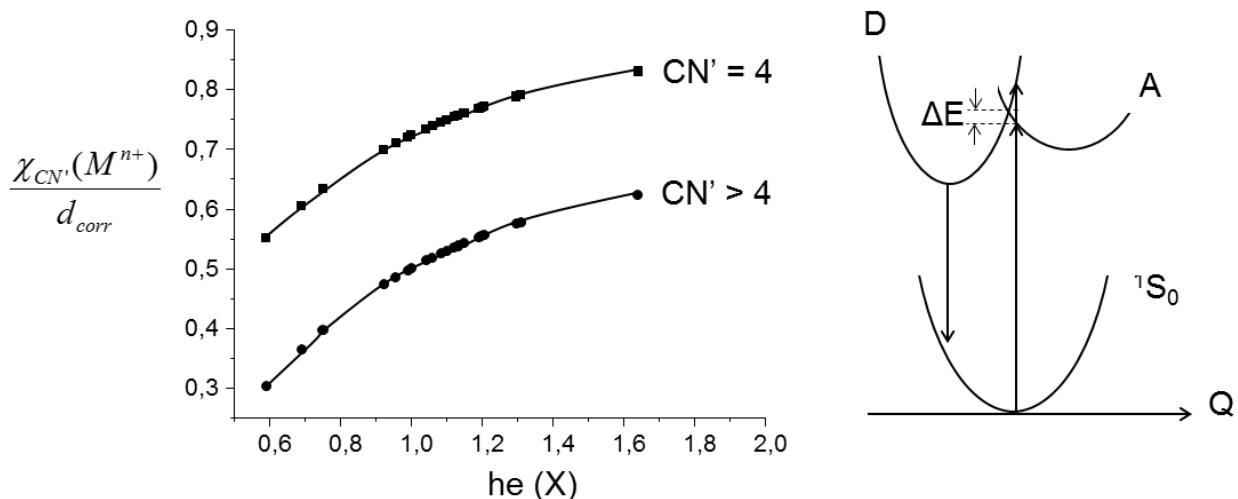


Figure 4. Left hand: $he(X)$ and $\chi_{CN'}(M^{n+})/d_{corr}$ values for which the corresponding Bi^{3+} -doped closed shell transition metal oxides are described with scheme 3(b). Right hand: schematic one-coordinate configuration diagram corresponding to scheme 3(c).

3.5. Criterion for the assignment of the luminescence signals in Bi^{3+} -doped transition metal oxides

We show in Figure 5 the energy difference $|MMCT(Bi^{3+})-E_A(X)-\Delta Stokes|$, expressed in absolute values. This energy difference is proposed as an empirical criterion to assign the character of the excitation signals in closed-shell transition metal oxides doped with Bi^{3+} (again, regardless of the possible contribution due to clusters in these compounds). Two dotted lines appear in this diagram. The line at 4000 cm^{-1} indicates the higher limit for compounds recognized as A-emitters in the literature ($La_2Zr_2O_7-Bi^{3+}$ (a) ⁽²⁰⁾, $CaZrO_3-Bi^{3+}$ ⁽¹⁸⁾, $Y_2Sn_2O_7-Bi^{3+}$ ⁽¹⁹⁾), while the line at 9000 cm^{-1} marks the lower limit for compounds recognized as D-emitters ^{(3),(6),(18),(21)}. We can see that the fluctuations on the input values of $E_{exp}(Bi^{3+},\text{ cm}^{-1})$ in $YNbO_4-Bi^{3+}$ have finally no impact on the assignments. For the three signals (a,b,c) in this compound, the same energy configuration can be drawn (Figure 3 (b)) and the transitions can be assigned to the D band in the three cases.

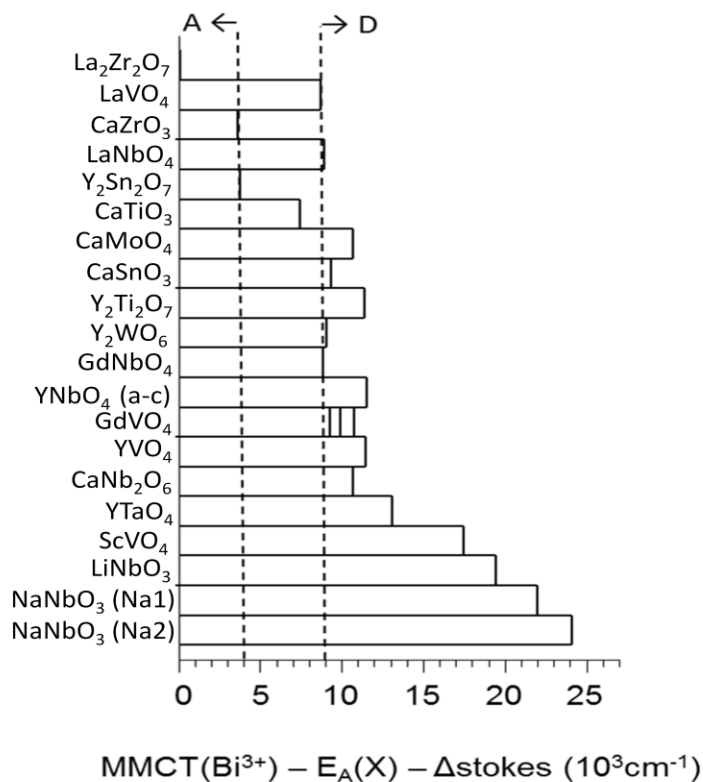


Figure 5. The proposed criterion for the assignment of the optical transitions (see text for details).

At first sight, it may appear unexpected that compounds obeying scheme 3(c) behave as D-like phosphors at normal temperature. This, actually, is the consequence of the large Stokes shift of the D emission which is concomitant with large Franck-Condon offset and large force constant of the corresponding excited potential energy curve. The situation is represented schematically on the one-coordinate Mott-Seitz configurational diagram of Figure 4. Owing to this diagram, the D state can be thermally populated from the lower-lying A state by overcoming the energy barrier separating the two states⁽²²⁾. At a given temperature, the efficiency of this process depends on $|\text{MMCT}(\text{Bi}^{3+}) - E_A(X)|$, on the lattice vibrational energy and on the excited states relaxation, which, unfortunately, is usually unknown. Owing to this diagram, we can however comment the situation for five lattices located at the top of Figure 3 that are characterized by scheme 3(c). For LaVO_4 and LaNbO_4 , the Stokes shift values (Figure 2) and the maximum phonon frequency are rather high ($\approx 810 \text{ cm}^{-1}$ for LaNbO_4 ⁽²⁴⁾ and $> 900 \text{ cm}^{-1}$ for LaVO_4 ⁽²⁵⁾). Then 3 to 4 phonons are required to bridge the energy gap separating A and D states in these lattices and certainly much less to bridge the gap ΔE separating A state to its cross-over with D state (see Figure 4, right hand). Once the energy barrier from A to D is overcome, D-like emission is observed for

these compounds at room temperature. For the three perovskites $\text{CaM}'\text{O}_3$ ($\text{M}' = \text{Zr, Ti, Sn}$), the maximum phonon frequency is significantly lower ($< 550 \text{ cm}^{-1}$). More than 5 phonons are required to bridge the A-to-D gap in $\text{CaZrO}_3\text{-Bi}^{3+}$ but less than 4 in $\text{CaTiO}_3\text{-Bi}^{3+}$ and $\text{CaSnO}_3\text{-Bi}^{3+}$. This accounts for the observation of A-like emission in the former ⁽¹⁸⁾ and D-like emission for the latter ^{(18),(16)}. We note however that in the case of $\text{CaTiO}_3\text{-Bi}^{3+}$, we have $|E_{\text{exp}}(\text{Bi}^{3+}) - E_{\text{A}}(\text{X})| < |E_{\text{exp}}(\text{Bi}^{3+}) - \text{MMCT}(\text{Bi}^{3+})|$ and $4000 < |\text{MMCT}(\text{Bi}^{3+}) - E_{\text{A}}(\text{X}) - \Delta\text{Stokes}| < 9000 \text{ cm}^{-1}$, meaning that some contribution from the A state ⁽¹⁶⁾ cannot be totally excluded in this compound. Further spectroscopic investigations have to be undertaken here to clarify the issue.

It is interesting, at this point, to challenge the model by investigating the complex case of Bi^{3+} -doped garnets. Host lattices like $\text{Y}_3\text{Ga}_5\text{O}_{12}$, $\text{Y}_3\text{Al}_5\text{O}_{12}$ and $\text{Lu}_3\text{Al}_5\text{O}_{12}$ show both UV and visible emissions when doped with Bi^{3+} . If the UV emission is always ascribed to regular A-like transition, the assignment of the visible emission is still subject of discussion; it is ascribed either to dimers or to bound excitons ⁽²⁶⁾⁻⁽³¹⁾. We have compiled the necessary data in Table 3 for discussion.

Table 3 Experimental ($E_{\text{exp}}(\text{Bi}^{3+})$ and Stokes shift) and calculated ($\text{MMCT}(\text{Bi}^{3+})$ or $E_{\text{A}}(\text{X})$) energies in garnets doped with Bi^{3+} . Some useful parameters required for the calculations are also provided.

	$\text{Y}_3\text{Ga}_5\text{O}_{12}$	$\text{Y}_3\text{Al}_5\text{O}_{12}$	$\text{Lu}_3\text{Al}_5\text{O}_{12}$
X (CN)	Y^{3+} (8)	Y^{3+} (8)	Lu^{3+} (8)
M^{n+} (CN')	Y^{3+} (8) ^a Ga^{3+} (6) ^b Ga^{3+} (4) ^c	Y^{3+} (8)	Lu^{3+} (8)
d_{corr} (Å)	3.82 ^a 3.50 ^b 3.14 ^c	3.74	3.73
he (X)	0.92	0.93	0.89
$\chi_{\text{CN}'} (\text{M}^{n+})$	1.29 ^a 1.58 ^b 1.75 ^c	1.29	1.37
$E_{\text{exp}}(\text{Bi}^{3+}, \text{cm}^{-1})$	35200 ⁽²⁶⁾ 35090 ⁽²⁷⁾ 32800 ⁽²⁸⁾	36500 ⁽²⁶⁾ 37420 ⁽²⁹⁾ 36860 ^{d (30)}	37340 ^{e (30), (31)}
Stokes shift (cm^{-1})	3950 ⁽²⁶⁾ 3340 ⁽²⁷⁾ 12030 ⁽²⁸⁾	3900 ⁽²⁶⁾ 5160 ⁽²⁹⁾ 4680 ^{d (30)} 14650 ^{d (30)}	4435 ^{e (30), (31)} 16130 ^{e (30), (31)}
$E_{\text{A}}(\text{X}, \text{cm}^{-1})$	33395	33225	33922
MMCT ($\text{Bi}^{3+}, \text{cm}^{-1}$)	39635 ^a 34460 ^b 41020 ^c	39305	37875

Letters ^{a-e} mark connected data.

As for Table 2, there is reasonably good agreement between calculated and experimental data. In the case of $\text{Y}_3\text{Ga}_5\text{O}_{12}\text{-Bi}^{3+}$, the lower lying MMCT state corresponds to a transition between Bi^{3+} and Ga^{3+} in six-fold coordination. Only this latter is retained in the following, the $\text{Bi}^{3+} \rightarrow \text{Y}^{3+}$ MMCT being located at much higher energy. The application of the criterion $|\text{MMCT}(\text{Bi}^{3+}) - E_A(X) - \Delta\text{Stokes}|$ confirms the assignment of the UV emission to the regular A transition in the three garnets. Despite some discrepancies in the energy values, the corresponding Stokes shifts remain below 5160 cm^{-1} . For the larger Stokes shifts, the calculation of our criterion gives 10965 cm^{-1} for $\text{Y}_3\text{Ga}_5\text{O}_{12}\text{-Bi}^{3+}$, 8570 cm^{-1} for $\text{Y}_3\text{Al}_5\text{O}_{12}\text{-Bi}^{3+}$ and 12180 cm^{-1} for $\text{Lu}_3\text{Ga}_5\text{O}_{12}\text{-Bi}^{3+}$. For all, these results confirm the assignment of the emission signals to MMCT (or exciton-like) transitions, in agreement with Refs. (28), (30) and (31).

At this stage, we conclude that the above criterion, although empirical, has some predictive value for the assignment of the emitting levels in closed shell transition metal oxides doped with Bi^{3+} . However, ambiguities still exist, e. g. in $\text{CaTiO}_3\text{:Bi}^{3+}$. In $\text{YVO}_4\text{:Bi}^{3+}$, an important luminescent compound, the criterion predicts a prominent D-like luminescence even though the A and D states are very close in energy. We found it interesting at this stage to check whether the action of high hydrostatic pressure could help lifting the degeneracy of the levels in this system and therefore clarify the situation from an experimental viewpoint. The compound $\text{CaTiO}_3\text{:Bi}^{3+}$ would have been, in this connection, an excellent candidate, but unfortunately, its room temperature luminescence is not high enough to make accurate measurement in the anvil cell that needs to be used to apply the pressure.

3.6. Energy Level Structure of Bi^{3+} in YVO_4 under high hydrostatic pressure

The sample of $\text{YVO}_4\text{-Bi}^{3+}$ was prepared by standard solid state reaction with a nominal doping rate of 1 mol % in bismuth. The sample was obtained in its zircon $I4_1/a$ form (hereafter denoted as Z- $\text{YVO}_4\text{-Bi}^{3+}$). The crystal building consists of chains of alternating edge-sharing VO_4 tetrahedra and YO_8 units extending parallel to the crystallographic c axis. The Y^{3+} ions occupy dodecahedrally coordinated sites with nominal D_{2d} point symmetry. It is known that a zircon-to-scheelite phase transition occurs at 7.5 GPa in YVO_4 . The scheelite polymorph has $I4_1/a$ space group and is noted as S- YVO_4 in the following. The crystal structure of these two polymorphs is shown in Figure 6.

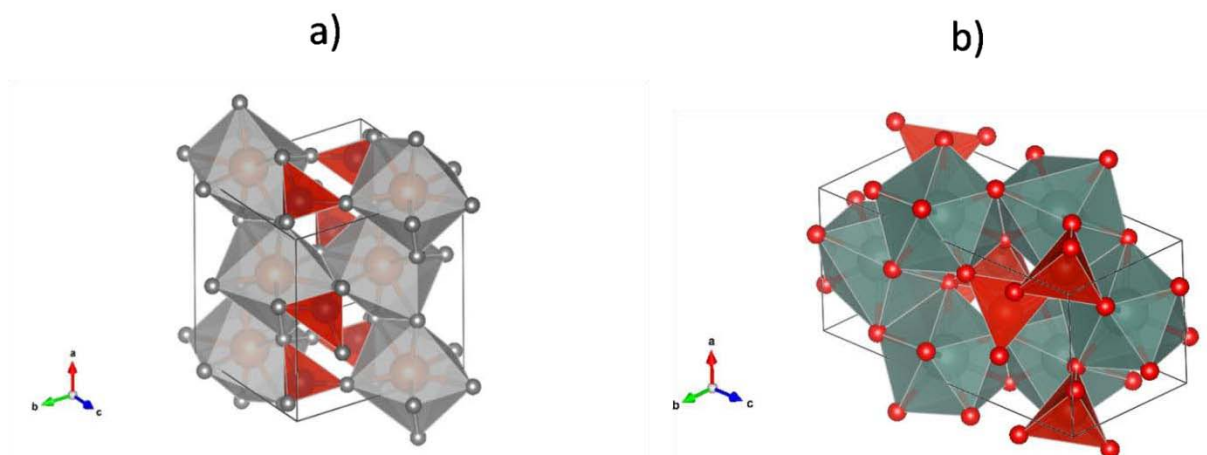


Figure 6. Crystal structure of YVO_4 in the (a) zircon and (b) scheelite polymorphs.

The phase transition from zircon to scheelite involves an expansion of the (VO_4) polyhedron and shrinkage of the (YO_8) polyhedron. This leads to a global decrease of the unit cell volume and of the interatomic distances as illustrated in Figure 7.

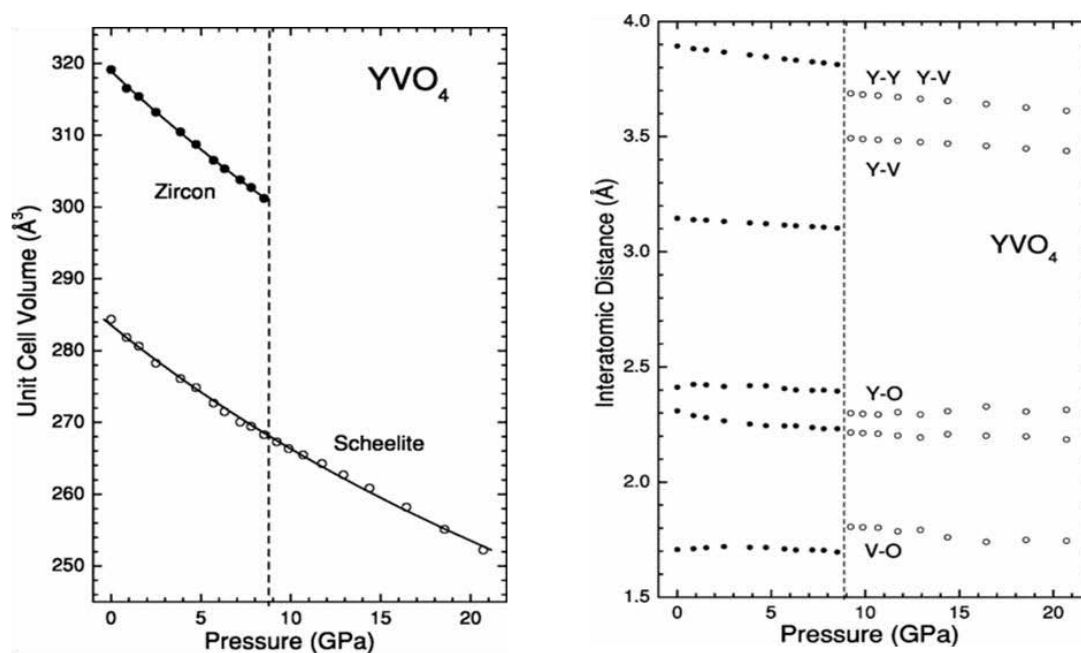


Figure 7. Pressure dependence of the unit cell volume (left hand side) and of the interatomic distances (right hand side) in Z-YVO4 and S-YVO4⁽³²⁾

The effective charges of the cations are very close to the formal Y^{3+} and V^{5+} oxidation states in the zircon phase but not in the scheelite where the formal charge of Y is 4.13 and that of V is 4.73⁽³³⁾. In the latter case, the values indicate stronger covalency within the (YO_8) polyhedron and lower covalency within the (VO_4) polyhedron. As is argued in ref. (34) and ref. (35), this could be the consequence of the transfer of some amount of charge from the oxygen atoms. The charge transfer energy between oxygen O2p (nonbonding t_1 orbitals) and vanadium V3d (antibonding e orbitals) is then lowered, which contributes to decrease the bandgap in the scheelite compared to the zircon (34). This effect is well established and confirmed by optical measurements carried out at the absorption edge of YVO_4 with respect to pressure (Figure 8)⁽³⁶⁾. As it is clear from this figure, the variation of the bandgap is progressive in the zircon phase then very sharp across the zircon-to-scheelite phase transition^{(32),(36)}.

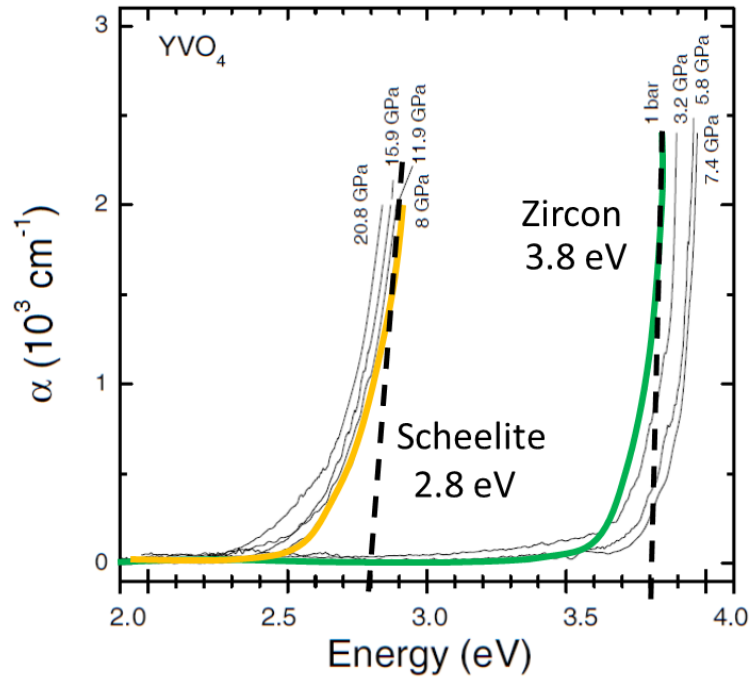


Figure 8. Pressure induced variation of the absorption edge of YVO_4 across zircon-to-scheelite phase transition⁽³⁶⁾.

At last, it happens that the zircon-to-scheelite phase transition is irreversible. This will allow us the investigation of the scheelite form of YVO_4-Bi^{3+} after decompression to ambient pressure.

We have thereby investigated the evolution of the luminescence properties of YVO_4-Bi^{3+} in the pressure range 0 – 20 GPa, at ambient temperature and in the temperature range 10 – 500 K, at ambient pressure. Luminescence excitation spectra were acquired using a system consisting of a 150 W

Xe lamp, two monochromators SPM2 and two photomultipliers (the first for the luminescence and the second for reference signal detection). Steady-state luminescence measurements were performed with an Andor SR-750-D1 spectrometer equipped with a CCD camera DU420A-OE type. Excitation source was a He–Cd laser using the wavelengths of 325 nm or 442 nm. To follow the luminescence kinetics, we used a system consisting of a PL 2143 A/SS laser and a PG 401/SH parametric optical generator. The emission signal was analyzed using a Bruker Optics 2501S spectrograph and a Hamamatsu Streak Camera model C4334-01⁽³⁷⁾. High hydrostatic pressure was applied in a Merrill Bassett type⁽³⁸⁾ diamond anvil cell (DAC). Polydimethylsiloxane oil was used as the pressure-transmitting medium, and pressure was measured by the shift of the luminescence lines of ruby.

The emission was intense enough in the zircon phase (i.e. up to 7.5 GPa) to record the corresponding excitation spectra and decay profiles. The luminescence data collected in the region 7.5 – 10 GPa were not retained as they contain contributions from both zircon and scheelite mixed phases. Pure scheelite polymorph (i. e. $\text{S-YVO}_4\text{-Bi}^{3+}$) was obtained above 10 GPa. In this phase, however, the emission intensity was too low to collect the excitation spectra. The temperature dependence of the emission spectra and decay profiles was recorded in the zircon phase prior application of pressure and in the scheelite phase after decompression from 20 GPa to ambient pressure.

3.6.1. Luminescence of $\text{Z-YVO}_4\text{:Bi}^{3+}$ under pressure ($P < 8\text{GPa}$)

We show in Figure 9 the pressure dependence of the emission and excitation spectra of $\text{Z-YVO}_4\text{-Bi}^{3+}$. The excitation spectra look very similar, but looking in more details, we find that the excitation edge (evaluated at the inflection point of the excitation profile) undergoes shifts that are not monotonous with pressure (Figure 10). This complex evolution can be understood by taking into account that the excitation features consist of overlapping transitions of different origins, both having a charge transfer character.

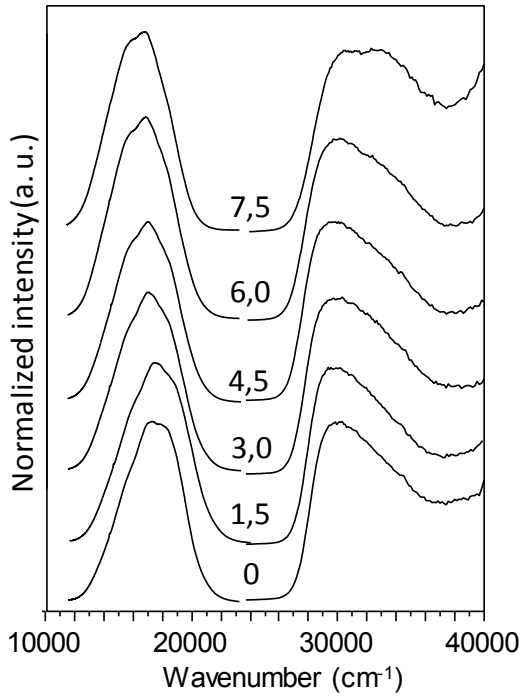


Figure 9. Pressure dependence of the emission and excitation spectra of Z-YVO₄-Bi³⁺. Pressures are mentioned on the graph. Excitation at 325 nm.

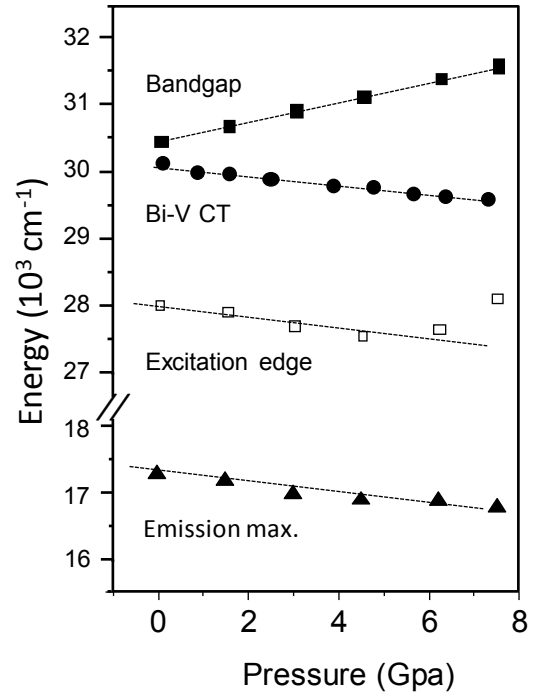


Figure 10. Energy position of the bandgap, the Bi-V CT, the excitation edge and the emission maximum in Z-YVO₄-Bi³⁺. Excitation at 325 nm

The first CT occurs within VO₄³⁻ molecular units and is ascribed to the spin allowed ¹T₁ ← ¹A₁ absorption⁽³⁹⁾. In pure YVO₄, this transition presents an excitation edge at 29850 cm⁻¹ in correspondence with an excitation maximum at 30770 cm⁻¹⁽⁷⁾. The energy bandgap E_{g0} has been estimated by Panchal et. al at 30570 cm⁻¹ (3.79 eV) which is consistent with the excitation edge at ambient pressure (i.e. P ≈ 0 GPa). As reported in ref. (36), this bandgap increases under pressure following:

$$Eg_P^Z = Eg_0 + 150.8P \quad (1)$$

with pressure P expressed in GPa and energies in cm⁻¹. The upper script Z stands for the zircon polymorph. The corresponding variation is plotted in Figure 10 with the label "Bandgap".

The second CT contributing to the excitation spectrum takes place between Bi³⁺ and V⁵⁺ and results from transitions between Bi³⁺(6s²)-V⁵⁺(3d⁰) and Bi⁴⁺(6s¹)-V⁴⁺(3d¹) configurations (i. e. Bi → V CT). The energy of this process is given by Equation (30) of Chapter 1.

For YVO₄ at ambient pressure, this Equation simplifies to:

$$MMCT(Bi^{3+}, cm^{-1}) = 70000 - 52000 \frac{\chi_4(V^{5+})}{d_{corr}} \quad (2)$$

Using $\chi_4(V^{5+}) = 2.46^{(40)}$ (see Appendix A) and $d_{corr} = 3.21 \text{ \AA}$, we locate the Bi-V CT maximum at 30150 cm^{-1} , i. e. very close to the VO_4^{3-} excitation at ambient pressure. We therefore estimate that both CT processes contribute to the edge of the excitation spectrum recorded at ambient pressure. Following the arguments developed recently in ref. (41), we estimate the action of pressure on the Bi \rightarrow V CT energy as follows:

$$MMCT(Bi^{3+}, cm^{-1}) = 70000 - 52000 \frac{\chi_4(V^{5+})}{d_p} \quad (3)$$

where d_p expresses the pressure dependence of the Bi-V distance in $YVO_4\text{-}Bi^{3+}$. Owing to Figure 7, we can write $d_p = d_{corr} - 0.0055P$ for the zircon polymorph, with $d_{corr} = 3.21 \text{ \AA}$. The corresponding pressure-dependence of the Bi-V CT is plotted in Figure 10. In the zircon phase, it comes that the pressure action induces an upward shift of the bandgap and a downshift of the Bi-V CT. In the pressure range 0 – 5 GPa, the excitation edge is governed by the Bi-V CT process, as attested by the similar slope of the corresponding curves. The blue shift of the excitation edge for pressures exceeding 5 GPa reveals prevailing contributions from higher-lying states whose origin has not been clearly identified in the context of this work.

Dealing with emission, we find that the band-like CT emission of $YVO_4\text{-}Bi^{3+}$ presents a complex, unresolved, structure consisting of at least 2 contributions that have previously been identified in ref. (7). There is no trace of emission from the vanadate units. This is due to $VO_4^{3-} \rightarrow Bi^{3+}$ energy transfer, the efficiency of which is very high at room temperature⁽⁷⁾. The application of pressure tends to favor the low energy contributions relative to the high energy ones, resulting in a progressive red shift of the band maximum under pressure. This variation is shown in Figure 10 with the label “emission max”. In the pressure range 0 – 7.5 GPa, the emission decays were found exponential with a time-constant varying progressively from 4.3 to 4.7 μs . There is no significant variation of the emission intensity in this pressure range.

We show in Figure 11 the dependence of the emission time-constant in the temperature range 10 – 500 K, at ambient pressure. The integrated emission area follows the same trend.

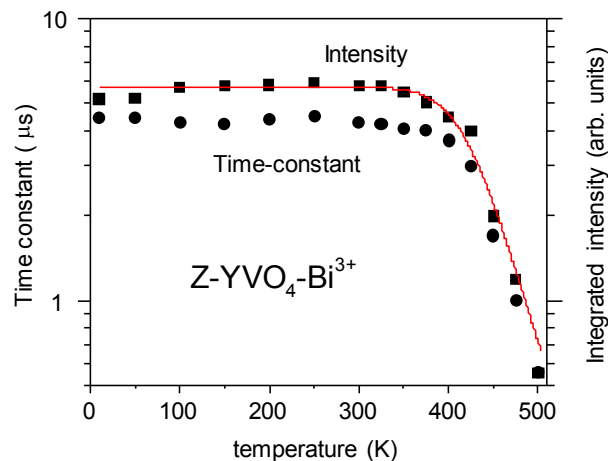


Figure 11. Temperature dependence of the emission time-constant and integrated emission area in $\text{Z-YVO}_4\text{-Bi}^{3+}$. Excitation at 325 nm, ambient pressure. The solid line is the fit of the data using Equation (4). See text for details.

These results account for a thermal quenching by cross-over to a Franck-Condon shifted state (here the Bi-V CT state) and can be reliably reproduced in the frame of the Struck and Fonger model⁽⁴²⁾:

$$\frac{I(T)}{I_0} = A \exp\left(-\frac{\Delta E}{KT}\right) \quad (4)$$

where $I(T)$ is the emission intensity at temperature T , I_0 the intensity at the lowest temperature, A is close to 10^7 and ΔE is the activation energy separating the emitting state to its crossover with the quenching state, i. e. the 1S_0 ground state of Bi^{3+} (Figure12).

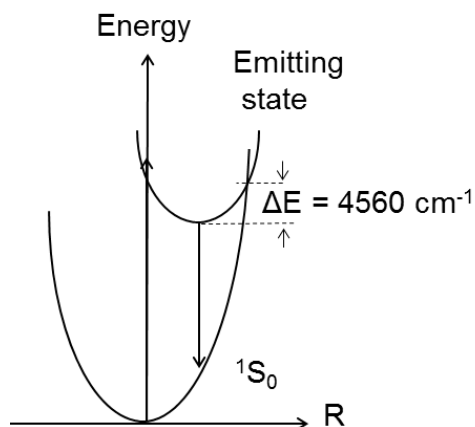


Figure 12. A schematic coordinate diagram representing the activation energy separating the emitting state with its crossover to the quenching ground state 1S_0 of Bi^{3+} in Z-YVO_4 .

An activation energy of 4560 cm⁻¹ for Z-YVO₄:Bi³⁺ compares well with the value (viz. 4000 cm⁻¹) reported previously for GdVO₄:Bi³⁺ (3). At this stage, still questionable is the exact nature of the emitting state in Z-YVO₄:Bi³⁺. As stated at the end of Section 3.5., the A and D states are very close from each other in the energy level diagram. To try lifting this ambiguity, we have calculated the pressure dependence of the A state energy for Bi³⁺ ions accommodated in the Y³⁺ sites (Viz energy E_A(Y³⁺)). For completeness, we have also calculated the pressure dependence of the energy E_C(Y³⁺) of C state and of the energy of the Bi³⁺-Y³⁺ MMCT. In the latter case, the lower electronegativity of Y³⁺ in eightfold coordination (viz. $\chi_8(Y^{3+}) = 1.28$, see Appendix A) compared to that of four-coordinated V⁵⁺ (viz. $\chi_4(V^{5+}) = 2.46$) will undoubtedly locate the Bi→Y CT at higher energy relative to the Bi→V CT.

The calculation of the pressure-dependence of E_A(Y³⁺) and E_C(Y³⁺) requires the calculation of the pressure-dependence of $\epsilon(Y^{3+})$, i. e. the calculation of the pressure dependence of all the involved parameters (see Chapter 1). This was achieved by implementing the available crystal data for each pressure in the range 0 – 7.5 GPa in VESTA and running our excel macros. The input data and generated results are listed in Table 4.

Table 4 Pressure dependence of the unit cell volume V and of distances Y-O and V-O in Z-YVO₄:Bi³⁺ and corresponding dependence of E_A(Y³⁺), E_C(Y³⁺), Bi-V and Bi-Y energies.

Pressure (Gpa)	V cell (Å)	Y-O (Å)	V-O(Å)	d _{corr} (Å)	E _A (Y ³⁺) (cm ⁻¹)	E _C (Y ³⁺) (cm ⁻¹)	Bi-YCT (cm ⁻¹)	Bi-VCT (cm ⁻¹)
0	319.56961	2.3639	1.7082	3.21	30152.59	40821.07	40175.88	30149.53
0.9	317.07889	2.3584	1.7043	3.1605	30089.81	40693.09	40157.33	30087.99
1.6	315.68369	2.3549	1.7017	3.122	30061.66	40635.64	40142.87	30039.99
2.5	313.40534	2.3494	1.6978	3.0725	30013.6	40537.48	40124.23	29978.1
3.8	310.64064	2.3424	1.6928	3.001	29957.91	40423.6	40097.24	29888.37
4.7	308.63353	2.3376	1.6894	2.9515	29913.06	40331.78	40078.49	29826.01
5.7	306.52408	2.332	1.6852	2.8965	29875.38	40254.54	40057.6	29756.5
6.2	305.16004	2.3285	1.6826	2.869	29849.43	40201.31	40047.14	29721.65
7.1	304.045	2.3257	1.6807	2.8195	29827.7	40156.72	40028.26	29658.78

The pressure dependence of the energy level scheme of Z-YVO₄:Bi³⁺ and the corresponding schematic coordinate diagram plotted in Figure 13 gives a synthetic view of the situation.

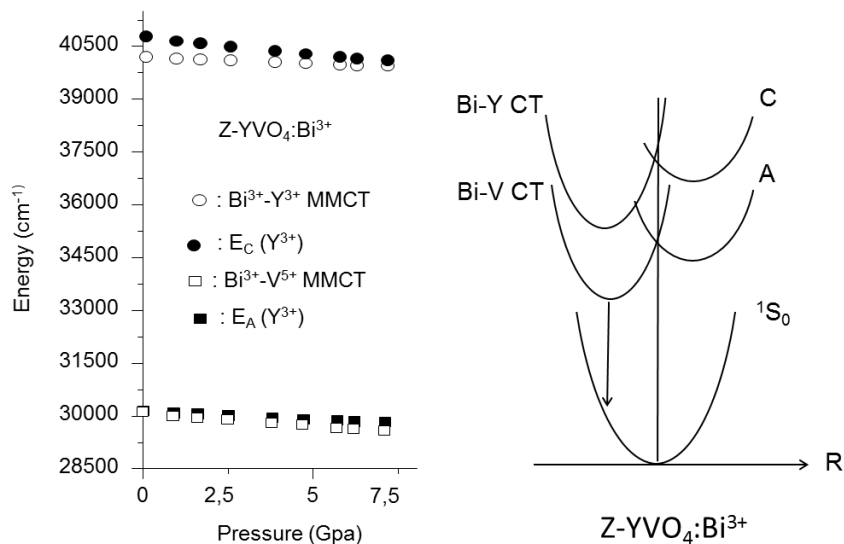


Figure 13. Left hand: Pressure dependence of the calculated energies Bi³⁺-Y³⁺ MMCT, Bi³⁺-V⁵⁺ MMCT, E_A(Y³⁺) and E_C(Y³⁺). Right hand: Corresponding schemetic diagram of the position of the different states of Bi³⁺ in Z-YVO₄.

Especially, we can see that A and Bi-V CT states can hardly be separated by the means of hydrostatic pressure limited to 7.5 GPa, although some trend is starting to appear to the high pressure side. It is interesting to note that C and Bi-Y CT have also very similar energy. In contrast to the lower lying levels, the action of pressure tends to increase the degeneracy of these levels. The schematic one-coordinate energy diagram displayed at right hand in Figure 13 is then proposed for Z-YVO₄:Bi³⁺. It is almost pressure independent (regardless the curvature of the parabola that may change a bit with pressure). This situation corresponds to scheme 3(b) with prominent emission from the Bi-V CT owing to the more pronounced electron-phonon relaxation in this state of excitonic character.

3.6.2. Luminescence of S-YVO₄:Bi³⁺ under pressure ($P \geq 9\text{ GPa}$)

Representative emission spectra of S-YVO₄:Bi³⁺ (at high pressure, $P = 20\text{ GPa}$ or at ambient pressure after decompression) are presented in Figure 14 upon excitation at 325 nm. The compound glowing very weakly at room temperature, the data were recorded at 10 K. They show a maximum at $\approx 14750\text{ cm}^{-1}$ (678 nm) that is nearly pressure independent. This makes a considerable red shift with respect to the yellow emission of Z-YVO₄:Bi³⁺. The corresponding decays, measured at ambient pressure in the temperature range 10 – 250 K, show a non-exponential behavior (Figure 14, inset).

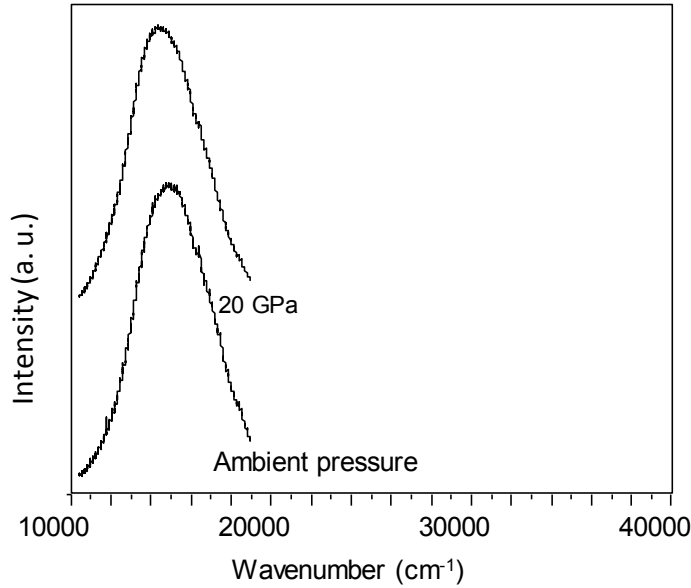


Figure 14. Emission spectrum ($T = 10$ K) and temperature dependence of the emission decays of $S\text{-YVO}_4\text{-Bi}^{3+}$.

Excitation at 325 nm.

At low temperature, the deviation from the exponential behavior is ascribed to defects created by the action of pressure in the scheelite lattice. These lattice defects could be associated with imperfect atomic re-ordering subsequent to the reconstructive mechanism prevailing during the first order zircon-to-scheelite phase transition⁽⁴³⁾. These defects may induce perturbation in the crystal field around the Bi^{3+} and/or V^{5+} ions, likely deforming the potential curve describing the CT emitting state and leading to the presence of non-equivalent optical centers with different quenching behaviors.

Average values of the corresponding time constants were calculated using the expression:

$$\tau_{av} = \int tI(t)dt / \int I(t)dt \quad (5)$$

where $I(t)$ is the luminescence intensity at time t .

We know that the scheelite phase does not luminescence when undoped, even at 10 K⁽⁴⁴⁾. This quenching is essentially due to the low bandgap value that images the low energy of the ${}^1T_1 \leftarrow {}^1A_1$ and ${}^3T_{1,2} \rightarrow {}^1A_1$ CT transitions within the VO_4^{3-} units. Following the arguments of Blasse and Brill⁽⁴⁵⁾, the low

energy position of the otherwise emitting ${}^3T_{1,2}$ states accounts for the absence of luminescence in this material. Therefore, we ascribe the 14750 cm^{-1} emission to the Bi^{3+} ions.

We show in Figure 15 the temperature dependence of the average time constant and of the emission intensity evaluated as the integrated area below the decay curves for $\text{S-YVO}_4\text{-Bi}^{3+}$.

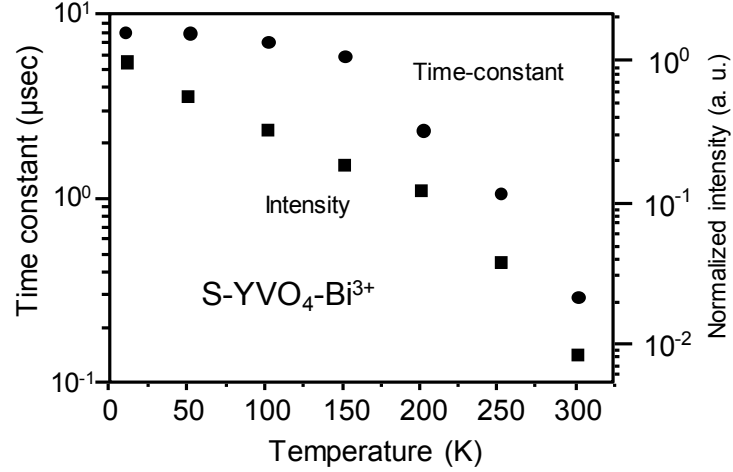


Figure 15. Temperature dependence of the emission intensity and average emission time-constant in $\text{S-YVO}_4\text{-Bi}^{3+}$. Excitation at 325 nm, ambient pressure.

These data cannot be reproduced by the only mean of Equation (4). This indicates that several processes contribute to the luminescence quenching in the scheelite phase. Going further in the interpretation of the above spectroscopic behaviors requires again the knowledge of the emitting level in this compound. We have therefore applied the same method as for $\text{Z-YVO}_4\text{-Bi}^{3+}$ but now in the pressure range 9-20 GPa. In this range, the pressure dependence of the bandgap value (in cm^{-1}) is given by⁽³²⁾:

$E_{g_{P>9}} = E_{g_9} - 50.8(P - 9)$. Concomitantly, the shortest Y-V distance in the scheelite polymorph varies according to: $d_{P>9} = 3.39 - 0.0046(P - 9)$, as deduced from Figure 6. The value of d_{corr} at ambient pressure was obtained by simple linear extrapolation. This allows calculating the pressure dependence of Bi-V and Bi-Y CT. The pressure dependence of $\text{he}(\text{Y}^{3+})$ and correlated $E_A(\text{Y}^{3+})$ and $E_C(\text{Y}^{3+})$ was obtained from the structural data listed in Table 5. The corresponding results are plotted in Figure 16.

Table 5 Pressure dependence of the unit cell volume V and of distances Y-O and V-O in $S\text{-YVO}_4\text{:Bi}^{3+}$ and corresponding dependence of $E_A(\text{Y}^{3+})$, $E_C(\text{Y}^{3+})$, Bi-V and Bi-Y energies. Fill the yellow columns

Pressure (Gpa)	V cell (Å)	Y-O (Å)	V-O(Å)	d_{corr} (Å)	$E_{g_{p>9}}$ (cm^{-1})	$E_A(\text{Y}^{3+})$ (cm^{-1})	$E_C(\text{Y}^{3+})$ (cm^{-1})	Bi-Y CT (cm^{-1})	Bi-VCT (cm^{-1})
9.3	267.46346	2.2917	1.7609	3.46422	22513.96	29804.87	38403.45	39715.43	33077.78
9.8	266.13863	2.288	1.7579	3.46192	22488.56	29777.53	38350.04	39705.28	33053.25
10.7	265.35655	2.2858	1.7562	3.45778	22442.84	28982.96	38315.52	39686.97	33009.02
11.7	264.3339	2.2827	1.754	3.45318	22392.04	28957.53	38267.48	39666.58	32959.75
12.9	262.77826	2.2783	1.7505	3.44766	22331.08	28941.11	38199.2	39642.03	32900.45
14.4	260.7486	2.2722	1.746	3.44076	22254.88	28918.26	38104.89	39611.24	32826.06
16.4	258.25067	2.2645	1.7406	3.43156	22153.28	28885.82	37982.56	39569.99	32726.4
18.6	255.29039	2.2551	1.7341	3.42144	22041.52	28841.06	37837.98	39524.36	32616.17
20.7	252.34781	2.2458	1.7276	3.41178	21934.84	28783.08	37690.74	39480.56	32510.33

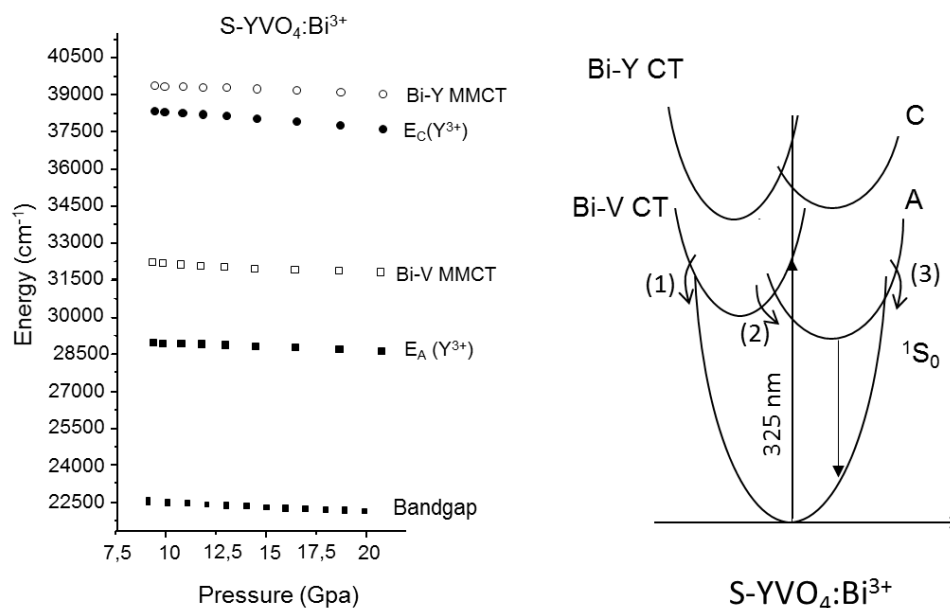


Figure 16. Pressure dependence of the energy level structure of Bi^{3+} in $S\text{-YVO}_4$ (left) and one-coordinate configuration diagram (right). See text for further details.

This situation differs notably from the previous case. Here, it is clear that in Bi^{3+} -related levels are located by more than 10000 cm^{-1} higher than the bandgap. This means that the absorption edge in $S\text{-YVO}_4\text{:Bi}^{3+}$ is shifted to higher energies compared to the host material.

$\text{YVO}_4\text{:Bi}^{3+}$ is now clearly defined by the vanadate groups. Consequently, the $^1\text{S}_0$ ground state of Bi^{3+} is now located in the valence band of the YVO_4 lattice. Dealing with the Bi^{3+} -related levels, we observe a clear splitting of the levels under pressure, the A state being now located lower in energy relative to the Bi-V CT. The corresponding situation is depicted on the schematic one-coordinate energy diagram in Figure 16. Following this diagram, absorption at 325 nm takes place essentially in the Bi-V-CT state. This state is then depopulated either by cross-over to the $^1\text{S}_0$ ground state (channel (1) in Figure 16) or to the lower-lying A state (channel (2) in Figure 16). At 10 K, only the latter is emitting. The lower energy of this state with respect to the $\text{Z-YVO}_4\text{:Bi}^{3+}$ case (see Figure 13) accounts well for the observed red shift of the emission when moving from the zircon to the scheelite polymorph of YVO_4 . Further, the low-lying position in the diagram also accounts for the strong quenching of this state cross-over to the $^1\text{S}_0$ ground state (channel (3) in Figure 16) as temperature is raised as clearly evidenced by Figure 15.

3.7. Conclusion

We have investigated in this chapter the origin of the emitting state in the Bi^{3+} -doped closed shell transition metal oxides GdVO_4 , LaVO_4 , CaMoO_4 , LiNbO_3 , NaNbO_3 , ANbO_4 ($\text{A}=\text{Y, Gd, La}$), CaNb_2O_6 , $\text{M}'\text{YTaO}_4$, LiNbO_3 and NaNbO_3 . Their optical spectra were measured by photoluminescence. Using the EF and MMCT models, the calculations of the A and C bands of Bi^{3+} in addition to the MMCT energies from Bi^{3+} to the transition metal were made for these compounds and for other compounds described in the literature. We were able to assign the origin of emission in these compounds by comparing the data on the low-lying excitation energies with the calculated energies with the help of a proposed criterion involving the values of the Stokes shifts. We have also studied the effect of high pressure on the luminescence of $\text{YVO}_4\text{:Bi}^{3+}$. Using the EF and MMCT models with our experimental measurements we were able to locate the energy states of this compound in its zircon polymorph and scheelite polymorph (at pressure >9 GPa) and study the origin of luminescence in both phases. The emission spectrum showed a red shift under the action of pressure in the zircon phase where the emitting state is the $\text{Bi}\rightarrow\text{V}$ charge transfer state and the excitation edge is governed by the Bi-V CT in the pressure range 0-5 GPa. The A and $\text{Bi}\rightarrow\text{V}$ CT states are located very close to each other in this polymorph which is the reason we do not observe the A band in the emission spectrum. When going from the zircon to the scheelite polymorph, the emission undergoes a drastic shift from 570 nm to 680 nm and an important splitting of the A and Bi-V CT states was observed with A being the low lying state. This makes it the emitting state

in the scheelite phase and the responsible for the red shift at 10 K. This state is otherwise strongly quenched at higher temperatures.

Bibliography

1. **A.M. Srivastava and H.A. Comanzo** . *The ultraviolet and visible luminescence of Bi^{3+} in the orthorhombic perovskite, GdAlO_3* . 2017, Optical Materials, Vol. 63, pp. 118-121.
2. **A.M. Srivastava and S.J. Camardello**. *Concentration dependence of the Bi^{3+} luminescence in LnPO_4 ($\text{Ln} = \text{Y}^{3+}, \text{Lu}^{3+}$)*. 2015, Optical Materials, Vol. 39, pp. 130-133.
3. **P. Boutinaud and E. Cavalli**. *Predicting metal-to-metal charge transfer in closed-shell transition metal oxides doped with Bi^{3+} or Pb^{2+}* . 2011, Chem. Phys. Lett, Vol. 503, pp. 239-243.
4. **S.Y.J. Zhang, X. Zhang, S. Lu, X. Ren, Z. Nie and X. Wang**. *Enhanced Red Emission in $\text{CaMoO}_4:\text{Bi}^{3+}, \text{Eu}^{3+}$* . 2007, Journal of Physical Chemistry C, Vol. 35, pp. 13256–13260.
5. **F. Xiao, Y.N. Xue and Q.Y. Zhang**. *Warm white light from $\text{Y}_4\text{MgSi}_3\text{O}_{13}:\text{Bi}^{3+}, \text{Eu}^{3+}$ nanophosphor for white light-emitting diodes*. 2009, Spectrochim Acta A: Molecular and Biomolecular Spectroscopy., Vol. 74, pp. 498-501.
6. **P. Boutinaud**. *Revisiting the Spectroscopy of the Bi^{3+} Ion in Oxide Compounds*. 2013, American Chemical Society, Vol. 52, pp. 6028–6038.
7. **E. Cavalli, F. Angiuli, F. Mezzardi, M. Trevisani, M. Bettinelli, P. Boutinaud, M.G. Brik**. *Tunable Luminescence of Bi^{3+} -Doped $\text{YPr}_x\text{V}_{1-x}$ ($0 < x < 1$)*. 2014, J.Phys.Condens.Matter, Vol. 26, pp. 385503-385515.
8. **S. Mahlik, M. Grinberg, E. Cavalli and M. Bettinelli**. *High pressure luminescence spectra of $\text{CaMoO}_4:\text{Pr}^{3+}$* . 2012, Journal of Physics Condensed Matter, Vol. 24, pp. 215402-215407.
9. **S. Mahlik, E. Cavalli, M. Bettinelli and M. Grinberg**. *Luminescence of $\text{CaWO}_4:\text{Pr}^{3+}$ and $\text{CaWO}_4:\text{Tb}^{3+}$ at ambient and high hydrostatic pressures*. 2013, Radiation Measurements, Vol. 56, pp. 1-5.
10. **M. de Jong and A. Meijerink**. *Color tuning of Bi^{2+} luminescence in barium borates*. 2016, Journal of Luminescence, Vol. 170, pp. 240-247.
11. **N. Zhang, J. Qiu, G. Dong, Z. Yang, Q. Zhang and M. Peng**. *Broadband tunable near-infrared emission of Bi-doped composite germanosilicate glasses*. 2012, Journal of Materials Chemistry, Vol. 22, pp. 3154-3159.
12. **M. Peng, N. Da, S. Krolkowski, A. Stiegelschmitt, and L. Wondraczek**. *Luminescence from Bi^{2+} -activated alkali earth borophosphates for white LEDs*. 2009, Optics Express, Vol. 17, pp. 21169-21178.
13. **G. Blasse and A. Brill**. *Luminescence phenomena in compounds with fergusonite structure*. 1970, Journal of Luminescence, Vol. 3, pp. 109-131.
14. **M. Wiegel, M.H.J. Emond, E.R. Stobbe and G. Blasse**. *Luminescence of Aalkali Tantalates AND Niobates* . 1994, Journal of Physical Chemistry, Vol. 55, pp. 773-778.

15. **M. Buryi, P. Bohacek, K. Chernenko, A. Krasnikov, V. V. Laguta, E. Mihokova, M. Nikl and S. Zazubovich.** *Luminescence and photo-thermally stimulated defect-creation processes in Bi^{3+} -doped single crystals of lead tungstate.* 2016, *Physica Status Solidi B*, Vol. 253, pp. 895-910.
16. **P. Boutinaud, E. Cavalli and R. Mahiou.** *Photon conversion in $\text{Bi}^{3+}/\text{Pr}^{3+}$ -codoped CaTiO_3 .* 2012, *Journal of Physics Condensed Matter*, Vol. 24, pp. 295502-295508.
17. **A.M. Srivastava, H.A. Comanzo and S.J. Cama.** *On the " $\text{Bi}^{3+}-\text{Ti}^{4+}$ " charge transfer transition in the pyrochlore $\text{Y}_2\text{Ti}_2\text{O}_7:\text{Bi}^{3+}$.* 2015, Vol. 48, pp. 31-35.
18. **A.M. Srivastava.** *Luminescence of Bi^{3+} in the orthorhombic perovskites $\text{CaB}^{4+}\text{O}_3$ ($\text{B}^{4+}=\text{Zr, Sn}$): Crossover from localized to D-state emission.* 2016, *Optical Materials*, Vol. 58, pp. 89-92.
19. **A.M. Srivastava.** *On the luminescence of Bi^{3+} in the pyrochlore $\text{Y}_2\text{Sn}_2\text{O}_7$.* 2002, *Materials Research Bulletin*, Vol. 37, pp. 745-751.
20. **A.M. Srivastava and W.W. Beers** *On the impurity trapped exciton luminescence in $\text{La}_2\text{Zr}_2\text{O}_7: \text{Bi}^{3+}$.* 1990, *Journal of Luminescence.*, Vol. 81, pp. 293-300.
21. **G. Blasse and A. Bril.** *Investigations on Bi^{3+} -Activated Phosphors.* 1968, *Journal of Chemical Physics*, Vol. 48, pp. 217-222.
22. **S.H. Shin, D.Y. Jeon and K.S. Suh.** *Charge-transfer nature in luminescence of $\text{YNbO}_4:\text{Bi}$ blue phosphor.* 2001, *Journal of Applied Physics*, Vol. 90, pp. 5986-5990.
23. **G. Boulon.** *Processus de photoluminescence dans les oxydes et les orthovanadates de terres rares polycristallins activés par l'ion Bi^{3+} .* 1971, *J. Phys. (Paris)*, Vol. 32, pp. 333-347.
24. **K.P.F. Siqueira, R.L. Moreira and A. Dias.** *Synthesis and Crystal Structure of Lanthanide Orthoniobates Studied by Vibrational Spectroscopy.* 2010, *Chemistry of Materials*, Vol. 22, pp. 2668-2674.
25. **L. Sun, X. Zhao, Y. Li, P. Li, H. Sun, X. Cheng and W. Fan.** *First-principles studies of electronic, optical, and vibrational properties of LaVO_4 polymorph.* 2010, *Journal of Applied Physics*, Vol. 108, pp. 093519-093528.
26. **A.A. Setlur and A.M. Srivastava.** *The nature of Bi^{3+} luminescence in garnet hosts.* 2006, *Optical Materials*, Vol. 29, pp. 410-415.
27. **M. Nikl, A. Novoselov, E. Mihoková, K. Polák, M. Dusek, B. McClune, A. Yoshikawa and T. Fukuda.** *Photoluminescence of Bi^{3+} in $\text{Y}_3\text{Ga}_5\text{O}_{12}$ single-crystal host.* 2005, *Journal of Physics Condensed Matter*, Vol. 17, pp. 3367-3375.
28. **M. Ilmer, B.C. Grabmaier and G. Blasse.** *Luminescence of Bi^{3+} in gallate garnets.* 1994, *Chemical Materials*, Vol. 6, pp. 204-206.

29. **Y. Zorenko, V. Gorbenko, T. Voznyak and M. Nikl.** *Luminescence spectroscopy of Bi^{3+} single and dimer centers in $\text{Y}_3\text{Al}_5\text{O}_{12}:\text{Bi}$ single crystalline films.* 2007, *Radiation Measurements*, Vol. 42, pp. 882-886.
30. **V. Babin, V. Gorbenko, A. Krasnikova, A. Makhova, M. Nikl, S. Zazubovich, Yu. Zorenko.** *Photoluminescence of $\text{Lu}_3\text{Al}_5\text{O}_{12}:\text{Bi}$ and $\text{Y}_3\text{Al}_5\text{O}_{12}:\text{Bi}$ single crystalline films.* 2010, *Radiation Measurements*, Vol. 45, pp. 331-335.
31. **V. Babin, V. Gorbenko, A. Krasnikov, A. Makhov, M. Nikl, K. Polak, S. Zazubovich and Yu. Zorenko.** *Peculiarities of excited state structure and photoluminescence in Bi^{3+} -doped $\text{Lu}_3\text{Al}_5\text{O}_{12}$ single-crystalline films.* 2009, *Journal of Physics Condensed Matter*, Vol. 21, pp. 415502-415510.
32. **X. Wang, I. Loa, K. Syassen, M. Hanfland, and B. Ferrand.** *Structural properties of the zircon- and scheelite-type phases of YVO_4 at high pressure.* 2004, *Physical Reviews B*, Vol. 70, pp. 064109-064114.
33. **P. Boutinaud.** *Optical Processes in $(\text{Y,Bi})\text{VO}_4$ Doped with Eu^{3+} or Pr^{3+} .* 2014, *Journal of Physics Condensed Matter*, Vol. 26, pp. 405501-405509.
34. **A. Jayaraman, G.A. Kourouklis, G.P. Espinosa, A.S. Cooper, L.G. Van Uitert.** *A high-pressure Raman study of yttrium vanadate (YVO_4) and the pressure-induced transition from the zircon-type to the scheelite-type structure.* 1987, *Journal of Physics and Chemistry of Solids*, Vol. 48, pp. 755-759.
35. **G. Chen, N.A. Stump, R.G. Haire, J.R. Peterson and M.M. Abraham.** *Pressure-induced phase transition in $\text{YVO}_4:\text{Eu}^{3+}$: A luminescence study at high pressure.* 1992, *Journal of Physics and Chemistry of Solids*, Vol. 53, pp. 1253-1257.
36. **V. Panchal, D. Errandonea, A. Segura, P. Rodríguez-Hernandez and A. Muñoz.** *The electronic structure of zircon-type orthovanadates: Effects of high-pressure and cation substitution.* 2011, *Journal of Applied Physics*, Vol. 110, p. 043732.
37. **A. Kubicki, P. Bojarski, M. Grinberg, M.S. adownik and B. Kuklin'ski .** *Time-Resolved Streak Camera System with Solid State Laser and Optical Parametric Generator in Different Spectroscopic Applications.* 2006, *Optics Communications*, Vol. 263, p. 275–280.
38. **L. Merrill and W.A. Bassett.** *Miniature Diamond Anvil Pressure Cell for Single Crystal X-Ray-Diffraction Studies.* 1974, *Review of Scientific Instruments*, Vol. 45, p. 290–294.
39. **W. Barendswaard, R.T. Weber and J. H. Van der Waals,** *An Electron Paramagnetic RES Study of the Luminescent Triplet State of VO_4^{3-} in YVO_4 and $\text{YP}_{0.96}\text{V}_{0.04}\text{O}_4$ Single Crystals at 1.2 K.* 1987, *Journal of Chemical Physics*, Vol. 87, p. 3731–3738.
40. **K.Y. Li and D.F. Xue.** *Estimation of Electronegativity Values of Elements in Different Valence States.* 2006, *Journal of Physical Chemistry*, Vol. 110, p. 11332–11337.
41. **S. Mahlik, E. Cavalli, M. Amer and P. Boutinaud.** *Energy Levels in $\text{CaWO}_4:\text{Tb}^{3+}$ at High Pressure.* 2015, *Physical Chemistry Chemical Physics*, Vol. 17, p. 32341–32346.

42. **C.W. Struck and W.H. Fonger.** *Thermal Quenching of Tb^{3+} , Tm^{3+} , Pr^{3+} and Dy^{3+} 4f n Emitting States in La_2O_2S .* 1971, Journal of Applied Physics, Vol. 42, p. 4515–4517.
43. **M.B. Smirnov, A.P. Mirgorodsky, V. Kazimirov and R. Guinebretière.** *Bond-Switching Mechanism for the Zircon-Scheelite Phase Transition.* 2008, Physical Review B, Condensed Matter and Material Physics, Vol. 78, p. 094109.
44. **S. Mahlik, A. Lazarowska, K. Szczodrowski, M. Grinberg, E. Cavalli and P. Boutinaud.** *Optical Processes in $YVO_4:Eu^{3+}$ Across Zircon-to-Scheelite Phase Transition.* 2015, Journal of Luminescence, Vol. 165, p. 19–22.
45. **G. Blasse and A. Bril.** *Influence of Crystal Structure on Fluorescence of Oxidic Niobates and Related Compounds.* 1968, Zeitschrift für Physikalische Chemie, Vol. 57, p. 187–202.

Chapter 4: Luminescence of Sb^{3+} in closed-shell transition metal oxides

4.1. Introduction

Trivalent antimony has an $5s^2$ electron configuration and thereby belongs to the mercury-like family like Bi^{3+} . Nevertheless, the luminescence of Sb^{3+} has much less been studied than that of Bi^{3+} . In this concern, the luminescence of Sb^{3+} in closed shell transition metal oxides is, to our knowledge, totally unknown. The most recent literature dealing with the luminescence properties of Sb^{3+} essentially date of the mid-eighties of the previous century⁽¹⁾⁻⁽¹¹⁾. These studies have demonstrated similarities of behaviors between Sb^{3+} and Bi^{3+} : in both cases, the luminescence shows strong dependence with temperature, excitation wavelength and nature of the nearby environment. For both, the optical properties are also affected by the stereochemical activity of the s^2 lone pair, i. e. with the degree of asymmetry of the coordination polyhedron and related Jahn-Teller effects⁽³⁾⁻⁽¹³⁾. At this stage, it should be noted that if Sb^{3+} and Bi^{3+} present similarities, they also have noticeable differences: (1) the former has a much smaller ionic radius and is not known with coordination numbers larger than 6⁽¹⁴⁾. This suggests a very marked off-centered position of Sb^{3+} in large crystal sites. This, in fact, accounts for the generally larger Stokes shifts of the Sb^{3+} emission with respect to the Bi^{3+} emission and its sensitivity to the Jahn-Teller effect. (2) The small Sb^{3+} ion may also possibly substitute for transition or post-transition metal cations (M^{n+}) contained in the host lattices to create antimonate units, from which luminescence may occur at low temperature. This doping possibility was discarded for Bi^{3+} in the previous chapter owing to the much bigger size of this ion. Consequently, we anticipate the luminescence processes of Sb^{3+} -activated compounds to be even more complex to interpret than those of Bi^{3+} . We Note here that we did not consider any possible luminescence activity from Sb^{5+} species that could eventually be stabilized in M^{5+} (i. e. Nb^{5+} , Ta^{5+}) or M^{6+} (i. e. Mo^{6+}) sites. To our knowledge, this activity has not yet been unambiguously demonstrated.

Among the Sb^{3+} -activated phosphors, the most famous is certainly the doubly doped Sb^{3+} , Mn^{2+} halophosphate $\text{Ca}_{10}(\text{PO}_4)_6(\text{F},\text{Cl})$ that shows so bright luminescence that it has been used as a commercial phosphor in lamps for decades. Sb^{3+} was shown to be responsible for the blue emission and for the sensitization of the yellow emission of Mn^{2+} in this material⁽⁴⁾. The Stokes shift of Sb^{3+} in this phosphate is as large as 19000 cm^{-1} , which should normally be concomitant with a low quenching temperature of the

corresponding luminescence⁽¹⁵⁾. To date, it is still unexplained why Sb^{3+} shows so intense luminescence at room temperature in this material⁽¹⁶⁾. The accommodating site of Sb^{3+} in the fluoroapatite $\text{Ca}_{10}(\text{PO}_4)_6\text{F}_2\text{-Sb}^{3+}$ is also still subject of discussion. Two Ca^{2+} sites Ca(1) and Ca(2) are basically available for Sb^{3+} in this lattice. It was thought that Sb^{3+} may substitute preferentially to Ca(2) but other studies say that it is in fact incorporated as $(\text{SbO}_3)^{3-}$ units replacing $(\text{PO}_4)^{3-}$ ^{(2),(4)}. The question is still open.

Our motivation in the present context is, first, to check if Sb^{3+} can show luminescence in closed shell transition metal oxides and, second, check if, by analogy with Bi^{3+} , D transitions could be present in these materials. To our knowledge, such transitions have never been identified yet for Sb^{3+} . In the frame of the present work, we will limit ourselves to systems in which the transition metal adopts a coordination of at least 6. This means that vanadates, molybdates or tungstates with zircon or scheelite crystal structure will not be the subject of deep investigations in this chapter. In this context, the (EF) and MMCT models will be adapted to help ascribing the origin of the luminescence signals. Hence, the environmental factors $he(X)$ will be calculated using Equation (9) of Chapter 1 for all cation sites X considered as possible doping sites for Sb^{3+} in all the investigated host lattices.

Two series of antimony doped compounds will therefore be investigated: the first series is composed of materials showing regular electron transitions for Sb^{3+} (i. e. A-like transitions), as ascribed in the archival literature. These lattices either do not contain transition metals or contain trivalent d^0 cations for which the electronegativity $\chi_{\text{CN}}(\text{M}^{3+})$ is rather small (Sc^{3+} , Y^{3+} , Lu^{3+} and La^{3+} , see Appendix A), i.e. the corresponding MMCT energy is expected to be higher relative to the A-like transitions. In this case, we will look for an empirical equation connecting the energy of the A transition and $he(X)$, the same as done by Wang for Bi^{3+} and Pb^{2+} (see Chapter 1). The second series will include the closed shell transition metal oxides that are expected to present transition with charge transfer character (i.e. D band) by referring to the supposed analogy between Bi^{3+} and Sb^{3+} . In this connection, we have prepared and studied the luminescence of the following materials: CaZrO_3 , SrZrO_3 , YNbO_4 , CaNb_2O_6 , SrNb_2O_6 and YTbO_4 doped with trivalent antimony. Their luminescence will be reported for the first time in this work and an empirical equation will be tentatively introduced on the model of Equation (30) in Chapter 1, to account for the observed data. In addition, the luminescence spectra of $\text{CaMoO}_4\text{-Sb}^{3+}$ and $\text{SrMoO}_4\text{-Sb}^{3+}$ will also be reported, although not discussed in details in this manuscript.

4.2. Synthesis of closed shell transition metal oxides doped with Sb³⁺

The raw chemicals and experimental conditions (temperature/duration) used for the synthesis of the Sb³⁺-doped transition metal oxides are given in Table 1. The nominal doping rate was 1 mol %. The obtained compounds were checked by XRD (X-ray diffraction) and their corresponding JCPDS numbers are shown in Table 1. Corresponding patterns are shown in Appendix C.

Table 1 Raw materials and experimental conditions used for the synthesis of several closed-shell transition metal oxides doped with Sb³⁺ and the JCPDS number of the obtained structure.

Host lattice	Raw chemicals (analytical grade)	Temperature (°C) / duration (h)	JCPDS standard
CaZrO ₃	CaCO ₃ , ZrO ₂	1100/12	01-72-7550
SrZrO ₃	SrCO ₃ , ZrO ₂	1200/10	01-076-9442
YNbO ₄	Y ₂ O ₃ , Nb ₂ O ₅	1500/12	01-072-2077
SrNb ₂ O ₆	SrCO ₃ , Nb ₂ O ₅	1200/12	45-0227
M'-YTao ₄	Y ₂ O ₃ , Ta ₂ O ₅	1200/10	9-0341
CaMoO ₄	CaCO ₃ , MoO ₃	780/6	7-0212
SrMoO ₄	SrCO ₃ , MoO ₃	1200/10	96-153-0911

4.3. Luminescence of transition metal oxides doped with Sb³⁺

The photoluminescence emission and excitation spectra were collected using the same set-up as in our previous studies. The spectra were corrected from the instrument response using sodium salicylate. Owing to the low efficiency of Sb³⁺ luminescence at room temperature, the spectra were collected at 77 K. At this temperature, self-luminescence of the corresponding host lattices is possible. This issue will be carefully checked on the basis of the archival literature.

4.3.1. Luminescence of Sb³⁺-doped Zirconates

Zirconate perovskites like CaZrO₃ and SrZrO₃ are examples of compounds in which the transition metal is tetravalent and octahedrally coordinated. Undoped CaZrO₃ is known to show optical absorption below 245 nm with a regular emission in the blue at 430 nm⁽¹⁷⁾. The situation is similar in undoped SrZrO₃⁽¹⁸⁾. Other works report on a photoluminescence emission at 395 nm (consisting of 3 overlapping contributions) excited at 246 nm in highly crystallized SrZrO₃⁽¹⁹⁾. Doping with Pb²⁺ induces an emission in the UV (365 nm, excited at 285 nm in CaZrO₃ or 360 nm, excited at 275 nm in SrZrO₃)^{(20),(21)}. These features were ascribed to A transitions. Doping with Bi³⁺ leads to a UV emission in CaZrO₃ (≈ 390 nm) for

a corresponding excitation at ≈ 310 nm. These features also possess an A character^{(22),(23)}. As shown in Figure 1, the emission spectra of CaZrO_3 and SrZrO_3 doped with Sb^{3+} consist of a broad green signal covering the 450 – 650 nm region. This band consists of at least two overlapping contributions. Its excitation spectrum covers a wide wavelength range from ≈ 340 nm to 250 nm (instrument limit) and probably below. The maximum of the lowest-lying excitation band is ≈ 310 nm for $\text{CaZrO}_3\text{-Sb}^{3+}$ and ≈ 305 nm for $\text{SrZrO}_3\text{-Sb}^{3+}$. These low-lying features are ascribed to Sb^{3+} . We note here that the position of the lowest-lying excitation band in $\text{CaZrO}_3\text{-Sb}^{3+}$ is consistent with that of $\text{CaZrO}_3\text{-Bi}^{3+}$. The resulting emission is however strongly red shifted, revealing a much larger Stokes shift in the case of Sb^{3+} . The same is anticipated for $\text{SrZrO}_3\text{-Sb}^{3+}$ relative to $\text{SrZrO}_3\text{-Bi}^{3+}$.

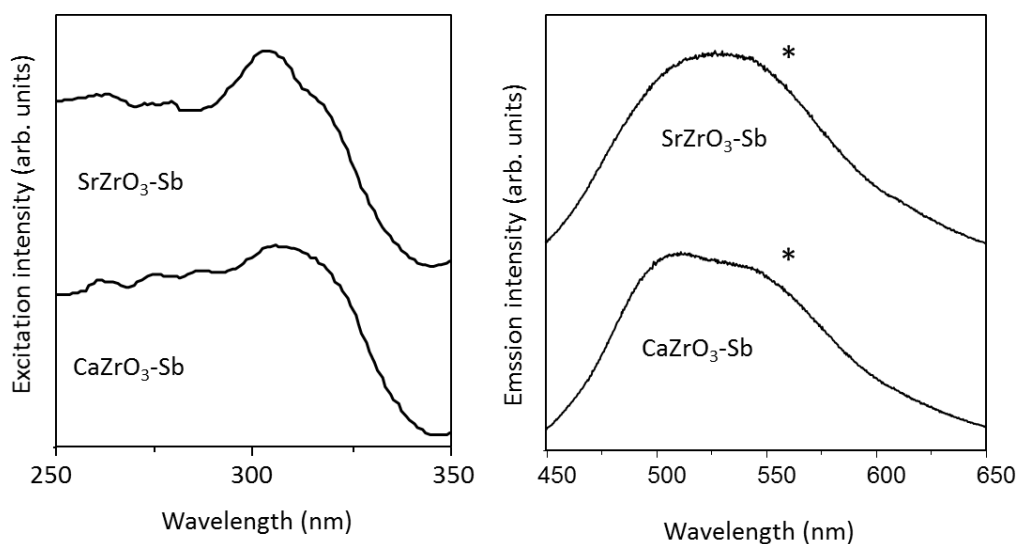


Figure 1. Excitation (left) and emission (right) spectra of the Sb^{3+} -doped zirconates at 77 K. Symbols* indicate the monitored wavelengths for the excitation spectra. Emission was collected upon excitation at 325 nm.

4.3.2. Luminescence of Sb^{3+} -doped niobates and tantalates

Niobates and M' -type tantalate are examples of lattices in which the transition metal is pentavalent and octahedrally coordinated. In this case, the values of electronegativities $\chi_6(\text{Nb}^{5+})$ and $\chi_6(\text{Ta}^{5+})$ exceed that of $\chi_6(\text{Zr}^{4+})$ (see Appendix A). Like for the zirconates, the luminescence of undoped YNbO_4 , SrNb_2O_6 and $\text{M}'\text{-YTao}_4$ is of charge transfer character. For YNbO_4 , the excitation band peaks at 265 nm for an emission at 420 nm^{(24),(25)}. We did not find information on the luminescence of undoped SrNb_2O_6 , but we found that CaNb_2O_6 shows an emission at 500 nm upon excitation at 275 nm⁽²⁶⁾. SrNb_2O_6 should

behave in a comparable way. For $M'-YTaO_4$, the excitation peaks at 230 nm for an emission at 340 nm⁽²⁵⁾. Doping with Bi^{3+} leads to a band-like emission in the blue (≈ 475 nm) in $YNbO_4$ for a low-lying excitation reported at 310⁽²⁷⁾, 314⁽²⁸⁾ or 324 nm (see Chapter 3). $M'-YTaO_4-Bi^{3+}$ glows in the green region (515 nm) for an excitation peaking at 343 nm. To our knowledge, the luminescence of $SrNb_2O_6-Bi^{3+}$ has not been reported yet, but $CaNb_2O_6-Bi^{3+}$ has been shown in Chapter 3 to emit at 490 nm for an excitation peaking at 325 nm. Doping with Sb^{3+} yields broad emissions that appear to be red shifted with respect to Bi^{3+} (Figure 2).

In the niobates, these bands consist of at least two overlapping contributions, as evidenced by the corresponding excitation spectra (* and α). The features located in the red spectral region (α) are excited at ≈ 335 nm. They are ascribed to Sb^{3+} . The other feature in the green region (*) are excited at ≈ 280 nm and are presumably host-related. In $YTaO_4-Sb^{3+}$, the red band observed in Figure 2 and its corresponding excitation are ascribed to Sb^{3+} .

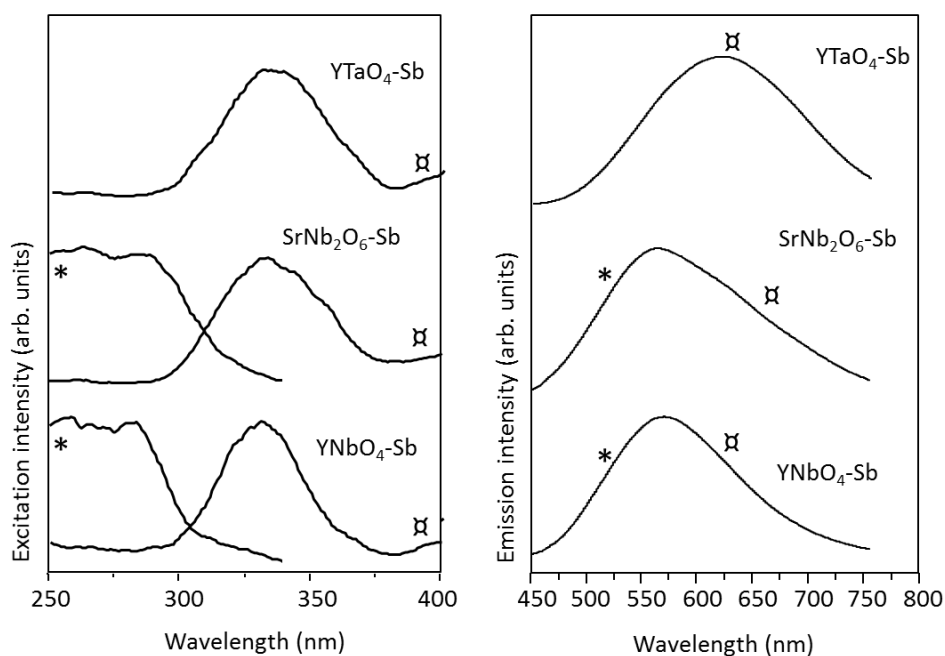


Figure 2. Excitation (left) and emission spectra (right) of the Sb^{3+} -doped niobates and tantalate at 77 K. Symbols * and α indicate the monitored wavelengths for the excitation spectra. Emission was collected upon excitation at 330 nm.

4.3.3. Luminescence of Sb^{3+} -doped molybdates

Molybdates SrMoO_4 and CaMoO_4 are examples of compounds in which the transition metal is octavalent and tetrahedrally coordinated. Undoped CaMoO_4 shows an emission at 534 nm when excited with 260 nm and another one at 546 nm when excited with 320 nm⁽²⁹⁾. Undoped SrMoO_4 shows an emission peaked at 429 nm when excited with 288 nm. Both compounds when doped with Sb^{3+} show very broad emission bands covering the blue, green and red regions from 450 to 750 nm. In $\text{SrMoO}_4:\text{Sb}^{3+}$, the emission band is peaking at ≈ 560 nm upon excitation at 300 nm (Figure 3). This could be host-related. The situation is different when the exciting wavelength is increased. At 330 nm excitation, the band has its maximum at ≈ 620 nm, while with 360 nm excitation the maximum emission is centred at ≈ 690 nm. These features are ascribed to Sb^{3+} .

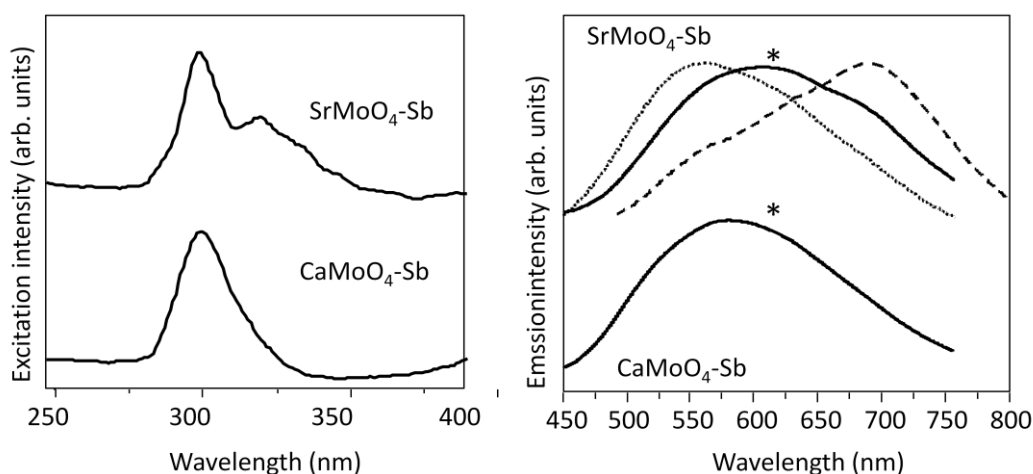


Figure 3. Excitation (left) and emission (right) of Sb^{3+} -doped molybdates at 77 K. The symbol * indicate the monitored wavelength for the excitation spectra. Emission corresponding to, dashed line, solid line and dotted line were recorded upon excitation at 300, 330 and 360 nm respectively in $\text{SrMoO}_4:\text{Sb}^{3+}$.

The excitation was recorded for the monitored emission wavelength of ≈ 620 nm and shows a doublet structure with a maximum at ≈ 310 nm and a shoulder at 326 nm. This is related to Sb^{3+} . This behaviour was observed in other Sb^{3+} -doped compounds for which the excitation band shows a doublet or a triplet structure. This was ascribed to the crystal field splitting of the $^3\text{P}_1$ level in some cases (i. e. in ScBO_3 and LuBO_3) and to a Jahn-Teller effect in other cases (i. e. in CaS , MgS , in the elpasolites $\text{Cs}_2\text{NaMCl}_6$ with $\text{M} = \text{Sc}$, Y , La and in the zircon-structured phosphate MPO_4 with $\text{M} = \text{Sc}$, Lu , Y)^{(3),(5),(6)}. In $\text{CaMoO}_4:\text{Sb}^{3+}$, the emission is maximum at ≈ 580 nm. The excitation was measured at ≈ 625 nm and

shows a band with max at ≈ 315 nm. When doped with Bi^{3+} , the compound shows yellow emission at 586 nm when excited at 320 nm⁽²⁹⁾. This means that the emission of Sb^{3+} is similar to that of Bi^{3+} in CaMoO_4 with a small red shift and larger stokes shift.

4.4. Application of the EF and MMCT models to Sb^{3+} -doped compounds

4.4.1. Calculation of environmental factors $he(X(i))$

We have compiled in Table 2 the values of the environmental factors $he(X)$ for all possible sites X in all the compounds of interest whose crystal structure is available from ICSD database⁽³⁰⁾. For lattices having several types of crystal structures, we have calculated the $he(X)$ values using the structure of the polymorph described in the references from where we found the luminescence characteristics. For compounds whose structure was not described in the references, we have carried out the calculations for all types of structures that could be found for the lattice. For the compounds prepared in this work, the calculations were made only for the type of crystal structure that was confirmed by XRD. As previously mentioned, doping of Sb^{3+} in the transition metal sites was considered as a possible option.

We have further noted that the vaterite structure of YBO_3 was shown to have either the space group $\text{P6}_3/\text{m}$ which led to Y^{3+} sites with 8-fold coordination⁽³¹⁾, or the space group $\text{P6}_3/\text{mmc}$ with Y^{3+} having the 6 and 6+6 fold coordination⁽⁵⁾. Owing to this structural uncertainty, we have decided to discard the lattice YBO_3 from our list. For the same reason, only the high temperature calcite polymorph of LuBO_3 is retained. The phosphates $\text{M}(\text{PO}_3)_3\text{-Sb}^{3+}$, with $\text{M} = \text{La}, \text{Gd}, \text{Y}, \text{Lu}, \text{Sc}$ are known to possess many polymorphs, which creates uncertainties regarding their exact crystal structure. $\text{La}(\text{PO}_3)_3$ has the crystal structure of $\text{Nd}(\text{PO}_3)_3$ (space group C222_1) while the others ($\text{M} = \text{Gd}, \text{Y}, \text{Lu}, \text{Sc}$) have the crystal structure of $\text{Yb}(\text{PO}_3)_3$ (space group $\text{P2}_1/\text{c}$)⁽¹⁾. These attributions were based on the work of Hong dated from the mid-seventies⁽³²⁾. More recently, however, a new space group (R-3h) has been proposed for $\text{Yb}(\text{PO}_3)_3$ ⁽³³⁾, which therefore raises perplexities. As a matter of fact, we found that $\text{Sc}(\text{PO}_3)_3$ is described in none of the above space groups, $\text{Gd}(\text{PO}_3)_3$ is described in the space group of $\text{Nd}(\text{PO}_3)_3$ instead of that of $\text{Yb}(\text{PO}_3)_3$, $\text{Lu}(\text{PO}_3)_3$ is described in space group R-3h and $\text{Y}(\text{PO}_3)_3$ exists with both space groups R-3h and $\text{P2}_1/\text{c}$. In this confusing context, we have decided to discard $\text{Sc}(\text{PO}_3)_3$ from our list and retain $\text{Gd}(\text{PO}_3)_3$ (C222_1), $\text{Lu}(\text{PO}_3)_3$ (R-3h), $\text{Y}(\text{PO}_3)_3$ (C222_1 and R-3h) and $\text{La}(\text{PO}_3)_3$ (R-3h) as plausible lattices.

We also give in Table 2 the experimental energy $E_{\text{exp}}(\text{Sb}^{3+})$ of the lowest-lying photoluminescence excitation signals of Sb^{3+} , as picked up from the literature or from the present work. The literature data

concern lattices from CaS to LaBO₃ in Table 2. For these (except AlPO₄⁽²⁾), the lowest lying excitation is nominally ascribed to A transitions. LaOCl-Sb³⁺ shows two emissions, a violet one ascribed to single Sb³⁺ ions and a green one ascribed to Sb³⁺ dimers⁽³⁴⁾. Only the former was included in Table 2.

Table 2 Corrected distance $d_{\text{corr}}(X)$ between Sb³⁺ and the cation site X, structural parameter $he(X)$ at site X and electronegativity $\chi_{\text{CN}}(M^{n+})$ of the metal cation in the lattice. CN is the coordination number at the considered X site. CN' is the coordination number at the closed shell transition metal site Mⁿ⁺. n.a. means not applicable.

Host lattice (ICSD)	X(CN)	$d_{\text{corr}}(X)$ (Å)	$he(X)$	$\chi_{\text{CN}}(M^{n+})$
CaS (619529)	Ca ²⁺ (6)	n.a.	1.96	1.16
MgS 30241	Mg ²⁺ (6)	n.a.	1.59	1.23
LaOCl (40297)	La ³⁺ (9)	3.55	3.01	1.26
Cs ₂ NaLaBr ₆ (426112)	Cs ⁺ (12) Na ⁺ (6) La ³⁺ (6)	4.43 5.63 8.01	0.16 0.85 1.74	n.a. n.a. 1.33
Cs ₂ NaYBr ₆ (65733)	Cs ⁺ (12) Na ⁺ (6) Y ³⁺ (6)	4.33 5.65 7.99	0.17 0.86 1.39	n.a. n.a. 1.34
Cs ₂ NaLaCl ₆ (425945)	Cs ⁺ (12) Na ⁺ (6) La ³⁺ (6)	4.72 5.46 7.72	0.15 0.73 1.45	n.a. n.a. 1.33.
Cs ₂ NaYCl ₆ (65732)	Cs ⁺ (12) Na ⁺ (6) Y ³⁺ (6)	4.09 5.37 7.59	0.16 0.72 1.21	n.a. n.a. 1.34
Y ₂ O ₃ (23811)	Y ³⁺ (6) - C2 Y ³⁺ (6) - S6	3.46 3.45	1.61 1.61	1.34 1.34
ScPO ₄ (74483)	Sc ³⁺ (8)	3.53	0.97	1.35
YPO ₄ (56113)	Y ³⁺ (8)	3.63	1.14	1.29
LuPO ₄ (2505)	Lu ³⁺ (8)	3.60	1.08	1.37
LaPO ₄ (21066)	La ³⁺ (9)	3.91	1.13	1.26
AlPO ₄ (16542)	Al ³⁺ (4)	n.a.	2.50	1.51
LiLaP ₄ O ₁₂ (416877)	Li ⁺ (6) La ³⁺ (8)	n.a. 5.49	2.16 1.32	n.a. 1.28
YP ₃ O ₉ (R-3h 98554)	Y(1) ³⁺ (6) Y(2) ³⁺ (6) Y(3) ³⁺ (6)	Y(1)-Y(2)=5.75	1.95 1.88 1.99	1.29 1.29 1.29
YP ₃ O ₉	Y(1) ³⁺ (6)	Y(1)-Y(2)=5.28	2.07	1.29

(P21/c 98556)	Y(2) ³⁺ (6) Y(3) ³⁺ (6) Y(4) ³⁺ (6)		2.05 2.05 2.06	1.29 1.29 1.29
LuP ₃ O ₉ (R-3h 260036)	Lu(1) ³⁺ (6) Lu(2) ³⁺ (6) Lu(3) ³⁺ (6)	Lu(1)-Lu(3) = 5.73	2.02 1.94 1.98	1.37 1.37 1.37
GdP ₃ O ₉ (155301)	Gd ³⁺ (8)	4.02	1.23	1.33
LaP ₃ O ₉ (202640)	La ³⁺ (8)	4.11	1.23	1.28
Sr ₃ (PO ₄) ₂ (69449)	Sr(1) ²⁺ (12) Sr(2) ²⁺ (10)	n.a. n.a.	1.01 0.29	n.a. n.a.
Ca ₁₀ (PO ₄) ₆ F ₂ (94082)	Ca(1) ²⁺ (9) Ca(2) ²⁺ (7)	n.a. n.a.	0.72 1.18	n.a. n.a.
ScBO ₃ (65010)	Sc ³⁺ (6)	3.74	1.49	1.41
LuBO ₃ (194864) calcite	Lu ³⁺ (6)	3.87	1.66	1.43
LaBO ₃ (35535)	La ³⁺ (9)	3.78	0.53	1.26
CaZrO ₃ (37264)	Ca ²⁺ (8+4) Zr ⁴⁺ (6)	3.08 4.02	1.19 1.78	n.a. 1.61
SrZrO ₃ (650)	Sr ²⁺ (8+4) Zr ⁴⁺ (6)	3.19 4.12	1.46 1.53	n.a. 1.61
SrNb ₂ O ₆ (20348)	Sr ²⁺ (8) Nb(1) ⁵⁺ (6) Nb(2) ⁵⁺ (6)	3.27 3.26 3.73	1.25 2.18 3.09	n.a. 1.86 1.86
YNbO ₄ (100176)	Y ³⁺ (8) Nb ⁵⁺ (6)	3.63 (Y) 3.41 (Nb) 3.60 (Y) 3.54 (Nb)	1.04 1.29	1.29 1.29 1.86 1.86
M'-YTaO ₄ (38420)	Y ³⁺ (8) Ta ⁵⁺ (6)	3.55 (Y) 3.36 (Ta) 3.55 (Y) 3.45 (Ta)	1.06 1.28	1.29 1.29 1.92 1.92
CaMoO ₄ (62219)	Ca ²⁺ (8)	n.a.	1.015	n.a.
SrMoO ₄ (28025)	Sr ²⁺ (8)	n.a.	1.18	n.a.

In a few cases, the excitation band shows a doublet or a triplet structure which is ascribed either to a crystal field splitting of the ³P₁ level (i. e. in ScBO₃ and LuBO₃, in their calcite form) or to a Jahn-Teller effect (i. e. in CaS, MgS, in the elpasolites Cs₂NaMCl₆ with M = Sc, Y, La and in the zircon-structured

phosphate MPO_4 with $\text{M} = \text{Sc, Lu, Y}$). In these cases, only the lowest-lying feature is retained. We have also added in Table 2 some useful data (i. e. d_{corr} and χ_{CN}) for the calculation of $\text{Sb}^{3+} \rightarrow \text{M}^{n+}$ MMCT energies. The necessary χ_{CN} values were taken from Appendix A. Note that incorporation of Sb^{3+} in the very small P^{5+} or B^{3+} sites was excluded in the present work. This is in line with the results reported in ref.(2) stating that in phosphate lattices, Sb^{3+} replaces a host lattice cation and is not substituted to $(\text{PO}_4)^{3-}$ groups to form $(\text{SbO}_3)^{3-}$ units. Therefore, in lattices like ScPO_4 , YPO_4 , LaP_3O_9 , ScBO_3 , LaBO_3 , etc..., the only possible doping site is a closed shell transition metal site (Sc^{3+} , Y^{3+} or La^{3+}). The same goes for Y_2O_3 in which two sites of point symmetry S_6 and C_2 . When a lattice incorporates more than one type of closed shell transition metal (e.g. Y^{3+} and Nb^{5+} in YNbO_4), more than one MMCT process may occur. Taking $\text{YNbO}_4\text{-Sb}^{3+}$, we may have $\text{Sb}^{3+} \rightarrow \text{Y}^{3+}$ and $\text{Sb}^{3+} \rightarrow \text{Nb}^{5+}$ MMCTs, the energy of which depending on the electronegativity of the cations and the shortest distance between them. This, of course, depends on the considered doping site (either Y^{3+} or Nb^{5+}) for Sb^{3+} . This raises therefore four different situations (for $\text{YNbO}_4\text{-Sb}^{3+}$ and $\text{M'-YTao}_4\text{-Sb}^{3+}$) that are detailed in Table 2. For YNbO_4 , for instance, we have indeed to consider the four shortest distances Y-Ta, Y-Y, Ta-Y and Ta-Ta, depending on the considered doping sites.

4.4.2. Establishing an empirical equation for A band transitions

We give in Table 3 the experimental energy values E_{exp} of the lowest-lying excitation bands that are ascribed to A-like transitions in the literature.

Table 3 Experimental E_{exp} and calculated E_A energies in a selection of Sb^{3+} -doped compounds. sh:shoulder.

Host	Cation site (CN)	$E_{\text{exp}}(\text{cm}^{-1})$	$E_A(X), \text{cm}^{-1}$
CaS	$\text{Ca}^{2+}(6)$	25000 ⁽⁶⁾	25160
MgS	$\text{Mg}^{2+}(6)$	24100 ⁽⁶⁾	31250
LaOCl	$\text{La}^{3+}(9)$	40000 ⁽⁷⁾	7875
$\text{Cs}_2\text{NaLaBr}_6$	$\text{Cs}^+(12)$	27300 ⁽¹¹⁾	54790
	$\text{Na}^+(6)$		43430
	$\text{La}^{3+}(6)$		28780
$\text{Cs}_2\text{NaYBr}_6$	$\text{Cs}^+(12)$	27450 ⁽¹¹⁾	54620
	$\text{Na}^+(6)$		43265
	$\text{Y}^{3+}(6)$		34540
$\text{Cs}_2\text{NaLaCl}_6$	$\text{Cs}^+(12)$	30900 ⁽³⁵⁾	54950
	$\text{Na}^+(6)$		45400
	$\text{La}^{3+}(6)$		33550
$\text{Cs}_2\text{NaYCl}_6$	$\text{Cs}^+(12)$	30900 ⁽³⁵⁾	54790
	$\text{Na}^+(6)$		45570
	$\text{Y}^{3+}(6)$		37500

Y ₂ O ₃	Y ³⁺ (6) - C2	27400 ⁽³⁶⁾	30920
	Y ³⁺ (6) - S6	30300 ⁽³⁶⁾	30920
ScPO ₄	Sc ³⁺ (8)	41670 ⁽³⁾	41450
YPO ₄	Y ³⁺ (8)	40815 ⁽³⁾	38650
LuPO ₄	Lu ³⁺ (8)	40815 ⁽³⁾	39640
LaPO ₄	La ³⁺ (9)	42765 ⁽²⁾	38820
AlPO ₄	Y(1) ³⁺ (6)	42500 ⁽²⁾	22865
	Y(2) ³⁺ (6)		24235
	Y(3) ³⁺ (6)		21915
YP ₃ O ₉ (P21/c)	Y(1) ³⁺ (6)	42500 ⁽¹⁾	23350
	Y(2) ³⁺ (6)		23680
	Y(3) ³⁺ (6)		23680
	Y(4) ³⁺ (6)		23515
LuP ₃ O ₉	Lu(1) ³⁺ (6)	40500 ⁽¹⁾	21320
	Lu(2) ³⁺ (6)		22925
	Lu(3) ³⁺ (6)		22275
GdP ₃ O ₉	Gd ³⁺ (8)	41000 ⁽¹⁾	37360
LaP ₃ O ₉	La ³⁺ (8)	41500 ⁽¹⁾	37170
Sr ₃ (PO ₄) ₂	Sr(1) ²⁺ (12)	40000 ⁽⁸⁾	40795
	Sr(2) ²⁺ (10)		52650
Ca ₁₀ (PO ₄) ₆ F ₂	Ca(1) ²⁺ (9)	38365 ⁽²⁾	45570
	Ca(2) ²⁺ (7)		38000
ScBO ₃	Sc ³⁺ (6)	32700 ⁽⁵⁾	32900
LuBO ₃	Lu ³⁺ (6)	33400 ⁽⁵⁾	30100
LaBO ₃	La ³⁺ (9)	42000 ⁽⁵⁾ sh	48690

Plotting E_{exp}(Sb³⁺) against *he*(X) reveals a linear decreasing variation but with an important dispersion of the data (Figure 4).

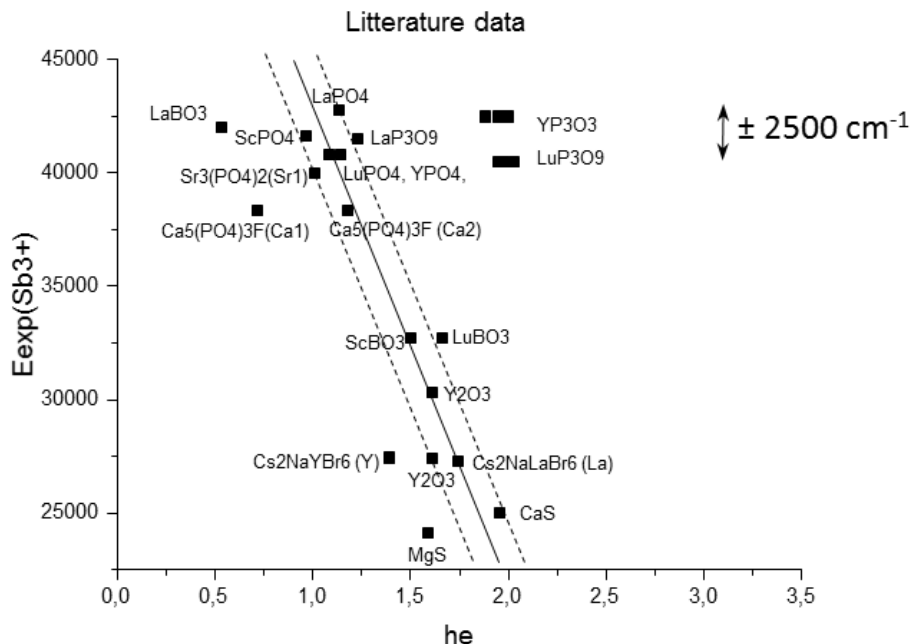


Figure 4. Plot of the structural parameter he versus the experimental energies of Sb^{3+} doped-materials, E_{exp} , identified as A bands in the literature.

Several factors may account for that:

- 1) The relatively low accuracy of the energy position of the lowest excitation band in the considered Sb^{3+} -doped systems; this position being collected either at liquid helium, liquid nitrogen or room temperature, depending on the reports.
- 2) The fact that Sb^{3+} is, in most of the cases, incorporated in cation sites of larger size relative to its ionic radius. This possibly induces an off-centering of the Sb^{3+} ions and creates uncertainties in the determination of interatomic distances which, in turn, affect the values of $he(X)$.
- 3) The nominal attribution of the optical transitions could be incorrect.
- 4) The fact that the calculated energies are carried out for all possible cation sites for which Sb^{3+} may substitute without any preconceived idea. Obviously, not all the considered sites are effectively occupied by Sb^{3+} in the material.

Considering these issues, we have decided to perform the fitting of the data within an accuracy of $\pm 2500 \text{ cm}^{-1}$ which looks, in these circumstances, acceptable in a first approximation. Sites located out of this interval are therefore considered as not currently occupied by Sb^{3+} in the host lattice. Taking this assumption, the best fitting was achieved using the following empirical linear equation (in cm^{-1}):

$$E_A(X) = 57420 - 16460 \text{ } he(X) \quad (1)$$

The corresponding values are listed in Table 3. We note at this stage that several lattices are not reproduced by the EF model. This concerns MgS, the two elpasolites $\text{Cs}_2\text{NaYBr}_6$ and $\text{Cs}_2\text{NaYCl}_6$, LaOCl , AlPO_4 , LaPO_4 , $\text{LiLaP}_4\text{O}_{12}$, MP_3O_9 with $M = \text{Y, Lu, Gd, La}$ and LaBO_3 . Questionable, here, is the fact that some lattices present similar or same type of structure but with different energies of E_A . This concerns for example, MgS and CaS that have the same crystal structure (Fm-3m) and both octahedrally coordinated sites. They both show similar experimental energies with a difference of less than 1000 cm^{-1} . Their values of $he(\text{Mg}^{2+})$ and $he(\text{Ca}^{2+})$ are however different, which led to E_A that differ by 6090 cm^{-1} . This makes $E_A(\text{Ca}^{2+})$ well reproduced by the EF model while $E_A(\text{Mg}^{2+})$ not. Going deeper in the calculations and structural parameters of the two compounds, we find that both of them have the same structural parameters: same coordination, i.e. same decomposition of binary crystals (see Chapter 1 and Appendix B) and same charge. The difference is only in the interatomic distances Mg-S (2.605 \AA) and Ca-S (2.847 \AA). Knowing that the ionic radius of Ca^{2+} in 6-coordination is 1 \AA and that of Mg^{2+} is 0.72 \AA ⁽¹⁴⁾, this suggests that the interatomic distances may change when Sb^{3+} is incorporated in Ca^{2+} due to the off center position (the ionic radius of Sb^{3+} being equal to 0.76 \AA , closer to that of Mg^{2+}). The case of $\text{Cs}_2\text{NaLaBr}_6\text{:Sb}^{3+}$ and $\text{Cs}_2\text{NaYBr}_6\text{:Sb}^{3+}$ is also similar. Further, if we assume that antimony substitutes in Y^{3+} and La^{3+} , then we have to consider the interatomic distances and charges (bond valence sum) of both Y^{3+} and La^{3+} that account to the difference in the values of $he(X)$ and the calculated energy E_A . This means that the nature of the cation is very important in Sb^{3+} compounds and the aspect that Sb^{3+} goes off center in some of these compounds can be responsible for limiting the efficiency of the EF model. For other lattices like Y_2O_3 , $\text{Sr}_3(\text{PO}_4)_2$ and $\text{Ca}_{10}(\text{PO}_4)_6\text{F}_2$, only the $\text{Y}^{3+}(\text{S}_6)$, $\text{Sr}(1)$ and $\text{Ca}(2)$ sites, respectively, are well reproduced. This suggests that these sites are preferably occupied by Sb^{3+} in the corresponding lattices. Dealing with the fluoro-apatite, our result is in good agreement with the studies that predict incorporation of Sb^{3+} in the $\text{Ca}(2)$ sites instead of the $\text{Ca}(1)$ sites⁽⁴⁾. Dealing with AlPO_4 , studies showed that Sb^{3+} is more probably located in interstitial sites than in the regular tetrahedrally-coordinated Al^{3+} sites⁽²⁾. This may explain why we cannot reproduce $E_{\text{exp}}(\text{Sb}^{3+})$ in this material by means of Equation (1). The case of LaPO_4 , $\text{LiLaP}_4\text{O}_{12}$, MP_3O_9 with $M = \text{Y, Lu, Gd, La}$ and LaBO_3 will be further discussed in Section 4.5.

4.4.3. Establishing an empirical equation for MMCT (or D-like) transitions

By reference to Equation (30) in Chapter 1, we tentatively introduce the following empirical equation to account for the $Sb^{3+} \rightarrow M^{n+}$ MMCT energy in closed shell transition metal oxides:

$$MMCT(Sb^{3+} - M^{n+}) = k_{CN'} \left[\chi(Sb^{3+}) - \alpha_{CN'}^{CN} \frac{\chi_{CN'}(M^{n+})}{d_{corr}(X)} \right] \quad (2)$$

where the parameters herein have the same meaning as in Chapter 1. In the present work, this equation will be applied to compounds in which $CN' \geq 6$, i. e. the transition metal cations occupy 6 (or more)-coordinated sites. We are then dealing with zirconates, niobates and lattices containing Sc^{3+} , Y^{3+} , Lu^{3+} and La^{3+} , which are also d^0 elements. As stated before, we anticipate that the D transitions in these materials should be located at higher energy than A transitions.

The crystal radius of Sb^{3+} used for the calculation of d_{corr} is known for coordination numbers lower or equal to 6 only. For this reason, this value (0.90 Å)⁽¹⁴⁾ will be used each time we have $CN \geq 6$ or $CN' = 6$ in case of an insertion of Sb^{3+} in the M^{n+} sites like Zr^{4+} , Nb^{5+} or Ta^{5+} . For the same reason, we will only retain one value for the electronegativity of Sb^{3+} : $\chi(Sb^{3+}) = 1.476$ ⁽³⁷⁾, i. e. the value in correspondence with a 6-fold coordination. Therefore, 2 parameters need to be determined to run Equation (1): $k_{CN'}$ and $\alpha_{CN'}^{CN}$. They were obtained by Plotting E_{exp} against $\frac{\chi_{CN'}(M^{n+})}{d_{corr}(X)}$ for all selected lattices and retaining data located within an interval of uncertainty of $\pm 2500 \text{ cm}^{-1}$. Doing so, we ended up on $k_{CN'} = 36900 \text{ cm}^{-1}$ (with $CN' \geq 6$) and $\alpha_{CN'}^{CN} = 1.22$ (whatever CN and $CN' \geq 6$), which finally gives the empirical equation:

$$MMCT(Sb^{3+} - M^{n+}) = 54243 - 45018 \frac{\chi(M^{n+})}{d_{corr}(X)} \quad (3)$$

Note that this equation is basically valid for oxides. It will not be used to calculate the MMCT energies in oxygen-free lattices.

4.5. Origin of the photoluminescence excitation in Sb^{3+} -doped closed shell transition metal oxides

We will now discuss the nature of the absorbing states of Sb^{3+} in closed shell transition metal oxides on the basis of the two models described above. To facilitate the discussion, we have plotted in Figure 5 the difference in absolute values between $E_{exp}(Sb^{3+})$ and $E_A(X)$, on one side and between $E_{exp}(Sb^{3+})$ and $MMCT(Sb^{3+})$ on the other side.

The vertical dotted lines figure the uncertainty interval $\pm 2500 \text{ cm}^{-1}$. Data beyond these limits should be considered as meaningless. This is typically the case for the Y^{3+} site in YNbO_4 and YTaO_4 and for the Zr^{4+} site in CaZrO_3 . In other words, our calculations suggest that Sb^{3+} is not incorporated in these sites of the corresponding lattices. Some other lattices are borderline with respect to the $\pm 2500 \text{ cm}^{-1}$ accuracy limits, namely Y_2O_3 (C_2 site), LaPO_4 , LuP_3O_9 , LuBO_3 and LaBO_3 . In the case of Y_2O_3 (C_2 site), our results suggest an insertion of Sb^{3+} in the S_6 site with a low-lying excitation ascribed to A transition. For the four other lattices, it is difficult to draw out reliable conclusions from our data owing to some possible off-centering position of Sb^{3+} in the much larger La^{3+} and Lu^{3+} sites or even formation of Sb^{3+} pairs. Nevertheless, dealing with the MP_3O_9 series ($\text{M} = \text{Y}, \text{Lu}, \text{La}$) and $\text{LiLaP}_4\text{O}_{12}$ (La^{3+} site only), our data strongly suggest that the low-lying excitation is of D character. In contrast, in the MPO_4 series ($\text{M} = \text{Sc}, \text{Lu}$), the low-lying excitation is more probably of A character. The case of YPO_4 is still ambiguous, since both A and D transitions fit the accuracy of $\pm 2500 \text{ cm}^{-1}$. Presumably, the two states are located close to each other in the energy level diagram, as for $\text{YVO}_4\text{:Bi}^{3+}$ (see Chapter 3). At last in $\text{LaBO}_3\text{:Sb}^{3+}$, we emphasize that the A transition is predicted at 48690 cm^{-1} from Equation (1). This value is in fact very close to the position of the major absorption band in this material (48000 cm^{-1}), which suggests correspondence, in good agreement with ref. (38). In this case, we would ascribe the shoulder signal at $\approx 42000 \text{ cm}^{-1}$ to a D band.

In the niobates and tantalates, the low-lying excitation features are undoubtedly ascribed to D transitions for Sb^{3+} ions located preferentially in the six-fold coordinated Nb^{5+} or Ta^{5+} sites. For the zirconates, Sb^{3+} seems more probably incorporated in the divalent alkaline-earth sites where it promotes the formation of a low-lying D state. Occupancy of the Zr^{4+} site seems excluded in CaZrO_3 but not in SrZrO_3 , which is somewhat puzzling. This particular point requires deeper investigation.

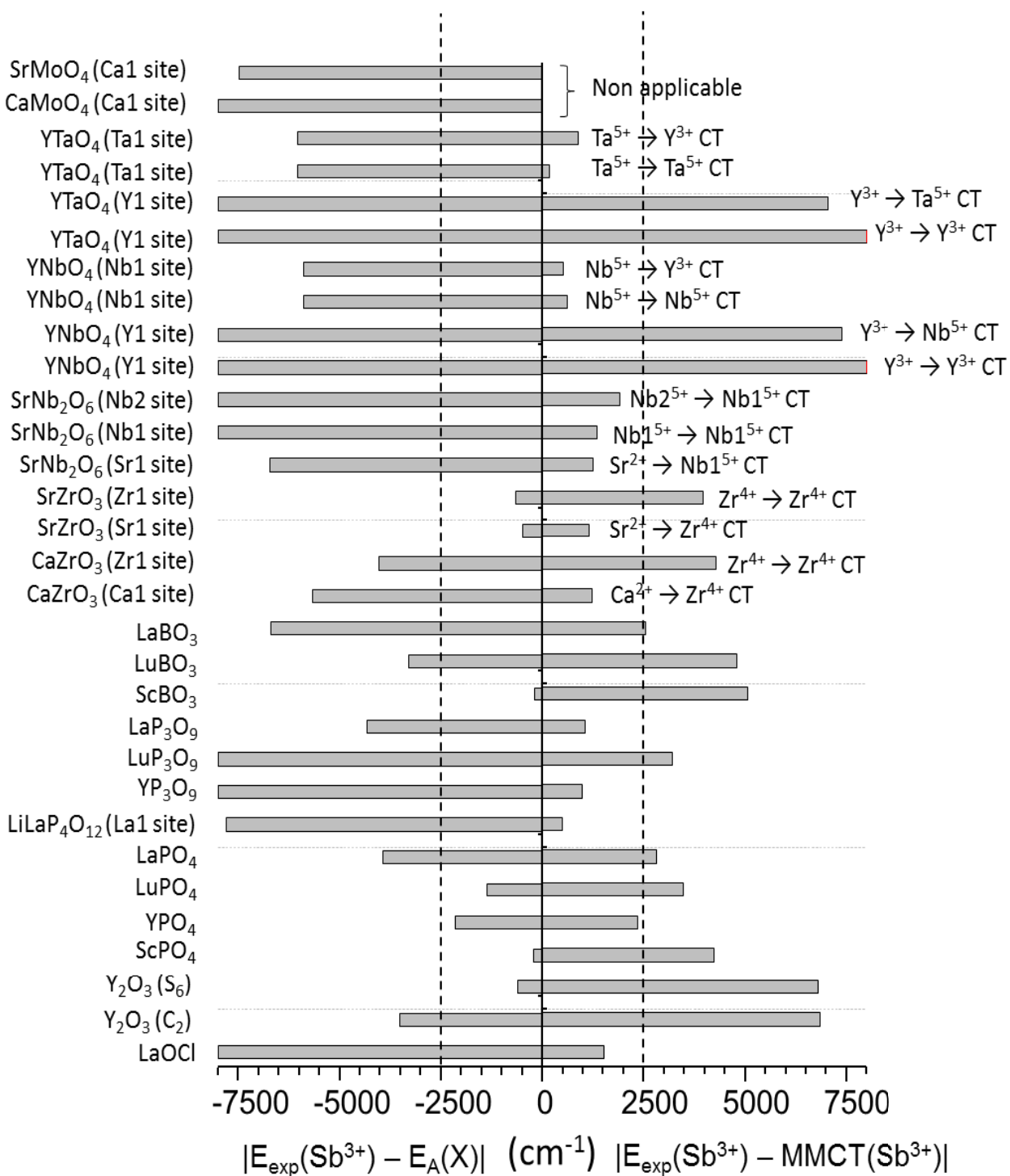


Figure 5. Difference in absolute values between the experimental energies $E_{\text{exp}}(\text{Sb}^{3+})$ and the calculated $E_A(X)$ or $\text{MMCT}(\text{Sb}^{3+})$ for a set of Sb^{3+} -doped compounds.

4.6. Conclusion

We have started the investigation of the luminescence properties of Sb^{3+} in closed shell transition metal oxides and have confirmed that the observed features are related to the dopant. The corresponding low lying excitation signals have tentatively been ascribed on the basis of two empirical equations allowing us to calculate the energy of A-like and D-like transitions from the knowledge of the crystal structure. The accuracy of the method is however not good enough today to make a robust diagnosis. This is certainly due to the tendency of the small Sb^{3+} ion to locate in off-centered position with respect to the well-defined crystallographic sites. This led to unknown alterations of the interatomic distances, which in turn alter the accuracy of the calculations. At present, only trends are evidenced. Going deeper in the accuracy requires further refinements of the equations based on a more accurate description of the immediate chemical surrounding of Sb^{3+} in the host lattices.

Bibliography

1. **E.W.J. L Oomen, R.C.M. Peeters, W.M.A. Smit and G. Blasse.** *The Luminescence of the Sb^{3+} Ion in $Ln(PO_3)_3$ ($Ln=Sc, Lu, Y, Gd, La$).* 1988, Journal of Solid State Chemistry, Vol. 73, pp. 151-159.
2. **E.W.J.L. Oomen, W.M.A. Smit and G. Blasse.** *Luminescence Of The Sb^{3+} Ion In Calcium Fluoroapatite and Other Phosphates.* 1988, Materials Chemistry and Physics , Vol. 19, pp. 357-368.
3. **E.W.J.L. Oomen, W.M.A. Smit and G. Blasse.** *Jahn-Teller effect in the Sb^{3+} emission in zircon-structured phosphates.* 1984, Chemical Physics Letters, Vol. 112, pp. 547-550.
4. **G. Blasse.** *Luminescence of Calcium Halophosphate- Sb^{3+} , Mn^{2+} at Low Temperatures.* 1983, Chemical Physics Letters, Vol. 104, pp. 160-162.
5. **E.W.J.L. Oomen, L.C.G. Van Gorkom, W.M.A. Smit and G. Blasse.** *Luminescence of Sb^{3+} in Rare earth orthoborates $LnBO_3$ ($Ln=Sc, Y, La, Gd, Lu$).* 1986, Journal of Solid State Chemistry, Vol. 65, pp. 156-167.
6. **H. Donker, N. Yamashita, W.M.A. Smit and G. Blasse.** *Luminescence Decay Times of the Sb^{3+} , Pb^{2+} and Bi^{3+} ions in Alkaline-Earths Sulfides.* 1989, Physica Status Solidi, Vol. 156, pp. 537-544.
7. **L.I. Van Steensel and G. Blasse.** *The Luminescence of Sb^{3+} in $LaOCl$.* 1996, Journal of Alloys and Compounds, Vol. 232, pp. 60-62.
8. **F. Wen, J. Chen, J. Moon, J.H. Kim, J. Niu and W. Li.** *Hydrothermal synthesis and luminescent properties of Sb^{3+} -doped $Sr_3(PO_4)_2$.* 2004, Journal of Solid State Chemistry, Vol. 177, pp. 3114-3118.
9. **L.I. Van Steensel, S.G. Bokhove, A.M. Van de Craats, J. de Blank and G. Blasse.** *The Luminescence of Bi^{3+} in $LaInO_3$ and Some Other Perovskites.* 1995, Materials Research Bulletin, Vol. 30, pp. 1359-1362.
10. **E.W.J.L. Oomen, W.M.A. Smit and G. Blasse.** *The Luminescence of Arsenic(III) in the cubic elapsolite $Cs_2NaScCl_6$.* 1987, Chemical Physics Letters, Vol. 138, pp. 584-586.
11. **E.W.J.L. Oomen, G.J. Dirksen, W.M.A. Smit and G. Blasse.** *On the luminescence of the Sb^{3+} ion in Cs_2NaMBr_6 ($M=Sc, Y, La$).* 1987, Journal of Physics C:Solid State Physics, Vol. 20, pp. 1161-1171.
12. **A.C. Van der Steen, J.J.A. Van Hesteren and A.P. Slok.** *Luminescence of the Bi^{3+} Ion in Compounds $LiLnO_2$ and $NaLnO_2$ ($Ln = Sc, Y, La, Gd, Lu$).* 1981, The Electrochemical Society, Vol. 128, pp. 1327-1333.
13. **A.G. Sykes.** *Advances in Inorganic Chemistry.* s.l. : Academic Press San Diego New York Boston, 1990. Vol. 35.
14. **R. D. Shannon.** *Revised effective ionic radii and systematic studies of interatomic distances in halides and chalcogenides.* 1976, Acta Crystallographica Section A, Vol. 32, pp. 751-767.

15. **D.L. Dexter, C.C. Klick, and G.A. Russell.** *Criterion for the Occurrence of Luminescence.* 1955, Physical Reviews, Vol. 100, pp. 603-605.
16. **G. Blasse.** *Classical phosphors: A Pandora's box.* 1997, Journal of Luminescence, Vols. 72-74, pp. 129-134.
17. **S.K. Gupta, P.S. Ghosh, N. Pathak and R. Tewari.** *Nature of defects in blue light emitting CaZrO_3 : spectroscopic and theoretical study.* 2015, Royal Society of Chemistry Advances, Vol. 5, pp. 56526-56533 .
18. **V.M. Longo, L.S. Cavalcante, R. Erlo, V.R. Mastelaro, A.T. de Figueiredo, J.R. Sambrano, S. de Lazaro, A.Z. Freitas, L. Gomes, N.D. Vieira Jr., J.A. Varela and E.Longo.** *Strong violet-blue light photoluminescence emission at room temperature in SrZrO_3 : Joint experimental and theoretical study.* 2008, Acta Materialia, Vol. 56, pp. 2192-2202.
19. **Z. Wang, J. Zhang, G. Zheng, X. Peng, H. Dai.** *Violet-blue afterglow luminescence properties of non-doped SrZrO_3 material.* 2013, Journal of Luminescence, Vol. 144, pp. 30-33.
20. **A.W.M. Braam and G. Blasse.** *Luminescence of Pb^{2+} -ions in calcium zirconate (CaZrO_3).* 1976, Solid State Communications, Vol. 20, pp. 717-719.
21. **G. Blasse, A.W. Braam and M. Heerschoep.** *Influence of crystal structure on the luminescence of ions with s^2 configuration.* 1977, Journal of Solid State Chemistry, Vol. 20, pp. 63-65.
22. **A.M. Srivastava.** *Luminescence of Bi^{3+} in the orthorhombic perovskites $\text{CaB}^{4+}\text{O}_3$ ($\text{B}^{4+}=\text{Zr, Sn}$): Crossover from localized to D-state emission.* 2016, Optical Materials, Vol. 58, pp. 89-92.
23. **A.A. Setlur and A.M. Srivastava.** *The nature of Bi^{3+} luminescence in garnet hosts.* 2006, Optical Materials, Vol. 29, pp. 410-415.
24. **S.K. Lee, H. Chang, C-H. Han, H-J. Kim, H.G. Jang and H.D. Park.** *Electronic Structures and Luminescence Properties of YNbO_4 and $\text{YNbO}_4\text{:Bi}$.* 2001, Journal of Solid State Chemistry, Vol. 156, pp. 267-273.
25. **W.J. Schipper, M.F. Oogendrop and G. Blasse.** *The luminescence and X-ray storage properties of Pr^{3+} and Ce^{3+} in YNbO_4 and $\text{M}'\text{-YTaO}_4$.* 1993, Journal of Alloys and Compounds, Vol. 202, pp. 283-287.
26. **P. Boutinaud, E. Cavalli and M. Bettinelli.** *Emission quenching induced by intervalence charge transfer in Pr^{3+} - or Tb^{3+} -doped YNbO_4 and CaNb_2O_6 .* 2007, Journal of Physics Condensed Matter, Vol. 19, pp. 386230-386240.
27. **G. Blasse and A. Brill.** *Investigations on Bi^{3+} -Activated Phosphors.* 1968, Journal of Chemical Physics, Vol. 48, pp. 217-222.
28. **S.H. Shin, D.Y. Jeon and K.S. Suh.** *Charge-transfer nature in luminescence of $\text{YNbO}_4\text{:Bi}$ blue phosphor.* 2001, Journal of Applied Physics, Vol. 90, pp. 5986-5990.

29. **F. Kang, M. Peng, S. Xu, Z. Ma, G. Dong, and J. Qiu.** *Broadly Tunable Emission from CaMoO₄:Bi Phosphor Based on Locally Modifying the Microenvironment Around Bi³⁺ Ions.* 2014, European Journal of Inorganic Chemistry, pp. 1373-1380.
30. **G. Bergerhoff and I. D. Brown.** *Crystallographic Databases Information Content, Software Systems, Scientific Applications; F.H.Allen, G.Bergerhoff and R.Sievers (eds).* International Union of Crystallography. Bonne,Germany, 1987.
31. **G. Chadeyron, M. El Ghazzi, R. Mahiou, A. Arbus and J.C. Cousseins.** *Revised Structure of the Orthoborate YBO₃* 1997, Journal of Solid State Chemistry, Vol. 128, pp. 261-266.
32. **H.Y.P. Hong.** *Crystal structures of neodymium metaphosphate (NdP₃O₉) and ultraphosphate (NdP₅O₁₄).* 1974, Acta Crystallographica B, Vol. 30, pp. 468-474.
33. **N.Yu. Anisimova, V.K. Trunov, N.B. Karmanovskaya and N.N. Chudinova.** *Synthesis and crystal structure of new modification of Yb (P O₃)₃.* 1992, Izvestiya Akademii Nauk SSSR, Neorganicheskie Materialy, Vol. 28, p. 441-444.
34. **L.I.Van Steensel and G. Blasse.** *The luminescence of Sb³⁺ in LaOCL.* 1996, Journal of Alloys and Compounds, Vol. 232, pp. 60-62.
35. **E.W.J.L. Oomen and G.J. Dirksen** *Crystal growth and luminescence of Sb³⁺-doped Cs₂NaMCl₆ (M = Sc, Y, La).* 1985, Materials Research Bulletin, Vol. 20, pp. 453-457,.
36. **A.M. Van de Craats and G.Blasse.** *The influence of d¹⁰ ions on the luminescence of Bismuth(III) in solids.* 1996, Materials Research Bulletin, Vol. 31, pp. 381-387.
37. **K. Li and D. Xue.** *Estimation of Electronegativity Values of Elements in Different Valence States.* 2006, Journal of Physical Chemistry, Vol. 110, pp. 11332-11337.
38. **E.W.J.L. Oomen, L.C.G. Van Gorkom, W.M.A. Smit and G. Blasse.** *Luminescence of Sb³⁺ in Rare Earth Orthoborates LnBO₃ (Ln=Sc,Y,La,Gd,Lu).* 1986, Journal of Solid State Chemistry, Vol. 65, pp. 156-167.

General Conclusion

LED-based lighting technology has witnessed important progressions in the last decades especially in the design of phosphors for warm white light. However, the materials found in the LED market today are strongly dependent on temperature and present some disadvantages like low color rendering index or low efficiency. This requires the development of new broad band emitting materials that can be excited in the UV region and emit in the visible region. For this reason, we have studied friendly and easy to use empirical methods for the design of band-like emitting compounds doped with Eu^{2+} which is widely used for LED lighting purposes, or mercury like ions (Bi^{3+} and Sb^{3+}). Trivalent bismuth, in addition to being a good sensitizer for trivalent lanthanides, is interesting in an economical point of view with respect to rare earths. Sb^{3+} , however is not widely studied as for Bi^{3+} but could present important properties to be explored following the analogy with Bi^{3+} .

Our results showed that the environmental factor model is reliable for designing $\text{A}^{\text{I}}\text{B}^{\text{II}}\text{PO}_4\text{:Eu}^{2+}$ phosphors where A is a monovalent and B is a divalent cation. Using the model we were able to identify the doping sites in this family of phosphates within an error of $\pm 1000\text{ cm}^{-1}$. The model was found efficient to predict the nature of the doping sites that contribute to the excitation edges in a series of $\text{A}^{\text{I}}\text{B}^{\text{II}}\text{PO}_4\text{:Eu}^{2+}$ phosphors that are not explored yet. This helped to suggest the members of this family that are good candidates for the design of blue-based LED materials. It was found that $\text{NaCdPO}_4\text{:Eu}^{2+}$ (Pna₂₁ polymorph) and $\text{LiCdPO}_4\text{:Eu}^{2+}$ (Pnma polymorph) are the best in this connection. Our attempts to prepare these two compounds unfortunately failed. Further chemistry work is required in this connection.

Concerning trivalent bismuth, the empirical models were found useful for the prediction of the character of luminescence in Bi^{3+} -doped closed shell transition metal oxides. This was accomplished by using the EF and MMCT models with a criterion involving the Stokes shift values. Depending on this method, the low-lying excitation signals in these compounds were identified as A ($^1\text{S}_0 \rightarrow ^3\text{P}_1$) or D ($\text{Bi}^{3+} \rightarrow \text{M}^{n+}$ charge transfer) bands, where M^{n+} is a transition metal cation with d^0 electron configuration. The set of closed shell transition metal oxides doped with Bi^{3+} prepared in this work showed yellow emission for the vanadates (GdVO_4 and LaVO_4), the molybdate CaMoO_4 and the two niobates $\text{LiNbO}_3\text{-Bi}^{3+}$ and $\text{NaNbO}_3\text{-Bi}^{3+}$. The other niobates (YNbO_4 , GdNbO_4 , LaNbO_4 , CaNb_2O_6) and the tantalate $\text{M}'\text{-YTaNbO}_4$ glowed in the blue region. The study of high pressure $\text{YVO}_4\text{:Bi}^{3+}$ showed important red shift in the emission energy from 570 nm at ambient pressure (in the zircon phase) to 680 nm at high pressure (in

the scheelite phase). With the help of the models, we showed that the energy bands A and D are very close in the zircon form and undergo important splitting under the action of high pressure. This helped interpreting the pressure induced red shift of Bi^{3+} emission to the fact that the emitting level is of A character in the scheelite form, whereas it is of D character in the zircon form.

The luminescence measurements of a group of Sb^{3+} -doped closed shell transition metal oxide compounds (CaZrO_3 , SrZrO_3 , YNbO_4 , SrNb_2O_6 , $\text{M}'\text{-YTao}_4$, CaMoO_4 and SrMoO_4) showed broad bands in the visible region ascribed to Sb^{3+} . The identification of the luminescence character in these compounds and in other compounds from the literature were tentatively made using two empirical equations proposed in this work on the basis of the EF and MMCT models. These equations, however, were not considered accurate enough due to the important crystallographic changes when Sb^{3+} is introduced in these compounds mainly the off-centered positions usually occupied by this ion. Additional work is then required to clarify the situation.

Appendix A: Electronegativities of different cations

In this appendix we show the tables of electronegativity (EN) values of different cations in different coordinations useful for the calculations of MMCT energies. The following tables are taken from the work of Keyan Li and Dongfeng Xue. In Table 1, the EN of six-coordinated cations are given denoted by χ_6 . The numbers in parantheses represent the oxidation states. L means low spin and H means high spin. In Table 2, the EN of elements in valence states with the most common coordination numbers (CN) for main group elements are listed. EN of cations with the most common CN for group IB-VB and VIB-VIIIB metals are gathered in Tables 3 and 4. In Table 5, the EN values of trivalent lanthanides with CN ranging from 6 to 12 are given.

Table 1 EN of the six-coordinated cations.

period	IA	IIA	IIIB	IVB	VB	VIB	VIIIB	VIIIIB			IB	IIB	IIIA	IVA	VA	VIA	VIIA
II	Li χ_i (1)0.009	Be (2)1.273											B (3)1.714	C (4)2.380	N (5)2.939 (3)2.164	O (6)3.758	F (7)4.368
III	χ_p 0.98	1.57											2.04	2.55	3.04	3.44	3.98
	Na χ_i (1)1.024	Mg (2)1.234											Al (3)1.513	Si (4)1.887	P (5)2.139 (3)1.642	S (6)2.659 (4)1.973	Cl (7)3.008 (5)2.274
IV	χ_p 0.93	1.31											1.61	1.90	2.19	2.58	3.16
	K χ_i (1)0.998	Ca (2)1.160	Sc (3)1.415	Ti (4)1.730 (3)1.499 (2)1.225	V (5)2.030 (4)1.795 (3)1.545 (2)1.267	Cr (6)2.475 (3)1.587 (2L)1.322 (2H)1.287	Mn (7)2.651 (4)1.912 (2L)1.343 (2H)1.263	Fe (3L)1.651 (3H)1.556 (2L)1.390 (2H)1.292	Co (3L)1.693 (3H)1.621 (2L)1.377 (2H)1.321	Ni (4)2.037 (3L)1.695 (3H)1.650 (2)1.367	Cu (2)1.372 (1)1.163	Zn (2)1.336	Ga (3)1.579	Ge (4)1.854 (2)1.314	As (5)2.159 (3)1.589	Se (6)2.448 (4)1.869	Br (7)2.744 (5)2.107
V	χ_p 0.82	1.00	1.36	1.54	1.63	1.66	1.55	1.83	1.88	1.91	1.90	1.65	1.81	2.01	2.18	2.55	2.96
	Rb χ_i (1)0.998	Sr (2)1.139	Y (3)1.340	Zr (4)1.610	Nb (5)1.862 (4)1.690 (3)1.501	Mo (6)2.101 (5)2.006 (4)1.808	Tc (7)2.384 (5)2.002 (4)1.773	Ru (5)2.099 (4)1.848 (3)1.576	Rh (5)2.167 (4)1.863 (3)1.622	Pd (4)1.876 (3)1.562 (2)1.346	Ag (2)1.333 (1)1.097	Cd (2)1.276	In (3)1.480	Sn (4)1.706 (2)1.181	Sb (5)1.971 (3)1.476	Te (6)2.180 (4)1.467	I (7)2.417 (5)1.587
VI	χ_p 0.82	0.95	1.22	1.33	1.60	1.66	1.90	2.20	2.28	2.20	1.93	1.69	1.78	1.96	2.05	2.10	2.66
	Cs χ_i (1)0.998	Ba (2)1.126	La (3)1.327	Hf (4)1.706	Ta (5)1.925 (4)1.735 (3)1.536	W (6)2.175 (5)1.991 (4)1.784	Re (7)2.507 (6)2.317 (4)1.853	Os (7)2.573 (6)2.362 (4)1.888	Ir (5)2.183 (4)1.881 (3)1.649	Pt (5)2.159 (4)1.895 (2)1.432	Au (5)2.195 (3)1.550 (1)1.113	Hg (2)1.326 (1)1.165	Tl (3)1.524 (1)1.050	Pb (4)1.746 (2)1.225	Bi (5)1.895 (3)1.399	Po (6)2.168 (4)1.575	At (7)2.423
	χ_p 0.79	0.89	1.10	1.30	1.50	2.36	1.90	2.20	2.20	2.28	2.54	2.00	2.04	2.33	2.02	2.00	2.20
	Fr χ_i (1)1.012	Ra (2)1.151	Ac (3)1.363	Ce (4)1.608 (3)1.348	Pr (4)1.646 (3)1.374	Nd (3)1.382	Pm (3)1.391	Sm (3)1.410	Eu (3)1.433 (2)1.181	Gd (3)1.386	Tb (4)1.733 (3)1.410	Dy (3)1.426 (2)1.213	Ho (3)1.433	Er (3)1.438	Tm (3)1.455 (2)1.231	Yb (3)1.479 (2)1.237	Lu (3)1.431
	χ_p 0.70	0.90		1.12	1.13	1.14		1.17		1.20		1.22	1.23	1.24	1.25		1.27

Table 2 EN of cations with the most common CN of main group elements.

IA			IIA			IIIA			IVA			VA			VIA			VIIA		
cations	CN	χ_i	cations	CN	χ_i	cations	CN	χ_i	cations	CN	χ_i	cations	CN	χ_i	cations	CN	χ_i	cations	CN	χ_i
Li ⁺	4	1.043	Be ²⁺	3	1.669	B ³⁺	3	3.189	C ⁴⁺	4	2.432	P ⁵⁺	4	3.003	S ⁶⁺	4	3.833	Cl ⁵⁺	3	3.469
	8	0.987		4	1.453		4	2.259	Si ⁴⁺	4	2.245	As ⁵⁺	4	2.499	Se ⁶⁺	4	2.977	Cl ⁷⁺	4	4.860
Na ⁺	4	1.028	Mg ²⁺	4	1.312	Al ³⁺	4	1.691	Ge ⁴⁺	4	2.116	Sb ³⁺	4	1.476	Te ⁴⁺	4	1.701	Br ⁵⁺	3	2.550
	8	1.004		8	1.173		5	1.571	Sn ⁴⁺	4	1.877	Bi ³⁺	5	1.434	Te ⁶⁺	4	2.480	Br ⁷⁺	4	3.419
	9	0.998	Ca ²⁺	7	1.145	Ga ³⁺	4	1.755		8	1.599							I ⁵⁺	3	2.224
	12	0.985		8	1.132	In ³⁺	4	1.627	Pb ²⁺	4	1.293							I ⁷⁺	4	2.722
K ⁺	4	0.999		12	1.092	Tl ⁺	8	1.040	Pb ⁴⁺	4	1.885									
	8	0.987	Sr ²⁺	8	1.123		12	1.030												
	12	0.978		10	1.106	Tl ³⁺	4	1.625												
Rb ⁺	8	0.991		12	1.093		8	1.468												
	10	0.987	Ba ²⁺	7	1.121															
	12	0.983		8	1.115															
Cs ⁺	8	0.993		12	1.087															
	10	0.989	Ra ²⁺	8	1.142															
	12	0.984		12	1.109															

Table 3 EN of cations with the most common CN for group IB-VB metals.

IB			IIB			IIIB			IVB			VB		
cations	CN	χ_i	cations	CN	χ_i	cations	CN	χ_i	cations	CN	χ_i	cations	CN	χ_i
Cu ⁺	2	1.318	Zn ²⁺	4	1.426	Sc ³⁺	8	1.347	Ti ⁴⁺	4	2.017	V ⁴⁺	5	1.865
	4	1.232		8	1.263	Y ³⁺	7	1.314		5	1.857	V ⁵⁺	4	2.466
Cu ²⁺	4	1.486	Cd ²⁺	4	1.353		8	1.291		8	1.597		5	2.185
	5	1.423		8	1.226		9	1.272	Zr ⁴⁺	4	1.743	Nb ³⁺	8	1.453
Ag ⁺	2	1.235	Hg ²⁺	2	1.511					8	1.518	Nb ⁵⁺	4	2.120
	4	1.128		4	1.352					9	1.487		7	1.802
Ag ²⁺	4	1.409		8	1.283				Hf ⁴⁺	4	1.858		8	1.749
Au ³⁺	4	1.693								8	1.602			

Table 4 EN of cations with the most common CN for group VIB-VIIIB metals.

VIB			VIIB			VIIIB								
cations	CN	χ_i	cations	CN	χ_i	cations	CN	χ_i	cations	CN	χ_i	cations	CN	χ_i
Cr ⁶⁺	4	3.200	Mn ²⁺	4	1.349	Fe ²⁺	4	1.376	Co ²⁺	4	1.426	Ni ²⁺	4	1.470
Mo ⁵⁺	4	2.292		8	1.216		8	1.236		8	1.253	Pd ²⁺	4	1.483
Mo ⁶⁺	4	2.506	Mn ⁴⁺	4	2.189	Fe ³⁺	4	1.726				Pt ²⁺	4	1.586
	7	1.902	Mn ⁷⁺	4	3.614		8	1.454						
W ⁶⁺	4	2.596	Tc ⁷⁺	4	2.950	Os ⁶⁺	5	2.493						
	5	2.356	Re ⁷⁺	4	2.982									

Table 5 EN of trivalent Ln with CN ranging from 6 to 12.

CN	La	Ce	Pr	Nd	Pm	Sm	Eu	Gd	Tb	Dy	Ho	Er	Tm	Yb	Lu
6	1.327	1.348	1.374	1.382	1.391	1.410	1.433	1.386	1.410	1.426	1.433	1.438	1.455	1.479	1.431
7	1.301	1.324	1.348	1.357	1.364	1.381	1.402	1.358	1.382	1.397	1.402	1.409	1.422	1.446	1.399
8	1.281	1.298	1.319	1.330	1.338	1.356	1.377	1.336	1.355	1.371	1.377	1.380	1.396	1.415	1.372
9	1.264	1.281	1.301	1.311	1.319	1.335	1.355	1.315	1.334	1.348	1.353	1.355	1.370	1.388	1.348
10	1.249	1.264	1.287	1.295	1.300	1.315	1.336	1.293	1.313	1.326	1.334	1.333	1.346	1.364	1.325
11	1.238	1.253	1.272	1.280	1.285	1.298	1.315	1.278	1.297	1.309	1.312	1.315	1.328	1.344	1.307
12	1.225	1.240	1.258	1.265	1.270	1.283	1.299	1.263	1.281	1.293	1.296	1.298	1.310	1.326	1.290

From **K.Li and D.Xue**. *Estimation of Electronegativity Values of Elements in Different Valence States*. 2006, Journal of Physical Chemistry A, Vol. 110, pp. 11332–11337.

Appendix B Coordination Matrices

In this appendix, the coordination matrices useful for the calculations of $he(X(i))$ and $Fc(X(i))$ for all the studied lattices in this work are given in addition to the formula and decomposition into binary crystals for each lattice.

Table 1 LiMgPO₄(Pnma)

	Li(1)	Mg(1)	P(1)	O(1)	O(2)	O(3)
O(1)	2	1	1			
O(2)	2	1	1			
O(3)	2	4	2			
Li(1)				2	2	1
Mg(1)				1	1	2
P(1)				1	1	1
Total	6	6	4	4	4	4
multiplicity	4	4	4	4	4	8

Z=4. The formula is : $Li(1)_1Mg(1)_1O(1)_1O(2)_1O(3)_2P(1)_1$. The compound is decomposed as:

$$Li(1)\frac{2 \times 1}{6}O(1)\frac{2 \times 1}{4} + Li(1)\frac{2 \times 1}{6}O(2)\frac{2 \times 1}{4} + Li(1)\frac{2 \times 1}{6}O(3)\frac{2 \times 1}{4} + Mg(1)\frac{1 \times 1}{6}O(1)\frac{1 \times 1}{4} +$$

$$Mg(1)\frac{1 \times 1}{6}O(2)\frac{1 \times 1}{4} + Mg(1)\frac{4 \times 1}{6}O(3)\frac{2 \times 2}{4} + P(1)\frac{1 \times 1}{4}O(1)\frac{1 \times 1}{4} + P(1)\frac{1 \times 1}{4}O(2)\frac{1 \times 1}{4} +$$

$$P(1)\frac{2 \times 1}{4}O(3)\frac{1 \times 2}{4}$$

Table 2 LiCdPO₄(Pnma)

	Li	Cd	P	O1	O2	O3
O1	2	1	1			
O2	2	1	1			
O3	2	4	2			
Li				2	2	1
Cd				1	1	2
P				1	1	1
Total	6	6	4	4	4	4
multiplicity	4	4	4	4	4	8

Z=4. The formula is : $Li(1)_1Cd(1)_1O(1)_1O(2)_1O(3)_2P(1)_1$. The compound is decomposed as:

$$Li(1)\frac{2\times1}{6}O(1)\frac{2\times1}{4} + Li(1)\frac{2\times1}{6}O(2)\frac{2\times1}{4} + Li(1)\frac{2\times1}{6}O(3)\frac{2\times1}{4} + Cd(1)\frac{1\times1}{6}O(1)\frac{1\times1}{4} +$$

$$Cd(1)\frac{1\times1}{6}O(2)\frac{1\times1}{4} + Cd(1)\frac{4\times1}{6}O(3)\frac{2\times2}{4} + P(1)\frac{1\times1}{4}O(1)\frac{1\times1}{4} + P(1)\frac{1\times1}{4}O(2)\frac{1\times1}{4} +$$

$$P(1)\frac{2\times1}{4}O(3)\frac{1\times2}{4}$$

Table 3 KSrPO₄(Pnma)

	K	Sr	P	O1	O2	O3
O1	3	2	1			
O2	6	4	2			
O3	1	3	1			
K				1	2	1
Sr				2	2	2
P				1	1	1
Total	10	9	4	4	5	4
multiplicity	4	4	4	4	8	4

Z=4. The formula is : $K(1)_1Sr(1)_1O(1)_1O(2)_2O(3)_1P(1)_1$. The compound is decomposed as:

$$K(1)\frac{3\times1}{10}O(1)\frac{1\times1}{4} + K(1)\frac{6\times1}{10}O(2)\frac{2\times2}{5} + K(1)\frac{1\times1}{10}O(3)\frac{1\times1}{4} + Sr(1)\frac{2\times1}{9}O(1)\frac{2\times1}{4} +$$

$$Sr(1)\frac{4\times1}{9}O(2)\frac{2\times2}{5} + Sr(1)\frac{3\times1}{9}O(3)\frac{1\times1}{4} + P(1)\frac{1\times1}{4}O(1)\frac{1\times1}{4} + P(1)\frac{2\times1}{4}O(2)\frac{1\times2}{5} + P(1)\frac{1\times1}{4}O(3)\frac{1\times1}{4}$$

Table 4 KBaPO₄(Pnma)

	K	Ba	P	O1	O2	O3
O1	6	4	2			
O2	1	3	1			
O3	3	2	1			
K				2	1	1
Ba				2	2	2
P				1	1	1
Total	10	9	4	5	4	4
multiplicity	4	4	4	8	4	4

Z=4. The formula is : $K(1)_1Ba(1)_1O(1)_2O(2)_1O(3)_1P(1)_1$. The compound is decomposed as:

$$K(1)\frac{6\times 1}{10}O(1)\frac{2\times 2}{5} + K(1)\frac{1\times 1}{10}O(2)\frac{1\times 1}{4} + K(1)\frac{3\times 1}{10}O(3)\frac{1\times 1}{4} + Ba(1)\frac{4\times 1}{9}O(1)\frac{2\times 2}{5} +$$

$$Ba(1)\frac{3\times 1}{9}O(2)\frac{2\times 1}{4} + Ba(1)\frac{2\times 1}{9}O(3)\frac{2\times 1}{4} + P(1)\frac{2\times 1}{4}O(1)\frac{1\times 2}{5} + P(1)\frac{1\times 1}{4}O(2)\frac{1\times 2}{4} +$$

$$P(1)\frac{1\times 1}{4}O(3)\frac{1\times 1}{4}$$

Table 5 NaCdPO₄(Pnma)

	Na	Cd	P	O1	O2	O3
O1	2	1	1			
O2	2	4	2			
O3	2	1	1			
Na				2	1	2
Cd				1	2	1
P				1	1	1
Total	6	6	4	4	4	4
multiplicity	4	4	4	4	8	4

Z=4. The formula is : $Na(1)_1Cd(1)_1O(1)_1O(2)_2O(3)_1P(1)_1$. The compound is decomposed as:

$$Na(1)\frac{2\times 1}{6}O(1)\frac{2\times 1}{4} + Na(1)\frac{2\times 1}{6}O(2)\frac{2\times 1}{4} + Na(1)\frac{2\times 1}{6}O(3)\frac{2\times 1}{4} + Cd(1)\frac{1\times 1}{6}O(1)\frac{1\times 1}{4} +$$

$$Cd(1)\frac{1\times 1}{6}O(2)\frac{1\times 1}{4} + Cd(1)\frac{4\times 1}{6}O(3)\frac{2\times 2}{4} + P(1)\frac{1\times 1}{4}O(1)\frac{1\times 1}{4} + P(1)\frac{1\times 1}{4}O(2)\frac{1\times 1}{4} +$$

$$P(1)\frac{2\times 1}{4}O(3)\frac{1\times 2}{4}$$

Table 6 RbBaPO₄(Pnma)

	Rb	Ba	P	O1	O2	O3
O1	3	2	1			
O2	1	3	1			
O3	6	4	2			
Rb				1	1	2
Ba				2	2	2
P				1	1	1
Total	10	9	4	4	4	5
multiplicity	4	4	4	4	4	8

Z=4. The formula is : $Rb(1)_1Ba(1)_1O(1)_1O(2)_1O(3)_2P(1)_1$. The compound is decomposed as:

$$Rb(1)\frac{3\times 1}{10}O(1)\frac{1\times 1}{4} + Rb(1)\frac{1\times 1}{10}O(2)\frac{1\times 1}{4} + Rb(1)\frac{6\times 1}{10}O(3)\frac{2\times 2}{5} + Ba(1)\frac{2\times 1}{9}O(1)\frac{2\times 1}{4} +$$

$$Ba(1)\frac{3\times 1}{9}O(2)\frac{2\times 1}{4} + Ba(1)\frac{4\times 1}{9}O(3)\frac{2\times 2}{5} + P(1)\frac{1\times 1}{4}O(1)\frac{1\times 1}{4} + P(1)\frac{1\times 1}{4}O(2)\frac{1\times 1}{4} +$$

$$P(1)\frac{2\times 1}{4}O(3)\frac{1\times 2}{5}$$

Table 7 CsMgPO₄(Pnma)

	Cs	Mg	P	O1	O2	O3
O1	4	1	1			
O2	4	2	2			
O3	3	1	1			
Cs				2	2	1
Mg				1	1	1
P				1	1	1
Total	11	4	4	4	4	3
multiplicity	4	4	4	4	8	4

Z=4. The formula is : $Cs(1)_1Mg(1)_1O(1)_1O(2)_2O(3)_1P(1)_1$. The compound is decomposed as:

$$Cs(1)\frac{4\times 1}{11}O(1)\frac{2\times 1}{4} + Cs(1)\frac{4\times 1}{11}O(2)\frac{2\times 2}{4} + Cs(1)\frac{3\times 1}{11}O(3)\frac{1\times 1}{3} + Mg(1)\frac{1\times 1}{4}O(1)\frac{1\times 1}{4} +$$

$$Mg(1)\frac{2\times 1}{4}O(2)\frac{1\times 2}{4} + Mg(1)\frac{1\times 1}{4}O(3)\frac{1\times 1}{3} + P(1)\frac{1\times 1}{4}O(1)\frac{1\times 1}{4} + P(1)\frac{2\times 1}{4}O(2)\frac{1\times 2}{4} +$$

$$P(1)\frac{1\times 1}{4}O(3)\frac{1\times 1}{3}$$

Table 8 NaBbaPO₄(C2/m)

	Na	Ba	(Na,Ba)	P	O1	O2	O3
O1	0	6	1	1			
O2	2	2	3	2			
O3	4	4	6	1			
Na						1	1
Ba					3	1	1
(Na,Ba)					1	3	3
P					1	1	1
Total	6	12	10	4	4	3	3
multiplicity	2	2	4	4	4	4	8

Z=4. The formula is : $Na(1)_{1/2}Ba(1)_{1/2}(Na,Ba)_1O(1)_1O(2)_1O(3)_2P(1)_1$. The compound is decomposed as:

$$\begin{aligned}
& Na(1) \frac{2 \times 1/2}{6} O(2) \frac{1 \times 1}{3} + Na(1) \frac{4 \times 1/2}{6} O(3) \frac{1 \times 2}{3} + Ba(1) \frac{6 \times 1/2}{12} O(1) \frac{3 \times 1}{4} + Ba(1) \frac{2 \times 1/2}{12} O(2) \frac{1 \times 1}{3} + \\
& Ba(1) \frac{4 \times 1/2}{12} O(3) \frac{1 \times 2}{3} + (Na, Ba) \frac{1 \times 1}{10} O(1) \frac{1 \times 1}{4} + (Na, Ba) \frac{3 \times 1}{10} O(2) \frac{3 \times 1}{3} + (Na, Ba) \frac{6 \times 1}{10} O(3) \frac{3 \times 2}{3} + \\
& P(1) \frac{1 \times 1}{4} O(1) \frac{1 \times 1}{4} + P(1) \frac{2 \times 1}{4} O(2) \frac{1 \times 1}{3} + P(1) \frac{1 \times 1}{4} O(3) \frac{1 \times 2}{3}
\end{aligned}$$

Table 9 LiCdPO₄(Pna₁)

	Li	Cd	P	O1	O2	O3	O4
O1	2	1	1				
O2	2	1	1				
O3	1	2	1				
O4	1	2	1				
Li				2	2	1	1
Cd				1	1	2	2
P				1	1	1	1
Total	6	6	4	4	4	4	4
multiplicity	4	4	4	4	4	4	4

Z=4. The formula is : $Li(1)_1 Cd(1)_1 P(1)_1 O(1)_1 O(2)_1 O(3)_1 O(4)_1$. The compound is decomposed as:

$$\begin{aligned}
& Li(1) \frac{2 \times 1}{6} O(1) \frac{2 \times 1}{4} + Li(1) \frac{2 \times 1}{6} O(2) \frac{2 \times 1}{4} + Li(1) \frac{1 \times 1}{6} O(3) \frac{1 \times 1}{4} + Li(1) \frac{1 \times 1}{6} O(4) \frac{1 \times 1}{4} + \\
& Cd(1) \frac{1 \times 1}{6} O(1) \frac{1 \times 1}{4} + Cd(1) \frac{1 \times 1}{6} O(2) \frac{1 \times 1}{4} + Cd(1) \frac{2 \times 1}{6} O(3) \frac{2 \times 1}{4} + Cd(1) \frac{2 \times 1}{6} O(4) \frac{2 \times 1}{4} + \\
& P(1) \frac{1 \times 1}{4} O(1) \frac{1 \times 1}{4} + P(1) \frac{2 \times 1}{4} O(2) \frac{1 \times 1}{4} + P(1) \frac{1 \times 1}{4} O(3) \frac{1 \times 1}{4} + P(1) \frac{1 \times 1}{4} O(4) \frac{1 \times 1}{4}
\end{aligned}$$

Table 10 LiSrPO₄(P6₃)

	Li	Sr	P	O1	O2	O3	O4
O1	1	2	1				
O2	1	2	1				
O3	1	2	1				
O4	1	2	1				
Li				1	1	1	1
Sr				2	2	1	1
P				1	1	1	1
Total	4	8	4	4	4	3	3
multiplicity	6	6	6	6	6	6	6

Z=6. The formula is : $Li(1)_1 Sr(1)_1 P(1)_1 O(1)_1 O(2)_1 O(3)_1 O(4)_1$. The compound is decomposed as:

$$\begin{aligned}
& Li(1)\frac{1\times 1}{4}O(1)\frac{1\times 1}{4} + Li(1)\frac{1\times 1}{4}O(2)\frac{1\times 1}{4} + Li(1)\frac{1\times 1}{4}O(3)\frac{1\times 1}{3} + Li(1)\frac{1\times 1}{4}O(4)\frac{1\times 1}{3} + \\
& Sr(1)\frac{1\times 1}{8}O(1)\frac{2\times 1}{4} + Sr(1)\frac{2\times 1}{8}O(2)\frac{2\times 1}{4} + Sr(1)\frac{2\times 1}{8}O(3)\frac{1\times 1}{3} + Sr(1)\frac{2\times 1}{8}O(4)\frac{1\times 1}{3} + \\
& P(1)\frac{1\times 1}{4}O(1)\frac{1\times 1}{4} + P(1)\frac{1\times 1}{4}O(2)\frac{1\times 1}{4} + P(1)\frac{1\times 1}{4}O(3)\frac{1\times 1}{3} + P(1)\frac{1\times 1}{4} + O(4)\frac{1\times 1}{3}
\end{aligned}$$

Table 11 NaCdPO₄(Pna₁)

	Na	Cd	P	O1	O2	O3	O4
O1	2	1	1				
O2	1	2	1				
O3	2	1	1				
O4	1	2	1				
Na				2	1	1	1
Cd				1	2	1	2
P				1	1	1	1
Total	6	6	4	4	4	3	4
multiplicity	4	4	4	4	4	4	4

Z=4. The formula is : $Na(1)_1Cd(1)_1P(1)_1O(1)_1O(2)_1O(3)_1O(4)_1$. The compound is decomposed as:

$$\begin{aligned}
& Na(1)\frac{2\times 1}{6}O(1)\frac{2\times 1}{4} + Na(1)\frac{1\times 1}{6}O(2)\frac{1\times 1}{4} + Na(1)\frac{2\times 1}{6}O(3)\frac{1\times 1}{3} + Na(1)\frac{1\times 1}{6}O(4)\frac{1\times 1}{4} + \\
& Cd(1)\frac{1\times 1}{6}O(1)\frac{1\times 1}{4} + Cd(1)\frac{2\times 1}{6}O(2)\frac{2\times 1}{4} + Cd(1)\frac{1\times 1}{6}O(3)\frac{1\times 1}{3} + Cd(1)\frac{2\times 1}{6}O(4)\frac{2\times 1}{4} + \\
& P(1)\frac{1\times 1}{4}O(1)\frac{1\times 1}{4} + P(1)\frac{1\times 1}{4}O(2)\frac{1\times 1}{4} + P(1)\frac{1\times 1}{4}O(3)\frac{1\times 1}{3} + P(1)\frac{1\times 1}{4} + O(4)\frac{1\times 1}{3}
\end{aligned}$$

Table 12 KBePO₄(Pna₂₁)

	K	Be	P	O1	O2	O3	O4
O1	3	1	1				
O2	3	1	1				
O3	3	1	1				
O4	2	1	1				
K				2	3	1	1
Be				1	1	1	1
P				1	1	1	1
Total	11	4	4	4	5	3	3
multiplicity	4	4	4	4	4	4	4

Z=4. The formula is : $K(1)_1Be(1)_1P(1)_1O(1)_1O(2)_1O(3)_1O(4)_1$. The compound is decomposed as:

$$\begin{aligned}
& K(1) \frac{3 \times 1}{11} O(1) \frac{2 \times 1}{4} + K(1) \frac{3 \times 1}{11} O(2) \frac{3 \times 1}{5} + K(1) \frac{3 \times 1}{11} O(3) \frac{1 \times 1}{3} + K(1) \frac{2 \times 1}{11} O(4) \frac{1 \times 1}{3} + \\
& Be(1) \frac{1 \times 1}{4} O(1) \frac{1 \times 1}{4} + Be(1) \frac{1 \times 1}{4} O(2) \frac{1 \times 1}{5} + Be(1) \frac{1 \times 1}{4} O(3) \frac{1 \times 1}{3} + Be(1) \frac{1 \times 1}{4} O(4) \frac{1 \times 1}{3} + \\
& P(1) \frac{1 \times 1}{4} O(1) \frac{1 \times 1}{4} + P(1) \frac{1 \times 1}{4} O(2) \frac{1 \times 1}{5} + P(1) \frac{1 \times 1}{4} O(3) \frac{1 \times 1}{3} + P(1) \frac{1 \times 1}{4} + O(4) \frac{1 \times 1}{3}
\end{aligned}$$

Table 13 KZnPO₄(Pna2₁)

	K	Zn	P	O1	O2	O3	O4
O1	3	1	1				
O2	2	1	1				
O3	2	1	1				
O4	2	1	1				
K				3	2	2	2
Zn				1	1	1	1
P				1	1	1	1
Total	9		4	5	4	4	4
multiplicity	4	4	4	4	4	4	4

Z=4. The formula is : $K(1)_1 Zn(1)_1 P(1)_1 O(1)_1 O(2)_1 O(3)_1 O(4)_1$. The compound is decomposed as:

$$\begin{aligned}
& K(1) \frac{3 \times 1}{9} O(1) \frac{3 \times 1}{5} + K(1) \frac{2 \times 1}{9} O(2) \frac{2 \times 1}{4} + K(1) \frac{2 \times 1}{9} O(3) \frac{2 \times 1}{4} + K(1) \frac{2 \times 1}{9} O(4) \frac{2 \times 1}{4} + \\
& Zn(1) \frac{1 \times 1}{4} O(1) \frac{1 \times 1}{5} + Zn(1) \frac{1 \times 1}{4} O(2) \frac{1 \times 1}{4} + Zn(1) \frac{1 \times 1}{4} O(3) \frac{1 \times 1}{3} + Zn(1) \frac{1 \times 1}{4} O(4) \frac{1 \times 1}{4} + \\
& P(1) \frac{1 \times 1}{4} O(1) \frac{1 \times 1}{4} + P(1) \frac{1 \times 1}{4} O(2) \frac{1 \times 1}{5} + P(1) \frac{1 \times 1}{4} O(3) \frac{1 \times 1}{4} + P(1) \frac{1 \times 1}{4} + O(4) \frac{1 \times 1}{4}
\end{aligned}$$

Table 14 KZnPO₄(Pnma)

	K	Zn	P	O1	O2	O3	O4
O1	2	1	1				
O2	2	1	1				
O3	1	1	1				
O4	2	1	1				
K				1	1	1	1
Zn				1	1	1	1
P				1	1	1	1
Total	7	4	4	3	3	3	3
multiplicity	4	4	4	4	4	4	4

Z=4. The formula is : $K(1)_1 Zn(1)_1 P(1)_1 O(1)_1 O(2)_1 O(3)_1 O(4)_1$. The compound is decomposed as:

$$\begin{aligned}
& K(1) \frac{2 \times 1}{7} O(1) \frac{1 \times 1}{3} + K(1) \frac{2 \times 1}{7} O(2) \frac{1 \times 1}{3} + K(1) \frac{1 \times 1}{7} O(3) \frac{1 \times 1}{3} + K(1) \frac{2 \times 1}{7} O(4) \frac{1 \times 1}{3} + \\
& Zn(1) \frac{1 \times 1}{4} O(1) \frac{1 \times 1}{3} + Zn(1) \frac{1 \times 1}{4} O(2) \frac{1 \times 1}{3} + Zn(1) \frac{1 \times 1}{4} O(3) \frac{1 \times 1}{3} + Zn(1) \frac{1 \times 1}{4} O(4) \frac{1 \times 1}{3} + \\
& P(1) \frac{1 \times 1}{4} O(1) \frac{1 \times 1}{3} + P(1) \frac{1 \times 1}{4} O(2) \frac{1 \times 1}{3} + P(1) \frac{1 \times 1}{4} O(3) \frac{1 \times 1}{3} + P(1) \frac{1 \times 1}{4} + O(4) \frac{1 \times 1}{3}
\end{aligned}$$

Table 15 NaZnPO₄(P₂/n)

	Na	Zn	P	O1	O2	O3	O4
O1	1	1	1				
O2	3	1	1				
O3	1	1	1				
O4	1	1	1				
Na				1	1	1	1
Zn				1	1	1	1
P				1	1	1	1
Total	6	4	4	3	3	3	3
multiplicity	4	4	4	4	4	4	4

Z=4. The formula is : $Na(1)_1 Zn(1)_1 P(1)_1 O(1)_1 O(2)_1 O(3)_1 O(4)_1$. The compound is decomposed as:

$$\begin{aligned}
& Na(1) \frac{1 \times 1}{6} O(1) \frac{1 \times 1}{3} + Na(1) \frac{3 \times 1}{6} O(2) \frac{1 \times 1}{3} + Na(1) \frac{1 \times 1}{6} O(3) \frac{1 \times 1}{3} + Na(1) \frac{1 \times 1}{6} O(4) \frac{1 \times 1}{3} + \\
& Zn(1) \frac{1 \times 1}{4} O(1) \frac{1 \times 1}{3} + Zn(1) \frac{1 \times 1}{4} O(2) \frac{1 \times 1}{3} + Zn(1) \frac{1 \times 1}{4} O(3) \frac{1 \times 1}{3} + Zn(1) \frac{1 \times 1}{4} O(4) \frac{1 \times 1}{3} + \\
& P(1) \frac{1 \times 1}{4} O(1) \frac{1 \times 1}{3} + P(1) \frac{1 \times 1}{4} O(2) \frac{1 \times 1}{3} + P(1) \frac{1 \times 1}{4} O(3) \frac{1 \times 1}{3} + P(1) \frac{1 \times 1}{4} + O(4) \frac{1 \times 1}{3}
\end{aligned}$$

Table 16 NH₄BePO₄(Pna2₁)

	NH ₄	Be	P	O1	O2	O3	O4
O1	3	1	1				
O2	3	1	1				
O3	2	1	1				
O4	2	1	1				
NH ₄				2	3	2	1
Be				1	1	1	1
P				1	1	1	1
Total	10	4	4	4	5	4	3
multiplicity	4	4	4	4	4	4	4

Z=4. The formula is : $NH_4(1)_1 Be(1)_1 P(1)_1 O(1)_1 O(2)_1 O(3)_1 O(4)_1$. The compound is decomposed as:

$$\begin{aligned}
& NH_4(1) \frac{3 \times 1}{10} O(1) \frac{2 \times 1}{4} + NH_4(1) \frac{3 \times 1}{10} O(2) \frac{3 \times 1}{5} + NH_4(1) \frac{2 \times 1}{10} O(3) \frac{2 \times 1}{4} + NH_4(1) \frac{2 \times 1}{10} O(4) \frac{1 \times 1}{3} + \\
& Be(1) \frac{1 \times 1}{4} O(1) \frac{1 \times 1}{4} + Be(1) \frac{1 \times 1}{4} O(2) \frac{1 \times 1}{5} + Be(1) \frac{1 \times 1}{4} O(3) \frac{1 \times 1}{4} + Be(1) \frac{1 \times 1}{4} O(4) \frac{1 \times 1}{3} + \\
& P(1) \frac{1 \times 1}{4} O(1) \frac{1 \times 1}{4} + P(1) \frac{1 \times 1}{4} O(2) \frac{1 \times 1}{5} + P(1) \frac{1 \times 1}{4} O(3) \frac{1 \times 1}{4} + P(1) \frac{1 \times 1}{4} + O(4) \frac{1 \times 1}{3}
\end{aligned}$$

Table 17 KMgPO₄(P2₁/c)

	K1	K2	Mg1	Mg2	P1	P2	O1	O2	O3	O4	O5	O6	O7	O8
O1	1	0	2	0	1	0								
O2	0	2	1	0	1	0								
O3	1	1	1	0	1	0								
O4	2	0	0	1	1	0								
O5	1	1	1	0	0	1								
O6	0	2	0	1	0	1								
O7	2	0	0	1	0	1								
O8	1	1	0	1	0	1								
K1							1	0	1	2	1	0	2	1
K2							0	2	1	0	1	2	0	1
Mg1							2	1	1	0	1	0	0	1
Mg2							0		1	1	1	2	1	1
P1							1	1	1	1	0	0	0	0
P2							0		0	0	1	1	2	1
Total	8	7	5	4	4	4	4	4	5	4	5	5	5	5
multiplicity	4	4	4	4	4	4	4	4	4	4	4	4	4	4

Z=8. The formula is :

$$K(1)_{1/2} K(2)_{1/2} Mg(1)_{1/2} Mg(2)_1 P(1)_1 P(2)_1 O(1)_1 O(2)_1 O(3)_1 O(4)_{1/2} O(5)_1 O(6)_1 O(7)_1 O(8)_1$$

The compound is decomposed as:

$$\begin{aligned}
& K(1) \frac{1 \times 1/2}{8} O(1) \frac{1 \times 1}{4} + K(1) \frac{1 \times 1/2}{8} O(3) \frac{1 \times 1}{5} + K(1) \frac{2 \times 1/2}{8} O(4) \frac{2 \times 1/2}{4} + K(1) \frac{2 \times 1/2}{8} O(5) \frac{2 \times 1/2}{4} + \\
& K(1) \frac{1 \times 1/2}{8} O(6) \frac{1 \times 1}{5} + K(1) \frac{2 \times 1/2}{8} O(7) \frac{2 \times 1}{5} + K(2) \frac{2 \times 1/2}{7} O(2) \frac{2 \times 1}{4} + K(2) \frac{1 \times 1/2}{7} O(3) \frac{1 \times 1}{5} + \\
& K(2) \frac{2 \times 1/2}{7} O(5) \frac{2 \times 1}{5} + K(2) \frac{1 \times 1/2}{7} O(6) \frac{1 \times 1}{5} + K(2) \frac{2 \times 1/2}{7} O(8) \frac{2 \times 1}{5} + Mg(1) \frac{2 \times 1/2}{5} O(1) \frac{2 \times 1}{4} + \\
& Mg(1) \frac{1 \times 1/2}{5} O(2) \frac{2 \times 1}{4} + Mg(1) \frac{1 \times 1/2}{5} O(3) \frac{1 \times 1}{5} + Mg(1) \frac{1 \times 1/2}{5} O(5) \frac{1 \times 1}{5} + Mg(2) \frac{1 \times 1}{4} O(4) \frac{1 \times 1/2}{4} + \\
& Mg(2) \frac{1 \times 1}{4} O(6) \frac{2 \times 1}{5} + Mg(2) \frac{1 \times 1}{4} O(7) \frac{1 \times 1}{5} + Mg(2) \frac{1 \times 1}{4} O(8) \frac{1 \times 1}{5} + P(1) \frac{1 \times 1}{4} O(1) \frac{1 \times 1}{4} + \\
& P(1) \frac{1 \times 1}{4} O(2) \frac{1 \times 1}{4} + P(1) \frac{1 \times 1}{4} O(3) \frac{1 \times 1}{5} + P(1) \frac{1 \times 1}{4} + O(4) \frac{1 \times 1/2}{4} + P(2) \frac{1 \times 1}{4} O(5) \frac{1 \times 1}{5} + \\
& P(2) \frac{1 \times 1}{4} O(6) \frac{1 \times 1}{5} + P(2) \frac{1 \times 1}{4} O(7) \frac{2 \times 1}{5} + P(2) \frac{1 \times 1}{4} O(8) \frac{1 \times 1}{5}
\end{aligned}$$

Table 18 NH_4ZnPO_4 (P6_3)

	NH4(1)	NH4(2)	Zn1	Zn2	P1	P2	O1	O2	O3	O4	O5	O6
O1	0	6	1	0	1	0						
O2	1	3	1	0	1	0						
O3	1	0	1	0	1	0						
O4	2	0	1	0	0	3						
O5	3	0	0	3	1	0						
O6	1	0	0	1	0	1						
NH4(1)								1	1	2	3	3
NH4(2)							2	1	0	0	0	0
Zn1							1	1	1	1	0	0
Zn2							0		0	1	1	1
P1							1	1	1	0	1	0
P2							0	0	0	1	0	1
Total	8	9	4	4	4	4	4	4	3	5	5	5
multiplicity	6	2	6	2	6	2	6	6	6	6	6	2

Table 19 LiCaPO_4 ($\text{P3}_1\text{c}$)

	Li	Ca	P1	P2	P3	O1	O2	O3	O4	O5	O6
O1	1	0	1	0	0						
O2	0	1	0	1	0						
O3	0	1	0	0	1						
O4	1	2	3	0							
O5	1	2	0	3							
O6	1	2	0	0	3						
Li						3		0	1	1	1
Ca						0	3	3	2	2	2
P1						1	0	0	1	0	0
P2						0	1	0	0	1	0
P3								1			1
Total	4	8	4	4	4	4	4	4	4	4	4
multiplicity	6	6	2	2	2	2	2	2	6	6	6

Table 20 NaMgPO₄ (P2₁2₁2₁)

	N a1	N a2	N a3	M g1	M g2	M g3	P 1	P 2	P 3	O 1	O 2	O 3	O 4	O 5	O 6	O 7	O 8	O 9	O 10	O 11	O 12
O1	0	1	1	0	1	0	0	0	1												
O2	1	1	0	0	1	0	0	1	0												
O3	1	1	0	1	0	1	0	1	0												
O4	1	0	1	0	0	1	1	0	0												
O5	1	1	0	0	0	0	1	0	0												
O6	0	0	2	1	0	0	0	0	1												
O7	1	0	1	1	1		0	1	0												
O8	0	1	1	1	1	0	1	0	1												
O9	1	1	0	0	0	2	0	0	0												
O10	0	2	0	1	1		1	0	1												
O11	1	0	1	1	1	0	0	0	0												
O12	1	0	1	0	0	2	0	1		0											
Na1										0	1	1	1	1	0	1	0	1	0	1	1
Na2										1	1	1	0	1	0	0	1	1	2	0	0
Na3										1	0	0	1	0	2	1	1	0	0	1	1
Mg1										0	0	1	0	0	0	1	1	0	1	1	0
Mg2										1	1	0	0	0	1	1	1	0	1	1	0
Mg3											0	0	1	1	0	0	0	2	0	0	2
P1										0	0	0	1	1	0	0	1	0	1	0	0
P2										0	0	1	0	0	0	1	0	0	0	0	1
P3										1	1	0	0	0	1	0	0	1	0	1	0
Total	8	8	8	6	6	6	4	4	4	4	4	4	4	4	4	5	5	5	5	5	5
multipl icity	4	4	4	4	4	4	4	4	4	4	4	4	4	4	4	4	4	4	4	4	4

Table 21 AgBePO₄ (P₂/n)

	A g1	Ag 2	Ag 3	Be 1	Be 2	Be 3	P 1	P 2	P 3	O 1	O 2	O 3	O 4	O 5	O 6	O 7	O 8	O 9	O 10	O 11	O 12
O1	2	0	0	0	0	1	1	0	0	0	0	0	0								
O2	2	0	0	1	0	0	0	1	0	0	0	0	0								
O3	2	0	0	0	1	0	0	0	1	0	0	0	0								
O4	0	1	1	1	0	0	1	0	0	0	0	0	0								
O5	0	1	1	0	1	0	0	1	0	0	0										
O6	0	1	1	0	0	1	0	0	1	0	0										
O7	0	1	0	0	1	0	1	0	0	0											
O8	0	0	1	0	0	1	0	1	0	0	0										
O9	0	1	0	1	0	0	0	0	1												
O10	1	0	1	1	0	0	1	0	0												
O11	1	1	0	0	1	0	0	1	0												
O12	1	0	1	0	0	1	0	0	1	0											
Ag1										2	2	2	0	0	0	0	0	0	1	1	1
Ag2										0	0	0	1	1	1	1	0	1	0	1	0
Ag3										0	0	0	1	1	1	0	1	0	1	0	1
Be1										0	1	0	1	0	0	0	0	1	1	0	0
Be2										0	0	1	0	1	0	1	0	0	0	1	0
Be3										1	0	0	0	0	1	0	1	0	0	0	1
P1										1	0	0	1	0	0	1	0	0	1	0	0
P2										0	1	0	0	1	0	0	1	0	0	1	0
P3										0	0	1	0	0	1	0	0	1	0	0	1
Total	9	6	6	4	4	4	4	4	4	4	4	4	4	4	4	3	3	3	4	4	4
multipl icity	4	4	4	4	4	4	4	4	4	4	4	4	4	4	4	4	4	4	4	4	4

Table 22 NaBePO₄ (P2₁/n)

	N a1	N a2	N a3	B e1	B e2	B e3	P 1	P 2	P 3	O 1	O 2	O 3	O 4	O 5	O 6	O 7	O 8	O 9	O 10	O 11	O 12
O1	2	0	0	0	0	1	1	0	0												
O2	2	0	0	1	0	0	0	1	0												
O3	2	0	0	0	1	0	0	0	1												
O4	0	1	1	1	0	0	1	0	0												
O5	0	1	1	0	1	0	0	1	0												
O6	0	1	1	0	0	1	0	0	1												
O7	0	1	0	0	1	0	1	0	0												
O8	0	0	1	0	0	1	0	1	0												
O9	0	1	0	1	0	0	0	0	1												
O10	1	0	1	1	0	0	1	0	0												
O11	1	1	0	0	1	0	0	1	0												
O12	1	0	1	0	0	1	0	0	1												
Na1										2	2	2	0	0	0	0	0	0	1	1	1
Na2										0	0	0	1	1	1	1	0	1	0	1	0
Na3										0	0	0	1	1	1	0	1	0	1	0	1
Be1										0	1	0	1	0	0	0	0	1	1	0	0
Be2										0	0	1	0	1	0	1	0	0	0	1	0
Be3										1	0	0	0	0	1	0	1	0	0	0	1
P1										1	0	0	1	0	0	1	0	0	1	0	0
P2										0	1	0	0	1	0	0	1	0	0	1	0
P3										0	0	1	0	0	1	0	0	1	0	0	1
Total	9	6	6	4	4	4	4	4	4	4	4	4	4	4	4	3	3	3	4	4	4
multipl icity	4	4	4	4	4	4	4	4	4	4	4	4	4	4	4	4	4	4	4	4	4

Table 23 NaCaPO₄ (P n m a)

	N a1	N a2	N a3	C a1	C a2	C a3	P 1	P 2	P 3	O 1	O 2	O 3	O 4	O 5	O 6	O 7	O 8	O 9	O 10	O 11	O 12
O1	0	1	0	0	1	1	1	0	0												
O2	3	0	0	1	0	1	1	0	0												
O3	1	0	1	1	1	0	1	0	0												
O4	2	0	1	1	1	0	1	0	0												
O5	1	0	0	0	1	1	0	1	0												
O6	0	1	1	0	1	1	0	1	0												
O7	0	2	0	0	1	1	0	1	0												
O8	0	1	1	0	1	1	0	1	0												
O9	0	0	1	2	0	0	0	0	1												
O10	0	1	2	1	1	0	0	0	1												
O11	0	1	1	1	0	1	0	0	1												
O12	1	0	1	1	0	1	0	0	1	0											
Na1										0	2	1	2	1	0	0	0	0	0	0	1
Na2										1	0	0	0	0	1	2	1	0	1	1	0
Na3										0	0	1	1	0	1	0	1	1	1	1	1
Ca1										0	1	1	1	0	0	0	0	2	1	1	1
Ca2										1	0	1	1	1	1	1	1	0	1	0	0
Ca3										1	1	0	0	1	1	1	1	0	0	1	1
P1										1	1	1	1	0	0	0	0	0	0	0	0
P2										0	0	0	0	1	1	1	1	0	0	0	0
P3										0	0	0	0	0	0	0	0	1	1	1	1
Total	8	7	9	8	8	8	4	4	4	4	5	5	6	4	5	5	5	4	5	5	5
multipl icity	4	4	4	4	4	4	4	4	4	4	4	4	4	4	4	4	4	4	4	4	4

Table 24 KZnPO₄ (P6₃)

	K 1	K 2	K 3	K 4	K 5	K 6	Z n 1	Z n 2	Z n 3	Z n 4	P 1	P 2	P 3	P 4	O 1	O 2	O 3	O 4	O 5	O 6	O 7	O 8	O 9	O 1 0	O 1 1	O 1 2	O 1 3	O 1 4	O 1 5	O 1 6
O1	1	0	0	6			1	0	0		0	0	1																	
O2	0	0	1	3			1	0	0		0	0	1																	
O3	1	1	1				0	0	1	0	1	0	0																	
O4	0	1	1				0	0	0	1	1	0	0																	
O5	1	0	1				1	0	0		0	0	1																	
O6	0	2	0				0	1	0		0	0	0	1																
O7	0	0	0		3	3	0	0	1	0	0	1	0																	
O8	0	0	0		3	3	0	0	0	1	0	0	0	1																
O9	1	0	2				0	1	0		0	0	1																	
O10	1	0	1				0	0	0	1	0	0	0	1																
O11	1	1	1				0	1	0		0	1	0																	
O12	2	0	1				1	0	0		1	0	0																	
O13	0	0	1		3		0	1	0					1																
O14	1	1	0				1				1																			
O15	0	2	0					1	0		1																			
O16	0	1	0			3				1		1																		
K1															1	0	1	0	1	0	0	0	1	1	1	2		1		
K2															0	0	1	1	0	2	0	0	0	0	1	0		1	2	1
K3															0	1	1	1	1	0	0	0	2	1	1	1	1			
K4															1	1														
K5																					1	1				0	1			
K6																					1	1								1
Zn1															1	1	0	0	1	0	0	0	0	0	0	1				
Zn2															0	0	0	0	0	1	0	0	1	0	1	0		1		
Zn3															0	0	1	0	0	0	1	0	0	0	0	0	1		1	
Zn4																	0	1			0	1		1			0		0	1
P1															0	0	1	1	0	0	0	0	0	0	0	1	0	1	0	0
P2															0	0	0	0	0	0	1	0	0	0	1	0			1	1
P3															1	1	0	0	1	0	0	0	1	0	0	0				
P4																				1		1		1			1			
Tot al	9	9	1 0	9	9	9	4	4	4	4	4	4	4	4	4	4	5	4	4	4	4	4	5	4	5	5	4	4	4	4
mul tipli city	6	6	6	2	2	2	6	6	6	6	6	6	6	6	6	6	6	6	6	6	6	6	6	6	6	6	6	6	6	6

Table 25 CaTiO₃(P b n m)

	Ca	Ti	O1	O2
O1	4	2		
O2	8	4		
Ca			2	2
Ti			2	2
Total	10	6	4	4
multiplicity	4	4	4	8

Z=4. The formula is : $Ca(1)_1Ti(1)_1O(1)_1O(2)_1$. The compound is decomposed as:

$$Ca(1)\frac{4\times 1}{12}O(1)\frac{2\times 1}{4} + Ca(1)\frac{8\times 1}{12}O(2)\frac{2\times 1}{4} + Ti(1)\frac{1\times 1}{6}O(1)\frac{2\times 1}{4} + Ti(1)\frac{4\times 1}{6}O(2)\frac{2\times 1}{4}$$

Table 26 Y₂Ti₂O₇(Fd-3m)

	Y	Ti	O1	O2
O1	2	0	0	0
O2	6	6	0	0
Y	0	0	4	2
Ti	0	0	0	2
Total	8	6	4	4
multiplicity	16	16	8	48

Z=8. The formula is : $Y(1)_2Ti(1)_2O(1)_1O(2)_6$. The compound is decomposed as:

$$Y(1)\frac{2\times 2}{8}O(1)\frac{4\times 1}{4} + Y(1)\frac{6\times 2}{8}O(2)\frac{2\times 6}{4} + Ti(1)\frac{6\times 2}{6}O(2)\frac{2\times 6}{4}$$

Table 27 PbWO₄(I 41/a)

	Pb	W	O1
O1	8	4	
Pb			2
W			1
Total	8	4	3
multiplicity	4	4	16

Z=8. The formula is : $Pb(1)_1W(1)_1O(1)_4$. The compound is decomposed as: $Pb(1)\frac{8\times 1}{8}O(1)\frac{2\times 4}{3} + W(1)\frac{4\times 2}{4}O(1)\frac{1\times 4}{3}$

Table 28 Lu₃Al₅O₁₂(I a -3 d)

	Lu	Al1	Al2	O
O	8	6	4	
Lu				2
Al1				1
Al2				1
Total	8	6	4	4
multiplicity	24	16	24	96

Z=8. The formula is : $Lu(1)_3Al(1)_2Al(2)_3O(1)_{12}$. The compound is decomposed as:

$$Lu(1)\frac{8 \times 3}{8}O(1)\frac{2 \times 12}{4} + Al(1)\frac{6 \times 2}{6}O(1)\frac{1 \times 12}{4} + Al(2)\frac{4 \times 3}{4}O(1)\frac{1 \times 12}{4}$$

Table 29 Y₃Al₅O₁₂(I a -3 d)

	Y	Al1	Al2	O
O	8	6	4	
Y				2
Al1				1
Al2				1
Total	8	6	4	4
multiplicity	24	16	24	96

Z=8. The formula is : $Y(1)_3Al(1)_2Al(2)_3O(1)_{12}$. The compound is decomposed as:

$$Y(1)\frac{8 \times 3}{8}O(1)\frac{2 \times 12}{4} + Al(1)\frac{6 \times 2}{6}O(1)\frac{1 \times 12}{4} + Al(2)\frac{4 \times 3}{4}O(1)\frac{1 \times 12}{4}$$

Table 30 Y₃Ga₅O₁₂ (I a -3 d)

	Y	Ga1	Ga2	O
O	8	6	4	0
Y	0	0		2
Ga1	0	0		1
Ga2				1
Total	8	6	4	4
multiplicity	24	16	24	96

Z=8. The formula is : $Y(1)_3Ga(1)_2Ga(2)_3O(1)_{12}$. The compound is decomposed as:

$$Y(1)\frac{8\times 3}{8}O(1)\frac{2\times 12}{4} + Ga(1)\frac{6\times 2}{6}O(1)\frac{1\times 12}{4} + Ga(2)\frac{4\times 3}{4}O(1)\frac{1\times 12}{4}$$

Table 31 ScVO₄(I 41/a m d)

	Sc	V	O1
O1	8	4	
Sc			2
V			1
Total	8	4	3
multiplicity	4	4	16

Z=4. The formula is : Sc(1)₁V(1)₁O(1)₄. The compound is decomposed as:

$$Sc(1)\frac{8\times 1}{8}O(1)\frac{2\times 4}{3} + V(1)\frac{4\times 1}{4}O(1)\frac{1\times 4}{3}$$

Table 32 YVO₄(I 41/a m d)

	Y	V	O1
O1	8	4	
Y			2
V			1
Total	8	4	3
multiplicity	4	4	16

Z=4. The formula is : Y(1)₁V(1)₁O(1)₄. The compound is decomposed as:

$$Y(1)\frac{8\times 1}{8}O(1)\frac{2\times 4}{3} + V(1)\frac{4\times 1}{4}O(1)\frac{1\times 4}{3}$$

Table 33 GdVO₄(I 41/a m d)

	Gd	V	O1
O1	8	4	0
Gd	0	0	2
V	0	0	1
Total	8	4	3
multiplicity	4	4	16

Z=4. The formula is : Gd(1)₁V(1)₁O(1)₄. The compound is decomposed as:

$$Gd(1)\frac{8\times 1}{8}O(1)\frac{2\times 4}{3}+V(1)\frac{4\times 1}{4}O(1)\frac{1\times 4}{3}$$

Table 34 LiNbO₃(R 3 c)

	Li	Nb	O1
O1	6	6	
Li			2
Nb			2
Total	6	6	4
multiplicity	6	6	18

Z=6. The formula is : $Li(1)_1Nb(1)_1O(1)_3$. The compound is decomposed as:

$$Li(1)\frac{6\times 1}{6}O(1)\frac{2\times 3}{4}+Nb(1)\frac{6\times 1}{6}O(1)\frac{2\times 4}{3}$$

Table 35 YNbO₄(C2/c)

	Y	Nb	O1	O2
O1	4	4		
O2	4	2		
Y			2	2
Nb			2	1
Total	8	6	4	3
multiplicity	4	4	8	8

Z=4. The formula is : $Y(1)_1Nb(1)_1O(1)_2O(2)_2$. The compound is decomposed as:

$$Y(1)\frac{4\times 1}{8}O(1)\frac{2\times 2}{4}+Y(1)\frac{4\times 1}{8}O(2)\frac{2\times 2}{3}+Nb(1)\frac{4\times 1}{6}O(1)\frac{2\times 2}{4}+Nb(1)\frac{2\times 1}{6}O(2)\frac{2\times 2}{3}$$

Table 36 YTaO₄(I2/a)

	Y	Ta	O1	O2
O1	4	2		
O2	4	4		
Y			2	2
Ta			1	2
Total	8	6	3	4
multiplicity	4	4	8	8

Z=4. The formula is : $Y(1)_1Ta(1)_1O(1)_2O(2)_2$. The compound is decomposed as:

$$Y(1)\frac{4\times 1}{8}O(1)\frac{2\times 2}{3} + Y(1)\frac{4\times 1}{8}O(2)\frac{2\times 2}{4} + Ta(1)\frac{2\times 1}{6}O(1)\frac{1\times 2}{3} + Ta(1)\frac{4\times 1}{6}O(2)\frac{2\times 2}{4}$$

Table 37 LaNbO₄(I2/c)

	La	Nb	O1	O2
O1	4	4		
O2	4	4		
La			2	2
Nb			2	2
Total	8	8	4	4
multiplicity	4	4	8	8

Z=4. The formula is : $La(1)_1Nb(1)_1O(1)_2O(2)_2$. The compound is decomposed as:

$$La(1)\frac{4\times 1}{8}O(1)\frac{2\times 2}{4} + La(1)\frac{4\times 1}{8}O(2)\frac{2\times 2}{4} + Nb(1)\frac{4\times 1}{8}O(1)\frac{2\times 2}{4} + Nb(1)\frac{4\times 1}{8}O(2)\frac{2\times 2}{4}$$

Table 38 CaSnO₃(P b n m)

	Ca	Sn	O1	O2
O1	2	2		
O2	6	4		
Ca			1	3
Sn			2	2
Total	8	6	3	5
multiplicity	4	4	4	8

Z=4. The formula is : $Ca(1)_1Sn(1)_1O(1)_1O(2)_2$. The compound is decomposed as:

$$Ca(1)\frac{4\times 1}{8}O(1)\frac{2\times 2}{4} + Ca(1)\frac{4\times 1}{8}O(2)\frac{2\times 2}{4} + Sn(1)\frac{4\times 1}{8}O(1)\frac{2\times 2}{4} + Sn(1)\frac{4\times 1}{8}O(2)\frac{2\times 2}{4}$$

Table 39 La₂Zr₂O₇(Fd-3m)

	La	Zr	O1	O2
O1	6	6		
O2	2	0		
La			2	4
Zr			2	0
Total	8	6	4	4
multiplicity	16	16	48	8

Z=8. The formula is : $La(1)_2Zr(1)_2O(1)_6O(2)_1$. The compound is decomposed as:

$$La(1)\frac{6 \times 2}{8}O(1)\frac{2 \times 6}{4} + La(1)\frac{2 \times 2}{8}O(2)\frac{4 \times 1}{4} + Zr(1)\frac{6 \times 2}{6}O(1)\frac{2 \times 6}{4}$$

Table 40 Y₂Sn₂O₇(Fd-3m)

	Y	Sn	O1	O2
O1	6	6		
O2	2	0		
Y			2	4
Sn			2	0
Total	8	6	4	4
multiplicity	16	16	48	8

Z=8. The formula is : $Y(1)_2Sn(1)_2O(1)_6O(2)_1$

The compound is decomposed as:

$$Y(1)\frac{6 \times 2}{8}O(1)\frac{2 \times 6}{4} + Y(1)\frac{2 \times 2}{8}O(2)\frac{4 \times 1}{4} + Sn(1)\frac{6 \times 2}{6}O(1)\frac{2 \times 6}{4}$$

Table 41 GdNbO₄(I2/a)

	Gd	Nb	O1	O2
O1	4	2		
O2	4	4		
Gd			2	2
Nb			2	2
Total	8	6	4	4
multiplicity	4	4	8	8

Z=4. The formula is : $Gd(1)_1Nb(1)_1O(1)_2O(2)_2$. The compound is decomposed as:

$$Gd(1) \frac{4 \times 1}{8} O(1) \frac{2 \times 2}{4} + Gd(1) \frac{4 \times 1}{8} O(2) \frac{2 \times 2}{4} + Nb(1) \frac{2 \times 1}{6} O(1) \frac{2 \times 2}{4} + Nb(1) \frac{4 \times 1}{6} O(2) \frac{2 \times 2}{4}$$

Table 42 CaZrO₃(P c m n)

	Ca	Zr	O1	O2
O1	2	2	0	0
O2	6	4	0	0
Ca	0	0	1	3
Zr	0	0	2	2
Total	8	6	3	5
multiplicity	4	4	4	8

Z=4. The formula is : $Ca(1)_1 Zr(1)_1 O(1)_1 O(2)_2$. The compound is decomposed as:

$$Ca(1) \frac{2 \times 1}{8} O(1) \frac{1 \times 1}{3} + Ca(1) \frac{6 \times 1}{8} O(2) \frac{3 \times 2}{5} + Zr(1) \frac{2 \times 1}{6} O(1) \frac{2 \times 1}{3} + Zr(1) \frac{4 \times 1}{6} O(2) \frac{2 \times 2}{5}$$

Table 43 CaNb₂O₆(P b c n)

	Ca	Nb	O1	O2	O3
O1	4	1			
O2	4	2			
O3	0	3			
Ca			2	2	0
Nb			1	2	3
Total	8	6	3	4	3
multiplicity	4	8	8	8	8

Z=4. The formula is : $Ca(1)_1 Nb(1)_2 O(1)_2 O(2)_2 O(3)_2$. The compound is decomposed as:

$$Ca(1) \frac{4 \times 1}{8} O(1) \frac{2 \times 2}{3} + Ca(1) \frac{4 \times 1}{8} O(2) \frac{2 \times 2}{4} + Nb(1) \frac{1 \times 2}{6} O(1) \frac{1 \times 2}{3} + Nb(1) \frac{2 \times 2}{6} O(2) \frac{2 \times 2}{4} + Nb(1) \frac{3 \times 2}{6} O(3) \frac{3 \times 2}{3}$$

Table 44 LaVO₄(P 21/n)

	La	V	O1	O2	O3	O4
O1	2	1				
O2	3	1				
O3	2	1				
O4	2	1				
La			2	2	2	2
V			1	1	1	1
Total	9	4	3	3	3	3
multiplicity	4	4	4	4	4	4

Z=4. The formula is : $La(1)_1V(1)_1O(1)_1O(2)_1O(3)_1O(4)_1$. The compound is decomposed as:

$$La(1)\frac{2\times 1}{9}O(1)\frac{2\times 1}{3} + La(1)\frac{3\times 1}{9}O(2)\frac{2\times 1}{3} + La(1)\frac{2\times 1}{9}O(3)\frac{1\times 1}{3} + La(1)\frac{2\times 1}{9}O(4)\frac{2\times 1}{3} + \\ V(1)\frac{1\times 1}{4}O(1)\frac{1\times 1}{3} + V(1)\frac{1\times 1}{4}O(2)\frac{1\times 1}{3} + V(1)\frac{1\times 1}{4}O(3)\frac{1\times 1}{3} + V(1)\frac{1\times 1}{4}O(4)\frac{1\times 1}{3}$$

Table 45 NaNbO₃(P b m a)

	Na1	Na2	Nb1	O1	O2	O3	O4
O1	4	0	1				
O2	0	4	1				
O3	4	4	2				
O4	4	4	2				
Na1				2	0	2	1
Na2				0	2	2	1
Nb1				2	2	2	2
Total	12	12	6	4	4	6	4
multiplicity	4	4	8	4	4	8	8

Z=8. The formula is : $Na(1)_{1/2}Na(2)_{1/2}Nb(1)_1O(1)_{1/2}O(2)_{1/2}O(3)_1O(4)_1$. The compound is decomposed as:

$$Na(1)\frac{4\times 1/2}{12}O(1)\frac{2\times 1/2}{4} + Na(1)\frac{4\times 1/2}{12}O(3)\frac{2\times 1}{6} + Na(1)\frac{4\times 1/2}{12}O(4)\frac{1\times 1}{4} + Na(2)\frac{1\times 1}{6}O(2)\frac{2\times 1/2}{4} + \\ Na(2)\frac{1\times 1}{6}O(3) - + Na(2) - O(4) - + Nb(1)\frac{1\times 1}{4}O(1)\frac{1\times 1}{3} + Nb(1)\frac{1\times 1}{4}O(2)\frac{1\times 1}{3} + \\ Nb(1)\frac{1\times 1}{4}O(3)\frac{1\times 1}{3} + Nb(1)\frac{1\times 1}{4}O(4)\frac{1\times 1}{3}$$

Table 46 CaMoO_4 (I 41/a)

	Ca	Mo	O1
O1	8	4	
Ca			2
Mo			1
Total	8	4	3
multiplicity	4	4	16

Z=4. The formula is : $\text{Ca}(1)_1\text{Mo}(1)_1\text{O}(1)_4$. The compound is decomposed as:

$$\text{Ca}(1)\frac{8 \times 1}{8}\text{O}(1)\frac{2 \times 4}{3} + \text{Mo}(1)\frac{4 \times 1}{4}\text{O}(1)\frac{1 \times 4}{3}$$

Table 47 $\text{CaS}(\text{Fm}-3\text{m})$

	Ca	S
S	6	
Ca		6
Total	6	6
multiplicity	4	4

Z=4. The formula is : $\text{Ca}(1)_1\text{S}(1)_1$. The compound is decomposed as: $\text{Ca}(1)\frac{6 \times 1}{6}\text{S}(1)\frac{6 \times 1}{6}$

Table 48 $\text{MgS}(\text{Fm}-3\text{m})$

	Mg	S
S	6	0
Ca	0	6
Total	6	6
multiplicity	4	4

Z=4. The formula is : $\text{Mg}(1)_1\text{S}(1)_1$. The compound is decomposed as: $\text{Mg}(1)\frac{6 \times 1}{6}\text{S}(1)\frac{6 \times 1}{6}$

Table 49 Y_2O_3 (Ia-3)

	Y1	Y2	O1
O1	6	6	
Y1			1
Y2			3
Total	6	6	4
multiplicity	8	24	48

Z=4. The formula is : $Y(1)_{1/2}Y(2)_{3/2}O(1)_3$. The compound is decomposed as:

$$Y(1)\frac{8\times 1}{8}O(1)\frac{2\times 4}{3} + Y(2)\frac{4\times 1}{4}O(1)\frac{1\times 4}{3}$$

Table 50 SrMoO₄(I 41/a)

	Sr	Mo	O1
O1	8	4	0
Sr	0	0	2
Mo	0	0	1
Total	8	4	3
multiplicity	4	4	16

Z=4. The formula is : $Sr(1)_1Mo(1)_1O(1)_4$. The compound is decomposed as:

$$Sr(1)\frac{8\times 1}{8}O(1)\frac{2\times 4}{3} + Mo(1)\frac{4\times 1}{4}O(1)\frac{1\times 4}{3}$$

Table 51 Cs₂NaLaBr₆(Fm-3m)

	Cs	La	Na	Br
Br	12	6	6	0
Cs	0	0		4
La	0	0		1
Na				1
Total	12	6	6	6
multiplicity	8	4	4	24

Z=4. The formula is : $Cs(1)_1La(1)_1Na(1)_1Br(1)_6$. The compound is decomposed as:

$$Cs(1)\frac{12\times 2}{12}Br(1)\frac{4\times 6}{6} + La(1)\frac{6\times 1}{6}Br(1)\frac{1\times 6}{6} + Na(1)\frac{6\times 1}{6}Br(1)\frac{1\times 6}{6}$$

Table 52 Cs₂NaYBr₆(Fm-3m)

	Cs	Y	Na	Br
Br	12	6	6	
Cs				4
Y				1
Na				1
Total	12	6	6	6
multiplicity	8	4	4	24

Z=4. The formula is : $Cs(1)_1Y(1)_1Na(1)_1Br(1)_6$. The compound is decomposed as:

$$Cs(1) \frac{12 \times 2}{12} Br(1) \frac{4 \times 6}{6} + Y(1) \frac{6 \times 1}{6} Br(1) \frac{1 \times 6}{6} + Na(1) \frac{6 \times 1}{6} Br(1) \frac{1 \times 6}{6}$$

Table 53 Cs_2NaYCl_6 (Fm-3m)

	Cs	Y	Na	Cl
Cl	12	6	6	
Cs				4
Y				1
Na				1
Total	12	6	6	6
multiplicity	8	4	4	24

Z=4. The formula is : $Cs(1)_1Y(1)_1Na(1)_1Cl(1)_6$. The compound is decomposed as:

$$Cs(1) \frac{12 \times 2}{12} Cl(1) \frac{4 \times 6}{6} + Y(1) \frac{6 \times 1}{6} Cl(1) \frac{1 \times 6}{6} + Na(1) \frac{6 \times 1}{6} Cl(1) \frac{1 \times 6}{6}$$

Table 54 $Cs_2NaLaCl_6$ (Fm-3m)

	Cs	La	Na	Cl
Cl	12	6	6	
Cs				4
La				1
Na				1
Total	12	6	6	6
multiplicity	8	4	4	24

Z=4. The formula is : $Cs(1)_1La(1)_1Na(1)_1Cl(1)_6$. The compound is decomposed as:

$$Cs(1) \frac{12 \times 2}{12} Cl(1) \frac{4 \times 6}{6} + La(1) \frac{6 \times 1}{6} Cl(1) \frac{1 \times 6}{6} + Na(1) \frac{6 \times 1}{6} Cl(1) \frac{1 \times 6}{6}$$

Table 55 YPO_4 (I 41/a m d)

	Y	P	O1
O1	8	4	
Y			2
P			1
Total	8	4	3
multiplicity	4	4	16

Z=4. The formula is : $Y(1)_1P(1)_1O(1)_4$. The compound is decomposed as:

$$Y(1)\frac{8\times 1}{8}O(1)\frac{2\times 4}{3} + P(1)\frac{4\times 1}{4}O(1)\frac{1\times 4}{3}$$

Table 56 ScPO₄ (I 41/a m d)

	Sc	P	O1
O1	8	4	
Sc			2
P			1
Total	8	4	3
multiplicity	4	4	16

Z=4. The formula is : $Sc(1)_1P(1)_1O(1)_4$. The compound is decomposed as:

$$Sc(1)\frac{8\times 1}{8}O(1)\frac{2\times 4}{3} + P(1)\frac{4\times 1}{4}O(1)\frac{1\times 4}{3}$$

Table 57 LuPO₄ (I 41/a m d)

	Lu	P	O1
O1	8	4	
Lu			2
P			1
Total	8	4	3
multiplicity	4	4	16

Z=4. The formula is : $Lu(1)_1P(1)_1O(1)_4$. The compound is decomposed as:

$$Lu(1)\frac{8\times 1}{8}O(1)\frac{2\times 4}{3} + P(1)\frac{4\times 1}{4}O(1)\frac{1\times 4}{3}$$

Table 58 LaPO₄ (P2₁/a)

	La	P	O1	O2	O3	O4
O1	2	1	0	0	0	0
O2	3	1	0	0	0	0
O3	3	1	0	0	0	0
O4	2	1	0	0	0	0
La	0	0	2	3	2	2
P	0	0	1	1	1	1
Total	10	4	3	4	3	3
multiplicity	4	4	4	4	4	4

Z=4. The formula is : $La(1)_1P(1)_1O(1)_1O(2)_1O(3)_1O(4)_1$. The compound is decomposed as:

$$La(1)\frac{3\times 1}{10}O(1)\frac{2\times 1}{4} + La(1)\frac{2\times 1}{6}O(2)\frac{2\times 1}{4} + La(1)\frac{1\times 1}{6}O(3)\frac{1\times 1}{4} + La(1)\frac{1\times 1}{6}O(4)\frac{1\times 1}{4} + \\ P(1)\frac{1\times 1}{4}O(1)\frac{1\times 1}{4} + P(1)\frac{2\times 1}{4}O(2)\frac{1\times 1}{4} + P(1)\frac{1\times 1}{4}O(3)\frac{1\times 1}{4} + P(1)\frac{1\times 1}{4}O(4)\frac{1\times 1}{4}$$

Table 59 LaOCl (P 4/n m m)

	La	O	Cl
O	4	0	
Cl	6	0	
La		1	2
Total	10	1	2
multiplicity	2	2	2

Z=2. The formula is : $La(1)_1O(1)_1Cl(1)_1$. The compound is decomposed as:

$$La(1)\frac{4\times 1}{10}O(1)\frac{1\times 1}{1} + La(1)\frac{6\times 1}{10}Cl(1)\frac{2\times 1}{2}$$

Table 60 Sr₃(PO₄)₂ (R-3m)

	Sr1	Sr2	P	O1	O2
O1	6	1	1		
O2	6	9	3		
Sr1				3	1
Sr2				1	3
P				1	1
Total	12	10	4	5	5
multiplicity	6	3	6	6	18

Z=3. The formula is : $Sr(1)_2Sr(2)_1P(1)_2O(1)_2O(2)_6$. The compound is decomposed as:

$$Sr(1)\frac{6\times 2}{12}O(1)\frac{3\times 2}{5} + Sr(1)\frac{6\times 2}{12}O(2)\frac{1\times 6}{5} + Sr(2)\frac{1\times 1}{10}O(1)\frac{1\times 2}{5} + Sr(2)\frac{9\times 1}{10}O(2)\frac{3\times 6}{5} + \\ P(1)\frac{1\times 2}{4}O(1)\frac{1\times 2}{5} + P(1)\frac{3\times 2}{4}O(2)\frac{1\times 6}{5}$$

Table 61 GdP₃O₉ (C 2 2 2 1)

	Gd	P1	P2	O1	O2	O3	O4	O5
O1	0	0	1					
O2	4	2	0					
O3	2	0	1					
O4	2	0	1					
O5	0	2	1					
Gd					2	1	1	0
P1					1	0	0	1
P2				2	0	1	1	1
Total	8	4	4	2	3	2	2	2
multiplicity	4	4	8	4	8	8	8	8

Z=4. The formula is : $Gd(1)_1P(1)_1P(2)_2O(1)_1O(2)_2O(3)_2O(4)_2O(5)_2$. The compound is decomposed as:

$$Gd(1)\frac{4\times 1}{8}O(2)\frac{2\times 2}{3} + Gd(1)\frac{2\times 1}{8}O(3)\frac{2\times 2}{2} + Gd(1)\frac{4\times 1}{8}O(4)\frac{1\times 2}{2} + P(1)\frac{2\times 1}{4}O(2)\frac{1\times 2}{3} + \\ P(1)\frac{2\times 1}{4}O(5)\frac{1\times 2}{2} + P(2)\frac{1\times 2}{4}O(1)\frac{2\times 1}{2} + P(2)\frac{1\times 2}{4}O(3)\frac{1\times 2}{2} + P(2)\frac{1\times 2}{4}O(4)\frac{1\times 2}{2} + P(2)\frac{1\times 2}{4}O(5)\frac{1\times 2}{2}$$

Table 62 LuP₃O₉ (R-3)

	Lu1	Lu2	Lu3	P1	P2	P3	P4	O1	O2	O3	O4	O5	O6	O7	O8	O9	O10	O11	O12
O1	1	0	0	0	1	0	0												
O2	1	0	0	0	1	0	0												
O3	0	0	0	1	1	0	0												
O4	0	0	0	1	0	0	1												
O5	0	0	0	0	1	1	0												
O6	1	0	0	0	0	1	0												
O7	0	6	0	1	0	0	0												
O8	0	0	0	0	0	1	1												
O9	1	0	0	0	0	1	0												
O10	1	0	0	0	0	0	1												
O11	0	0	6	0	0	0	1												
O12	1	0	0	1	0		0	0											
Lu1								1	1	0	0	0	1	0	0	1	1	0	1
Lu2								0	0	0	0	0	0	1	0	0	0	0	0
Lu3								0	0	0	0	0	0	0	0	0	0	1	0
P1								0	0	1	1	0	0	1	0	0	0	0	1
P2								1	1	1	0	1	0	0	0	0	0	0	0
P3								0	0	0	0	1	1	0	1	1	0	0	0
P4								0	0	0	1	0	0	0	1	0	1	1	0
Total	6	6	6	4	4	4	4	2	2	2	2	2	2	2	2	2	2	2	2
multiplicity	18	3	3	18	18	18	18	18	18	18	18	18	18	18	18	18	18	18	18

Table 63 Ca₁₀(PO₄)₆F₂ (P63/m)

	Ca1	Ca2	P	O1	O2	O3	F
O1	3	1	1				
O2	3	1	1				
O3	3	4	2				
F	0	1	0				
Ca1				2	2	1	
Ca2				1	1	2	3
P				1	1	1	0
Total	9	7	4	4	4	4	3
multiplicity	4	6	6	6	6	12	2

Z=2. The formula is : $Ca(1)_2Ca(2)_3P(1)_3O(1)_3O(2)_3O(3)_6F(1)_1$. The compound is decomposed as:

$$\begin{aligned}
& Ca(1) \frac{3 \times 2}{9} O(1) \frac{2 \times 3}{4} + Ca(1) \frac{3 \times 2}{9} O(2) \frac{2 \times 3}{4} + Ca(1) \frac{3 \times 2}{9} O(3) \frac{1 \times 6}{4} + Ca(2) \frac{1 \times 3}{7} O(1) \frac{1 \times 3}{4} + \\
& Ca(2) \frac{1 \times 3}{7} O(2) \frac{1 \times 3}{4} + Ca(2) \frac{4 \times 3}{7} O(3) \frac{2 \times 6}{4} + Ca(2) \frac{1 \times 3}{7} F(1) \frac{3 \times 1}{3} + P(1) \frac{1 \times 3}{4} O(1) \frac{1 \times 3}{4} + \\
& P(1) \frac{1 \times 2}{4} O(2) \frac{1 \times 3}{4} + P(1) \frac{2 \times 3}{4} O(3) \frac{1 \times 6}{4}
\end{aligned}$$

Table 64 $SrNb_2O_6$ (P21/c)

	Sr	Nb1	Nb2	O1	O2	O3	O4	O5	O6
O1	2	2	0						
O2	2	0	2						
O3	1	2	0						
O4	1	0	2						
O5	1	1	1						
O6	1	1	1						
Sr				2	2	1	1	1	1
Nb1				2	0	1	0	1	1
Nb2				2		0	2	1	1
Total	8	6	6	6	2	2	3	3	3
multiplicity	4	4	4	4	4	4	4	4	4

Z=4. The formula is : $Sr(1)_1 Nb(1)_1 Nb(2)_1 O(1)_1 O(2)_1 O(3)_1 O(4)_1 O(5)_1 O(6)_1$. The compound is decomposed as:

$$\begin{aligned}
& Sr(1) \frac{2 \times 1}{8} O(1) \frac{2 \times 1}{6} + Sr(1) \frac{2 \times 1}{8} O(2) \frac{2 \times 1}{2} + Sr(1) \frac{1 \times 1}{8} O(3) \frac{1 \times 1}{2} + Sr(1) \frac{1 \times 1}{8} O(4) \frac{1 \times 1}{3} + \\
& Sr(1) \frac{1 \times 1}{8} O(5) \frac{1 \times 1}{3} + Sr(1) \frac{1 \times 1}{8} O(6) \frac{1 \times 1}{3} + Nb(1) \frac{2 \times 1}{6} O(1) \frac{1 \times 1}{2} + Nb(1) \frac{2 \times 1}{6} O(3) \frac{1 \times 1}{2} + \\
& Nb(1) \frac{1 \times 1}{6} O(5) \frac{1 \times 1}{3} + Nb(1) \frac{1 \times 1}{6} O(6) \frac{1 \times 1}{3} + Nb(2) \frac{2 \times 1}{6} O(2) \frac{2 \times 1}{2} + Nb(2) \frac{2 \times 1}{6} O(4) \frac{2 \times 1}{3} + \\
& Nb(2) \frac{1 \times 1}{6} O(5) \frac{1 \times 1}{3} + Nb(2) \frac{1 \times 1}{6} O(6) \frac{1 \times 1}{3}
\end{aligned}$$

Table 65 LaLiPO₄ (C2/c)

	La	Li	P1	P2	O1	O2	O3	O4	O5	O6
O1	2	0	1	0						
O2	0	0	1	1						
O3	0	0	1	1						
O4	2	2	1	0						
O5	2	2	0	1						
O6	2	0	0	1						
La					1	0	0	1	1	1
Li					0	0	0	1	1	0
P1			0		1	1	1	1	0	0
P2					0	1	1	0	1	1
Total	8	4	4	4	2	2	2	3	3	2
multiplicity	4	4	8	8	8	8	8	8	8	8

Table 66 YP₃O₉ (P2₁/c)

	Y1	Y2	Y3	P1	P2	P3	P4	O1	O2	O3	O4	O5	O6	O7	O8	O9	O10	O11	O12
O1	1	0	0	0	1	0	0												
O2	1	0	0	0	1	0	0												
O3	0	0	0	1	1	0	0												
O4	0	0	0	1	0	0	1												
O5	0	0	0	0	1	1	0												
O6	1	0	0	0	0	1	0												
O7	0	6	0	1	0	0	0												
O8	0	0	0	0	0	1	1												
O9	1	0	0	0	0	1	0												
O10	1	0	0	0	0	0	1												
O11	0	0	6	0	0	0	1												
O12	1	0	0	1	0		0	0											
Y1								1	1	0	0	0	1	0	0	1	1	0	1
Y2								0	0	0	0	0	0	1	0	0	0	0	0
Y3								0	0	0	0	0	0	0	0	0	0	1	0
P1								0	0	1	1	0	0	1	0	0	0	0	1
P2								1	1	1	0	1	0	0	0	0	0	0	0
P3								0	0	0	0	1	1	0	1	1	0	0	0
P4								0	0	0	1	0	0	0	1	0	1	1	0
Total	6	6	6	4	4	4	4	2	2	2	2	2	2	2	2	2	2	2	2
multiplicity	18	3	3	18	18	18	18	18	18	18	18	18	18	18	18	18	18	18	18

Table 67 AlPO_4 (P 31 2 1)

	Al	P	O1	O2
O1	2	2		
O2	2	2		
Al			1	1
P			1	1
Total	4	4	2	2
multiplicity	3	3	6	6

Z=4. The formula is : $\text{Al}(1)_1\text{P}(1)_1\text{O}(1)_2\text{O}(2)_2$. The compound is decomposed as:

$$\text{Al}(1)\frac{2 \times 1}{4}\text{O}(1)\frac{2 \times 2}{2} + \text{Al}(1)\frac{2 \times 1}{4}\text{O}(2)\frac{1 \times 2}{2}\text{P}(1)\frac{2 \times 1}{4}\text{O}(1)\frac{1 \times 2}{2} + \text{P}(1)\frac{2 \times 1}{4}\text{O}(2)\frac{1 \times 2}{2}$$

Table 68 $\text{ScBO}_3(\text{R-3c})$

	Sc	B	O1
O1	6	3	
Sc			2
B			1
Total	6	3	3
multiplicity	6	6	18

Z=6. The formula is : $\text{Sc}(1)_1\text{B}(1)_1\text{O}(1)_3$. The compound is decomposed as:

$$\text{Sc}(1)\frac{6 \times 1}{6}\text{O}(1)\frac{1 \times 3}{3} + \text{B}(1)\frac{3 \times 1}{3}\text{O}(1)\frac{2 \times 1}{3}$$

Table 69 $\text{LuBO}_3(\text{R-3c})$

	Lu	B	O1
O1	6	3	
Lu			2
B			1
Total	6	3	3
multiplicity	6	6	18

Z=6. The formula is : $\text{Lu}(1)_1\text{B}(1)_1\text{O}(1)_3$. The compound is decomposed as:

$$\text{Lu}(1)\frac{6 \times 1}{6}\text{O}(1)\frac{1 \times 3}{3} + \text{B}(1)\frac{3 \times 1}{3}\text{O}(1)\frac{2 \times 1}{3}$$

Table 70 LaBO₃(P m c n)

	La	B	O1	O2
O1	3	1		
O2	6	2		
La			1	3
B			1	1
Total	9	3	2	4
multiplicity	4	4	4	8

Z=4. The formula is : $La(1)_1B(1)_1O(1)_1O(2)_2$. The compound is decomposed as:

$$La(1)\frac{3\times 1}{9}O(1)\frac{2\times 1}{2} + La(1)\frac{6\times 1}{9}O(2)\frac{3\times 2}{4} + B(1)\frac{1\times 1}{3}O(1)\frac{1\times 1}{2} + B(1)\frac{2\times 1}{3}O(2)\frac{1\times 2}{4}$$

Table 71 SrZrO₃ (P b n m)

	Sr	Zr	O1	O2
O1	6	4		
O2	2	2		
Sr			2	2
Zr			2	2
Total	8	6	4	4
multiplicity	4	4	8	4

Z=4. The formula is : $Sr(1)_1Zr(1)_1O(1)_2O(2)_1$. The compound is decomposed as:

$$Sr(1)\frac{6\times 1}{8}O(1)\frac{2\times 1}{4} + Sr(1)\frac{2\times 1}{8}O(2)\frac{2\times 1}{4}Zr(1)\frac{4\times 1}{6}O(1)\frac{2\times 2}{4} + Zr(1)\frac{2\times 1}{6}O(2)\frac{2\times 1}{4}$$

Appendix C: XRD patterns of Sb^{3+} -doped compounds

In this appendix we show the XRD patterns of Sb^{3+} -doped closed shell transition metal oxides that were prepared in this work with the corresponding JCPDS reference spectrum (in red) of the obtained structure. The patterns were in general considered acceptable despite the presence of few weak reflections represented by (*) on some spectra that do not correspond to the obtained phase. These were not considered as important enough to affect the luminescent properties.

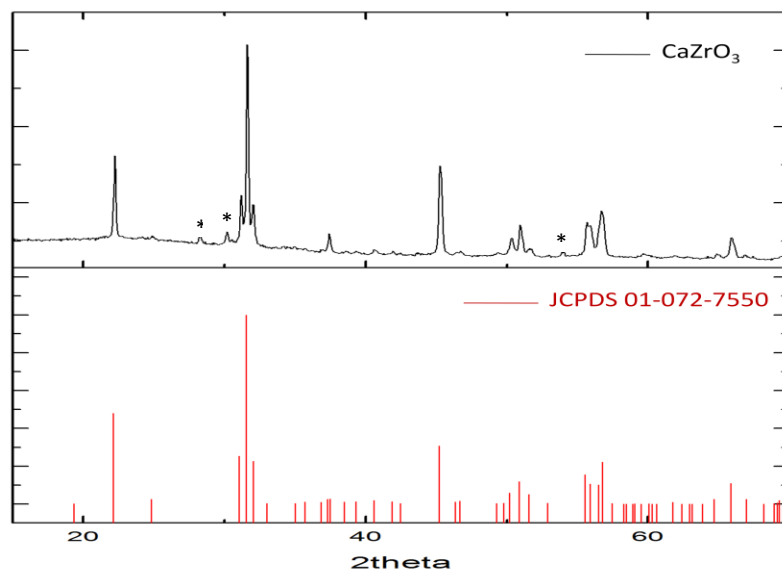


Figure 23 XRD pattern of $\text{CaZrO}_3\text{-Sb}^{3+}$ with JCPDS standard 01-072-7550

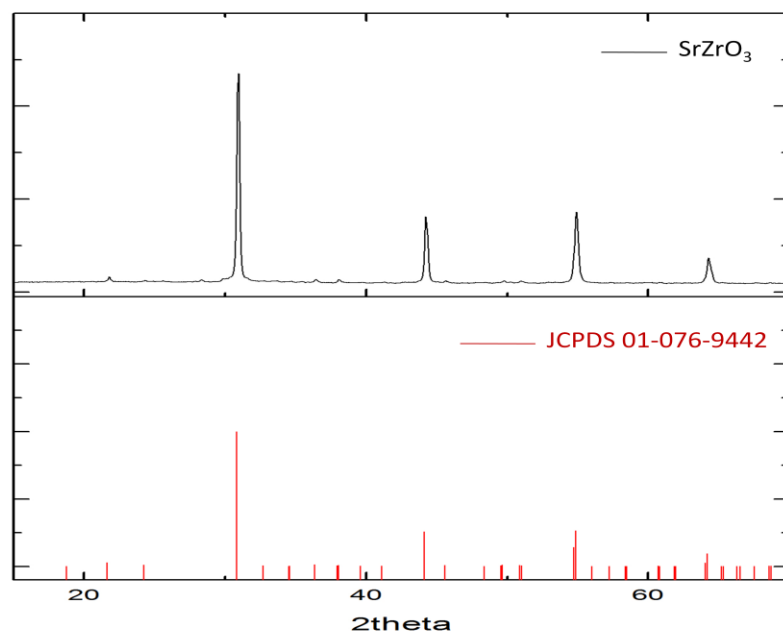


Figure 24 XRD pattern of $\text{SrZrO}_3\text{-Sb}^{3+}$ with JCPDS standard 01-076-9442

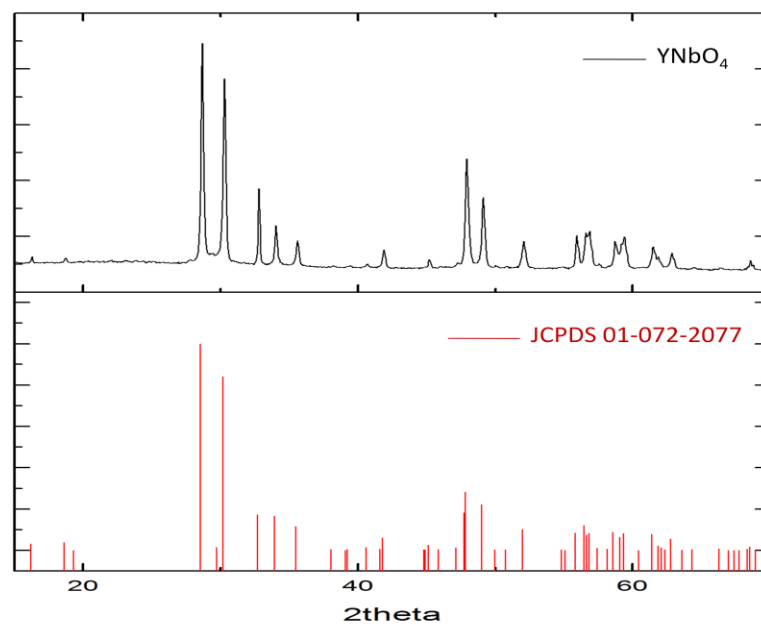


Figure 25 XRD pattern of $\text{YNbO}_4\text{-Sb}^{3+}$ with JCPDS standard 01-072-2077

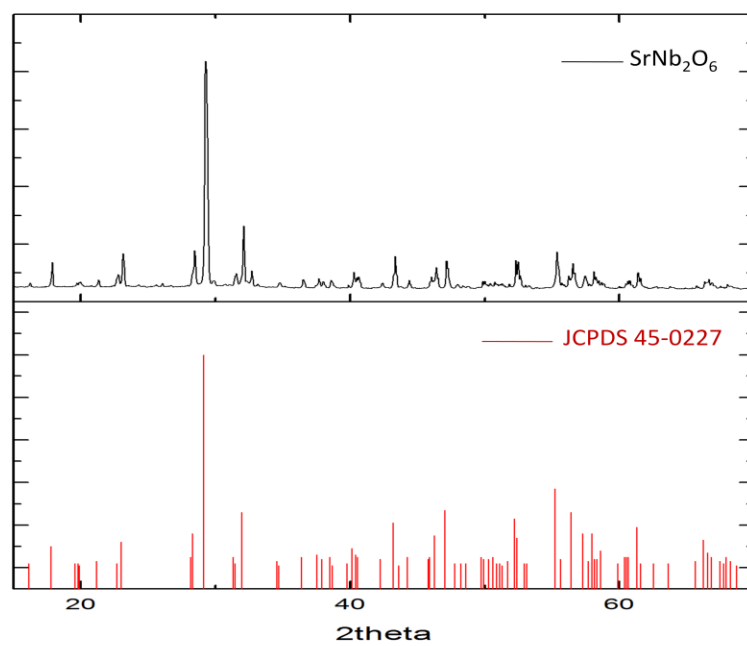


Figure 26 XRD pattern of $\text{SrNb}_2\text{O}_6\text{-Sb}^{3+}$ with JCPDS standard 45-0227

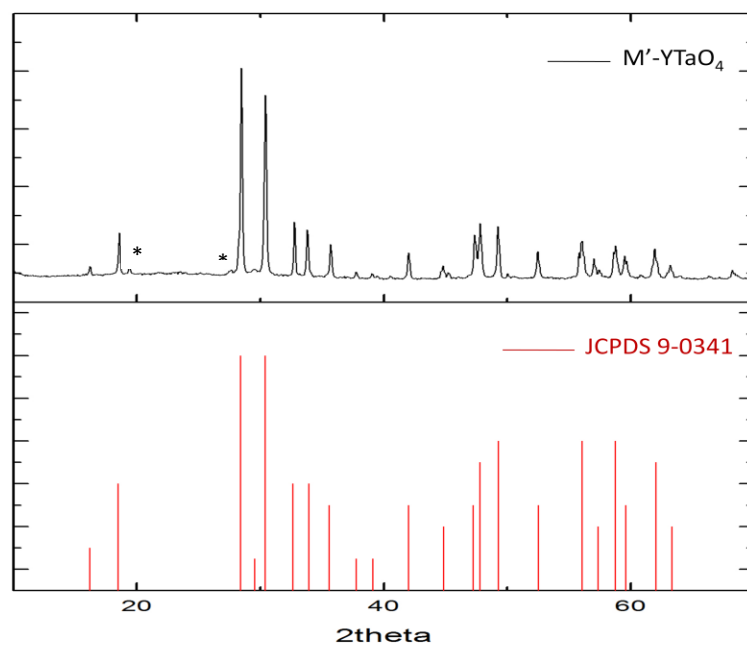


Figure 27 XRD pattern of $\text{M}'\text{-YTao}_4\text{-Sb}^{3+}$ with JCPDS standard 9-0341

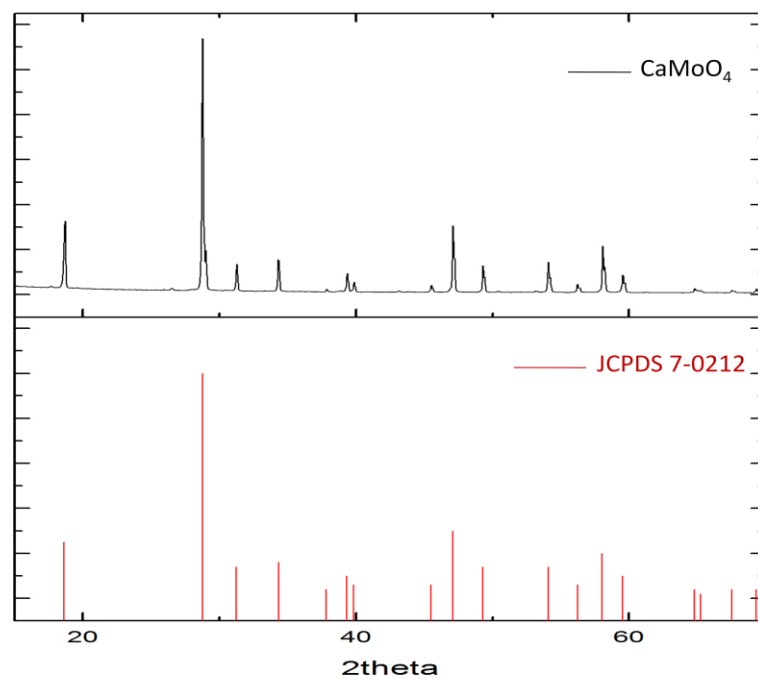


Figure 28 XRD pattern of $\text{CaMoO}_4\text{-Sb}^{3+}$ with JCPDS standard 7-0212

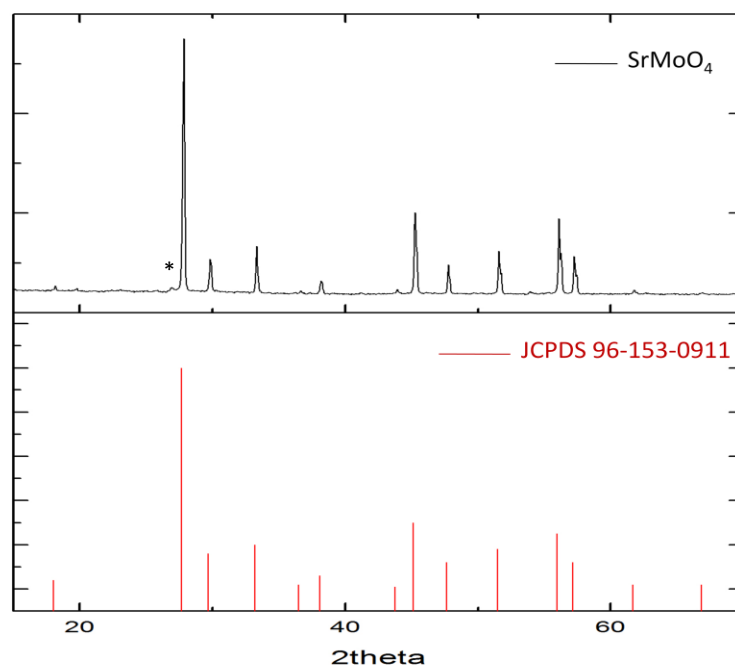


Figure 29 XRD pattern of $\text{SrMoO}_4\text{-Sb}^{3+}$ with JCPDS standard 96-153-09

